A Prototype Remote Structural Health and Security Monitoring System for Bridges

Submitted by
Jason K. Herrman and
Kirk A. Grimmelsman

MBTC 3014
October 2014

Prepared for
Mack-Blackwell Rural Transportation Center
University of Arkansas

ACKNOWLEDGEMENT
This material is based upon work supported by the U.S. Department of Transportation under Grant Award Number DTRT07-G-0021. The work was conducted through the Mack-Blackwell Rural Transportation Center at the University of Arkansas.

DISCLAIMER
The contents of this report reflect the views of the authors, who are responsible for the facts and the accuracy of the information presented herein. This document is disseminated under the sponsorship of the Department of Transportation, University Transportation Centers Program, in the interest of information exchange. The U.S. Government assumes no liability for the contents or use thereof.

ABSTRACT

The main objective of this research project was to develop and utilize a prototype structural health monitoring system for bridge and to evaluate and refine corresponding experimental methods for quantitatively characterizing the global condition of the structure. Furthermore, various experimental methods considered to be suitable for conducting rapid and quantitative safety evaluations of bridges following natural or manmade hazards were the specific focus of this research. Presently, the safety and serviceability of bridges critical for use in emergency response and recovery operations are evaluated through on-site visual inspections of individual structures by teams of specially trained engineers or technicians; a process that is manpower-intensive, subjective, and slow. Analytical and controlled static testing methods were employed to create baseline characterizations of the structural state and different strategies and procedures employing dynamic testing methods for evaluated in conjunction with the baselines to assess their potential for rapid and reliable assessments of bridge structures both during their normal service operation and in the immediate aftermath of hazard events. The quantitative obtained for prototype structure evaluated in this research were compared using a modified load rating developed from the relevant AASHTO bridge evaluation specifications. The research was conducted using instrumented physical models to minimize the influences of some uncertainties associated with the behavior of full-scale structures and make the comparisons more transparent, and because it was not possible to implement and evaluate controlled damage scenarios on a full-scale, in-service bridge. The effectiveness of different dynamic testing and characterization strategies, different instrumentation schemes and data acquisition architectures, data processing and analysis approaches, and their optimal integration was systematically evaluated in the laboratory using a structural identification framework, and this framework is also suitable for implementing these approaches on full-scale bridges.

TABLE OF CONTENTS

LIST OF FIGURES

LIST OF TABLES

1. INTRODUCTION

1.1 BACKGROUND

A safe and efficient transportation infrastructure system is vital to sustaining the nation's economic and societal well-being. The U.S. economy is implicitly supported by the widespread access and interconnectedness of different cities distributed over vast geographic distances. Businesses depend on goods being delivered from all over the country in a timely and efficient manner. Metropolitan areas depend on food being delivered to the cities by trucks from adjacent farming communities, or in many cases, farming communities in other states. The fact that many infrastructure assets are becoming aged beyond their expected life-span poses serious concerns about the welfare of our nation's infrastructure system.

Natural or man-made hazard events can adversely impact the normal utility of transportation infrastructure systems, but more importantly, they can limit the serviceability and safety of transportation infrastructure systems for emergency response and recovery operations that occur in the aftermath of such events. This is especially true for bridges since the function of these structures is to allow the transportation system to overcome the various natural and other physical obstructions that would otherwise limit the continuity of the transportation network.

Furthermore, the occurrence of a hazard event will impact the utility of bridge structures whether or not they have actually sustained damage during the event. The loads that are associated with hazard events have the potential to damage bridge structures, and until the condition of a bridge that has experienced a hazard event has actually been evaluated, it is practically impossible to reliably assess its serviceability and safety. It follows that using bridges with unknown serviceability and safety characteristics must be restricted due to life-safety considerations. Those bridges that are found to have actually sustained damage as a result of a hazard must be further evaluated to determine if they can safely and reliably handle their normal operational loads in addition to the live loads associated with emergency response and post-hazard recovery operations.

Most bridges in urban areas are subject to high levels of service demands, and if the use of one or more of these structures is restricted as a result of a hazard event, it would impact vast numbers of people. Furthermore, the ability to quickly move the manpower and supplies critical for the ensuing emergency response and recovery operations would also be reduced, since many critical transportation pipelines into and out of that city would be shut down. Given the high population densities found in cities, even having a small number of bridges shut down would create a large demand on the remaining bridges on any available detour routes. The traffic would back up, and the bridges located on alternate routes would be subject to usage in excess of their normal service level demands.

It can also be argued that the effect of hazard events on the utility of bridge structures is just as critical in rural regions as it is for densely populated urban areas. While population density leading to high demand is not an issue, increased travel times and distances are critical concerns. In rural areas, the loss of a single bridge can easily lead to very long detours that in some cases can exceed 50 miles or more. The amount of traffic would not be great, but the added time for emergency response and recovery vehicles to make a given route would be greatly affected. Rural areas often have few alternative routes, and they are typically spread over very large distances.

It is clear that bridges are vital to sustaining the nation's economic and societal well-being and play a critical role in emergency response and recovery operations after hazard events. In the aftermath of a hazard event, it is vitally important to be able to rapidly and reliably determine if critical bridges were damaged, and to evaluate if those bridges are functional for emergency response and recovery operations.

1.2 CURRENT STATUS OF U.S. BRIDGES

President Dwight D. Eisenhower championed the campaign to connect the country with an Interstate Highway System by signing into law the Federal-Aid Highway Act of 1956 (Weingroff, 1996). This Act started a wave of construction of highways and bridges across the country. Unfortunately, a significant percentage of this transportation infrastructure has been inadequately maintained and renewed in subsequent years.

The U.S. has a considerable number of bridges built in the 1950's and 1960's that are in need of serious repair or replacement. Many of the bridges constructed during this period were only expected to be in service for 50 years, and the average bridge in this country today is 43 years old (AASHTO, 2010). Furthermore, many of the bridges constructed during this period may have received minimal to no maintenance during their lifespans. According to the 2009 ASCE Infrastructure Report Card, the overall condition of America's bridges merits a 'C' grade, while the overall infrastructure rates as a 'D' (ASCE, 2009).

When one looks at the Bureau of Transportation Statistics (2010), it can be seen that of the 603,259 total U.S. Highway Bridges, 149,654, or 24.8%, of them are “Structurally Deficient” or “Functionally Obsolete.” Figure 1.1 provides additional details on the overall condition of U.S. Bridges. It is notable that the percentage of structurally deficient bridges in the total bridge inventory was only marginally decreased over a 10 year timeframe. Clearly, the overall performance and condition of the U.S. bridge inventory is a problem that likely will not be resolved in the short-term at current funding levels. Furthermore, the aged and deteriorated condition of the nation’s bridges adds significant uncertainty to the problem of rapid and reliable safety evaluations of these structures following hazard events.

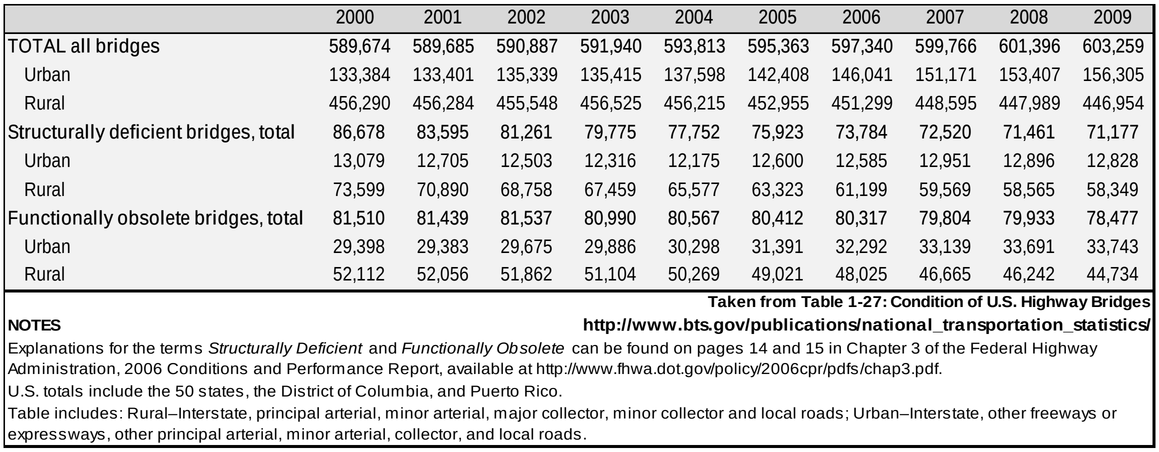

	2000	2001	2002	2003	2004	2005	2006	2007	2008	2009
TOTAL all bridges	589,674	589,685	590,887	591,940	593,813	595,363	597,340	599,766	601,396	603,259
Urban	133,384	133,401	135,339	135,415	137,598	142,408	146,041	151,171	153,407	156,305
Rural	456,290	456,284	455,548	456,525	456,215	452,955	451,299	448,595	447,989	446,954
Structurally deficient bridges, total	86,678	83,595	81,261	79,775	77,752	75,923	73,784	72,520	71,461	71,177
Urban	13,079	12,705	12,503	12,316	12,175	12,600	12,585	12,951	12,896	12,828
Rural	73,599	70,890	68,758	67,459	65,577	63,323	61,199	59,569	58,565	58,349
Functionally obsolete bridges, total	81,510	81,439	81,537	80,990	80,567	80,412	80,317	79,804	79,933	78,477
Urban	29,398	29,383	29,675	29,886	30,298	31,391	32,292	33,139	33,691	33,743
Rural	52,112	52,056	51,862	51,104	50,269	49,021	48,025	46,665	46,242	44,734

Taken from Table 1-27: Condition of U.S. Highway Bridges

NOTES **http://www.bts.gov/publications/national_transportation_statistics/**

Explanations for the terms *Structurally Deficient* and *Functionally Obsolete* can be found on pages 14 and 15 in Chapter 3 of the Federal Highway Administration, 2006 Conditions and Performance Report, available at http://www.fhwa.dot.gov/policy/2006cpr/pdfs/chap3.pdf.

U.S. totals include the 50 states, the District of Columbia, and Puerto Rico.

Table includes: Rural–Interstate, principal arterial, minor arterial, major collector, minor collector and local roads; Urban–Interstate, other freeways or expressways, other principal arterial, minor arterial, collector, and local roads.

Figure 1.1: Summary of U.S. Bridge Conditions (Bureau of Transportation Statistics, 2010)

1.3 CONDITION ASSESSMENT AND EVALUATION PRACTICE FOR BRIDGES

The condition of U.S. bridges is assessed and evaluated on a regular basis as required by the National Bridge Inspection Program (NBIP). The NBIP was initiated in 1968 following the catastrophic collapse of the Silver Bridge over the Ohio River, and since then has required that most bridges be inspected every 24 months to evaluate their condition, with a 30 day grace period (National Bridge Inspection Standards, 2004). Currently, the condition of a bridge is assessed and evaluated primarily on the basis of visual inspection (VI) data. VI data is obtained by an inspector physically looking over the structure and reporting deterioration and damage such as rust, cracks, proper weld terminations, changes in cross-section, stress concentrations, etc. (Michael Baker Jr., Inc., 1995). This data is then translated into a bridge condition rating, and a load rating. Although this is the accepted approach for supporting routine maintenance management decisions for bridges, there are several important limitations with this condition assessment and evaluation method. There are also challenges and limitations related to the use of this approach for evaluating bridges that have experienced hazard events. In such cases, the serviceability and safety of many bridges needs to be assessed and evaluated very rapidly and reliably to support critical emergency response and recovery operations.

1.3.1 Limitations of Visual Inspection

There are a number of important limitations associated with the use of VI as a method for condition assessment and evaluation of bridges for routine maintenance management decisions or for supporting emergency response and recovery operations after hazard events. While the percentage of "Structurally Deficient" or "Functionally Obsolete" bridges is seen to be slowly decreasing as a function of time (see Figure 1.1), the ASCE Report Card gives five points of action in order to raise the grade of our bridge system, with one of the items being "Update Bridge Inspection Standards…," (ASCE, 2009). While visual inspection does take a great deal of experience and knowledge to be performed reliably, it provides subjective descriptions of bridge condition. Furthermore, visual inspection techniques are prone to a number of other limitations, which have been shown to affect the reliability of the resulting evaluations. A study evaluating the visual inspection results for bridges that was conducted by the Federal Highway Administration (FHWA) found that between different inspectors, 95% of bridge condition ratings would vary within 2 points on the same structure (Moore, 2001). Several other inconsistencies were noted within the inspection procedures and the results obtained, further showing that visual inspection can be subjective and variable.

Visual inspection is also inherently qualitative in nature, resulting in qualitative descriptions of the overall bridge health. An inspector is often limited to what can be described by the accessibility of different parts of the bridge, and is also mostly limited to surface defects and not subsurface conditions. While nondestructive evaluation (NDE) methods are sometimes used in conjunction with the visual inspection to mitigate some of these limitations, it still will only yield a very local description of a given problem. Being able to take these local descriptions and translate them into a global assessment of the bridge still only provides a qualitative description of the overall bridge health. Extrapolating data from localized descriptions of problems into a global picture of the condition of the structure also amplifies any uncertainties that are present in the initial visual descriptions. Visual inspection techniques also require a significant amount of manpower, time, and money to both collect the data and to process the data into usable results, like a bridge rating.

The visual inspection method of evaluating a bridges' overall structural health is an inefficient method for a rapid, post-hazard condition assessment and evaluation of bridges. It takes both man-power and time to complete, and produces only qualitative results based on subjective descriptions. Further, this method does not provide a global picture of the overall bridge health, and it is difficult to see hidden problems.

There are also other challenges that make it difficult to evaluate the safety of bridge structures rapidly and reliably following a hazard event. It is seen that the only baseline available is a qualitative one based on visual inspection. Each structure is also unique, and has its own characteristics. Furthermore, there is limited knowledge on how the effects of existing defects, damage and deterioration will ultimately affect the safety and serviceability of a bridge that has been exposed to a hazard event. Given these challenges, a more reliable method is needed for rapidly evaluating the safety of bridge structures following hazard events.

1.3.2 Assessment of Bridges following Hazard Events

In the aftermath of a hazard event, the most immediate assessment and evaluation need with respect to bridges is to determine if a structure is still serviceable and safe for the live loads associated with emergency response and recovery operations. One can see that visual inspection techniques alone clearly do not address the needs present when determining the safety of a bridge following a hazard event. VI is neither rapid nor remote, it requires a person or team to carry out the inspection on site, it is subjective, and it takes local damage information and infers a global safety rating of a structure. Clearly a different approach is needed.

There are two basic approaches that can be employed to evaluate the safe load carrying capacity of a bridge structure following a hazard event. The first approach is to rely almost exclusively on analysis. In this approach, the loads that would be induced on the bridge as a result of various hazard events are predicted based on empirical and/or probabilistic analysis. The structure can then be evaluated using analytical or finite element models and engineering mechanics principles to predict where damage may occur and to evaluate the effects of this damage on the serviceability and safe load capacity of the structure. However, several problems exist with this approach. Given the uncertainties and existing knowledge gaps related to failure modes and mechanics, limitations exist in the ability to accurately predict actual loads due to any number of possible hazard events. Obtaining reliable predictions of the damage that will occur due to a hazard event is not a simple task, especially considering the variety of structural designs and details.

Furthermore, “as-built” plans are often hard to come by, and pose problems for creating accurate base-line models. Without knowing all the details of a bridge design, including materials and geometry, it would be nearly impossible to create an accurate finite element model. These details present a significant challenge for obtaining a very reliable prediction of the safe load carrying capacity of even a new structure in “perfect condition” following a hazard event. The task is further complicated by the constructed nature of bridges that leads to additional uncertainties related to how any existing defects, deterioration or damage will affect the overall safety and serviceability of a bridge. Incorporating these attributes of an aged in-service structure into the prediction of safe load carrying capacity introduces even more uncertainty to the evaluation. Clearly this approach is not the most efficient or effective.

A second approach is to experimentally characterize the structure. Experimental characterization methods include local Non-Destructive Evaluation (NDE), static testing methods, and dynamic testing methods. NDE still contains the problem of only being able to pinpoint a local defect or damage, and a global picture of stability must still be inferred. Static testing techniques would include doing static load tests measuring the displacement and/or strains induced on the structure. This technique can be rather cumbersome in setup, and also may require applying heavy loads to a structure where the safety is in question, as seen in Figure 1.2. Dynamic testing, on the other hand, can be done remotely and provide a global picture of health. Continuous monitoring is achievable, and a variety of test methods are available.

It is proposed that in using dynamic testing with modal analysis, one can determine a benchmark characteristic response of a bridge that can be used in lieu of, or along side with, visual inspection techniques to rate a bridge's safety. Dynamic characterization includes dynamic properties, which are structural characteristics of a system. These characteristics are functions of the structural configuration, stiffness, boundary conditions, mass, etc. Any changes in structural characteristics due to damage, whether over time or from a hazard event, may be reflected in the dynamic properties. A benefit of experimental characterization is that no assumptions are made; the properties obtained are the actual properties of the structure. The only error induced is human error in measurements, which can be limited if tested properly.

It is clear that dynamic testing techniques prove to be the most effective testing strategy for objectively characterizing a structure. Static testing is hard to implement on real structures, and analytical methods are only as good as the models used. Therefore, this research thesis primarily addressed dynamic testing methods, and focused on strategies and practices for optimizing remote monitoring systems on bridges in order to rapidly characterize a bridge after a hazard event.

Figure 1.2: Static Bridge Testing Example

2. SCOPE OF WORK

The objective of this research project was to devise and refine Structural Health Monitoring (SHM) methods and the associated quantitative characterization methods with the specific goal of enabling rapid and reliable safety evaluations of critical transportation infrastructure elements, and in particular bridges, following natural or manmade hazards. Presently, the safety and serviceability of these transportation infrastructure assets for use in emergency response and recovery operations are evaluated through on-site visual inspections of individual structures by teams of specially trained engineers or technicians; a process that is manpower-intensive, subjective, and slow.

The researchers were able to identify and evaluate different strategies and procedures using dynamic testing methods to rapidly and reliably characterize in-service structures both during their normal operation, and in the immediate aftermath of hazard events. The global level quantitative characterization of a bridge obtained through dynamic testing can serve as a baseline for SHM of the structure. The research program included laboratory investigations of this approach using two small scale physical model structures. The effectiveness of different dynamic testing and characterization strategies, different instrumentation schemes and data acquisition architectures, data processing and analysis approaches, and their optimal integration was systematically evaluated in the laboratory using a structural identification framework, and will be implemented in the future in a field study. Specifically, modal flexibility was the main comparison tool within the dynamic testing, given that it provides an accurate representation of the structure, and provides a global picture of the structural response.

2.1 RESEARCH OBJECTIVES

The research presented had four objectives, each of which are described below and explained in the following sections.

2.1.1 Optimum Bridge Health Monitoring Strategy

The overarching objective of the research was to recommend an optimum bridge health monitoring strategy. This strategy was to be a dynamic testing system able to rapidly and remotely asses the damages acquired by a bridge following a hazard event. It would include the best “before” and “after” testing strategies (analytical, static, impact, shaker, ambient, or combinations) for assessing the bridge’s global safety. In order to fulfill this objective, three additional objectives were created as supporting objectives, and are explained in the following sections.

2.1.2 Dynamic Testing Strategies

A secondary goal was to evaluate the effectiveness of different dynamic testing and characterization strategies, different instrumentation schemes and different data acquisition architectures. Three different types of dynamic tests were evaluated: impact testing, shaker testing, and ambient testing. In the first two cases, both the inputs and outputs were measured. With ambient testing, only the outputs were measured.

Dynamic testing has been around for a long time, with pioneering work on bridges starting in the 1950's and 1960's (Varney & Galambos, 1966). Cantieni (1984) summarized a series of dynamic tests on bridges using several different input types, with the goal of relating frequencies to span length. In the 1980's and 1990's structural identification procedures were heavily studied, with Douglas and Reid (1982) being the first. Aktan et al. (1997) developed a structural identification framework for analyzing structures, and provided examples using impact, shaker, and ambient testing. Results showed very similar modal properties from the impact and shaker testing, but relied on ambient vibrations only for long term monitoring. Farrar et al (2000) reported on the variability of modal parameters and used impact as well as ambient vibration testing. Analysis revealed that relying on modal frequencies and mode shapes alone was not adequate for identifying damage. Moyo et al. (2004) used shaker and ambient testing to study the change in modal parameters of a bridge that underwent renovations in Singapore. While the previously mentioned studies were excellent studies that were important to the field, none of them studied the direct differences between the types of tests when it came to pre- and post-change. The research tended to rely on forced input testing to create an initial characterization, with long term monitoring done with ambient testing to monitor changes in frequencies and mode shapes.

Many other studies have been done with intentionally applied damage scenarios to develop methods to detect and/or locate damage. Most of these relied on the same type of test before and after the damage was induced, and therefore did not provide input into the differences between impact, shaker, and ambient testing, nor did they provide insight into which type of test would be best suited for rapid condition assessment following a hazard event. Raghavendrachar and Aktan (1992) presented a method for obtaining modal flexibility from multi-reference impact testing. The modal flexibility indices proved more reliable than using the modal parameters alone to identify damage. Toksoy and Aktan (1994) carried out multiple reference impact tests during several levels of damage induced to a bridge structure, and used modal flexibility to locate the damage. Aktan et al (1993) carried out shaker testing of a structure tested to failure. To further investigate damage detection possibilities, the Seymour Avenue Bridge in Cincinnati, OH was subjected to several damage scenarios and tested extensively (Aktan et al. 1997; Catbas et al. 2004; Catbas & Aktan, 2002). The bridge was subjected to multi-reference impact testing and truck loading tests, and modal flexibility and static flexibility were compared. In these research papers, the authors use dynamic testing and modal flexibility to locate or identify that damage has occurred, with no further action taken. One goal of the research presented here was to use the modal flexibility matrix to quantify the damage that may be present due to some hazard event.

While there has been a significant amount of work done towards dynamic testing, most studies have focused on structural identification, damage detection, and long term monitoring with ambient vibrations. Little work has been done to establish what types of tests would be optimal for pre-incident and post-incident testing to obtain the best characterization. Some papers have pointed out that modal frequencies and mode shapes are similar from the different tests, but this notion was not fully carried out to compare structural characterizations before and after damage. In this research, the goal was to systematically evaluate the different testing methods and determine the best pre- and post-incident testing procedures in order to quantify damage obtained by a bridge due to some hazard event.

The final part of dynamic testing strategies that was briefly explored was hardware and software issues. Each of the different testing methods (impact, shaker, and ambient) had the ability to be employed with any number of instrumentation schemes or data acquisition architectures. In this research, three different data acquisition architectures were used in various stages of testing in order to evaluate the effectiveness of each one and note any serious differences. These are explained in later sections. In addition, several different software packages were used to facilitate the testing and for post-processing of the experimental data. M+P International produces an off-the-shelf modal testing and analysis software package called, "Smart Office," and was evaluated in order to assess its effectiveness and ease of use in modal testing. National Instruments produces a software package called, "Signal Express," that was also used for data collection in two of the different architectures. Data Physics Corporation produces proprietary software to be used with its dynamic signal analyzer hardware, which was one of the architectures used. Finally, post-processing techniques were carried out in MATLAB in order to obtain modal properties not found from the other packages.

2.1.3 Experimental Sensor Optimization

Some work has been done with regard to sensor location optimization, but configuration is often decided upon based on experience and engineering judgment. Kripakaran et al. (2007) developed a global search algorithm for optimizing sensor placement, and found it to be effective for designing measurement systems on previously unmonitored structures. The main objective in sensor placement was to be able to detect damage. The algorithm developed took several proposed damaged scenarios and ran them through a looped process that reduced the number of sensors needed. This approach proved to be unfeasible due to the need for several damage scenarios to be envisioned with finite element (FE) models, and the specific algorithm obtained. Another researcher compared six different methods of sensor placement optimization (Meo, 2005). The test structure was a narrow width suspension bridge, and took the first three modes as the controlling modes of the structure. Catbas (2006) compared the mode shapes of a bridge based on sensors placed on two girders vs. all six girders, and found that the smaller set of nodes was adequate in the determination of mode shapes and frequencies. A similar work was undertaken by Wang (1998) showing the differences with mode shapes and frequencies when taking a small subset of nodes of a long span bridge. The methods employed for optimizing the structures were based on specific algorithms, while this research focused on optimal sensor placement determined through experimental methods.

Ideally, a large number of sensors would be used on a given structure to most closely identify all of the contributing modes and accurately depict the associated mode shapes. Using more sensors increases the spatial resolution of any identified modes, and also provides redundancy to the instrumentation setup. If a sensor is later found to have malfunctioned, it could be disregarded and one could rely on the remaining sensors. In reality though, sensors cost money, and each additional channel in a given Data Acquisition Unit will add cost to the system. This research compared the effects of different sensor setups on the identification results in an attempt to find the most critical sensors for each setup.

Therefore, a systematic removal of sensors from the testing setup was performed. The actual sensors were not removed from the structure and a new test was not performed each time. Instead, the response readings were removed from the full test data sets in the form of removing an entire column from the frequency response function (FRF) matrix. This way, the exact same test data was used and the uncertainty from taking new data was removed. The modal flexibility was re-calculated and compared with the results containing the full set of sensors. While these results were solely based off a laboratory study, they help to show where sensors are of the most use in a testing setup of a bridge. Since more sensors equals more money in hardware, software, and setup time, these results will be extremely useful for bridge testers.

2.1.4 Modified Load Rating

There exists a need for obtaining a load rating, or modified load rating, from the dynamic characterization of a structure. Static load testing as a means of load rating has been practiced for some time. Many authors have developed load ratings for bridges in previous research, but they primarily do so from updated finite element models of the structure of concern. Brownjohn et al. (2001) summarized efforts and presented a case study on condition assessment through FEM updating. Kangas et al. (2004) summarized work from the University of Cincinnati Infrastructure Institute aimed at obtaining load ratings from updated FE models. Ren et al. (2004) created an accurate finite element model of the Roebling Suspension Bridge, and using dynamic testing, updated the model to match the measured characteristics of the bridge. From the updated model, the authors were able to come up with a bridge load capacity. Catbas, Ciloglu, & Aktan (2005) worked to identify parameters common to populations of bridges, and identify variation from statistical samples. This work was achieved through field calibrated finite element models.

Several researchers have shown that load rating is possible through finite element model updating. The problem with the approach used is that a FE model must be made for each structure and updated with any damage in order to achieve a load rating. The updating of the model to match the characterization found from dynamic testing is a time consuming process. Eliminating the need for a calibrated FE model would greatly shorten the time needed to obtain a load rating. One goal of the research presented here was to investigate if there was a way to obtain a load rating from the flexibility matrix produced from the dynamic testing, thereby bridging the gap between dynamic characterization and usable results for bridge owners.

2.2 CHARACTERIZATION METHODS USED

Results from dynamic testing and the characterization strategies were confirmed by the use of static and analytical evaluation techniques. Static testing produced a static flexibility matrix, which was directly compared to the modal flexibility matrix obtained from dynamic testing. Analytical techniques included a finite element model of both of the test structures in SAP2000, and the implementation of a theoretical solution for the simple cantilever case. The SAP2000 model allowed for dynamic and static characterization. It also performed modal analysis of the test structures, and was compared with the other testing techniques in order to validate the results. See Figure 2.1 for more information.

Structural flexibility was used as the baseline characterization compared in this study. The flexibility matrix of a structure has been shown to be a reliable signature reflecting the existing condition of a bridge (Aktan, 1994; Catbas, 2002), and has been shown to be able to detect localized damage (Raghavendrachar & Aktan, 1992; Catbas, 2006). Mode shapes and frequencies have been used in the past as a comparison tool, but a study on the Alamosa Canyon Bridge showed that the natural frequency would vary by as much as 10% throughout the year due to weather changes (Farrar, 1997). A study done by Toksoy and Aktan showed that localized damage showed a 5.8% frequency shift, and that post-processing errors and temperature effects also caused a 5% shift, concluding that a frequency shift alone could not be taken as a definite damage indicator (Toksoy, 1994). It was also shown in this paper that flexibility and deflected shapes based off of flexibility proved to be damage sensitive indices. Another study done by Catbas, Gul, and Burkett used flexibility based curvature and deflection for damage detection and found these indices performed well as indicators and locators of damage (Catbas, 2008). Modal flexibility and deflected shapes based on loading patterns applied to the flexibility matrix were used by the author as part of the structural condition evaluation in this research.

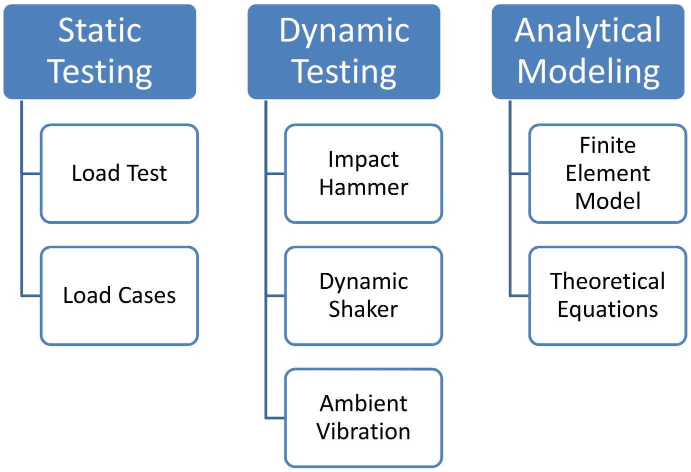

Figure 2.1: Characterization Techniques

2.3 OVERVIEW OF RESEARCH PROCESS

The validation of characterization techniques was implemented on two separate laboratory test structures, a cantilever model and a steel grid model structure. The testing procedure implemented was a four tiered approach, as shown in Figure 2.2. Several of the different types of tests were performed in each of the tiers. Static load testing was the first test, followed by impact hammer dynamic testing, then dynamic shaker testing, and finally ambient input testing. In the first tier, a cantilever beam was used as the test structure. The reason for choosing such a structure was because it was a simple structure to conceptualize and analyze, and numerous closed-form solutions describing its static and dynamic behavior are readily available. The testing performed on the cantilever beam served a number of objectives including validating: (1) execution of the different dynamic testing methods, (2) the sensors and data acquisition settings, (3) the data analysis and post-processing methods (CMIF algorithm, M+P software, and MATLAB code), and (4) the modal flexibility computation from the dynamic properties.

After testing was completed on the cantilever beam, the testing approaches and analysis methods were applied to a more complicated structure. A steel grid model was constructed in the research lab which provided an excellent avenue of expanding the proposed test methods to a bridge-type structure. This structure will be referred to as the "grid" for the remainder of this document. The grid was built of standard W8X10 beam sections and bolted with gusset plates at the joints. Since this structure did not contain a concrete deck, it was not as stiff as a girder bridge would be, but still provided excellent characteristics for evaluating an optimal SHM method on simply supported bridge type structures. The grid was tested in a similar manner as the cantilever beam, starting with static loading and ending with ambient vibration testing.

The grid testing was used to explore and verify the capabilities of the testing and data analysis methods for detecting damage applied to the structure. Several different damage scenarios were induced on the grid, and the same series of dynamic tests done after each damage case. The results from these tests showed how the structure changed globally due to localized damage scenarios. The specific damage scenarios that were evaluated with the grid model included:

1. Removal of support pillar.
2. Removal of transverse beam(s).
3. Removal of gusset plate(s).

Finally, a systematic removal of sensors from the testing setup was performed. For each damage case, the modal flexibility was re-calculated and then compared with the results containing the full set of sensors. The results from these tests helped to show where sensors were of the most use in a testing setup of a bridge.

Overall, the capabilities of the different dynamic characterization approaches were evaluated to determine the most reliable and effective strategies and procedures needed to rapidly evaluate the safety and serviceability of full-scale bridges following hazard events. Strategies for enabling the safety and serviceability evaluation to be performed remotely were also evaluated. Specifically, the recommended experimental, analytical and data analysis procedures to accomplish this were identified and evaluated.

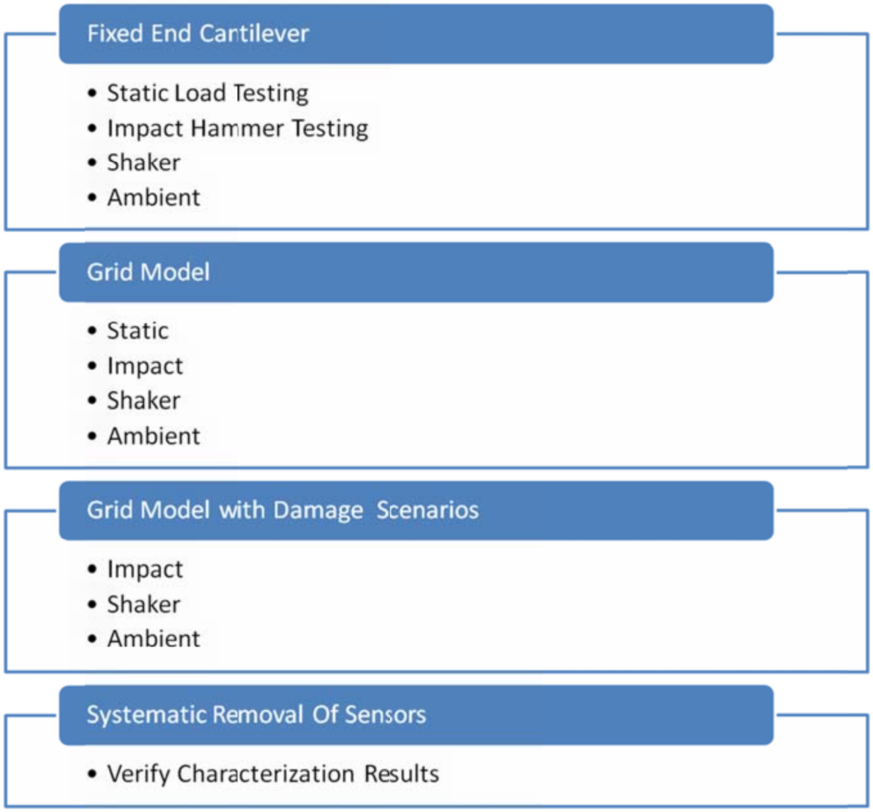

Figure 2.2: Testing Process

3. DATA PROCESSING METHODS

There are many post-processing techniques available for extracting the dynamic characteristics (modal frequencies, modal vectors and modal scaling) of a structure using the measured input and its measured vibrations. Several different methods exist in both the time domain (Complex exponential algorithm, Least squared complex exponential, Polyreference time domain, Ibrahim time domain, Eigensystem realization algorithm, etc.) and the frequency domain (Polyreference frequency domain, Simultaneous frequency domain, Multi-reference frequency domain, Rational fraction polynomial, Complex mode indicator function, etc). Each of these modal parameter estimation techniques has its own set of advantages and disadvantages. Catbas (1997) and Ciloglu (2006) thoroughly explored the formulation and background of the different methods as well as some of the advantages and disadvantages in their respective doctoral dissertations. Both are recommended as excellent sources of additional background information. Allemang (1999) also provides a comprehensive background on the different types of available post-processing techniques in his Vibrations III course notes from the University of Cincinnati.

The Complex Mode Indicator Function (CMIF) based parameter estimation is one technique that has been successfully used to extract the dynamic characteristics from bridge vibration measurements and to identify modal flexibility (Catbas, Brown, & Aktan, 2004). Given that the CMIF algorithm has a well-documented application history for the dynamic characterization of bridges, it was selected as the primary modal parameter estimation technique that would be used for the post-processing of the dynamic measurements obtained from this research. The CMIF algorithm is often combined with another algorithm, the Enhanced Frequency Response Function (eFRF), to accurately scale the mode shape vectors. This is a critical step for obtaining an accurate estimate of modal flexibility. These two algorithms were combined and coded in MATLAB, and implemented with additional data processing procedures to identify the dynamic characteristics and modal flexibility of the laboratory grid model. The details of the data processing approach are further described in the following sections.

3.1 DATA POST PROCESSING TECHNIQUES USED

In order to minimize the inherent variations associated with the use of different post-processing techniques, only one method was used to process the vibration measurements from this research project. The flowchart shown in Figure 3.1 provides an overview of the flow of all dynamic tests performed and the processing steps required to obtain the modal parameters, which then lead to modal flexibility. The details of each step are further described in the following sections.

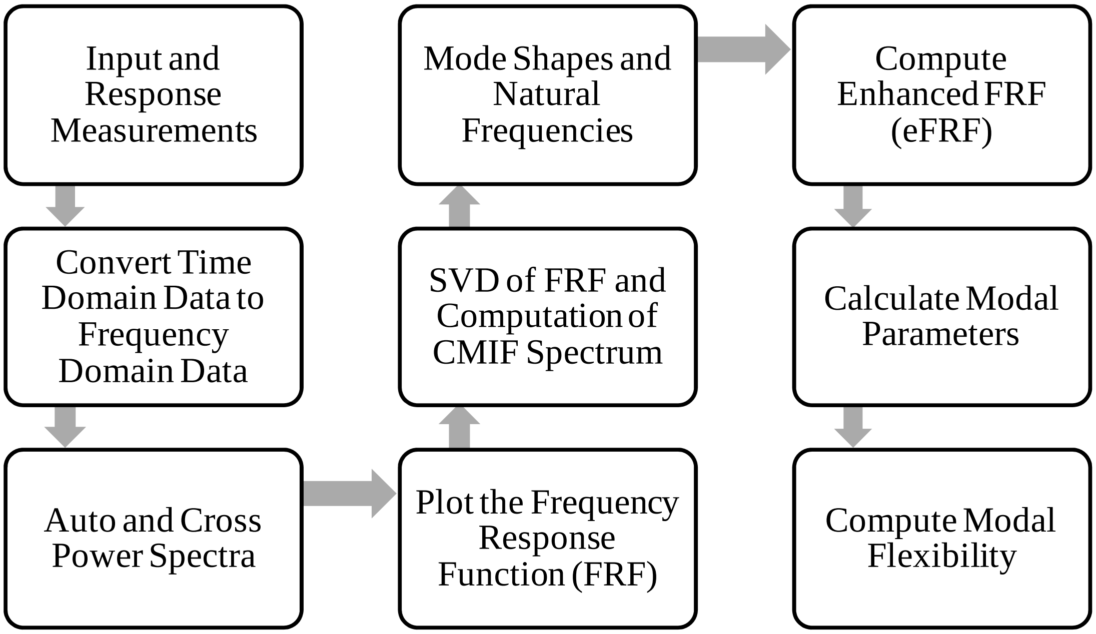

Figure 3.1: Post Processing Flow Chart

3.1.1 Input and Response Measurements

Both input and response data were collected in the time domain using a sampling rate of 1,000 Hz. As noted earlier, dynamic inputs including impact testing, shaker testing, and ambient testing were used in order to compare the differences between the results of different tests. It was important to accurately capture the initial equilibrium state of the structure before the controlled dynamic excitation was applied to the structure, and was accomplished by setting the DAQ unit to acquire data 30 time steps before the trigger. The force data from the instrumented hammer had some non-zero terms away from the pulse input, which were filtered out before continuing since these non-zero terms were not actually forces applied to the structure. The response data were de-trended around the zero axis in order to remove any DC offset. With shaker testing, no filtering was applied, but the data was still de-trended. In the case of ambient vibration testing, the dynamic excitation was un-measurable, and the measured responses were processed in a slightly different manner. The specific procedures used for processing the ambient vibration measurements are described in Section 5.4.

3.1.2 Convert Time Domain Data to Frequency Domain Data

The input and response data were recorded in the time domain. To compute frequency response functions from the time domain data, the data must first be transformed into the frequency domain. The most common and direct approach to accomplish this was to employ the Fast Fourier Transform. This was easily implemented in MATLAB.

3.1.3 Auto and Cross Power Spectra

The frequency domain data were used to compute cross power spectra and auto power spectra. Averaging of the multiple data sets was also taken care of in this stage. As noted by Allemang (1999), using several averages will reduce errors from noise and leakage, and will result in better coherence. These effects were observed for the grid model test data when multiple averages were computed.

The expressions that were used to compute the cross power spectra are shown in Equations (3.1) and (3.2). The expressions that were used for computing the autopower spectra are given in Equations (3.3) and (3.4).

$$GFX_{qp} = \sum_{1}^{N_{avg}} F_q X_p^* \qquad \textbf{\textit{(3.1)}}$$

$$GXF_{pq} = \sum_{1}^{N_{avg}} X_p F_q^* \tag{3.2}$$

$$GXX_{pp} = \sum_{1}^{N_{avg}} X_p X_p^* \tag{3.3}$$

$$GFF_{qq} = \sum_{1}^{N_{avg}} F_q F_q^* \tag{3.4}$$

where

F = input force spectrum (in frequency domain).

X = response spectrum (in frequency domain).

p is the output Degree of Freedom (DOF).

q is the input DOF.

N_{avg} = number of averages used in the data set.

* denotes the complex conjugate of the spectra.

G refers to one sided spectrum.

3.1.4 Frequency Response Functions

Two different methods were used to compute frequency response functions (FRFs) from the measured data, namely the H1 algorithm and the H2 algorithm. The H1 algorithm, shown in Eq. (3.5), is the most common formulation of the FRF, and tends to minimize the noise on the output measurements. Another formulation of the FRF is the H2 algorithm, shown in Eq. (3.6), which tends to minimize the noise on the input measurement (Allemang, 1999). The FRFs generated by each of these algorithms were plotted together and evaluated to make sure that no extraneous noise was present in either the response or input measurements. Ultimately, the H1 method was used for the singular value decomposition and CMIF algorithm.

$$H1_{pq} = \frac{GXF_{pq}}{GFF_{qq}} \tag{3.5}$$

$$H2_{pq} = \frac{GXX_{pp}}{GFX_{qp}} \tag{3.6}$$

where

GXF and GFX are the cross power spectra.

GFF and GXX are the autopower spectra.

Since the response data consisted of accelerations, the resulting FRF is known as “inertance,” or A/F (acceleration spectrum divide by force spectrum). Each spectral line was then divided by $j\omega^2$ in order to convert the acceleration data into the displacement data and the resulting FRF is known as “receptance,” or X/F (displacement spectrum divided by force spectrum).

3.1.5 SVD of FRF and Computation of CMIF Spectrum

The FRF matrix, designated by *H(ω),* was computed using the H1 method with each location in the matrix representing an input (column) location and output (row) location. In order to obtain the Complex Mode Indicator Function (CMIF) spectrum, the FRF matrix is decomposed at every frequency line. The most efficient approach for decomposing the FRF is Singular Value Decomposition (SVD) at each spectral line (Allemang & Brown, 2006). The CMIF method is different from other algorithms in the sense that a good estimate of the number of modes in a given frequency interval is needed, and is accomplished by plotting the singular values, *S(ω)*, of the FRF matrix at each spectral line (Catbas et al., 2004). SVD can be described at each spectral line, *ω*, by Eq. (3.7).

$$\left[imag(H(\omega))\right]_{N_o x N_i} = \left[U(\omega)\right]_{N_o x N_i}\left[S(\omega)\right]_{N_i x N_i}\left[V(\omega)\right]^{H}_{N_i x N_i} \tag{3.7}$$

where

'*imag*' refers to the imaginary part of the matrix.

U(ω) = left singular vectors.

H(ω) = right singular vectors.

N_o = number of outputs.

N_i = number of inputs.

small ^{H} denotes the Hermitian transpose.

Employing SVD on the imaginary part of the FRF plot produces real-valued singular vectors, which are easier to interpret and use for identifying modal frequencies. The singular values can then be plotted over the entire frequency band of interest. CMIF spectra generated using 4 different input DOFs from the cantilever model is shown in Figure 3.2. It can be observed from this figure that a separate singular value spectrum is produced for each input location utilized in the CMIF formulation.

The peaks in the CMIF spectra represent possible modes of the system. It should be noted that experimental error and other factors can lead to spurious peaks in the CMIF spectra that are not natural modes of the structure. An automated peak-picking algorithm was implemented for the CMIF spectra as shown in Figure 3.2. The peaks corresponding to possible modes of the structure have been circled, while the spurious peaks have been identified by a star and were not used in further processing.

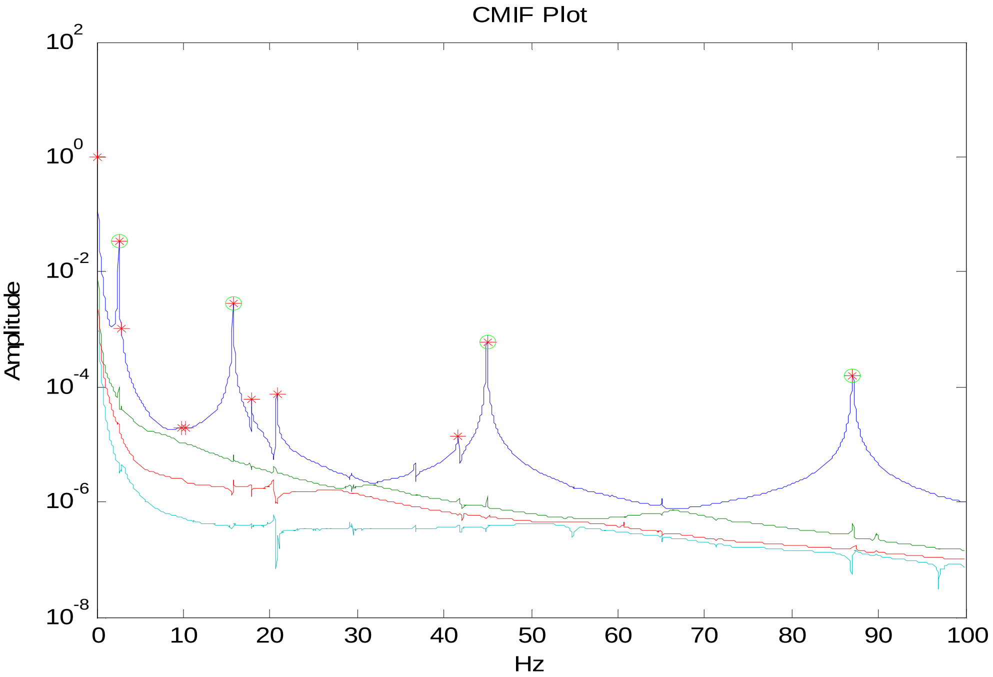

Figure 3.2: CMIF Plot for Cantilever Model using 4 Input DOFs

3.1.6 Mode Shapes and Natural Frequencies

Modal parameter estimation using the CMIF method is a two-stage approach, with the first stage estimating the spatial information, or modal vectors (Phillips & Allemang, 1998). Besides producing a clear plot of the possible locations of modes of the structure, singular value decomposition provides approximate mode shape vectors at every frequency line. The approximate mode shape vectors at any frequency line are found in the left singular vectors, $U(\omega)$. By taking the left singular vector at the same spectral line corresponding to a peak in the CMIF spectra, one can plot that vector to obtain a visual representation of the mode shape. Since the mode shapes that contribute to each peak do not change much around each peak, any given number of spectral lines around the peak of interest may give the same shape (Allemang & Brown, 2006). These mode shapes are important for verifying the resonant vibration modes of the structure, but in this form have arbitrary scaling and will not produce an accurate estimate of modal flexibility. Therefore, scaling of the mode shapes is important, and is found in the second stage of the CMIF method.

3.1.7 Compute Enhanced FRF (eFRF)

The second stage of parameter estimation estimates the temporal information, or modal frequencies and modal scaling (Phillips & Allemang, 1998). These parameters are found through the creation of an Enhanced Frequency Response Function, or eFRF, which decouples the MDOF system into a series of SDOF systems. The eFRF utilizes the mode shape vector *U(ω)* as a modal filter to represent the overall FRF as a single degree of freedom system for each mode. In order to get the correct scaling for the eFRF, a scaling vector created from the left and right singular vectors is used. The *H(ω)* matrix is then pre- and post-multiplied by the corresponding filter and scaling vectors at each frequency line to obtain the eFRF, as seen below (Phillips & Allemang, 1998; Catbas, Brown, & Aktan, 2004).

$$\begin{aligned} u &= U(\omega_r) \\ v_{sc} &= pinv(V(\omega_r))*u(dpt)*V(\omega_r) \\ eFRF(\omega) &= u^T * H(\omega)*v_{sc} \end{aligned} \tag{3.8}$$

where r is the mode of interest. u is the modal filter vector, taken as a column from *U(w)* corresponding to the singular value chosen. v_{sc} is the modal scaling vector, where '*pinv*' is the pseudo-inverse of the matrix, and '*dpt*' are the driving points of the structure. The transpose of u is denoted as with a small ^{T}.

To better illustrate this concept, Figure 3.3 shows a CMIF spectra containing 8 separate modes, then shows the corresponding eFRF for the first 3 modes (or peaks) in the CMIF.

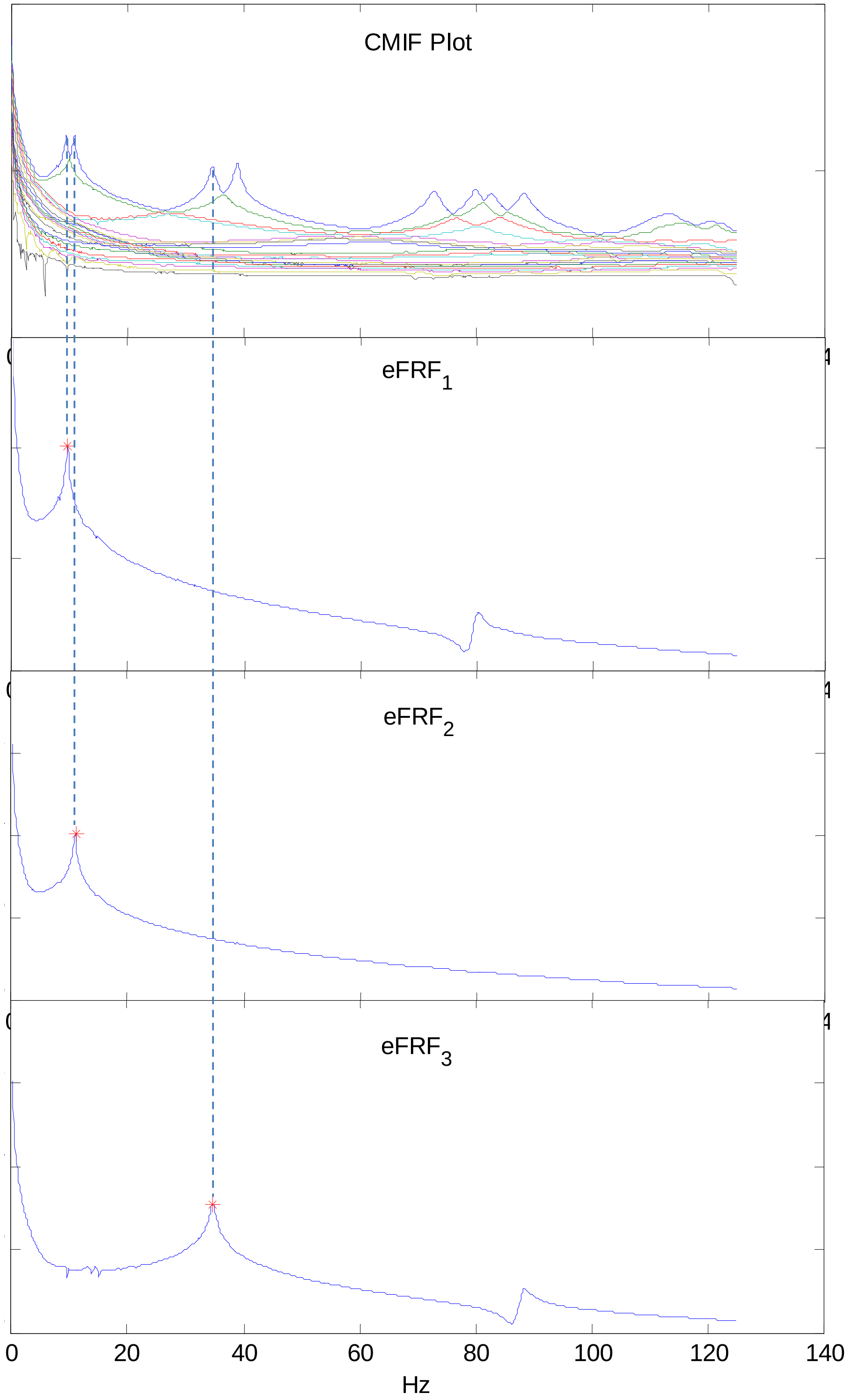

Figure 3.3: Decoupling Modes with eFRF Creation

3.1.8 Calculate Modal Parameters

Once the eFRF was obtained, a least squares, curve fitting algorithm was used to fit a curve to the peak in each eFRF. The least squares estimation produces a complex modal frequency, containing frequency and damping, for each mode (Allemang, 1999).

$$\begin{bmatrix} eFRF(\omega_p)-eFRF(\omega_1) \\ eFRF(\omega_p)-eFRF(\omega_2) \\ eFRF(\omega_p)-eFRF(\omega_p) \\ \vdots \\ eFRF(\omega_p)-eFRF(\omega_s) \end{bmatrix} \lambda_r = \begin{bmatrix} j\omega_p * eFRF(\omega_p) - j\omega_1 * eFRF(\omega_1) \\ j\omega_p * eFRF(\omega_p) - j\omega_2 * eFRF(\omega_2) \\ j\omega_p * eFRF(\omega_p) - j\omega_p * eFRF(\omega_p) \\ \vdots \\ j\omega_p * eFRF(\omega_p) - j\omega_s * eFRF(\omega_s) \end{bmatrix} \quad \textbf{\textit{(3.9)}}$$

where

ω_p = frequency of the peak of interest.

$\omega_1 - \omega_s$ = frequencies above and below the peak of interest.

λ_r = complex modal frequency for each mode *r*.

The above over determined set of linear equations was then solved using a pseudo-inverse approach to solve for the complex modal frequency. The scaling factor (Modal A) was found in a similar manner. This factor is important because it allows the modal vectors to be mass unit normalized without assuming a mass matrix, thereby allowing the proper scaling of the modal flexibility matrix (Catbas, Brown, & Aktan, 2004).

$$M_{A_r} = s_1 * s_2 * B * pinv(A) \quad \textbf{\textit{(3.10)}}$$

where

M_{Ar} = scaling factor (Modal A) for each mode *r*.

$$s_1 = \phi_r^{\,T} * \phi_r$$

$$s_2 = \phi_r (dpt)^T * v_{sc}$$

$$A = \begin{bmatrix} eFRF(\omega_1) \\ eFRF(\omega_2) \\ eFRF(\omega_p) \\ \vdots \\ eFRF(\omega_s) \end{bmatrix}$$

$$B = \begin{bmatrix} 1/(j\omega_1 - \lambda_r) \\ 1/(j\omega_2 - \lambda_r) \\ 1/(j\omega_p - \lambda_r) \\ \vdots \\ 1/(j\omega_s - \lambda_r) \end{bmatrix}$$

ϕ_r = mode shape vector for each mode *r*.

3.1.9 Compute Modal Flexibility

The modal parameters found in the previous steps are then combined to find modal flexibility, the end goal of the data analysis. Modal flexibility was selected as the result that would be used to compare the different characterization approaches used in this project. Modal flexibility, *MF*, is defined by Catbas, Brown, and Aktan (2006) as shown in Eq. (3.11):

$$MF = \sum_{r=1}^{\#MODES} \frac{\phi_r \cdot \phi_r^T}{M_{A_r}\left(-\lambda_r\right)} + conj\left(\frac{\phi_r \cdot \phi_r^T}{M_{A_r}\left(-\lambda_r\right)}\right) \tag{3.11}$$

where

ϕ_r = mode shape vector for mode *r.*

M_{A_r} = modal A for mode *r.*

λ_r = complex modal frequency for mode *r.*

'conj' denotes the complex conjugate of the value.

It is important to note that modal flexibility is an approximation of the actual flexibility for a structure, and is subject to uncertainty since it is derived from measurement data. Experimental data always contains some amount of error and noise that can lead to some differences between the estimated modal flexibility and the actual flexibility for a given structure. The parameters used to calculate modal flexibility (modal frequencies, modal vectors, Modal A) are affected by the quality of the measurement data used to estimate them. Finally, the modal flexibility equation contains a summation over the number of modes observed. The exact flexibility for most structures would be the summation over an infinite number of modes. Using only a subset of these modes to determine the modal flexibility will never provide an exact estimate of the actual structural flexibility. That being said, if enough modes are used in the summation, a very close approximation of the flexibility of the structure can be obtained. Fortunately, the dynamic response of most structures is largely determined by its first few fundamental modes. Furthermore, the error in the modal flexibility identified from a finite number of modes is likely to be less than the uncertainty levels associated with the in-situ mechanical characteristics of constructed systems.

3.2 VERIFICATION OF THE CMIF ALGORITHM – VIRTUAL IMPACT TEST

The author developed coding to implement the CMIF algorithm and to find modal flexibility in MATLAB. In order to validate the coding and to verify that the results obtained were correct and accurate, a benchmark evaluation of the data processing procedures was performed. This was accomplished by applying the code to mathematically generated input and response time domain data for a structural system having known parameters. The resulting virtual impact test data contained no experimental noise or errors that could corrupt the modal parameter identification results or the modal flexibility estimate. The simulated dynamic response data was generated for a cantilever beam structure with well-defined geometric, section and material properties. The cantilever beam structure was idealized as a 4 translational degree-of-freedom (DOF) system with mass lumped at the nodes. The flexibility matrix was computed for the cantilever beam using closed-form deflection equations available in the AISC Manual of Steel Construction (AISC, 2005). If the CMIF algorithm was implemented properly, the modal flexibility identified from the virtual impact test data would very closely match the flexibility found from deflection equations. The properties of the cantilever beam structure used for the virtual impact test were the same as the experimental model, and are summarized in Ch. 4.

A numerical procedure was used to generate the dynamic response data at each DOF due to a simulated impact at one DOF on the structure. The numerical procedure used for the simulation was based on linear interpolation of the excitation over each time interval as developed by Chorpa (2007). This numerical method is applicable to linear structures, which was assumed to be the case for the cantilever beam. The dynamic response due to an arbitrary excitation is computed by implementing recurrence equations at discrete time steps. The recurrence equations are derived from the exact solution to the equation of motion for an underdamped, single degree of freedom (SDF) system (Chopra, 2007), and provide the displacement and velocity of the system at each time step used in the analysis. Because the recurrence equations are only applicable to SDF systems, modal analysis was first used to uncouple the equations of motion for the 4 DOF cantilever beam and transform the excitation and responses into modal coordinates. The numerical evaluation was executed in modal coordinates and modal superposition was used to obtain the total response at each DOF. The total response at each DOF was subsequently transformed back into physical coordinates to obtain the displacement and velocity records. The recurrence equations used to compute the displacement and velocity of a SDF system are given by Eq. (3.12) and (3.13), respectively. The coefficients in these equations are summarized in Table 3.1:

$$u_{i+1} = Au_i + B\dot{u}_i + Cp_i + Dp_{i+1} \tag{3.12}$$

$$\dot{u}_{i+1} = A'u_i + B'\dot{u}_i + C'p_i + D'p_{i+1} \tag{3.13}$$

where

u is the displacement.

$\dot{u}$ is the velocity.

p is the forcing function.

i is the current time step.

The dynamic excitation applied to the cantilever beam was a virtual impact force that was simulated by a half-cycle sine wave with a peak amplitude of 10 lbf. The frequency response of the impact force varies with the time duration of the impulse. An impact force having a longer time duration will lead to a dynamic excitation with a more narrow band in the frequency domain than an impact force with a shorter time duration. The frequency band associated with the dynamic excitation is important as only the normal modes of the structure that are located within the same frequency band of the excitation will contribute significantly to the dynamic response of the structure. Ideally, the time duration of the impact force would approach zero imparting a pure unit impulse load to the structure. Because the actual impact force provided by the instrumented hammer was expected to be somewhere in between a pure impulse force and a half-cycle sine wave pulse, an impact force time record from an instrumented impact hammer was analyzed to determine a realistic pulse time duration. The data from the instrumented impact hammer revealed that a time duration of 0.003 seconds would represent a reasonable simulation of the actual impact force supplied by the instrumented impact hammer. Figure 3.4 compares the simulated impact force used for the numerical analysis and an actual impact force record from the instrumented hammer. From this plot, it can be seen that more energy was input into the structure from the virtual impact test, both due to the amplitude and due to the shape of the impact.

Table 3.1: Coefficients in Recurrence Equations (from Chorpa, 2007)

$$A = e^{-\zeta\omega_n\Delta t}\left(\frac{\zeta}{\sqrt{1-\zeta^2}}\sin\,\omega_D\Delta t + \cos\,\omega_D\Delta t\right)$$

$$B = e^{-\zeta\omega_n\Delta t}\left(\frac{1}{\omega_D}\sin\,\omega_D\Delta t\right)$$

$$C = \frac{1}{k}\left\{\frac{2\zeta}{\omega_n\Delta t} + e^{-\zeta\omega_n\Delta t}\left[\left(\frac{1-2\zeta^2}{\omega_n\Delta t} - \frac{\zeta}{\sqrt{1-\zeta^2}}\right)\sin\,\omega_D\Delta t - \left(1+\frac{2\zeta}{\omega_n\Delta t}\right)\cos\,\omega_D\Delta t\right]\right\}$$

$$D = \frac{1}{k}\left\{1 - \frac{2\zeta}{\omega_n\Delta t} + e^{-\zeta\omega_n\Delta t}\left(\frac{2\zeta^2-1}{\omega_n\Delta t}\sin\,\omega_D\Delta t + \frac{2\zeta}{\omega_n\Delta t}\cos\,\omega_D\Delta t\right)\right\}$$

$$A' = -e^{-\zeta\omega_n\Delta t}\left(\frac{\omega_n}{\sqrt{1-\zeta^2}}\sin\,\omega_D\Delta t\right)$$

$$B' = e^{-\zeta\omega_n\Delta t}\left(\cos\,\omega_D\Delta t - \frac{\zeta}{\sqrt{1-\zeta^2}}\sin\,\omega_D\Delta t\right)$$

$$C' = \frac{1}{k}\left\{-\frac{1}{\Delta t} + e^{-\zeta\omega_n\Delta t}\left[\left(\frac{\omega_n}{\sqrt{1-\zeta^2}} + \frac{\zeta}{\Delta t\sqrt{1-\zeta^2}}\right)\sin\,\omega_D\Delta t + \frac{1}{\Delta t}\cos\,\omega_D\Delta t\right]\right\}$$

$$D' = \frac{1}{k\Delta t}\left\{1 - e^{-\zeta\omega_n\Delta t}\left(\frac{\zeta}{\sqrt{1-\zeta^2}}\sin\,\omega_D\Delta t + \cos\,\omega_D\Delta t\right)\right\}$$

Three different tests were performed virtually on the cantilever beam structure, with each test placing the dynamic excitation at the tip DOF only. The first test used an impact time duration of 0.003 seconds based on the analysis described above and also utilized Rayleigh damping coefficients which ranged from 2% in the 1st mode to 7% in the 4th mode. The second virtual impact test utilized the same damping coefficients, but the pulse time duration was changed to 0.001 seconds. This test resulted in less displacement at the tip of the cantilever due to less energy being imparted to the structure. The third test performed used an impact time duration of 0.003 seconds but utilized a constant damping of 5% across all 4 modes. Figure 3.5 shows the displacement at the tip due to these two different damping cases.

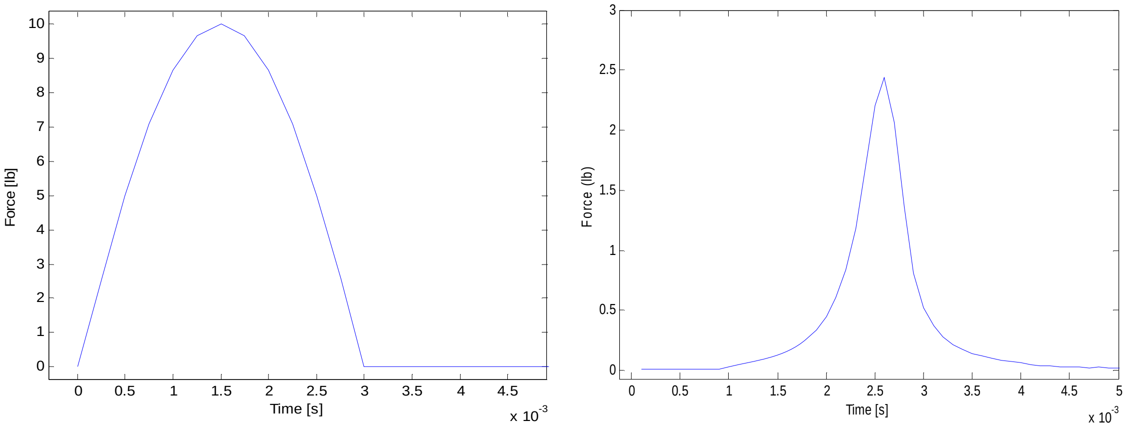

Virtual Impact Actual Impact

Figure 3.4: Virtual Impact vs. Actual Impact

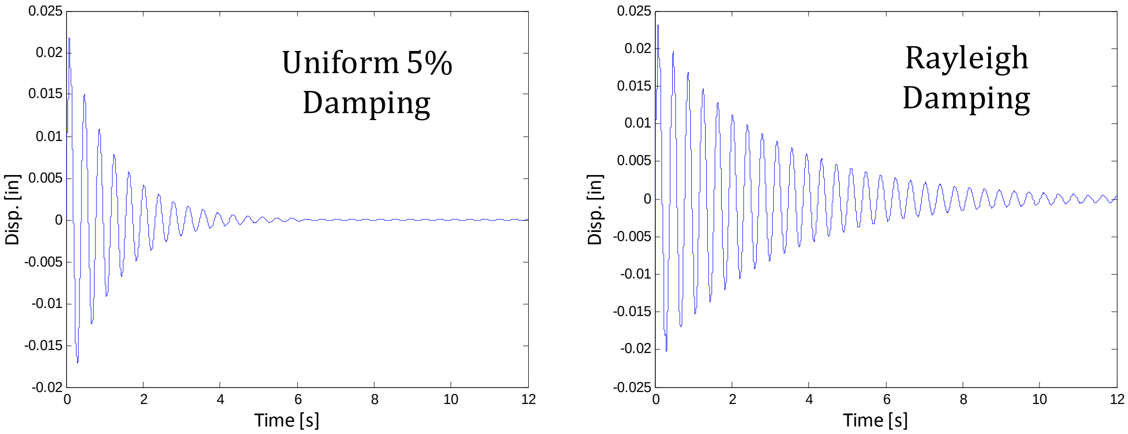

Figure 3.5: Tip Displacement due to Virtual Impact at DOF1 (Mode 1)

As expected, the peak dynamic response was definitely affected by the time duration of the simulated impact force. When the longer time duration used for the impact force, a larger maximum deflection resulted at the free end of the cantilever beam. A nearly exact simulation of the impact force and dynamic response for the cantilever beam could be created by additional modifications to the impact time duration, the damping ratio for each mode, and the shape of the impact force time record, but this is beyond the scope of the benchmark evaluation study. The benchmark evaluation of the virtual impact test did show that the algorithms implemented in MATLAB could accurately estimate the modal parameters and modal flexibility for a structure. As shown in Table 3.2, the modal flexibilities computed for each virtual impact test were very close to the flexibility computed for the cantilever beam from closed-form deflection equations. Also, when the modal flexibility matrices derived from the virtual impact tests are multiplied by a uniform load vector, the resulting deflected shapes for the cantilever beam are very close to the deflected shape computed from closed-form deflection equations for the same load pattern, as shown in Figure 3.6. Finally, the natural frequencies located by the peaks in the CMIF spectrum computed from the simulated dynamic response data (Figure 3.7) are the same as the natural frequencies computed by solving the characteristic matrix of the cantilever beam (see Table 3.3).

Table 3.2: Virtual Impact Test Results

Analytical Static Flexibility				*Modal Flexibility - Test #1*			
0.07193	0.04552	0.02248	0.00618	0.07163	0.04532	0.02238	0.00615
0.04552	0.03034	0.01573	0.00450	0.04532	0.03042	0.01552	0.00465
0.02248	0.01573	0.00899	0.00281	0.02238	0.01552	0.00910	0.00265
0.00618	0.00450	0.00281	0.00112	0.00615	0.00465	0.00265	0.00131

Analytical Static Flexibility				*Modal Flexibility - Test #2*			
0.07193	0.04552	0.02248	0.00618	0.07163	0.04532	0.02238	0.00615
0.04552	0.03034	0.01573	0.00450	0.04532	0.02869	0.01705	0.00285
0.02248	0.01573	0.00899	0.00281	0.02238	0.01705	0.00774	0.00424
0.00618	0.00450	0.00281	0.00112	0.00615	0.00285	0.00424	0.00055

Analytical Static Flexibility				*Modal Flexibility - Test #3*			
0.07193	0.04552	0.02248	0.00618	0.07285	0.04612	0.02279	0.00627
0.04552	0.03034	0.01573	0.00450	0.04612	0.03073	0.01593	0.00455
0.02248	0.01573	0.00899	0.00281	0.02279	0.01593	0.00908	0.00284
0.00618	0.00450	0.00281	0.00112	0.00627	0.00455	0.00284	0.00112

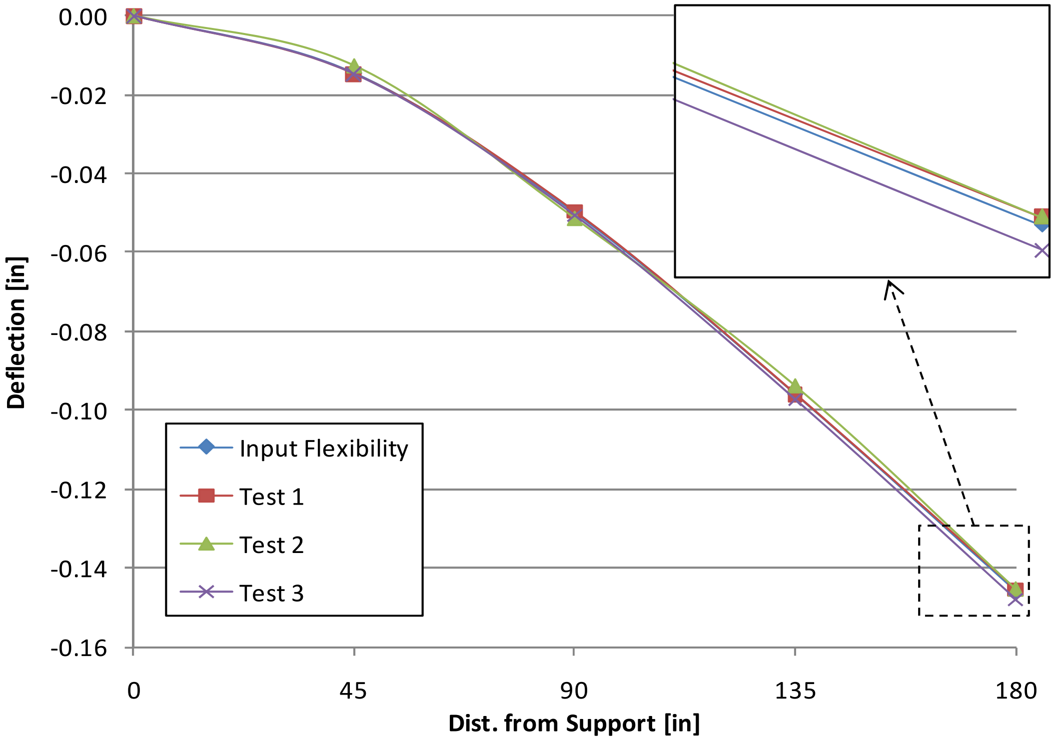

Figure 3.6: Vertical Deflection from Virtual Impact Test Results

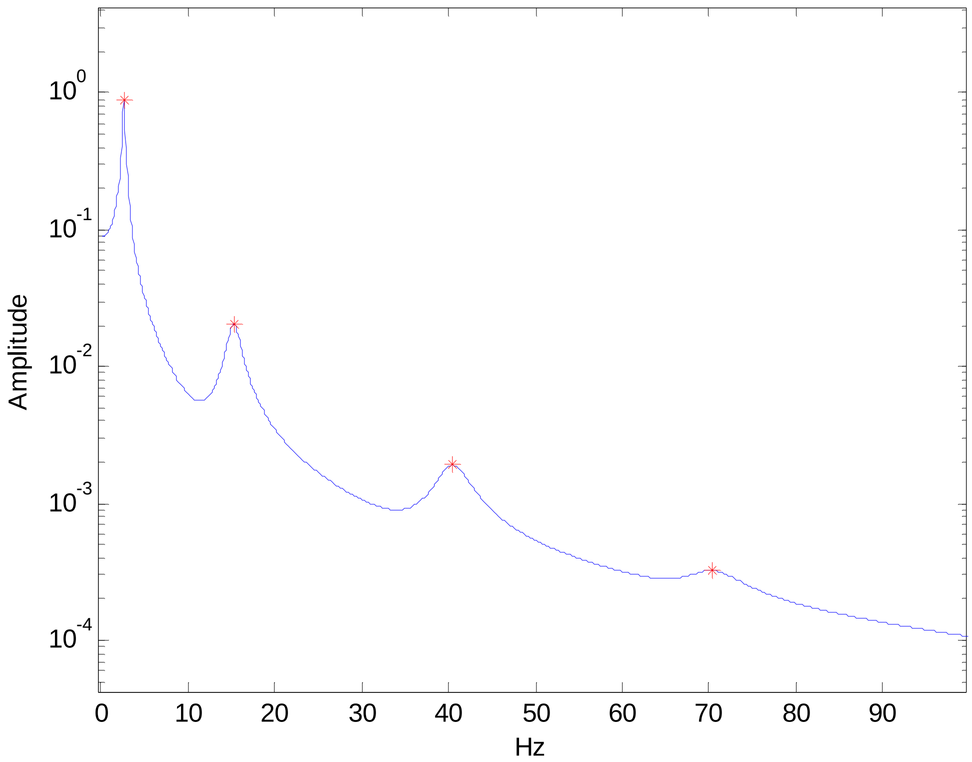

Figure 3.7: CMIF Plot from Virtual Impact Test Results

Table 3.3: Natural Frequencies Comparison for Virtual Impact Test

	Frequency from Characteristic Matrix (Hz)	***Frequency from Virtual Impact (Hz)***
Mode 1	2.5965	2.5898
Mode 2	15.2617	15.2503
Mode 3	40.4148	40.4678
Mode 4	70.4426	70.7186

4. CHARACTERIZATION OF A CANTILEVER BEAM MODEL

Laboratory testing of physical models is an efficient and effective approach for identifying and mitigating the errors associated with a given experimental characterization approach and for validating data processing and analysis procedures. A laboratory evaluation program was developed and executed for a cantilever beam structure as part of this research program to serve a number of objectives:

1. To evaluate and validate the sensors and data acquisition devices that would be used for dynamic characterization of the grid model structure and in-service bridge structures.
2. To determine the most effective configuration and use of the available data acquisition hardware and software for static and dynamic characterization of constructed systems.
3. To identify, validate, and evaluate the data processing and analysis approaches needed to characterize the dynamic characteristics of in-service constructed systems.

A small scale, steel cantilever beam model was selected for use in this evaluation because it a very simple structure and there is a relatively low amount of uncertainty associated with its analytical and experimental characterization compared to in-service constructed systems, which generally feature more complex structural systems, material characteristics, loadings, and existing deterioration and damage characteristics. The cantilever beam model is a statically determinate structure and its static and dynamic responses can be readily described using very basic mechanics principles.

The cantilever beam model was characterized using several different analytical approaches in addition to the experimental methods to provide a baseline characterization that could be compared with the static and dynamic test results. The dynamic response of the cantilever beam was characterized analytically using mathematical equations of motion for both uniform and lumped-mass models implemented in MATLAB. The model was also characterized using the commercially available structural analysis program SAP2000 to provide another independent point of comparison. The analytical characterization results for the cantilever beam provided several baseline descriptions of the cantilever beam model employing different levels of idealization, and these descriptions served to aid in the design of the experimental characterization program and as rational limits for the results of the experimental characterization program.

4.1 PHYSICAL AND MECHANICAL CHARACTERISTICS OF THE MODEL

The cantilever beam structure evaluated and discussed in this Chapter was constructed from a single 20 ft. long piece of hollow structural steel (HSS 3x2x 3/16) that was oriented for bending about its weak axis. The section was made of ASTM A500 Grade B steel, which has a yield strength of 46 ksi and a tensile strength of 58 ksi. The beam was clamped and bolted to the top of a 3 ft. tall steel support pedestal whose base was anchored into the concrete floor slab. The resulting span length of the cantilever beam, as measured from the clamped end to the free end, was 15 ft. Figure 4.6 shows a picture of the cantilever beam model as constructed in the laboratory and a picture of its clamped support.

The relevant section and material properties of the cantilever beam that were used for the analytical characterizations described in subsequent sections are summarized in Table 4.1.

Table 4.1: Properties of the Cantilever Beam Model

Parameter	***Value***
Modulus of Elasticity, E	29,000 ksi
Cross Sectional Area, A	1.54 in^2
Moment of Inertia, I	0.932 in^4
Section Modulus, S	0.932 in^3
Shear Area	N/A (Bernoulli Beam Assumed)
Weight Density, γ	490 lb/ft^3

4.2 ANALYTICAL CHARACTERIZATION OF THE CANTILEVER BEAM MODEL

The cantilever beam model described in the previous section was characterized analytically using two separate approaches. The first approach involved solving the partial differential equation governing the dynamics of a uniform cantilever beam. The second approach involved constructing and analyzing an analytical model of the beam in SAP2000, a commercially available structural analysis software package. The details of these analytical characterizations are further described in the following sections.

4.2.1 Partial Differential Equation Analysis

The cantilever beam physical model is a system with uniformly distributed mass and stiffness parameters. Given that the mass of the accelerometers installed on the physical model for the experimental testing were very small relative to the total mass of the cantilever beam, it is quite reasonable to expect that the measured dynamic responses for model should match the responses predicted by the solution of the equation of motion for a cantilever beam with uniformly distributed mass and stiffness reasonably well.

The partial differential equation (PDE) governing the transverse free vibration response *u(x, t)* of a beam with distributed mass and stiffness can be shown to have the following form (Craig & Kurdila, 2006):

$$m(x)\frac{\partial^2 u}{\partial t^2}+\frac{\partial^2}{\partial x^2}\left[EI(x)\frac{\partial^2 u}{\partial x^2}\right]=0 \tag{4.1}$$

where $m(x)$ is the distributed mass and $EI(x)$ is the distributed flexural rigidity, u is the vertical displacement, t is time, and x is the distance from the point of reference. Since the mass and stiffness of the cantilever beam model are assumed to be uniformly distributed along its length of the beam, the mass and flexural rigidity terms in Eq. (3.7) can be replaced by $m(x) = m$ and $EI(x) = EI$. It should be noted that the above equation is based on Euler-Bernoulli beam theory and therefore excludes the effects of shear deformation.

The general solution of the above equation is assumed to have the form:

$$U(x) = C_1 \sinh(\beta x) + C_2 \cosh(\beta x) + C_3 \sin(\beta x) + C_4 \cos(\beta x) \qquad \textit{(4.2)}$$

where C_1 through C_4 are constants and $\beta^4 = \omega^2 m / EI$. The constants C_1 through C_4 can be determined by evaluating the boundary conditions for a fixed end cantilever beam. Substituting these constants into Eq. (4.2) and simplifying yields the characteristic equation:

$$\cos \beta L \cosh \beta L + 1 = 0 \qquad \textit{(4.3)}$$

The roots of the characteristic equation are:

$$\beta_n L = 1.8751, 4.6941, 7.8548, \textit{and } 10.996 \text{ for n = 1, 2, 3, 4} \qquad \textit{(4.4)}$$

$$\beta_n L \approx (2n-1)\frac{\pi}{2} \quad \text{for n > 4} \qquad \textit{(4.5)}$$

The circular natural frequencies (ω_n) are then given by the following expression:

$$\omega_n = \frac{\beta_n^{\ 2}}{L^2}\sqrt{\frac{EI}{m}} \quad \text{for n = 1, 2, 3, 4, etc.} \qquad \textit{(4.6)}$$

where m is the mass per unit length, L is the span length of the beam, E is Young's Modulus, and I is the moment of inertia for the beam section. The mode shapes ϕ_n corresponding to the natural frequencies can then be computed by (Craig & Kurdila, 2006):

$$\phi_n(x) = C\left[\cosh \beta_n x - \cos \beta_n x - \frac{\cosh \beta_n L + \cos \beta_n L}{\sinh \beta_n L + \sin \beta_n L}\left(\sinh \beta_n x - \sin \beta_n x\right)\right] \qquad \textit{(4.7)}$$

where C is an arbitrary constant.

The transverse natural frequencies and mode shapes for the cantilever beam model were computed for the first 8 modes using the previous equations. The results are tabulated as cyclic natural frequencies (Hz) and were used as a basis for comparison with the dynamic characterization results obtained from the SAP2000 analytical model and the dynamic testing. The mode shapes associated with the first four natural frequencies computed from the partial differential equation solution are shown in Figure 4.1. For clarity purposes, the mode shapes were computed and plotted at 64 discrete points that were evenly distributed along the length of the cantilever beam. The mode shape vectors were also unit normalized such that the largest element in each modal vector had a value of one.

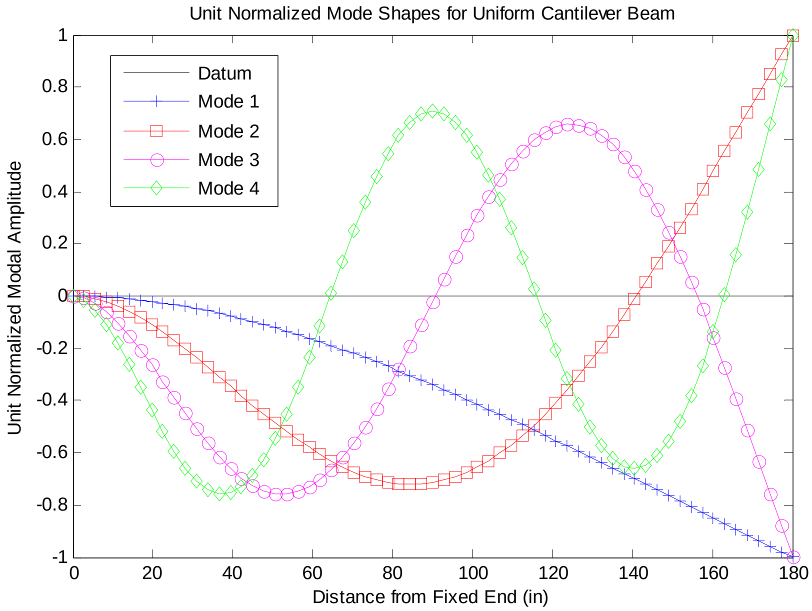

Figure 4.1: Transverse Mode Shapes Computed from the PDE Solution

4.2.2 Analytical Characterization in SAP2000

An analytical model of the cantilever beam was also created and analyzed in SAP2000. Although the analytical model was constructed from 3D frame (beam) elements with 6 degrees of freedom per node, only the planar degrees of freedom (DOF) were considered for the static and dynamic characterizations with this model. The planar DOF consisted of a translation and an in-plane rotation at each unrestrained node. Figure 4.2 shows isometric and elevation views of the SAP2000 model of the cantilever beam with four unrestrained nodes.

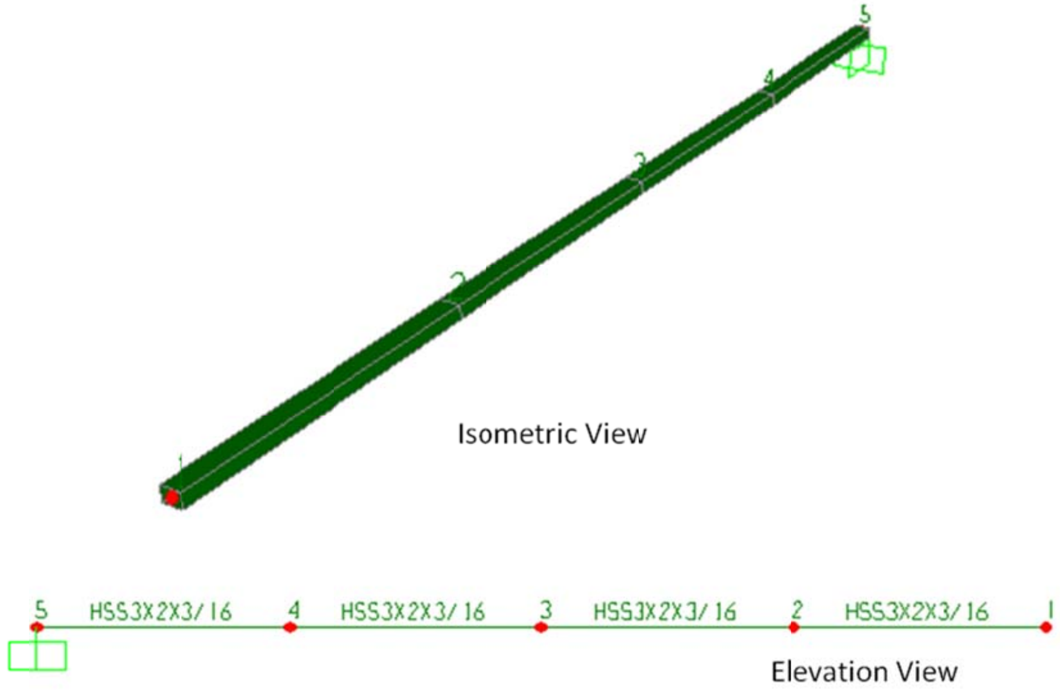

Figure 4.2: SAP2000 Model of Cantilever Beam

Static and dynamic analyses were conducted for the SAP2000 model of the cantilever beam. The static analysis was performed to determine the effective static flexibility matrix for cantilever beam. The effective static flexibility matrix is defined with respect to only the four translational DOF (the rotational DOF are excluded). The effective static flexibility matrix was computed by placing a unit load as a separate load case at each of the translational DOF locations in the model. The resulting translational displacements computed at each of the four nodes for a given load case are the flexibility coefficients in one column of the effective static flexibility matrix. The effective static flexibility matrix computed for the cantilever beam from SAP2000 analysis is shown in Table 4.3, and is discussed further in subsequent sections.

A dynamic modal analysis of the analytical model was performed in SAP2000 to determine the dynamic properties (natural frequencies and mode shapes) for the beam. SAP2000 computes nodal masses for frame elements using the material mass density and by default assigns these masses to the unrestrained translational DOF. The user has the option to assign masses to the other DOF; however, this was not done for the analytical model discussed herein. As a result, the modal analysis results computed from the SAP2000 model are basically the same as those that would be computed by using a lumped mass idealization to formulate the equations of motion for the multiple degree of freedom system. The initial SAP2000 analytical model consisted of four unrestrained nodes located at the same points where the accelerometers were placed on the physical model in the laboratory. The amount of mass lumped at each of the four translational DOF is shown schematically in Figure 4.3. The SAP2000 model was subsequently analyzed for an increasing number of nodes to identify the number of translational DOFs required to obtain a reasonable convergence to the results from the partial differential equation (PDE) solution. The convergence plot shown in Figure 4.4, indicates that a difference of less than 4% relative to the natural frequencies for each of the first 8 modes computed from the PDE solution was achieved when the SAP2000 model included 64 unrestrained nodes (and translational DOF). The percent differences for the natural frequencies computed from SAP2000 relative to the PDE solution for different numbers of unrestrained translational DOFs are summarized in Table 4.2. The mode shapes computed for the first four modes of the cantilever beam computed from the SAP2000 analytical model (with 64 translational DOF) are illustrated in Figure 4.5.

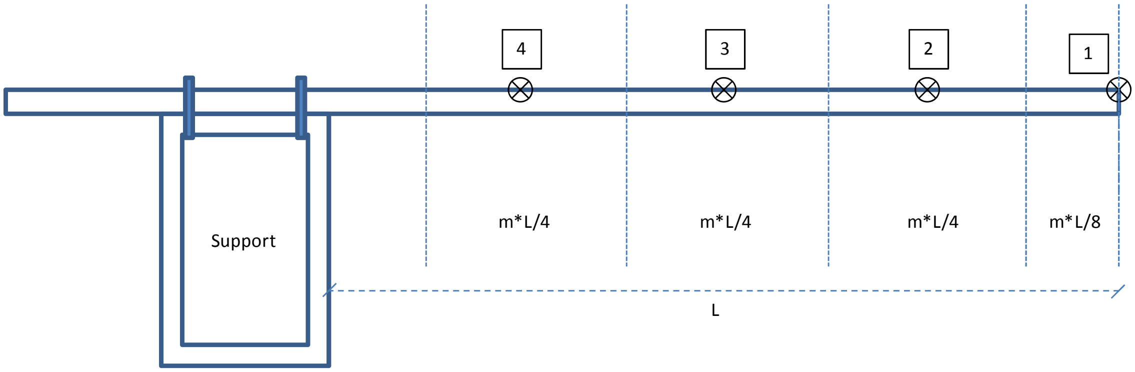

Figure 4.3: Lumped Mass Parameter Model

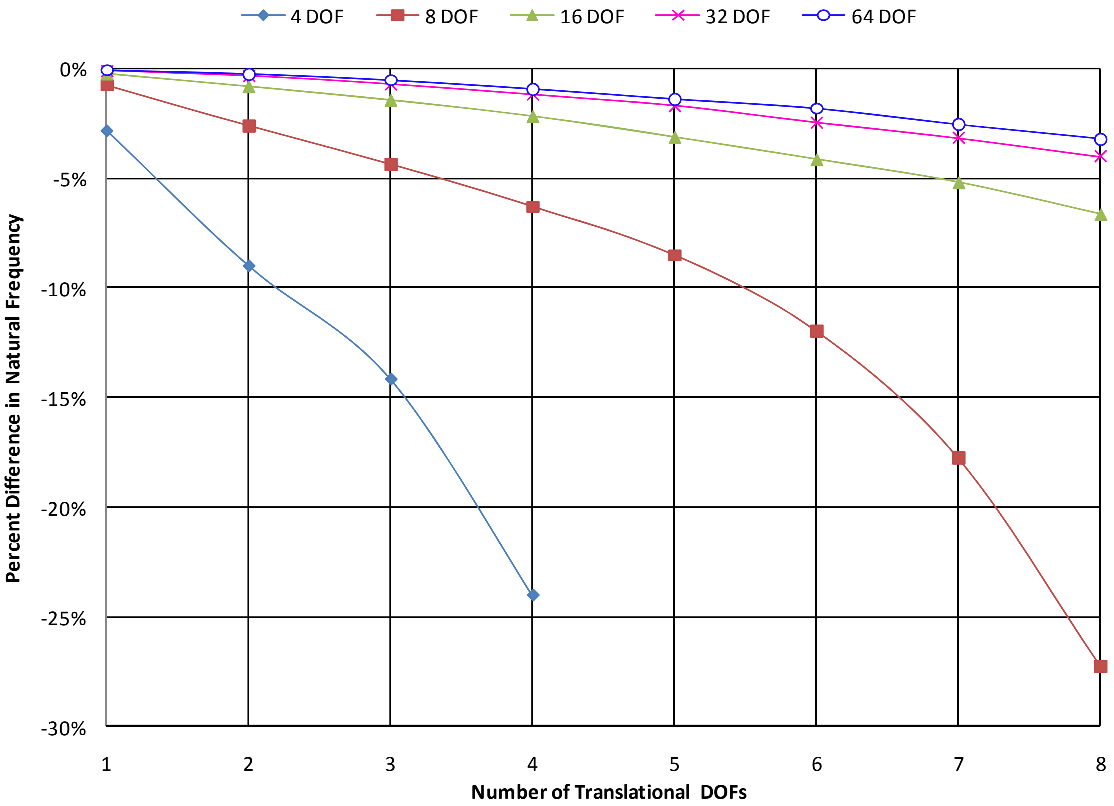

Figure 4.4: Natural Frequencies from PDE Solution and SAP2000 Analysis

Table 4.2: Natural Frequencies Computed from PDE Solution and from Different Analytical Model Discretizations in SAP2000

	PDE Solution	SAP2000 4 DOF Model		SAP2000 64 DOF Model	
Mode Number	Natural Frequency (Hz)	Natural Frequency (Hz)	% Difference[1]	Natural Frequency (Hz)	% Difference[1]
1	2.6709	2.5948	-2.85	2.6689	-0.07
2	16.7386	15.2300	-9.01	16.6973	-0.25
3	46.8689	40.2253	-14.17	46.6200	-0.53
4	91.8509	69.7837	-24.03	90.9918	-0.94
5	151.8235	-	-	149.7006	-1.40
6	226.7980	-	-	222.6420	-1.83
7	316.7675	-	-	308.6420	-2.57
8	421.7318	-	-	408.1633	-3.22

Notes: [1]relative to the PDE solution

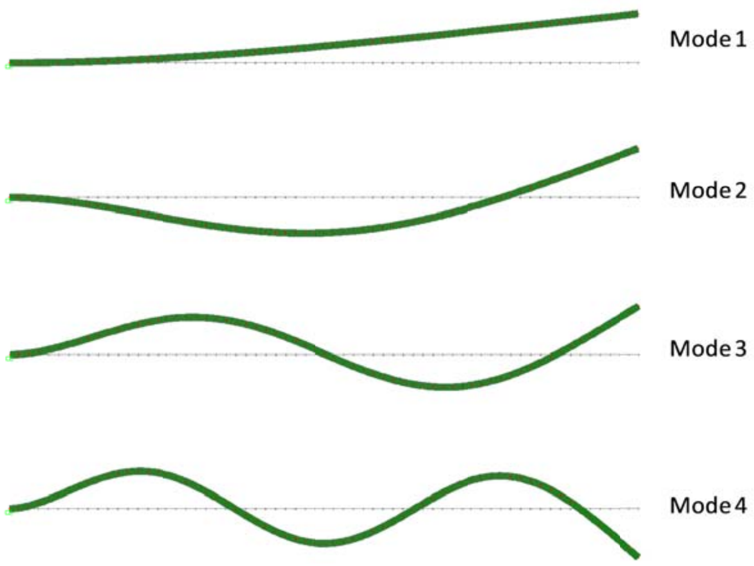

Figure 4.5: First Four Mode Shapes Computed from the SAP2000 Model

4.3 EXPERIMENTAL CHARACTERIZATION OF THE CANTILEVER BEAM MODEL

The cantilever beam model was characterized by both static and dynamic testing methods. The execution of these tests and their results are described in the following sections.

4.3.1 Instrumentation Scheme

The cantilever beam model was instrumented with a combination of accelerometers, strain gages and displacement transducers. The strain gages and displacement transducers were used for the static testing. The accelerometers were used to measure the vibrations of the beam for the different dynamic tests that were performed.

The strain gages installed on the cantilever beam were 350 Ohm weldable gages from Hitec Products, Inc. A total of two strain gages were installed on the top and bottom surfaces of the beam near the fixed support. The gages were wired in a Quarter Bridge configuration with the data acquisition system. During the static testing, the measured strains were used to determine the bending moment the gage location and this was used to calculate the deflected shape of the beam using mechanics of materials principles. The displacements at discrete points along the length of the beam were also measured directly using a Model PT510 wire potentiometer from Celesco. This transducer was moved to different points along the length of the beam to record its displacements for the different static load cases.

The beam was initially instrumented with five accelerometers that were evenly spaced along its length. Two different types of accelerometers were used for the dynamic testing of the beam. The first type used was the Model 3711 DC accelerometer from PCB Piezotronics, and the second type was the Model 393BO5 from the same company. These accelerometers are very small and light-weight sensors and their installation did not add any significant mass to the beam. This is consistent with assumption made for the analytical characterizations of the beam.

The locations of the individual sensors on the cantilever beam are shown in Figure 4.7. Photographs of the different sensors used are provided in Figure 4.8.

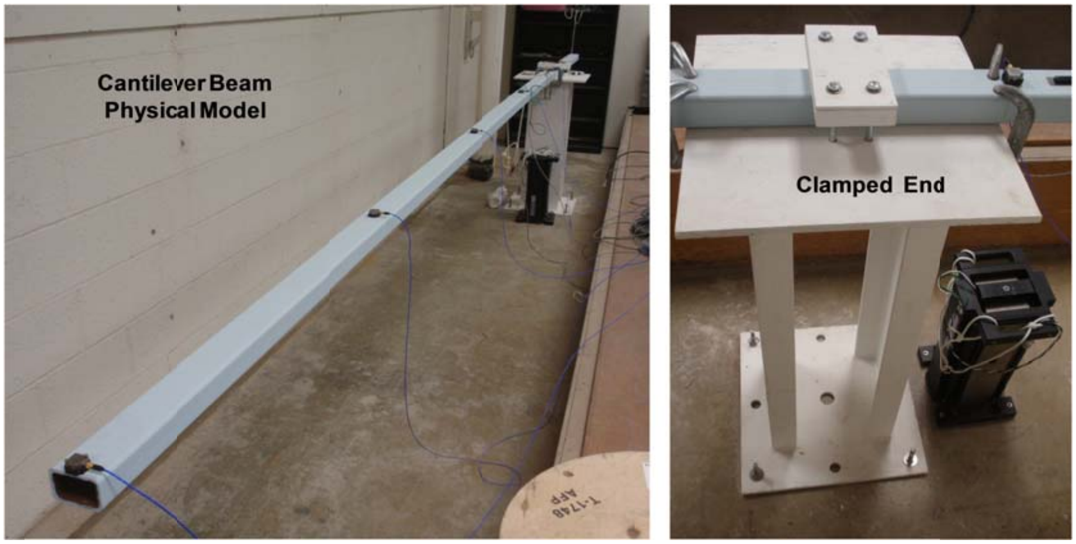

Figure 4.6: Cantilever Beam Model in the Laboratory

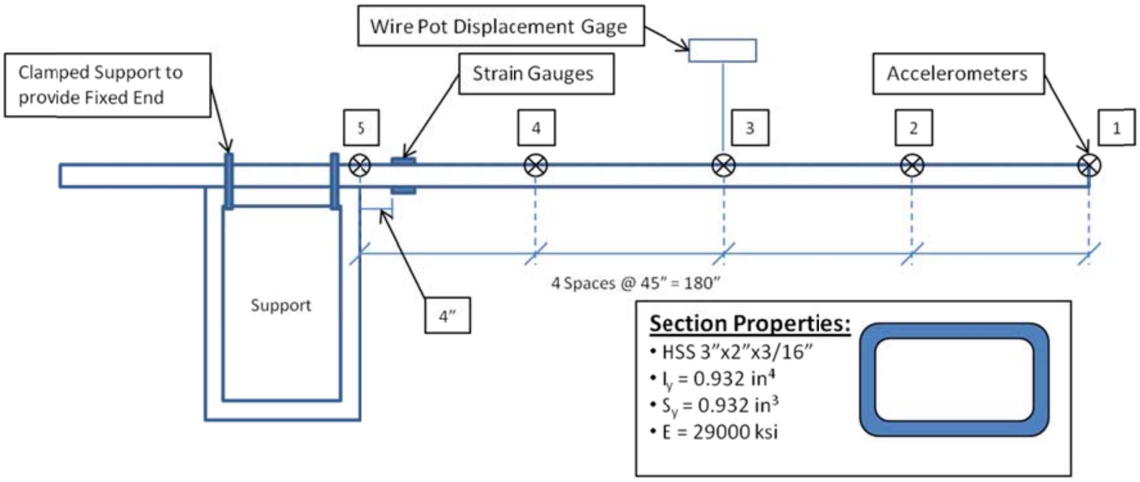

Figure 4.7: Cantilever Beam Setup

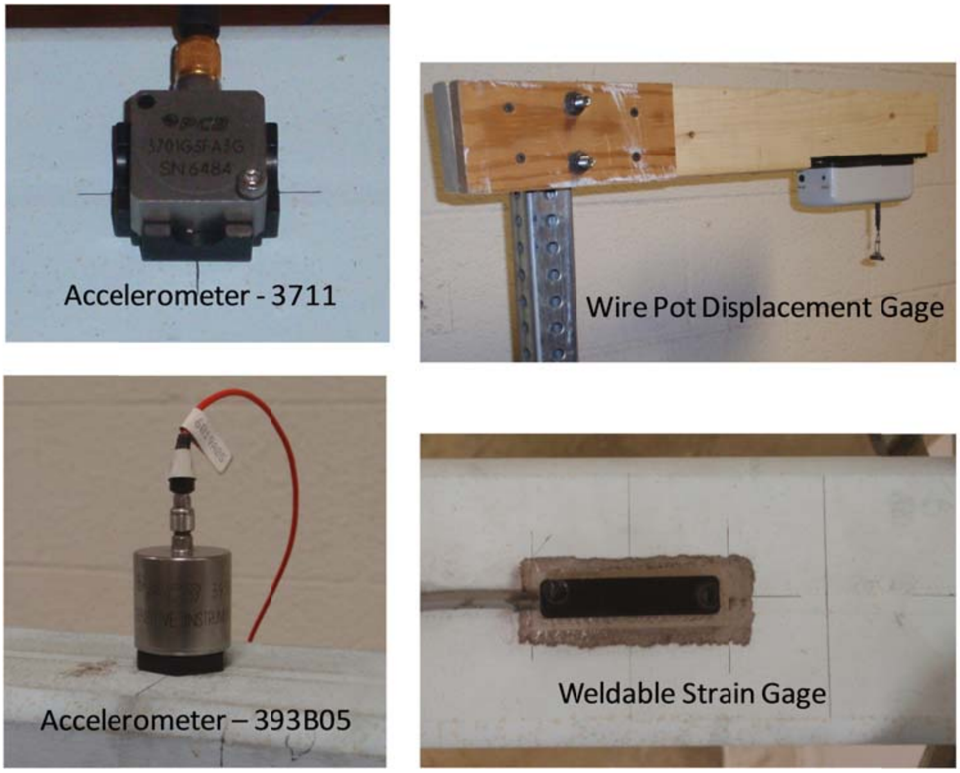

Figure 4.8: Sensors Used on Cantilever Model

4.4 STATIC TESTING OF THE CANTILEVER BEAM MODEL

4.4.1 Static Flexibility

A static load test was executed with the cantilever beam to determine its static flexibility matrix with respect to its translational DOFs. The coefficients of this static flexibility matrix, f_{ij}, are given by the deflection computed at DOF*i* due to a unit load applied at DOF*j*. These flexibility coefficients could be readily computed using closed-form deflection equations (AISC, 2005) as shown in Figure 4.9.

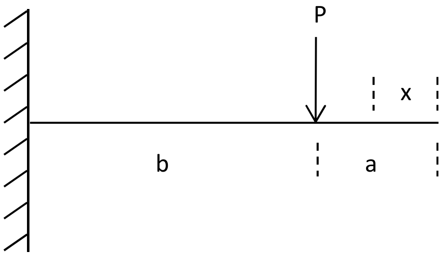

$$\Delta\ @\ point\ of\ load\ = \frac{P * b^3}{3 * E * I}$$

$$\Delta \text{ when x} < \text{a} \ = \frac{P * b^2}{6 * E * I} * (3L - 3x - b)$$

$$\Delta \text{ when x} > a \ = \frac{P(L - x)^2}{6 * E * I} * (3b - L + x)$$

Figure 4.9: Closed-form Deflection Equations for a Cantilever Beam (from AISC, 2005)

The actual test consisted of physically loading the structure at one node location with a 10 lb weight and measuring the resulting transverse deflections at each of the nodes. The node locations corresponded to the locations of the accelerometers installed along the length of the beam. This process was repeated until all of the four nodes locations were loaded. Each load case produced one column of the final 4 x 4 flexibility matrix.

The flexibility matrix obtained using this procedure was based on a 10 lb load. Each flexibility coefficient was subsequently divided by a constant value of 10 to make the matrix equivalent to what would be produced by a unit load. The theoretical flexibility matrix computed from the closed-form deflection equations, the analytical flexibility matrix obtained from a unit load analysis of the analytical model of the beam in SAP2000, and the experimental static flexibility matrix determined from the static load testing of the beam are given in Table 4.3. The theoretical and analytical flexibility matrices are nearly identical, and any discrepancies are most likely due to rounding errors in the numerical calculations. The experimentally identified flexibility matrix also shows good agreement with the theoretical and analytical flexibility matrices. The percent error between the experimental and analytical flexibility matrices is very small for coefficients associated with the deflection measurements taken near the free end of the cantilever beam. The error increases for flexibility coefficients associated with the deflection measurement recorded closer to the fixed end of the beam. This error can be attributed to the beam not deflecting as much at these locations due to the applied loads, and these small deflections were difficult to measure accurately. The numerical deflection equations and the SAP2000 analytical model both indicate that the displacement at DOF 4 (Node 4) due to a 10 lb load placed at DOF 4 would be 0.011 in. The actual measured displacement for this load case was 0.01589 in. This indicates that the displacement transducer used may lack precision beyond 0.01 in. In addition, shear deformation might be contributing the measured displacement at this location since it is close to the support and this effect is not considered by the numerical deflection equations that were used or by the analytical model.

Table 4.3: Cantilever Beam Static Flexibility

Theoretical Flexibility

	DOF1	DOF2	DOF3	DOF4
DOF1	0.071925	0.045515	0.022477	0.006181
DOF2	0.045515	0.030344	0.015734	0.004495
DOF3	0.022477	0.015734	0.008991	0.002810
DOF4	0.006181	0.004495	0.002810	0.001124

Analytical Flexibility

	DOF1	DOF2	DOF3	DOF4
DOF1	0.07195	0.04553	0.02249	0.00619
DOF2	0.04553	0.03036	0.01575	0.00450
DOF3	0.02249	0.01575	0.00900	0.00282
DOF4	0.00619	0.00450	0.00282	0.00113

Experimental Flexibility

	DOF1	DOF2	DOF3	DOF4
DOF1	0.072492	0.046872	0.024429	0.007646
DOF2	0.046176	0.030983	0.016683	0.005462
DOF3	0.024329	0.017378	0.010129	0.003774
DOF4	0.007646	0.005561	0.003376	0.001589

% Error from Experimental to Analytical

	DOF1	DOF2	DOF3	DOF4
DOF1	-0.8%	-3.0%	-8.7%	-23.7%
DOF2	-1.5%	-2.1%	-6.0%	-21.5%
DOF3	-8.2%	-10.5%	-12.7%	-34.3%
DOF4	-23.7%	-23.7%	-20.2%	-41.4%

Evaluating and comparing flexibility matrices by examining the individual coefficient values can be cumbersome and one can become quickly lost in the array of numbers. This is especially true when the number of DOFs is very large. In order to permit a more conceptual comparison to be made, this thesis compares the deflection profiles created by virtually loading the various flexibility matrices. The flexibility matrix can be multiplied by a virtual load vector, resulting in the displacement of each point due to that load. These displacements can be plotted producing a deflection profile associated with the virtual loading.

Consider the 4 x 4 flexibility matrix identified for the cantilever beam. If a 4 x 1 virtual load vector consisting of 30 lbs applied to Node 2, 10 lbs. applied to Node 3, and no load at Node 1 and Node 4 was multiplied by the flexibility matrix, a 4 x 1 vector of the displacements at each node would be obtained. These displacements u1 through u4 represent the displacement of DOF1 through DOF4 respectively, due to the applied load vector. This computation is illustrated schematically in Figure 4.10.

$$\begin{bmatrix} f11 & \cdots & f14 \\ \vdots & \ddots & \vdots \\ f41 & \cdots & f44 \end{bmatrix} \begin{Bmatrix} 0\ lbs \\ 30\ lbs \\ 10\ lbs \\ 0\ lbs \end{Bmatrix} = \begin{Bmatrix} u1 \\ u2 \\ u3 \\ u4 \end{Bmatrix}$$

Figure 4.10: Multiplication of Flexibility Matrix with Virtual Load Vector

Figure 4.11 shows the deflection profiles produced for the cantilever beam by multiplying the numerical, analytical and experimental flexibility matrices with a virtual uniform load vector consisting of a 1 lb force applied to each node. There is very good agreement between the flexibility matrices computed analytically and theoretically. Qualitatively, the flexibility matrix obtained from the experiment is only slightly different from the matrices obtained analytically. The experimental static flexibility matrix is also very nearly symmetric, and the differences between the analytically and experimentally obtained flexibilities can be primarily attributed to experimental error.

It should be noted that the experimental flexibility matrix was obtained from a single load test of the cantilever beam. It may be possible to further minimize the experimental error repeating the test several more times and taking the average of the results. The most important observation that can be made from these results is that even with a very simple and mechanically transparent physical model tested under ideal conditions in the laboratory, there will be experimental errors and uncertainty in the quantitative characterization results.

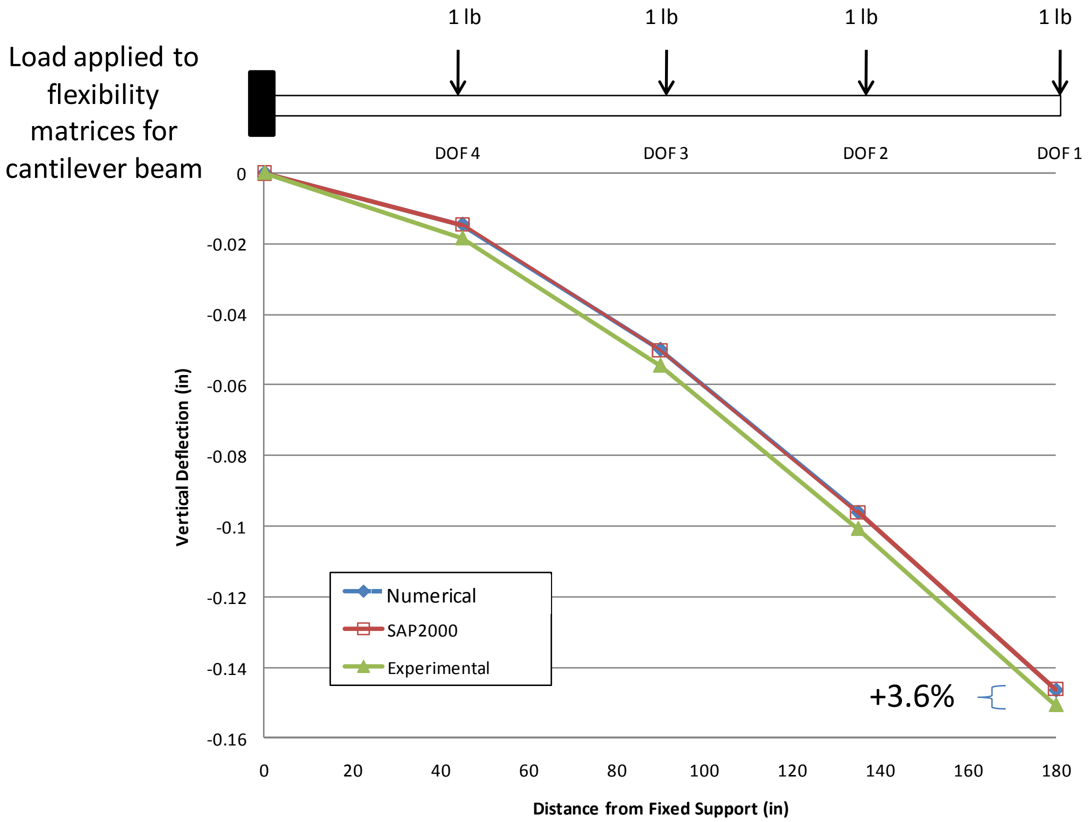

Figure 4.11: Deflection Profiles from Virtual Uniform Load Applied to Flexibility Matrices

4.5 DYNAMIC TESTING OF THE CANTILEVER BEAM MODEL

The primary objective of the dynamic testing program executed for the cantilever beam model was to evaluate the different dynamic testing strategies, procedures and their associated data analysis requirements to determine an optimal full-scale dynamic characterization approach for rapidly evaluating the condition and safety of bridge structures. The static and dynamic responses of a cantilever beam are very simple to conceptualize and predict for a broad range of loadings, so the physical model represented an ideal test specimen for starting such an evaluation. The dynamic testing and characterization of the cantilever beam was performed using several different types of dynamic excitation. Controlled dynamic testing of the beam was accomplished using an instrumented impact hammer and a linear mass shaker device. These devices permitted the dynamic excitation supplied to the structure to be measured. The measured input permitted the modal vectors identified from the results to be scaled and enabled a scaled modal flexibility matrix to be computed from the results. The beam was also characterized by ambient vibration testing in which the dynamic excitation is neither controlled nor measured, and only the vibration responses of the beam were utilized to characterize the structure. The dynamic tests provided quantitative descriptions of the cantilever beam in terms of its natural frequencies, mode shapes, damping ratios, and modal scaling (controlled dynamic tests). The different dynamic testing methods applied to the cantilever beam and their results are further described in the following sections.

4.5.1 Impact Hammer Testing

Dynamic testing via an instrumented impact hammer has several advantages. The frequency band of the dynamic excitation provided by an impact hammer is broad-banded, which permits many modes to be excited simultaneously. The impact hammer can be equipped with a variety of rubber tips having different stiffnesses. The different rubber tips allow both the amplitude and the frequency band of the dynamic excitation to be modified to some extent. Impact hammers are relatively inexpensive and can be used to dynamically characterize a structure quickly. Instrumented impact hammers are available in different sizes, but they must be sized correctly for a given test structure. Using too small of a hammer on a large structure will not provide enough energy into the system to fully excite the modes. The hammer tip selection is also an important consideration in designing a test. The soft hammer tip provides an impulse force that has a longer time duration than a hard tip. The frequency band associated with a long duration pulse is narrow and will only excite the lower modes of the structure. Conversely, a hard tip has a very short impulse time duration which results in a larger frequency range for the input. Using too small of a frequency range will limit the modes captured, while using too large of a range may excite non-linearities of the system present at higher modes. In addition, the larger frequency band may not provide as much energy to each of the individual modes.

The impact testing of the cantilever beam was accomplished using a Model 086C03 instrumented impact hammer from PCB Piezotronics. This hammer provides a range of ±500 lbf, with a sensitivity of 10 mV/lbf. Initially a soft black tip was used for this test. It was thought that this tip would adequately excite the lower modes, as these are the modes that will contribute most to the dynamic response of the structure. After further testing, a softer red tip was used, and better results were obtained. Figure 4.12 shows the time domain and frequency domain representations of the impulse force created by the impact hammer. As seen in the figure, the energy input rolls off rather quickly when the frequency is increased. Using this soft tip better excited the first bending mode, and gave a better coherence in the impact test performed, thus producing the closest approximation of the structures response.

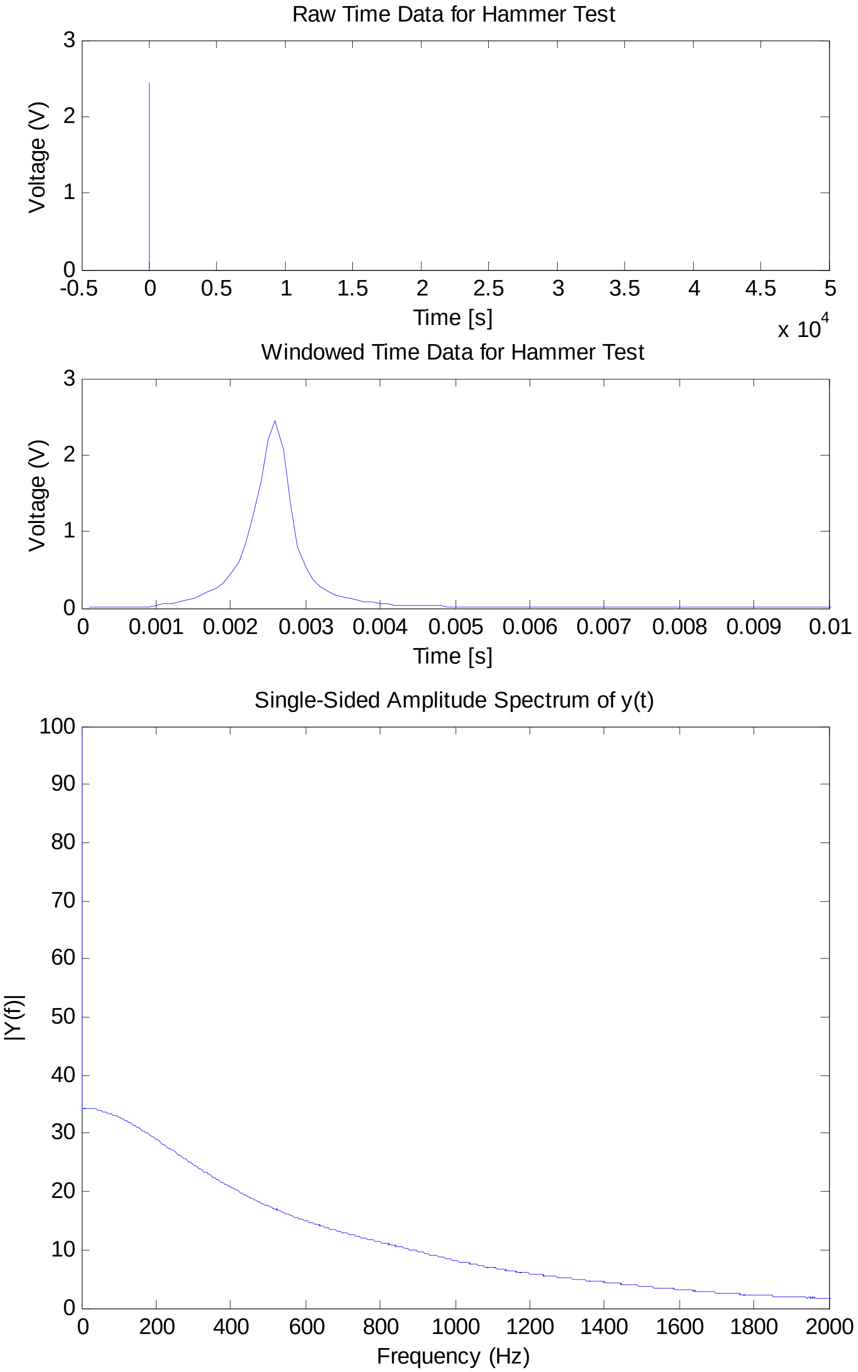

Figure 4.12: Time and Frequency Response of Impact Hammer

To conduct the impact dynamic test for the beam, the data acquisition system was set up with five channels of data, one for the hammer and four for the accelerometers at each node, excluding the support accelerometer. The system was set to detect the rising voltage of the impact hammer, and then collect data starting 20 data points before the rise was detected. This ensured that the equilibrium state before the impact was applied and the entire impact force were captured. The system collected for 20 sec on all channels to ensure that the vibration died out while the data was being collected, so as to not have any leakage.

Each node was impacted five times to average out any noise present in the measurements. All four of the nodes were impacted in this manner, thus giving a full dynamic test of the structure. When the measurements were converted into Frequency Response Functions (FRFs), a full 4 x 4 FRF matrix was compiled. A plot of the FRF matrix is shown in Figure 4.13. One can see that from this figure, that the same peaks are present in nearly every plot. These peaks are the natural frequencies of the structure. If the impact and response location were at a nodal point, a stationary point in the mode shape, that peak does not show up. This can be seen in the FRF plot shown in the second column of the second row in Figure 4.13. The peak observed at approximately 15 Hz in the FRFs for the other locations on the beam is not very clear in this FRF. This frequency is associated with the second bending mode of the structure, which has a stationary node point located very near to DOF2 (Figure 4.18). With this FRF data, the CMIF algorithm was implemented in order to find the modal flexibility matrix.

Dynamic impact hammer testing was found to be very sensitive to several testing parameters. The initial testing was done with PCB 3711 capacitive accelerometers and the data was recorded using a National Instruments SCXI data acquisition device. This device had a 16 bit analog to digital converter (ADC), and the constant current excitation for the accelerometers was provided by an external source. The FRF plots, phase angle plots, and coherence function plots obtained from these measurements were all found to be very noisy, as shown in Figure 4.14. When this data was further processed, the resulting modal flexibility as represented by a deflection profile was around 15% stiffer than the analytical SAP2000 model.

Another series of impact dynamic tests were performed using different sensors and a different data acquisition device. For this test, Model 393B05 accelerometers were used with a National Instruments PXI data acquisition system that had 24bit ADC dynamic input modules. The same black hammer tip that was used for the previous impact testing was also used in this test. The resulting FRF plots were much cleaner, and this can be attributed to the better ADC resolution and more sensitive and accurate accelerometers that were used for the second test. Even though the FRF plots were cleaner, the modal flexibility matrix was found to be around 16% more flexible than the flexibility matrix extracted from the analytical model, a swing from the previous test of more than 30%. After looking closer, it was found that the coherence function in the first 10 Hz of the FRF was not very good. Given that the first bending mode was found in this range, and also that the first mode was the controlling mode of the modal flexibility matrix, it was decided that a new series of tests must be employed to carefully consider the coherence from the measurements.

The black hammer tip was then used in full test of the cantilever structure, with the average coherence of each subsequent hit carefully observed. It was found that the coherence function would diverge at low frequencies when the cantilever was not completely damped out to zero movement before the next hit was applied to the structure. This point of zero movement could not be detected with the naked eye but was found by looking at the real time acceleration response of the structure. The resulting test produced clean FRFs, with good coherence, but the modal flexibility was still roughly 40% different from the analytical flexibility matrix..

The tip was then changed to a softer red tip, to help excite the first bending mode better. Again, a close observation of coherence was implemented, and very good results were obtained. One can see from Figure 4.15 that the data is much cleaner, and the coherence only diverges at anti-resonance, which is reasonable (Allemang, 1999). A representation of the modal flexibility in terms of a deflection profile for these results is shown in Figure 4.16. Note that the error was reduced to less than 4% by using the proper tip, watching the coherence closely, and using better sensors and data acquisition equipment.

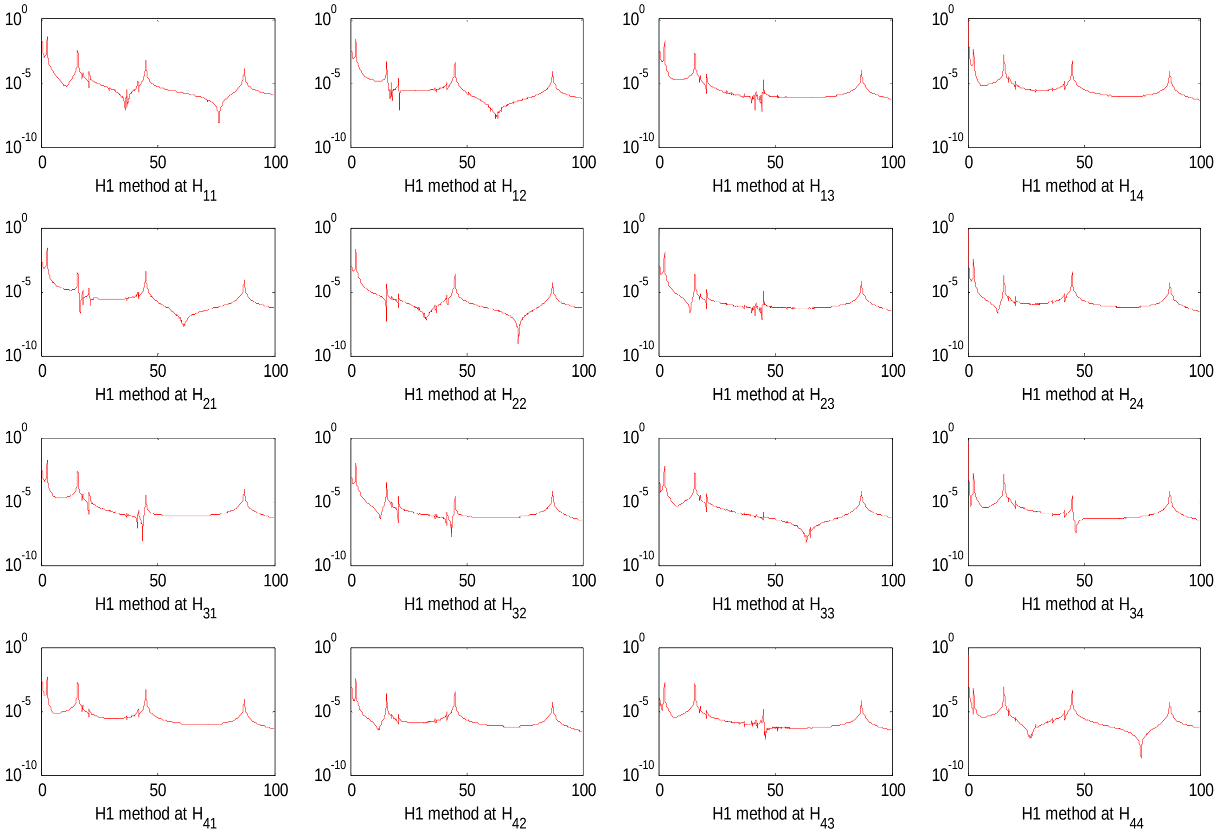

Figure 4.13: FRF Plot of Cantilever Beam due to Impact Test

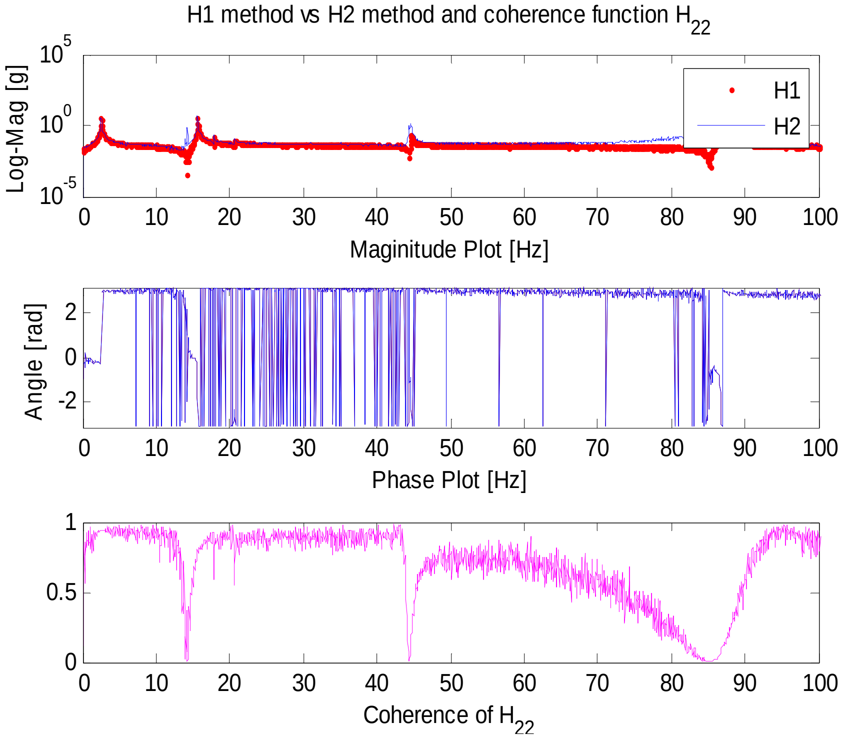

Figure 4.14: Noisy FRF Plot due to Inferior Equipment

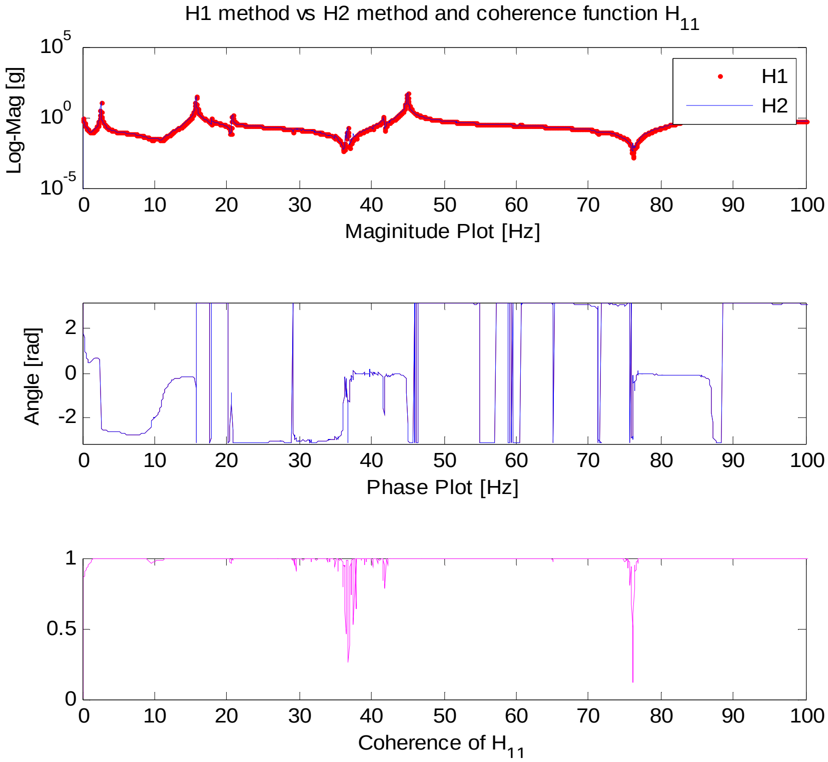

Figure 4.15: Clean FRF Plot with Good Coherence

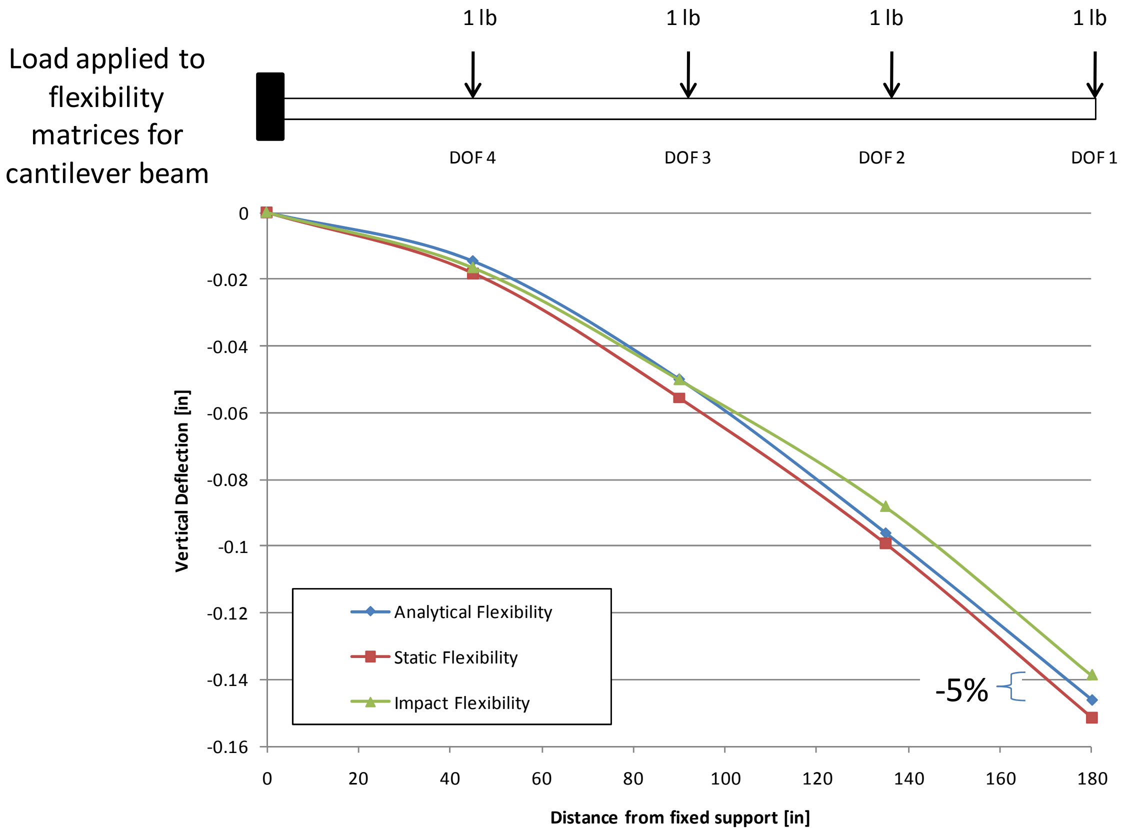

Figure 4.16: Deflection Profile for Impact Hammer Test

4.5.2 Dynamic Shaker Testing

The beam was also tested using a linear mass shaker device to provide the dynamic excitation. The nature of the excitation supplied by a linear mass shaker is able to replicate any type of signal passed to its amplifier. Some important benefits of shaker testing include being able to accurately control the input into the system, being able to cover any frequency range of interest, and being able to input large forces into large structures. Some of the disadvantages include: that is may be expensive and difficult to deploy dynamic shakers in the field, and a need for an ample power supply for the shaker-amplifier setup.

One advantage of shaker testing in a structural health monitoring situation would be that a shaker could be set up on the bridge and left there to be controlled by personnel offsite. If an impact test were desired, a live body would need to be present on the structure to impact at all the locations of interest for the test. The shaker must be attached to the model using a stinger. The affects of a stinger on the response of the structure is an important detail not to be overlooked. Stinger location, stinger alignment, stinger length, and stinger type can all affect the FRFs obtained from a given test. Cloutier and Avitabile (2009) thoroughly explored each of these different effects on the measured FRF's obtained from modal testing, and are great resources on the topic. In order to minimize the effects mentioned, a single setup was used for the entire series of tests. Therefore, if any error was introduced, it would be common to all measurements taken.

Mayes (2006) pointed out seven different challenges associated with shaker testing and how to overcome those challenges. Included in the list was how to obtain good results, minimize noise, and what types of signals to use. Mayes, along with Allemang (1999), talk about the differences in excitation signals, and show the advantages and disadvantages to each type. From these resources, it was found that the best excitation source was either a burst-random type, or a swept sine. After consulting the literature on dynamic shaker testing, it was decided that a burst random signal type would be the best type of input for the desired results. A 20 seconds long burst random signal was input to the structure. The burst random signal contained a flat line input on both ends of the signal, so that a periodic input could be simulated, and the decay due to the structures natural damping could be analyzed. Figure 4.17 represents the input signal used. This shaker excitation was provided at all of the nodes in separate setups, and the response was measured at all nodes in each setup. A total of five averages were recorded for each input location. The results obtained were close to the analytical and impact results. It was observed that placing the shaker close to the support produced very noisy and erroneous data. The FRF and coherence plots became much clearer as the shaker was moved to nodes located farther away from the fixed support. It is hypothesized that shaking the beam near the support produced floor vibrations that traveled through the support into the structure, further exciting it. Since this was unaccounted for in the load cell attached to the shaker armature, the result was bad coherence.

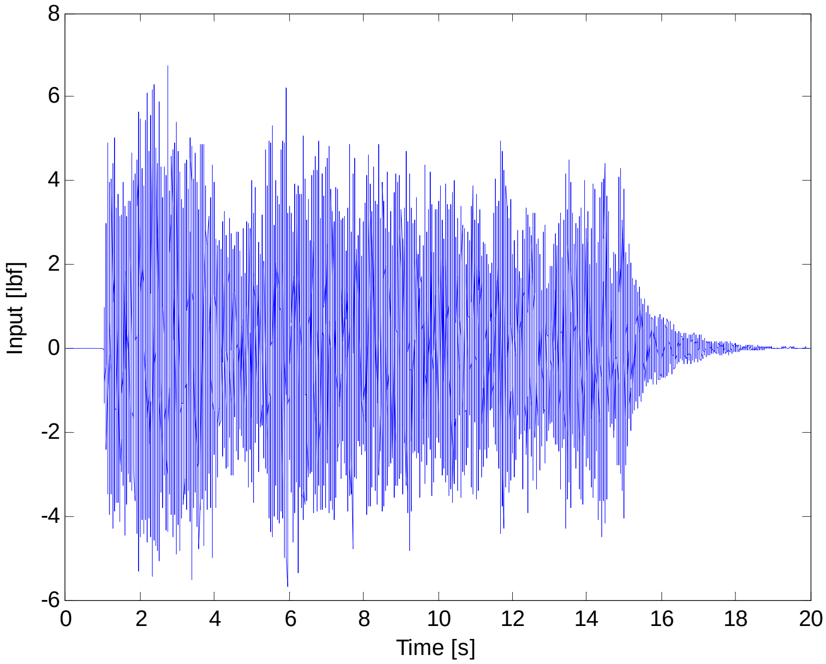

Figure 4.17: Burst Random Shaker Input

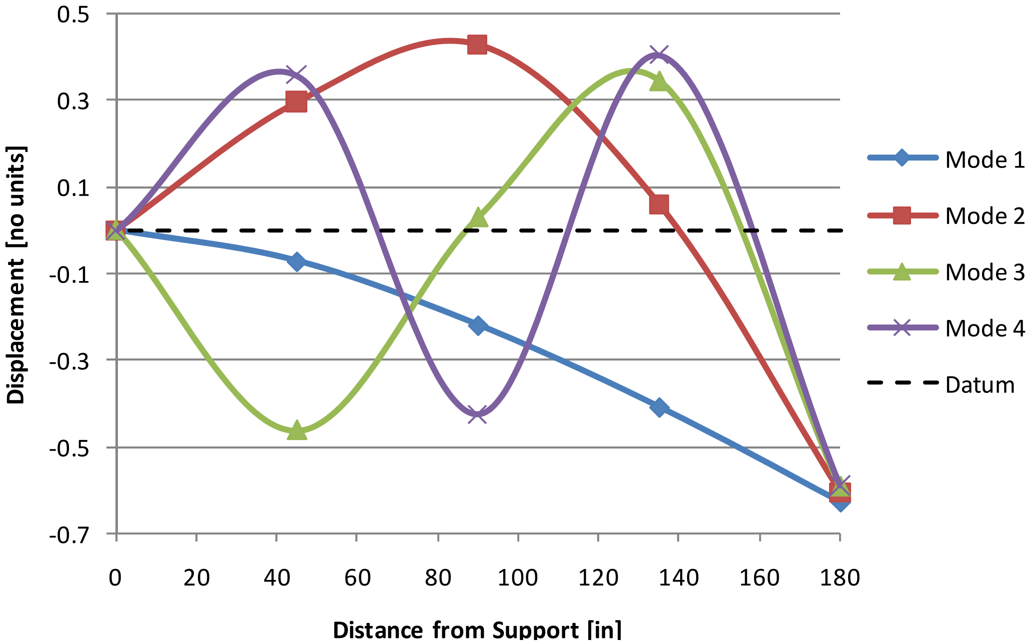

Figure 4.18: Mode Shapes from Shaker Test

Using the peaks in the CMIF, the mode shapes and frequencies of the system were found. This data lead to the modal flexibility matrix, which was then multiplied by a uniform load vector to obtain the deflection profile shown in Figure 4.19.

The flexibility matrix obtained from the shaker testing was very consistent with the flexibility matrix obtained from the static testing and the analytical model. The errors present may be attributed to testing errors and ambient noise present in the laboratory during the dynamic testing. It should be noted that the shaker test contained noisier results, which may have contributed to it being slightly less accurate.

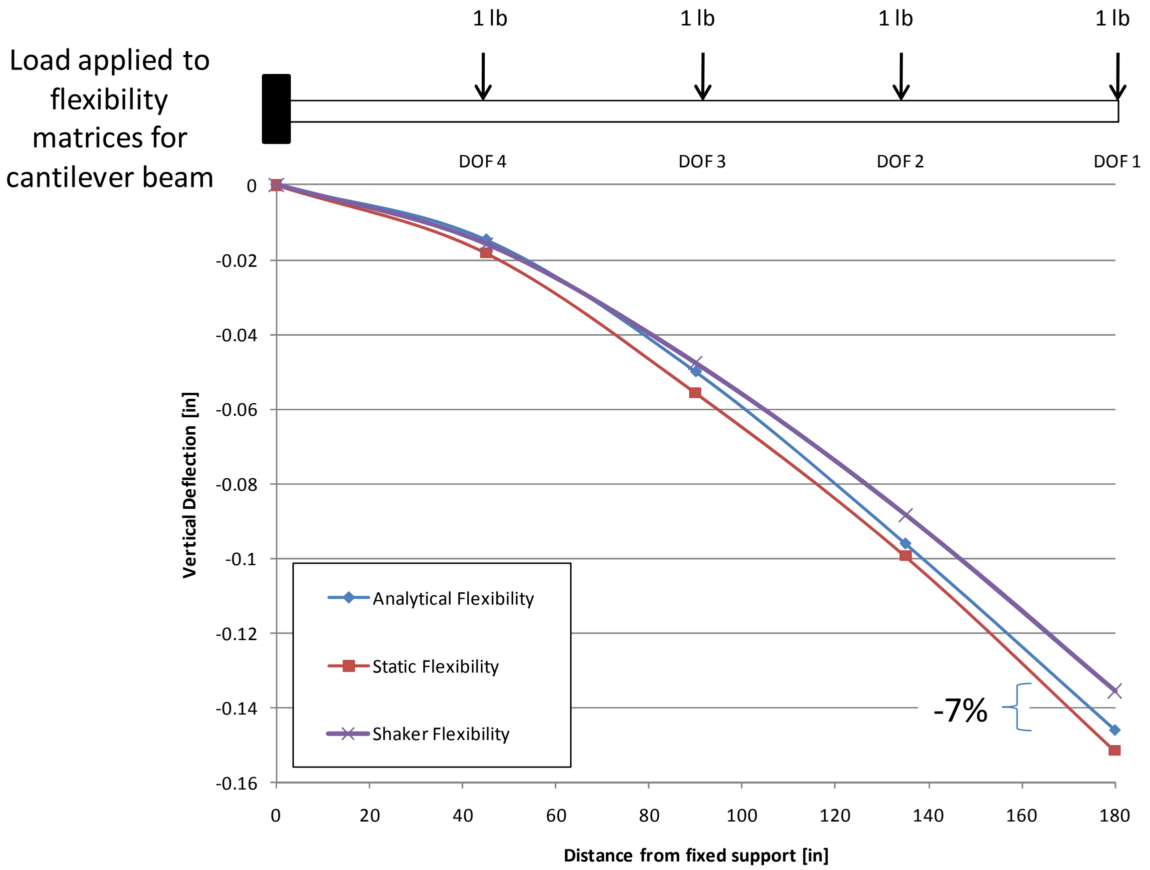

Figure 4.19: Deflection Profile for Shaker Test

4.5.3 Ambient Vibration Testing

Ambient testing has many benefits, and has been used for numerous years in structural health monitoring and structural identification systems. The main benefit of using an ambient vibration test is that an excitation device is not needed to perform this test. The dynamic excitation of the structure is provided by ambient sources including wind, traffic, etc. Since the excitation input is not measured, scaled mode shapes and therefore scaled modal flexibility is not obtainable. The problem with not having a scaled modal flexibility is that an accurate scaled deflection profile or load rating is not possible. On the other hand, a pseudo flexibility can be found, as well as natural frequencies and mode shapes. Doebling and Farrar (1996) have done some work on obtaining scaled modal flexibility from ambient data with marginal results, showing there is still work to be done in this area. Despite this setback, ambient data has important long term structural health monitoring benefits (Aktan, 2002). The FHWA has initiated a long-term bridge performance program, where a number of bridges are to be instrumented to provide continuous, long term structural performance data (Friedland, 2006). The modal parameters obtained can be compared to the scaled values, and conclusions drawn regarding the effect of structural changes seen in the change in modal parameters.

Initially, 8 Model 3711 accelerometers were used to capture the ambient noise present in the room during data collection. Collecting raw “noise” data proved to be inconclusive, and no quantifiable frequencies or mode shapes were obtained. When a small excitation was provided by light finger taps along the cantilever, the structure became excited and some of the lower modes did show up. Several attempts were made to obtain these parameters using only the ambient excitation in the laboratory, but this proved to be difficult. The resulting Power Spectral Density (PSD) plot obtained from finger tapping excitation of the cantilever beam can be seen in Figure 4.20. Notice that the first peak shows up well, while the second peak is more of a band of power near the natural frequency.

The capacitive accelerometers on the beam were replaced by Model 393B05 accelerometers. Much clearer results (with the exception of DOF8 close to the support) were obtained from this setup. The first four modes could be identified (Figure 4.21), and the natural frequencies were consistent with the natural frequencies found from the other dynamic tests and analyses. It was determined from both the ambient test and the impact test that the combination of capacitive accelerometers coupled with a 16 bit ADC did not provide enough resolution to clearly capture modal parameters, and was therefore not used on the grid structure.

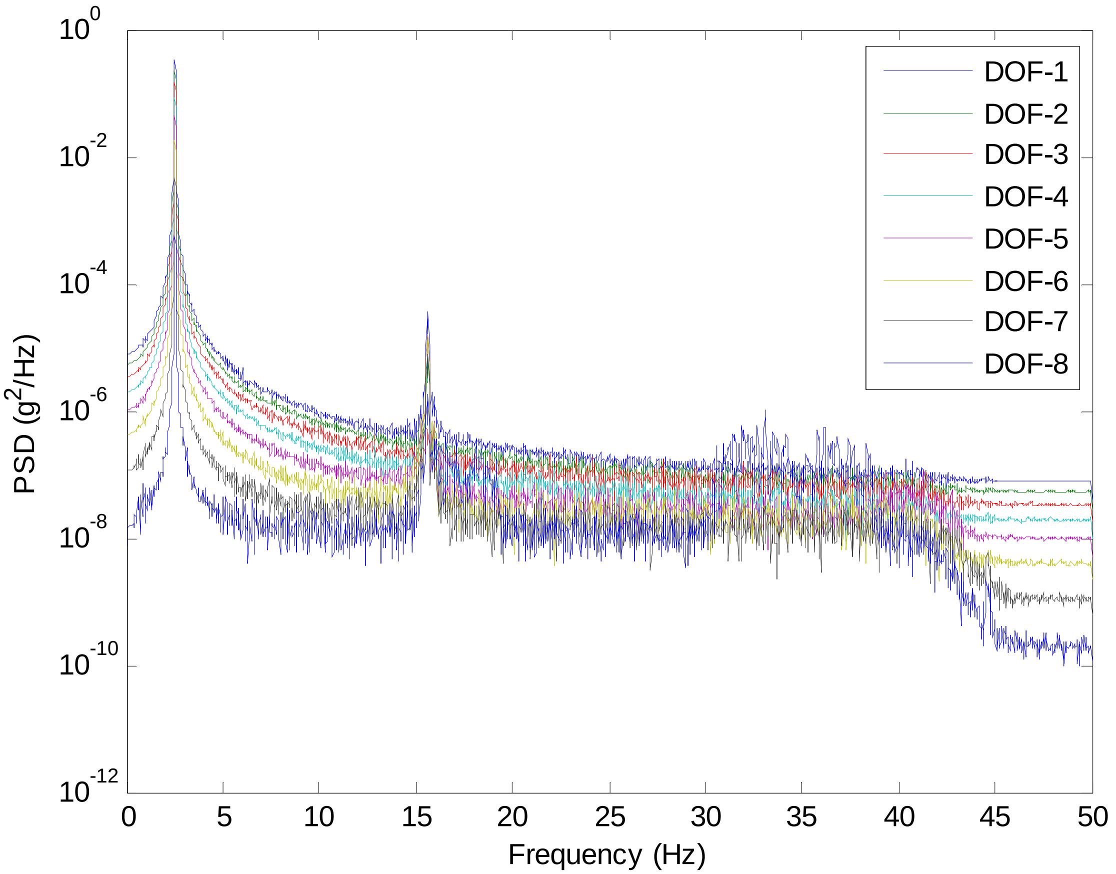

Figure 4.20: PSD of Cantilever Beam with PCB 3711 Accelerometers

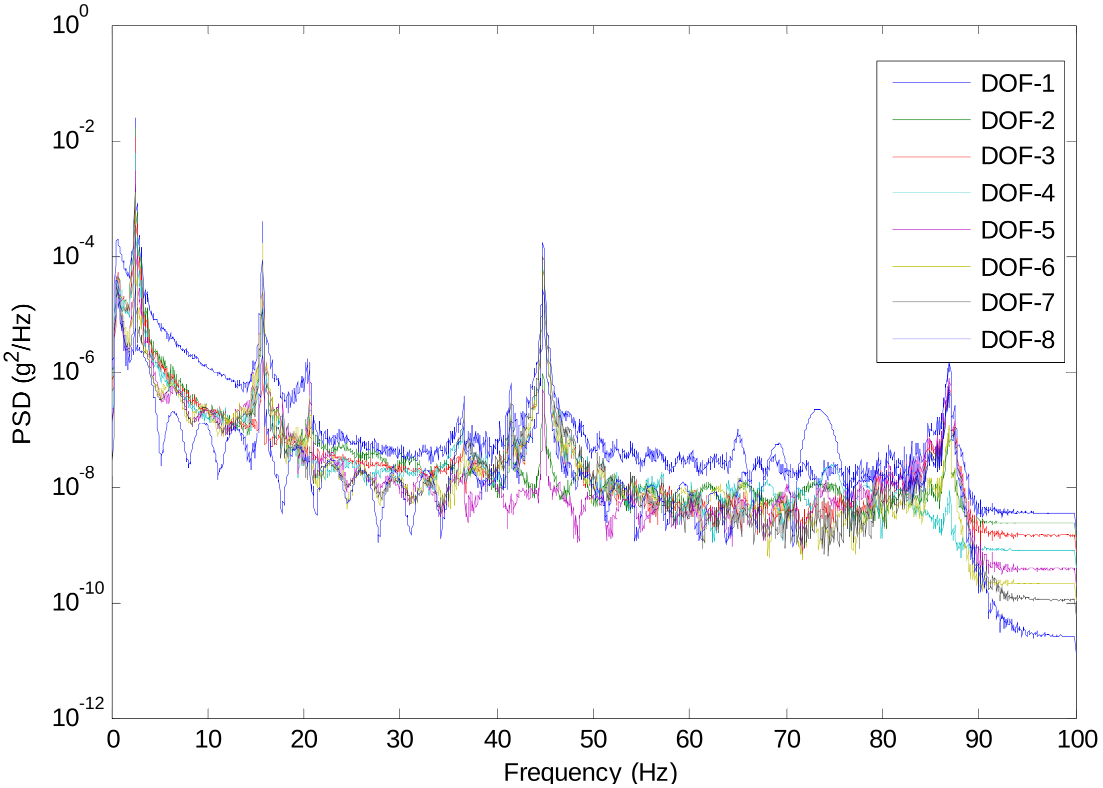

Figure 4.21: PSD of Cantilever Beam with PCB 393B05 Accelerometers

4.6 SUMMARY

Several things were learned from the full scale testing of the cantilever beam, and are summarized here. First, it should be noted that there is very good agreement between the different testing methods used. The natural frequencies and damping found from the different approaches are summarized in Table 4.4. One can see that between experimental tests, all of the natural frequencies are relatively consistent. It can also be seen that the analytical model is slightly off from the experimental model, thereby showing that even on the simplest structure, tested in a controlled laboratory setting, exact representation is not easily obtainable. This point is further verified by looking at the deflection profiles from the modal flexibility matrices, as seen in Figure 4.22. The different experimental tests vary in total by about 10%, with the closest approximation being the static flexibility. The two modal flexibilities were obtained using only the first four modes, and were expected to be less than the static or analytical because of the limited inclusion of modal contributions.

Table 4.4: Modal Properties Summary for Cantilever Beam

	Analytical Model	***Impact Test***	***Shaker Test***	***Ambient Test***
Mode Number	Natural Frequencies (Hz)			
1	2.67	2.54	2.54	2.54
2	16.70	15.72	15.61	15.72
3	46.63	44.93	44.65	44.82
4	91.03	87.04	88.09	86.87
Mode Number	Damping (%)			
1	-	0.12	1.44	-
2	-	0.08	0.12	-
3	-	0.07	0.01	-
4	-	0.11	0.10	-

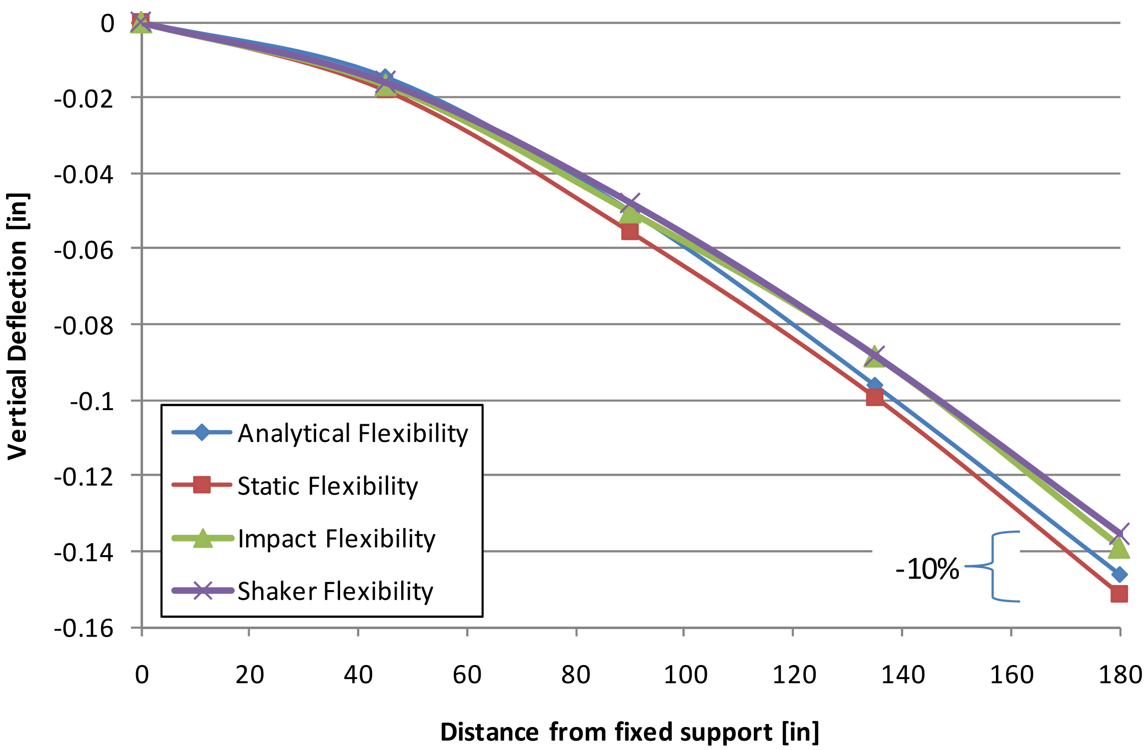

Figure 4.22: Deflection Profile for Cantilever from Tests

Another important matter to consider is modal contribution. Having a good estimation of the contribution of each mode is important when designing the test in order to know how many modes to capture and how the overall flexibility is affected by those modes.

Furthermore, when estimating modal parameters it was observed that changing which peak value used for the eFRF creation affected the modal flexibility a considerable amount. Figure 4.23 shows a close up view of the first modal peak in the CMIF plot for the cantilever. The left circled peak corresponded to a more accurate mode shape, and was therefore initially chosen for the eFRF creation. When changing this peak to the higher amplitude, the final modal flexibility obtained changed by over 10%. This shows that peak picking can be a very delicate process, and that small changes may produce large differences. This is especially true in the first mode of the cantilever, which controls 62% of the flexibility. Therefore clear understandings of the controlling modes, and the effect of peak picking on the calculated modal flexibility, are crucial for proper modal parameter estimation.

Overall, an important observation that can be made from these results is that even with a very simple and mechanically transparent physical model tested under ideal conditions in the laboratory, there will be experimental errors and uncertainty in the quantitative characterization results.

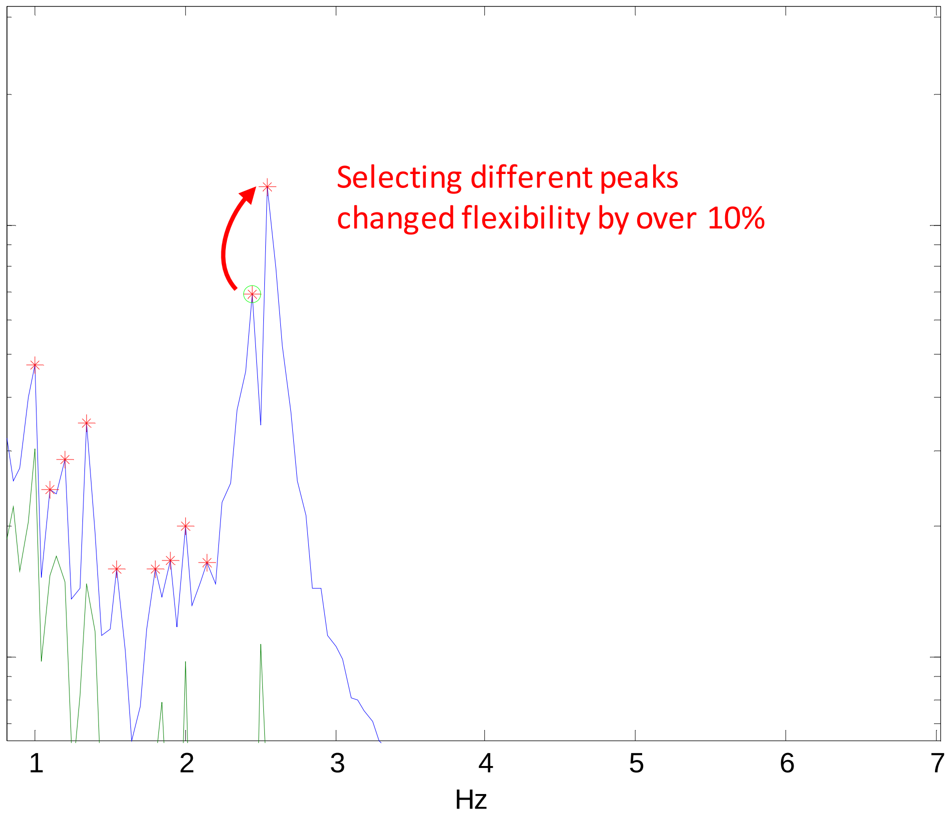

Figure 4.23: Effect of Peak Picking on Modal Flexibility

5. CHARACTERIZATION OF AN UNDAMAGED GRID MODEL

Starting with a simple model, such as the fixed end cantilever beam, allowed the research methods and procedures used for sensor setup, data collection, and post-processing techniques to be verified. Once this was accomplished, a second laboratory test evaluation program ensued on the grid model, which can be seen in Figure 5.1. This grid model was assembled in the research lab, and thus provided an excellent avenue for expanding the test methods proposed into a bridge type structure. The grid was composed of W8X10 beams bolted with gusset plates at the joints. Since this structure did not contain a concrete deck, it was not as stiff as a girder bridge with a deck would be, but still provided an excellent avenue for evaluating an optimal SHM method on simply supported, girder-bridge type structures. The grid was tested in a similar manner as the cantilever, starting with static testing and ending with ambient vibration testing. One difference between the grid model and the cantilever model was in the solution of mathematical equations for the governing equations of motion and static flexibility. While closed form equations were available for a cantilevered structure, they were not easily compiled for a steel grid model like the one used. Therefore, the SAP2000 analytical model was a stand-alone analytical model, and was not verified with mathematical solutions.

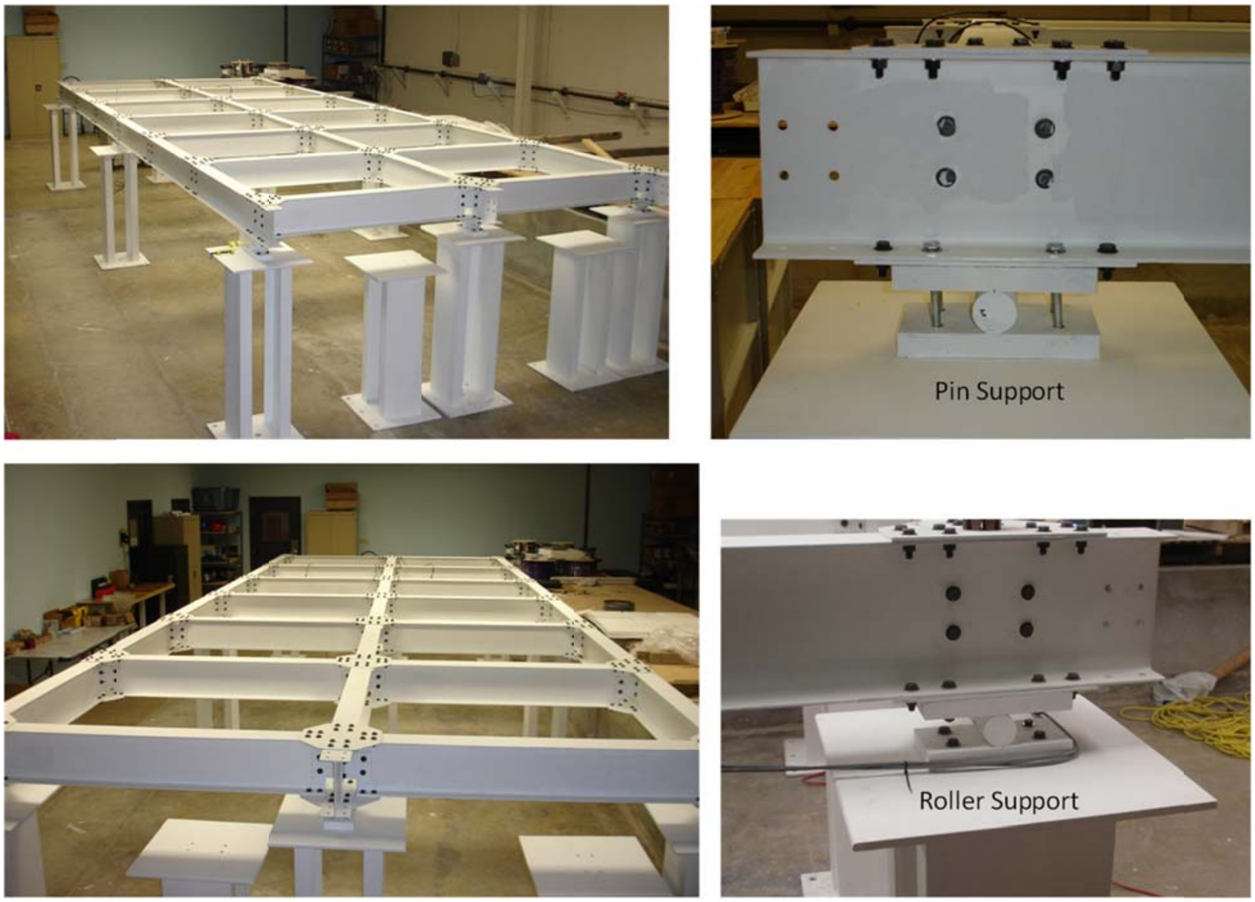

Figure 5.1: Simple Span Steel Grid Model

5.1 PHYSICAL GRID MODEL IMPLEMENTATION AND SETUP

The grid model structure used for this project consisted of longitudinal and transverse W8x10 rolled steel beams that were bolted together. The model included three primary longitudinal beams and 14 transverse beams. The width of the model was 9 ft. measured between the centers of the supports. The transverse beams were spaced at 4 ft. increments along the length of the longitudinal beams. The transverse beams were rigidly connected to the longitudinal beams using 3/16 in. thick steel gusset plates that were bolted to the top and bottom flanges of the beams, and by 4 x 3 x 1/4 in. vertical clip angles that were bolted to the beam webs. All of the bolted connections in the grid model used 3/8 in. diameter standard grade bolts. Each end of the main longitudinal beams was supported on pin or roller bearings that were attached to steel pedestals, with an overall span length of 24 ft. Several photographs of the grid model in the laboratory are shown in Figure 5.1.

A numbering system was devised to describe locations on the grid structure in which the intersections of each transverse and longitudinal member was assigned a letter between A and G corresponding to the locations of the transverse members, and the number 1, 2, or 3 corresponding to each of the main longitudinal beams. The numbering convention adopted for the grid model is shown in Figure 5.2. In the simple span configuration, the support bearings were located at grid points A1, A2, A3, G1, G2, and G3.

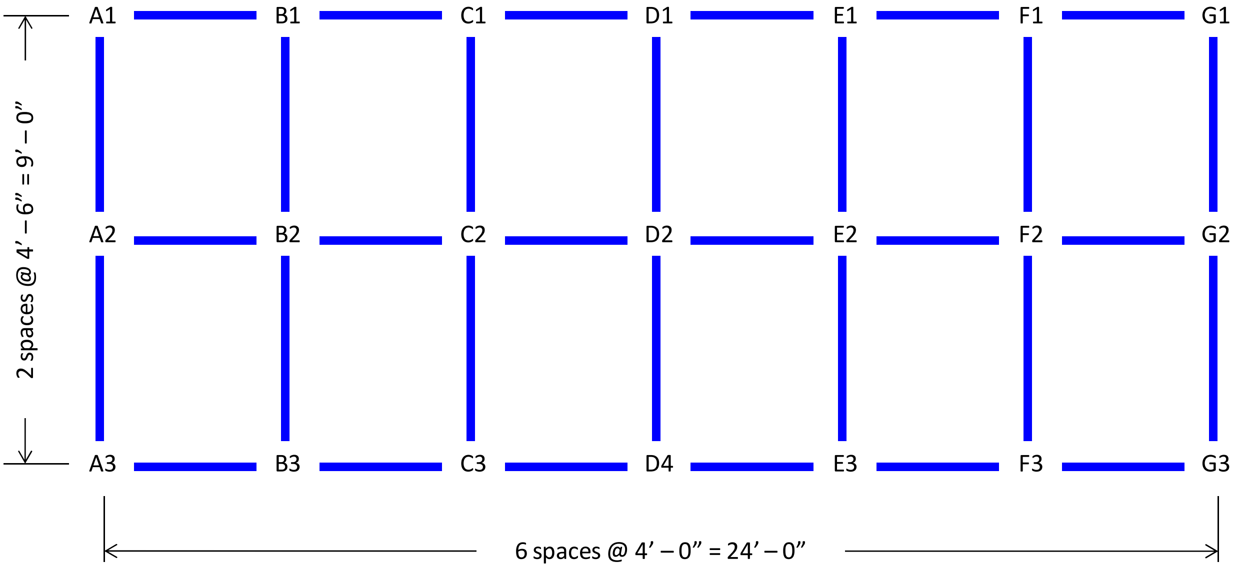

Figure 5.2: Numbering Convention for Grid Model

The grid model was instrumented with strain gages, accelerometers, and linear displacement sensors. The instrumentation scheme devised for this model was adequately able to reliably characterize this structure using both static testing and dynamic testing methods.

5.1.1 Strain Gages

A total of 26 strain gages were installed on the grid model in order to further calibrate the finite element model created in SAP2000 through static testing. The gages were installed at several locations along the length of the longitudinal beams at the top and bottom flanges, and on the underside of the bottom flanges of several transverse beams. Each strain gage was assigned a name that corresponded to its geographic location on the grid model and to its location on the beam's cross section. The strain gages used for the grid model were 350 Ohm weldable gages from Hitec Products, Inc. The strain gages were installed using a capacitive discharge spot welder and were axial gages that measured strain in one principal direction. They had a one inch active grid a nominal gage factor of 2.00. The gages were wired into the data acquisition system using a three wire Quarter Bridge circuit configuration. A photograph of a typical strain gage installed on the grid model is shown in Figure 5.3.

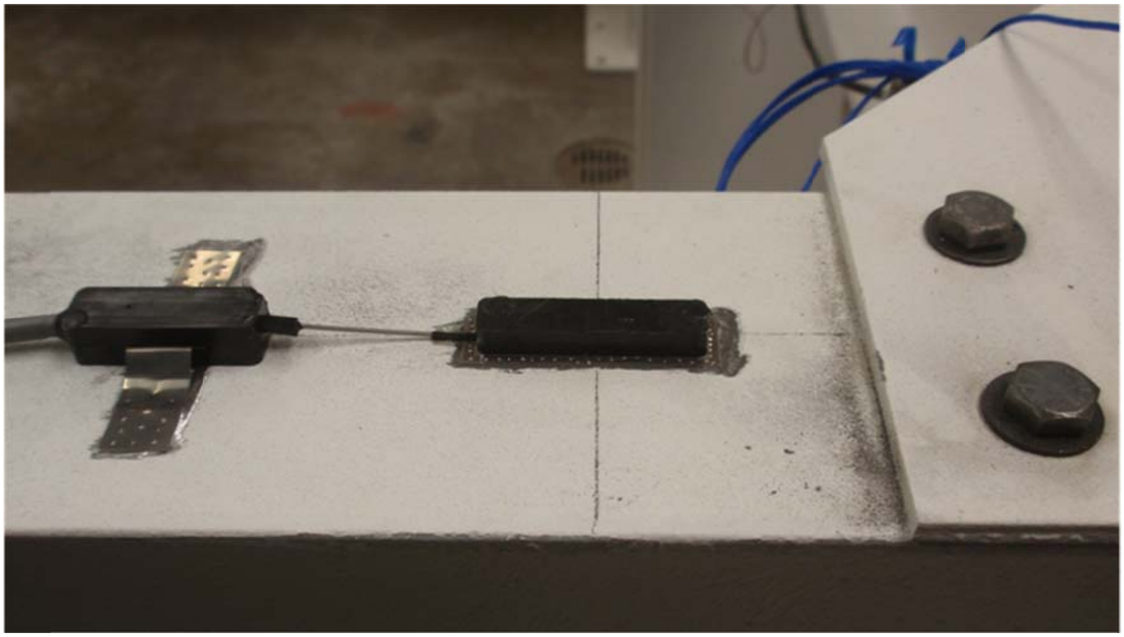

Figure 5.3: Typical Strain Gage Installed on Grid Model

5.1.2 Accelerometers

Two different types of accelerometers were used to instrument the grid model. The first type was the Model 393C seismic accelerometer from PCB Piezotronics, Inc. The second type was the Model 393B05 seismic accelerometer from the same company. Both accelerometers were integrated circuit piezoelectric (ICP) sensors, and featured built-in signal conditioning electronics. The Model 393C accelerometer used a quartz compression element to sense vibration while the Model 393B05 accelerometers used a ceramic flexural element. Both types of accelerometers required a constant current excitation, provided through the data acquisition system. The relevant performance specifications for each accelerometer type are summarized in Table 5.1.

The accelerometers were physically located at the intersections of the longitudinal beams and the transverse beams of the grid model. A total of 21 accelerometers were installed on the model and were oriented to measure the vibrations of the model in the vertical direction only. The actual attachment of the accelerometers to the model was accomplished using magnetic mounting bases (393C) and hot glue (393B05). The more sensitive Model 393B05 accelerometers were located above the support bearings for the grid model. Although very little vibration was expected to occur at the support locations these accelerometers served a valuable role in evaluating the condition of the structure for damage scenarios that were implemented, particularly those associated with changes to the support conditions. The Model 393C accelerometers were placed at the unsupported grid intersection points on the model. These accelerometers had a reasonably large measurement range and facilitated impact and shaker testing of the model, and were also sensitive enough to be useful for characterizing the model due to ambient vibrations. Each accelerometer that was installed followed the naming convention shown in Figure 5.2, and pictures of the accelerometers can be seen in Figure 5.4.

Table 5.1: Performance Specifications for Accelerometers on Grid Model

Specification	***Model 393C***	***Model 393B05***
Sensitivity	1 V/g	10 V/g
Measurement Range	2.5 g peak	0.5 g peak
Frequency Range (± 5% accuracy)	0.025 to 800 Hz	0.7 to 450 Hz
Broadband Resolution (1 to 1000 Hz)	100 micro g	4 micro g

5.1.3 Displacement Sensors

A total of three different types of linear displacement sensors were used in conjunction with each other for characterizing the grid model structure. The different types of displacement sensors were used because the instrumentation scheme for the grid model required a total of 15 displacement sensors and only limited quantities of each type were available in the laboratory. The displacement sensors used included the Model CDP25 displacement sensor from TML, and the Models SP2 and PT510 string pots from Celesco Transducer Products, Inc. The displacement sensors were installed to measure the vertical displacements of the grid model at each intersection of the longitudinal and transverse beam members (excluding the support locations). The locations and naming convention adopted for the displacement sensors installed on the grid model followed the naming scheme in Figure 5.2. A table showing the performance specifications of the different gages can be seen in Table 5.2.

Table 5.2: Performance Specifications for Displacement Gages

Specification	***TML CDP25***	***Celesco SP2-12***	***Celesco PT510***
Sensitivity	0.25 mV/mm	0.8 V/in	1.0 V/in
Range	0-25 mm	2-12 in.	0-5 in.
Type	Spring-pin	Cable Extension	Cable Extension
Quantity Used	7	2	6

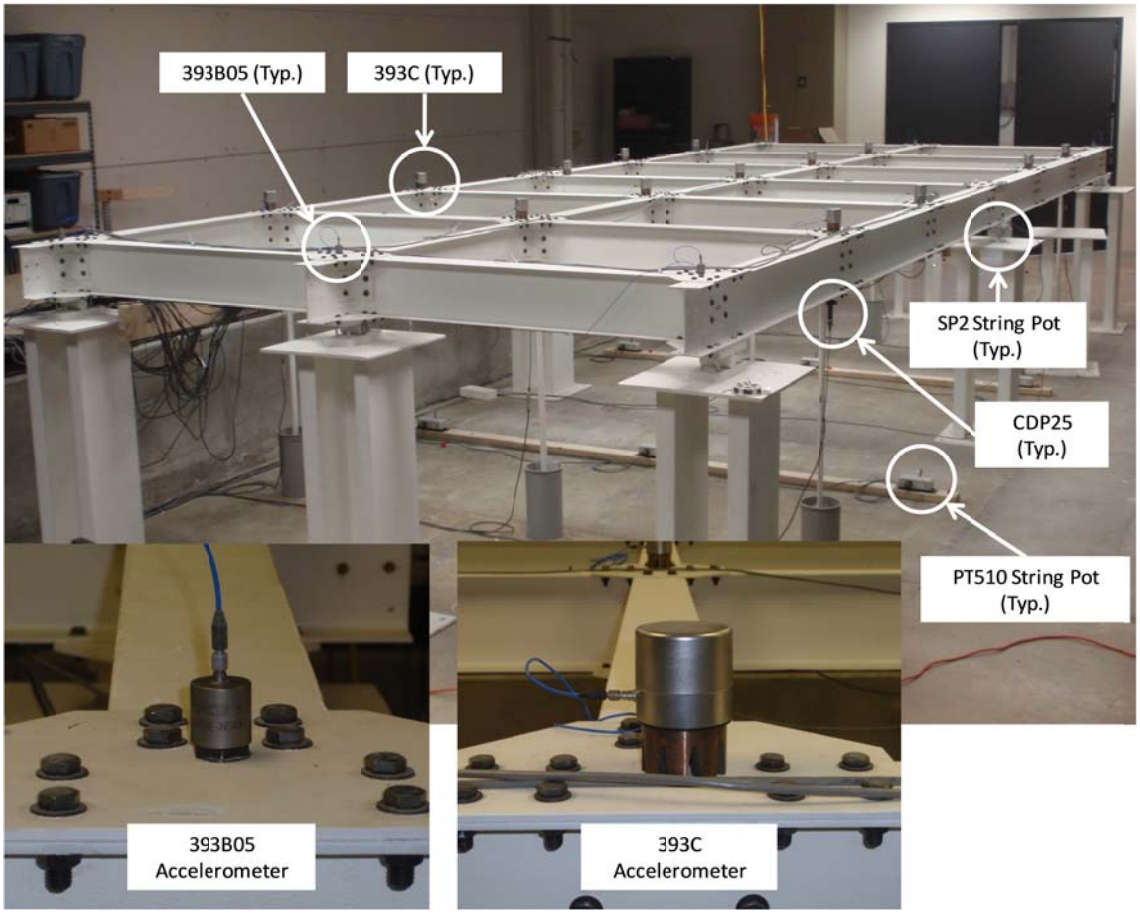

Figure 5.4 : Instrumentation of the Grid Model

5.2 ANALYTICAL CHARACTERIZATION OF THE UNDAMAGED GRID MODEL

The steel grid model described in the previous section was characterized analytically using the program SAP2000. The model used frame elements to represent the W8x10 longitudinal and transverse beams. Nodes (DOFs) were located at the intersections of the longitudinal and transverse beams. Although the analytical model was constructed from 3D frame (beam) elements with 6 degrees of freedom per node, only the planar degrees of freedom (DOF) were considered for the static and dynamic characterizations with this model. The planar DOF consisted of a translation and an in-plane rotation at each unrestrained node. The analytical characterization for the grid model identified the flexibility matrix from static analysis and the natural frequencies and mode shapes from dynamic modal analysis within SAP2000.

5.2.1 Static Analysis and Calibration

The initial analytical model developed in SAP2000 was somewhat idealized. The intersections of the longitudinal and transverse beam members were modeled as rigid joints; however, the additional bending stiffness provided by the top and bottom gusset plates was not included in the initial model. After performing the experimental static analysis and comparing to the static analysis results from SAP2000, it was found that this initial model was not accurate. Therefore, an updated model was created, taking into account some of the added stiffness associated with the gusset plates at the joints by replacing the frame members near the nodes with members that had additional flange thickness on top and bottom, as seen in Figure 5.5. This updated model produced a much more accurate representation of the grid model, and was therefore used as the baseline comparison tool for the different experimental tests performed on the grid.

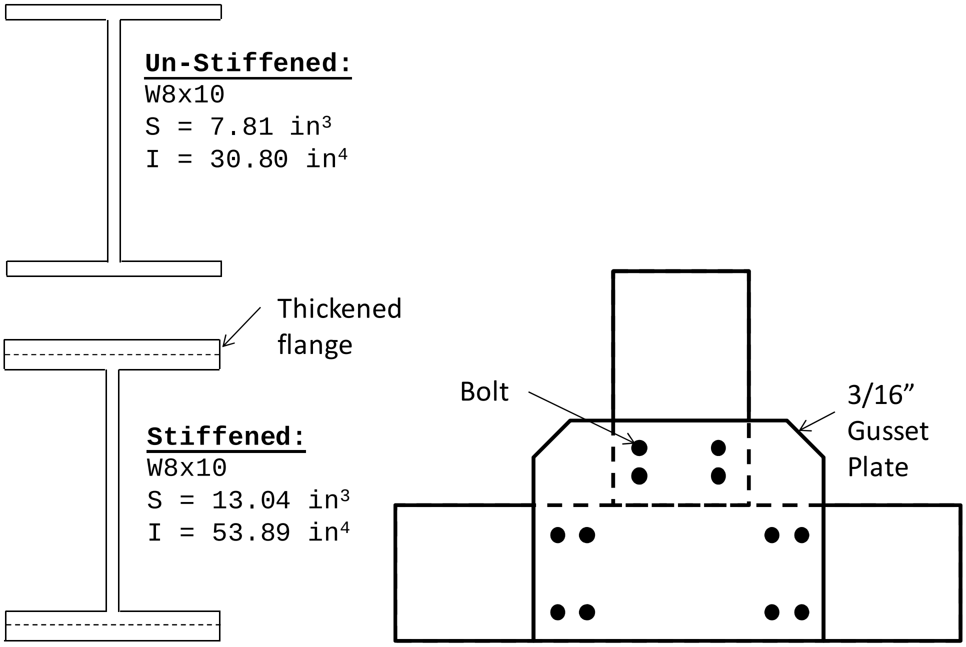

Figure 5.5: Stiffened vs. Un-stiffened Frame Members

The flexibility matrix was extracted from the model by performing a series of unit load analyses. A series of individual static load cases were created in which a unit load (1 kip) was place at each node (intersection of longitudinal and transverse beam elements) and the vertical deflections of all nodes were determined. The nodes corresponding to the support locations were not included in the analysis. The resulting flexibility matrix was a square symmetric matrix of size 15 x 15, and was normalized in order to get units of [lbf] and [in].

5.2.2 Dynamic Modal Analysis

A dynamic modal analysis of the grid analytical model was also conducted in SAP2000 to determine the dynamic properties of the system (natural frequencies and mode shapes). Centerline and extruded views of the analytical model are shown in Figure 5.6. In order to ensure the results of the analytical characterization were consistent with the experimental characterization program that was being performed on the grid model the DOFs were limited to the vertical direction only. It was expected that the modal flexibility found experimentally would not exactly match the static or analytical flexibility due to modal truncation. By analyzing the analytical model created in SAP2000, it was decided that only the first 8-9 modes could be reliably found and characterized experimentally due to spatial resolution of sensors and the frequency range of the sensors. Including these modes in the calculation of modal flexibility provided a good overall characterization of the structure and served as the baseline of comparison.

The calibrated FE model in SAP2000 was able to produce reasonably accurate mode shapes and natural frequencies that were able to serve as a comparison tool for the subsequent experimental tests performed. Without this baseline, it would be very easy to accept a wrong characterization of the grid structure, not knowing what a reasonable answer would be. From the analysis performed, the first nine modes and corresponding natural frequencies (in the vertical direction only) can be seen in Figure 5.7.

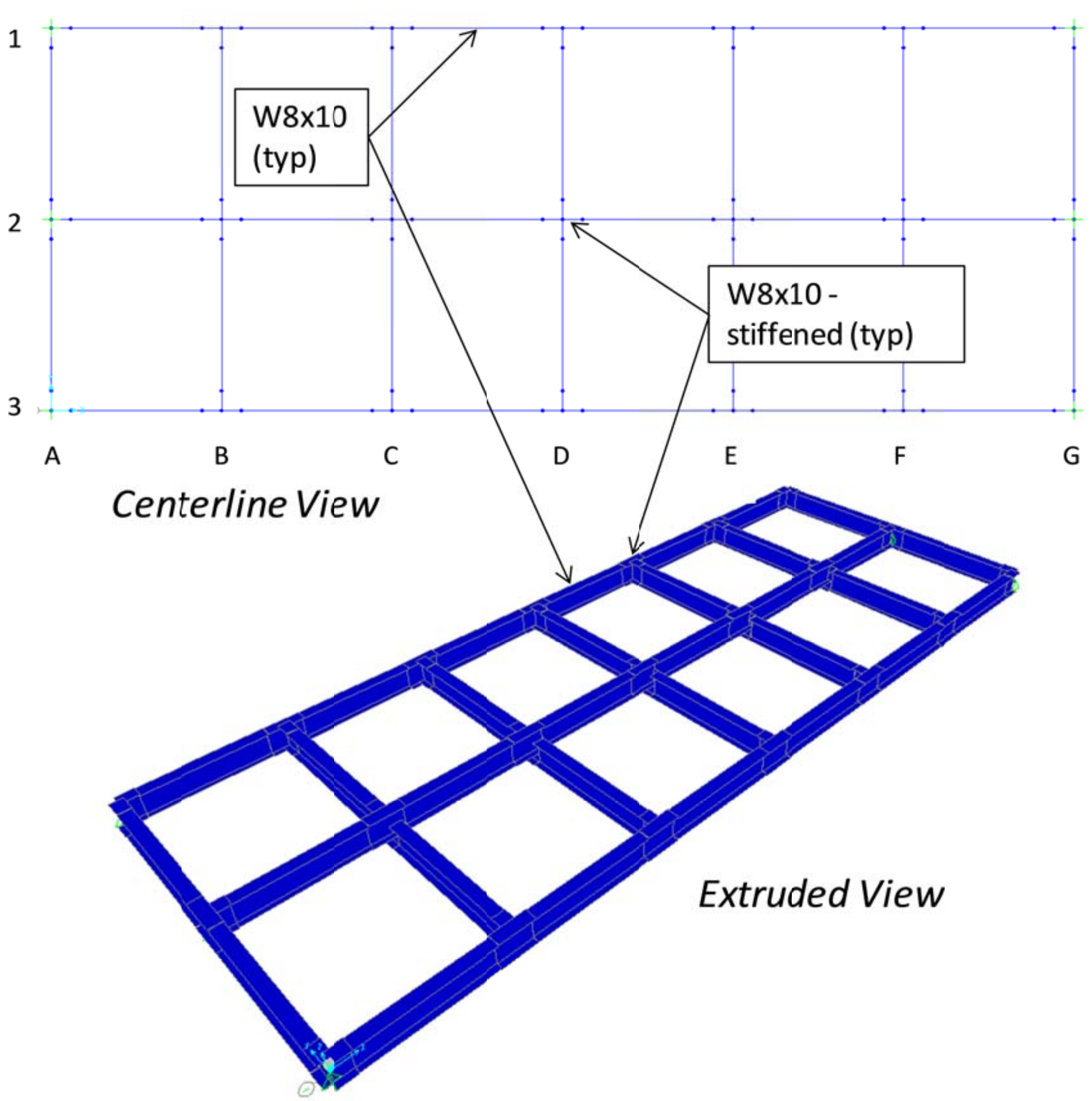

Figure 5.6: FEM Grid Model

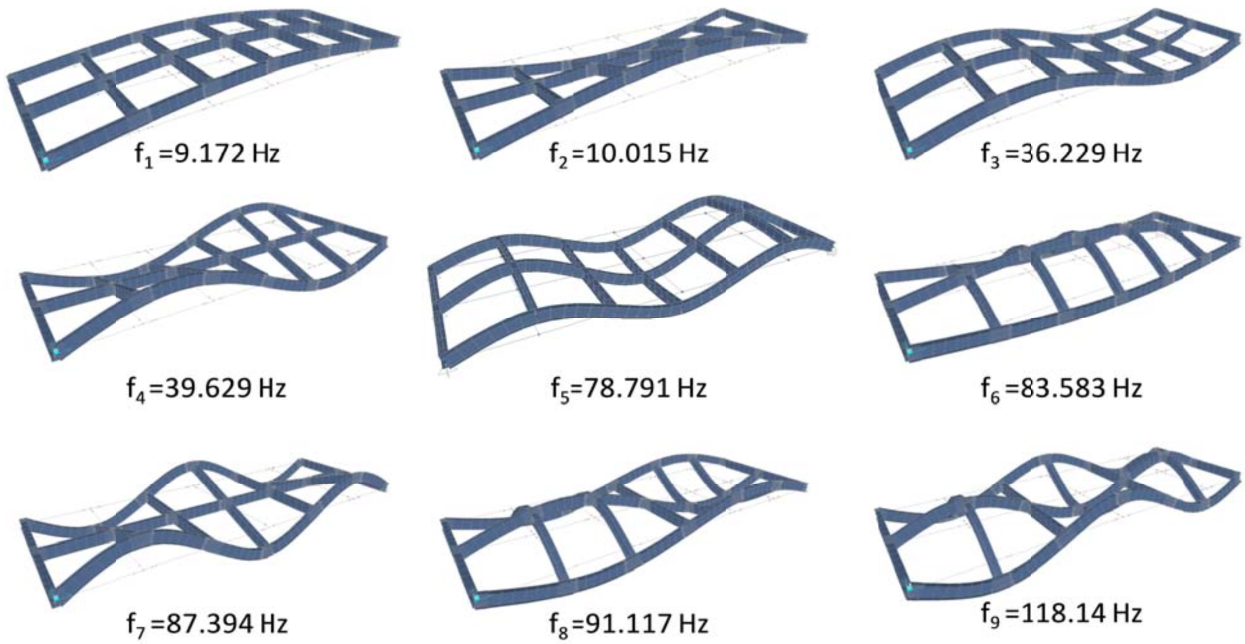

Figure 5.7: Grid Model Vertical Modes from SAP2000

5.3 STATIC TESTING OF THE UNDAMAGED GRID MODEL

5.3.1 Static Flexibility

In order to have a baseline of comparison, both for the analytical analysis as well as the dynamic characterization, several static tests were performed. As with the cantilever, the first test was a full static load test which entailed loading every node and measuring the resulting transverse deflections at each of the nodes. As noted earlier, the coefficients of this static flexibility matrix, f_{ij}, are given by the deflection computed at DOF*i* due to a unit load applied at DOF*j*.

The test consisted of four loading stages at each node, starting from 0 lbs and increasing to 600 lbs in 200 lb increments. A few locations were loaded to 800 lbs to see if the added weight mitigated the error present when compared to the analytical model. The loading was done by placing several 20 lb steel plates at each node, as seen in Figure 5.8. Careful attention was paid to calibration of the sensors and making sure the range on the digital to analog converter (DAC) was properly set so as to avoid producing a phenomenon know as quantization error. The results produced a stair-step type graph typical for each node, and is seen in Figure 5.9.

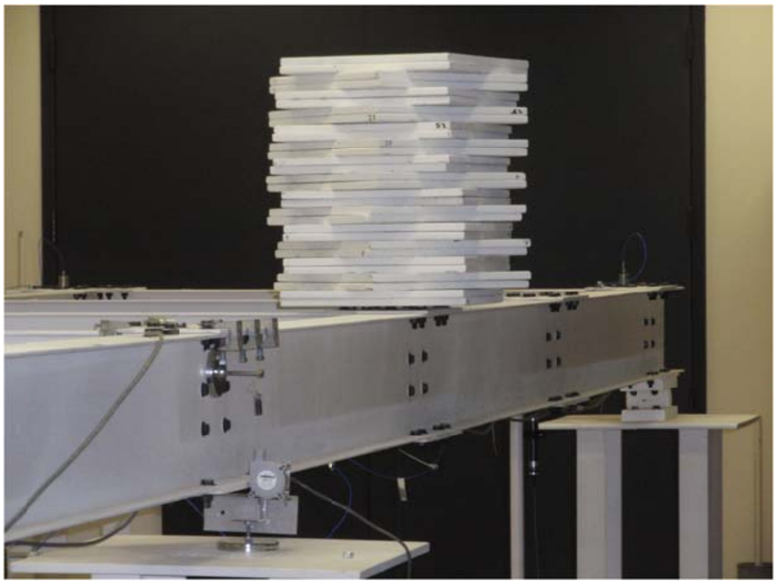

Figure 5.8: Static Load Testing of Grid Model

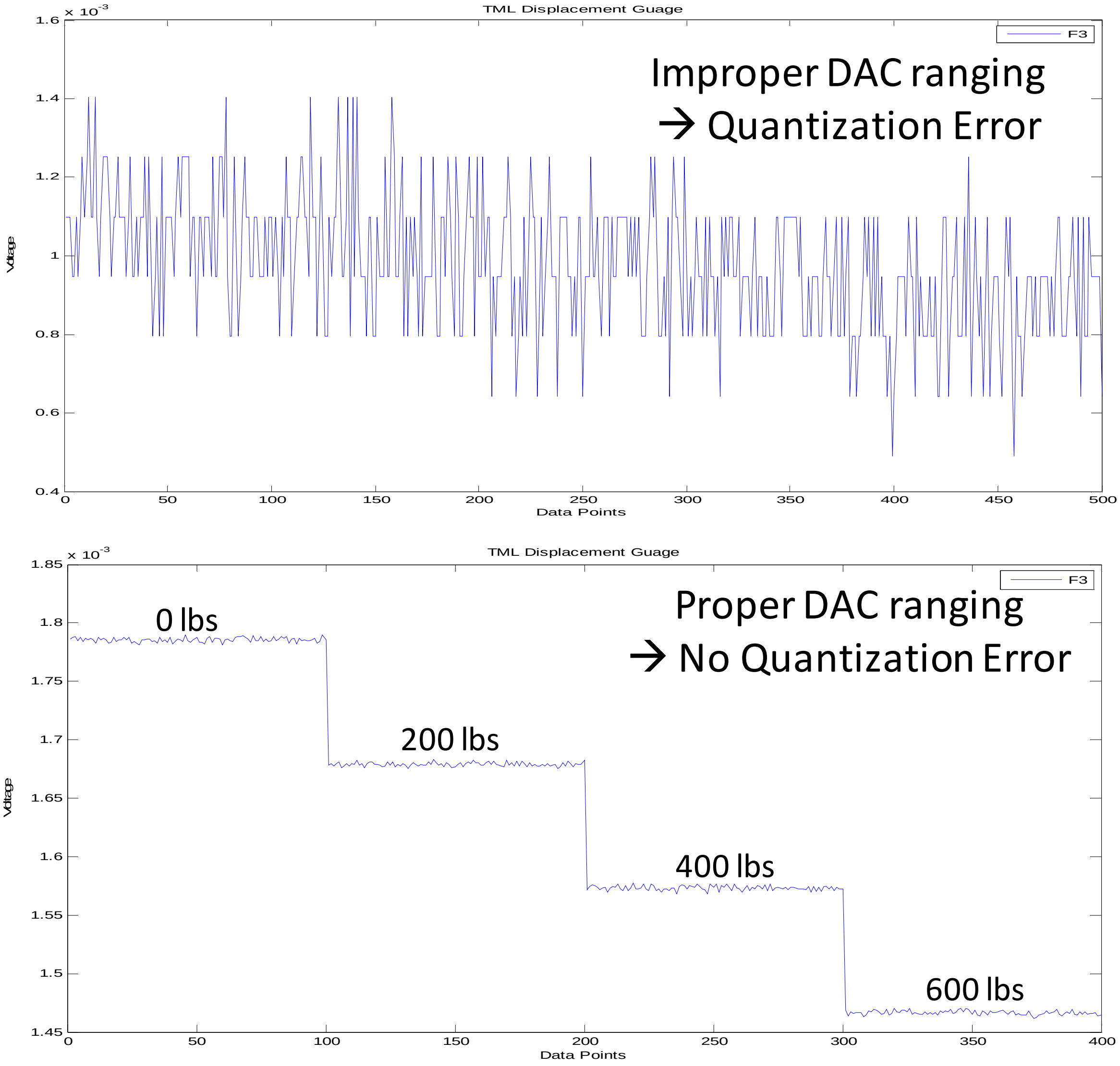

Figure 5.9: Displacement Reading from Static Grid Loading

Each loading scenario produced one column of the flexibility matrix, and was repeated until the full static flexibility matrix was obtained for each level of load (200 lbs, 400 lbs, 600 lbs) and was normalized for comparison purposes. This test was done three times, and the results were averaged. When compared to the first analytical model produced in SAP2000, the resulting flexibility matrix was off by a substantial amount, raising questions pertaining to why the analytical model was more flexible than the physical model. After further investigation, the analytical model was updated to account for the added bending stiffness resulting from gusset plates at each connection (as noted in Section 5.2).

After updating the model a new set of tests were run, and new normalized static flexibility matrices were found that produced good results. As seen in Table 5.3, the average error of the matrix decreased with the higher weights used, but did not reduce further with the 800 lb loads. Since errors are inevitably present in any experimental testing procedure, a perfect representation of flexibility was not achievable. It was decided that a value of 10% error was within reason, and the analytical model was kept. It should be noted that the finite model could have been updated several more times in order to be very close to the experimental data. Given that the static flexibility matrix contained experimental errors and was non-symmetric, the 10% range was acceptable. Since the different flexibility matrices were obtained for comparison purposes only, updating the analytical model to perfectly match the static model was unnecessary.

Table 5.3: Percent Error in Flexibility Matrix

Load Case [lb per node]	***Average % Error* [%]***
200	17
400	12
600	10
800	10

* Percent error between Static and Analytical

5.3.2 Static Load Cases

Further verification of the analytical static flexibility compared to the experimental static flexibility was done through the means of six additional loading scenarios. These different loading cases were meant to mimic different loading stages that an in-service bridge might be subject too. Given the limitations of loading masses available in the laboratory, the load cases did not contain heavy loads. Figure 5.10 summarizes the six different load cases enacted on the grid model. During each load case, the deflections at every node were measured. The deflections due to a given load case were found from the analytical model by taking the normalized flexibility found in SAP2000 and multiplying it by a load vector representing each load case. In effect, the analytical flexibility was multiplied by a virtual load to obtain a virtual displacement, which resulted in a displacement value for each node. These analytical displacements were then compared with the actual physical displacements measured to compare the accuracy of the model. A representation of the displacement plots, both in 3D and in planar view, can be seen in Figure 5.11 and Figure 5.12. From these figures, it was found that the maximum displacement generally was around 5% off, showing very good agreement between the tests. It can also be seen from these deflection profiles, that discrepancies are present, like sensor E2 (which was later found to be a bad sensor). Other errors were attributed to the size of deflections being measured. When loaded, the static displacement gages were only deflecting a few thousandths of an inch, and were affixed to the structure by thin wire (wire pots) or by direct contact (TML gages). Even a very small amount of play in the mounting device or wire would be enough to drastically change the recorded result.

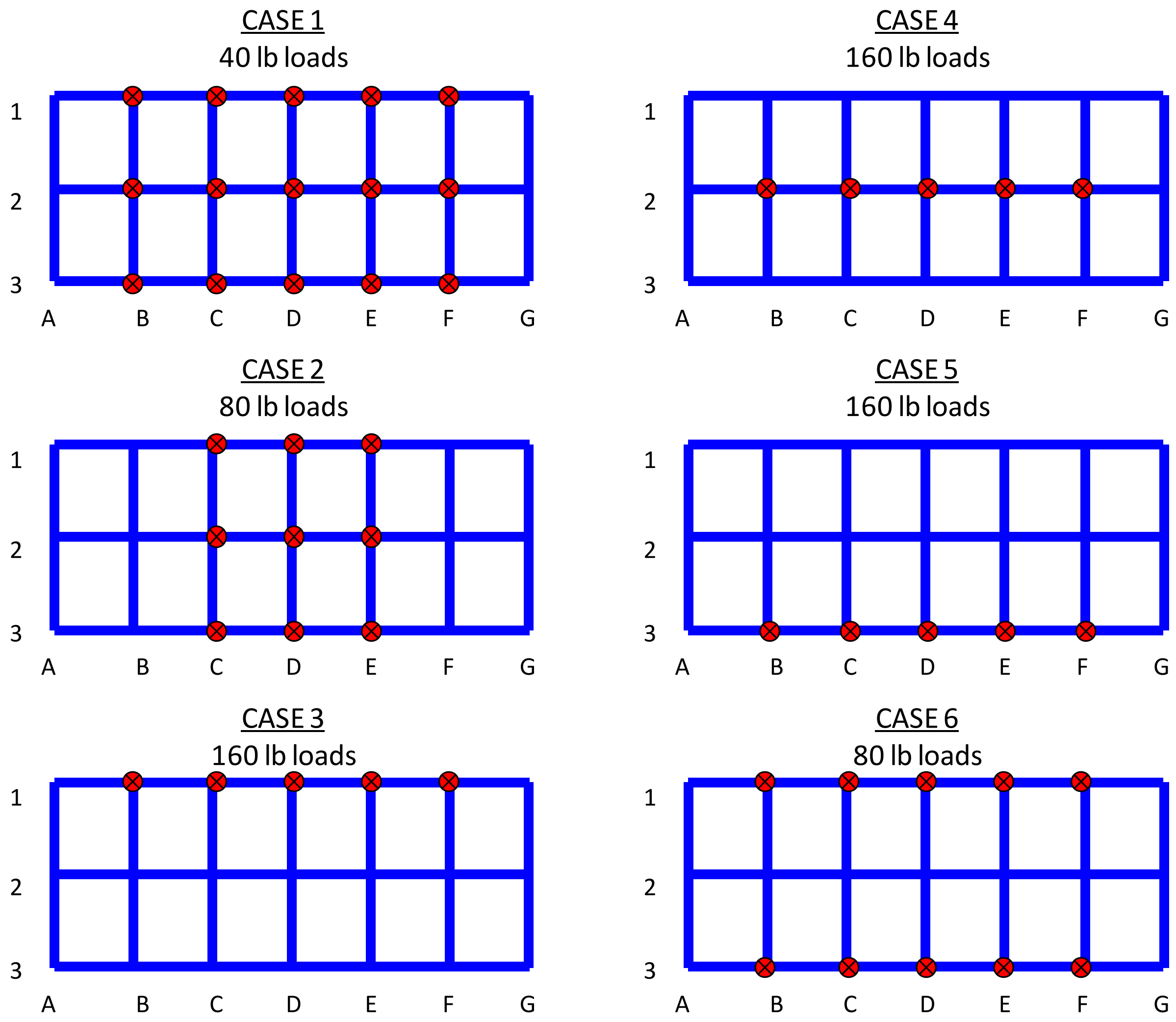

Figure 5.10: Grid Model Static Load Cases

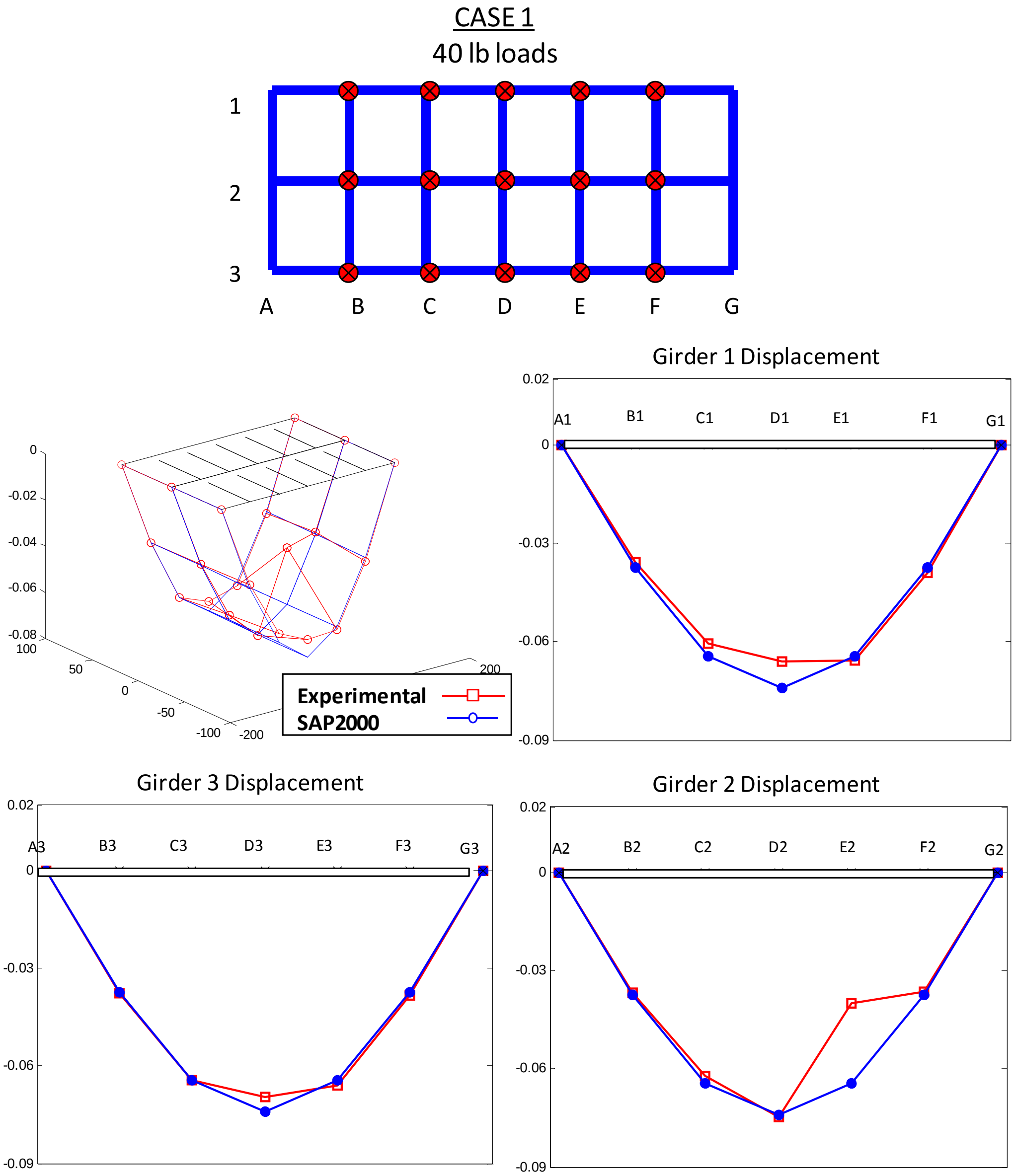

Figure 5.11: Static Load Case #1

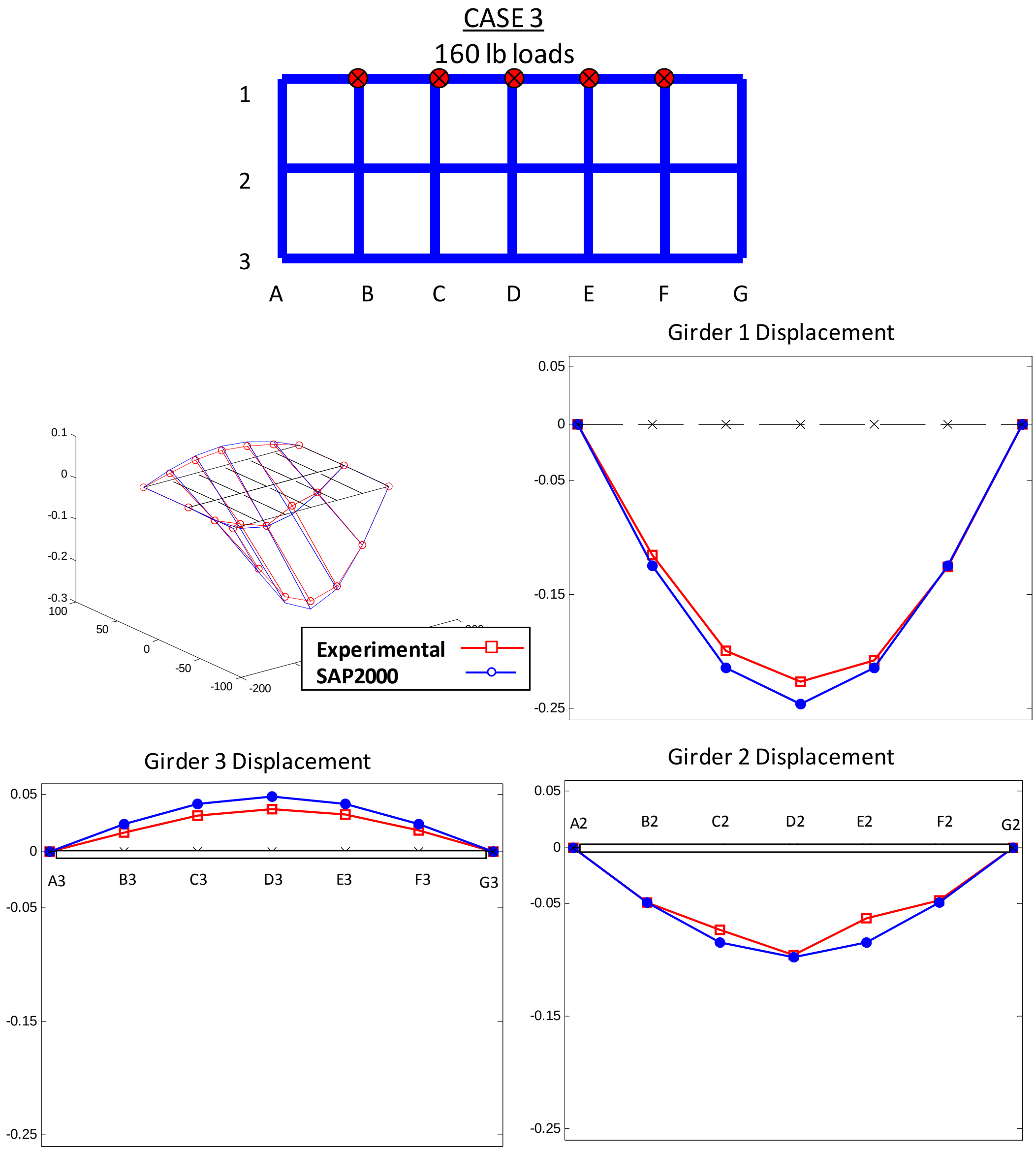

Figure 5.12: Static Load Case #3

5.3.3 Moments from Strain Measurements

During both the full grid static load testing and the six different loading cases, the strains at key locations were also recorded. Since the initial static test started with 0 lbs and increased to 600 lbs on any given node, the change in strain could be easily calculated.

Bending moments from the static load tests were computed from measured strains and section properties and were compared with the corresponding moments found from the SAP2000 analytical model.

The internal bending moment at a given strain gage location was computed using the following relationship that exists between bending stress, σ_b, on a cross section and the internal moment:

$$\sigma_b = \frac{My}{I}$$

where M is the internal bending moment at the cross section being evaluated, y is the distance from the neutral axis of the cross section to the point where stress is being evaluated, and I is the moment of inertia of the cross section about the axis of bending.

The relationship between the bending stress and longitudinal strain is given by Hooke's Law and can be expressed as follows:

$$\sigma_b = \varepsilon \times E$$

where ε is the longitudinal strain measured by the strain gage and E is Young's Modulus for steel. By setting the two stress equations equal, and solving for the bending moment, an equation for determining the bending moment at a location on the grid model from the measured strain at that location is obtained:

$$M = \varepsilon \times E \times S$$

where the section modulus $S = I/y$.

The experimentally determined bending moment at each strain gage location was compared with the analytically determined bending moment from the SAP2000 model of the grid structure for each load case. Large errors and differences were found between the experimental and analytical models. One end of the model had errors in the 3-10% range, while the other end had errors in the 10-30% range. Since the static deflection results showed good agreement, the strain results were not used to further update the model.

5.4 DYNAMIC TESTING OF THE UNDAMAGED GRID MODEL

Static testing was implemented on the grid model as a means of validating the SAP2000 analytical model and for comparing to the dynamic characterization. As noted earlier, static testing of an in-service bridge would be extremely difficult, and not very practical. Therefore the bulk of the research focused on dynamic testing of the grid model, including impact hammer testing, dynamic shaker testing, and ambient vibration testing.

5.4.1 Impact Hammer Testing

The grid model was tested using a model 086D20 instrumented hammer from PCB Electronics, Inc., which provided a range of ±5000 lbf with a sensitivity of 1 mV/lbf. A medium hardness red tip was used for the test. The data acquisition system was set up with 22 channels of data, 1 for the hammer input and 21 for the accelerometers, one at each node including the support locations. An off-the-shelf testing and processing software was used to help facilitate the testing. Using this software allowed the researcher to explore the capabilities of one software package and compare its capabilities with algorithms and processing techniques developed in MATLAB. The software chosen was a package from M+P International called “Smart Office”. This software allowed for easy setting of the testing parameters including block size, frequency resolution, settling time, pre-trigger delay, and other useful properties.

The test was set to collect data for 8 sec. after the triggered impact, with sampling rate of 2048 Hz. Each node was impacted five times to average out any noise present in the measurements. All 21 of the nodes were impacted in this manner, thus producing a full dynamic test of the structure. The M+P software package converted the time data into frequency data, and produced FRFs and coherence for each hit in real time, which was monitored for any sign of bad hit implementation.

Smart Office allowed for modal analysis within the software, but proved to be difficult to use and tended to crash often. Modal flexibility was not directly obtainable, and the modal parameters that were available were not easily exported. Because of these reasons, it was found to be easier to use the processing described in Chapter 3, implemented in MATLAB. The time data from the impact tests were therefore exported into MATLAB and processed using the CMIF and eFRF algorithms.

Two separate full impact tests of the grid model were carried out. Each test used the same parameters and input device, and the results were very similar. A representative figure showing the driving point FRF and coherence from location B3 is seen in Figure 5.13. Note the good coherence at the peaks, and the clean peaks representing natural frequencies. In theory, the FRF matrix should be symmetric. For example, the response at 13 due to an input at 9 should be equal to the response at 9 due to an input at 13. This comparison is referred to as reciprocity. Reciprocity was used to check that the signals were being properly captioned, and an example of a reciprocity spectrum with acceptable values can be seen in Figure 5.14. Notice that the peaks are very uniform between the two different FRFs, and divergence only occurs at the anti-resonance locations.

After the full FRF matrix was compiled and reciprocity was verified for each test set, the CMIF process, as outlined in Chapter 3, was implemented. Singular Value Decomposition was performed and the CMIF plot was formed, as seen in Figure 5.15. The first eight modes were selected, and can be seen with circles around the asterisks.

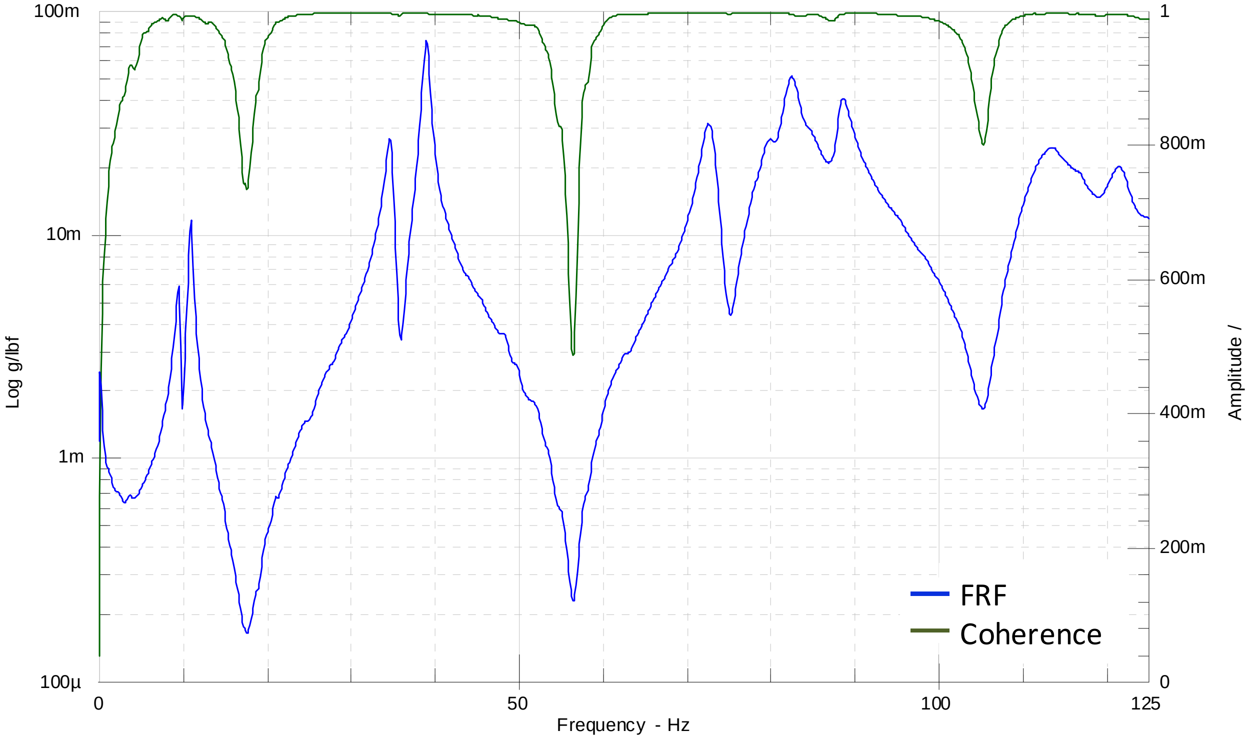

Figure 5.13: Impact FRF and Coherence at B3

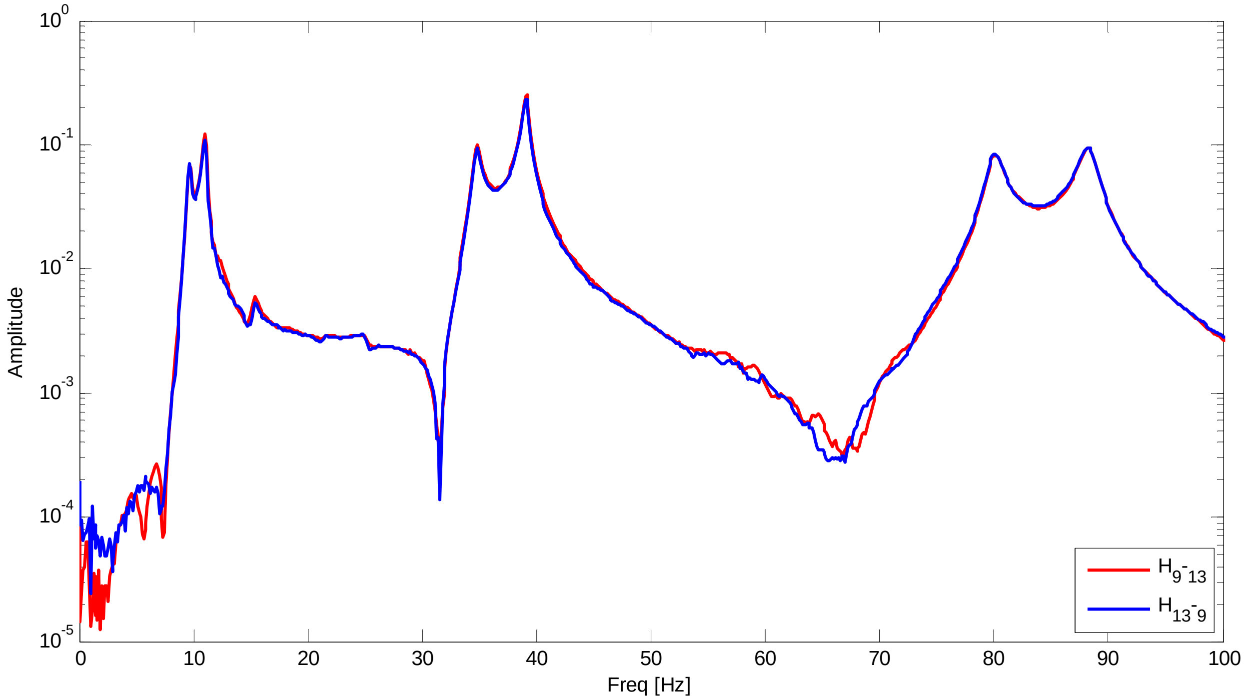

Figure 5.14: Reciprocity Check from Grid Impact Test

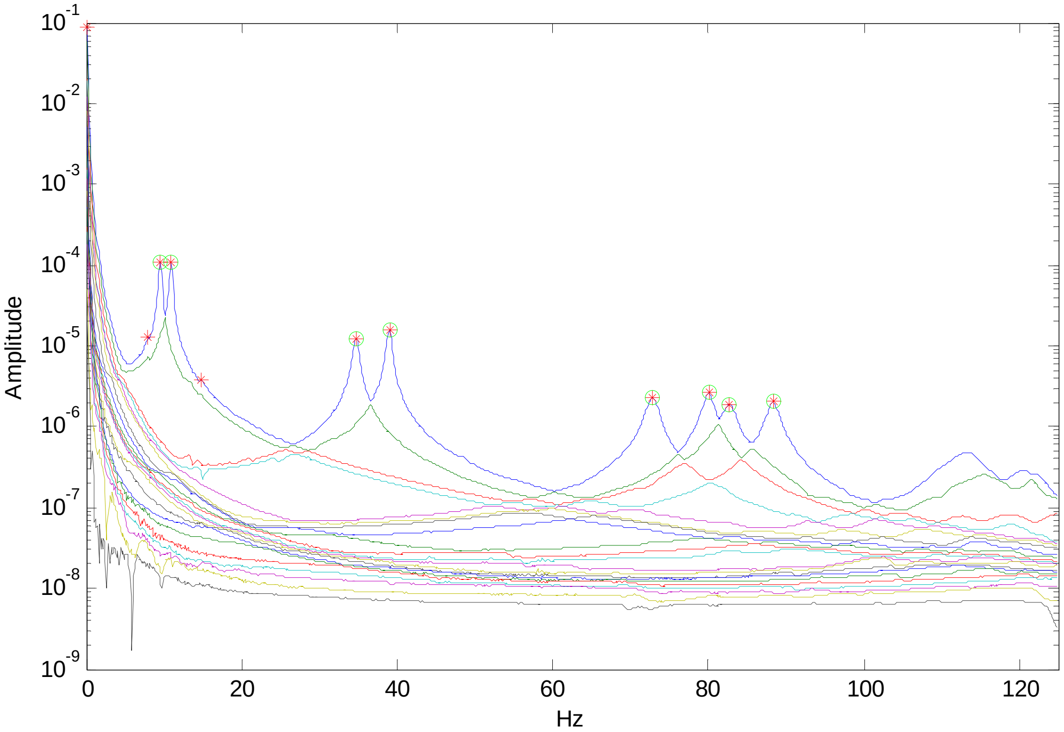

Figure 5.15: CMIF Plot for Undamaged Grid from Impact Hammer Test

From the peaks in the CMIF plot, eFRFs were created in order to estimate the modal parameters. From the eFRFs modal frequencies, mode shapes, and modal scaling coefficients were found, and are summarized in Table 5.4 and Figure 5.16. These parameters were compiled and processed to find modal flexibility, the comparison tool for all the different tests performed. In the undamaged model, since there were 21 DOFs modal flexibility consisted of a 21x21 matrix of numbers. Looking at such a matrix can be difficult to understand, and one can easily get lost in the array of numbers present. Therefore, as in the case of the cantilever, the modal flexibility was multiplied by a virtual load vector (40 lb distributed load) and the resulting deflection profile was plotted as the comparison tool between static, analytical, and impact testing. Figure 5.17 shows a 3D plot of these deflections, and Figure 5.18 shows the elevation views of the different girders. As expected, the flexibility was less than that of the analytical or static results. Since only the first eight modes were captured, the resulting flexibility did not contain the contributions of higher modes. Including more modes theoretically would have increased the value of the modal flexibility matrix, but was not possible given the constraints of the testing setup. The actual resulting deflection profile was found to be 14% from the analytically predicted profile. It can also be seen that the two different impact tests performed gave nearly the same results, showing consistency and reliability in the testing methods used.

Table 5.4: Impact Test Dynamic Properties

		Analytical Model	***Impact Hammer Test***		
Mode Number	*Mode Description*	*Natural Frequency (Hz)*	*Natural Frequency (Hz)*	*Damping (%)*	*% Difference[1]*
1	1st Bending	9.172	9.570	1.37	4.34
2	1st Torsion	10.015	10.958	1.32	9.41
3	2nd Bending	36.229	34.714	0.94	-4.18
4	2nd Torsion	39.629	38.996	0.7	-1.60
5	3rd Bending	78.791	72.831	1.03	-7.56
6	1st Butterfly	83.583	80.058	0.85	-4.22
7	3rd Torsion	87.394	82.695	1.15	-5.38
8	2nd Butterfly	91.117	88.324	0.89	-3.07

Notes: [1]from the Analytical natural frequencies

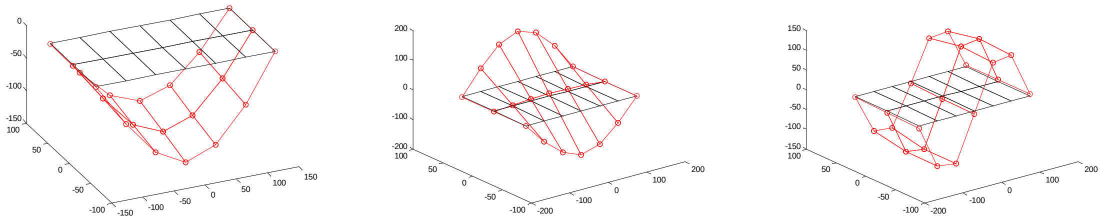

Bending Mode 1
f_1 =9. 570 Hz

Torsion Mode 1
f_2 =10.958 Hz

Bending Mode 2
f_3 =34.714 Hz

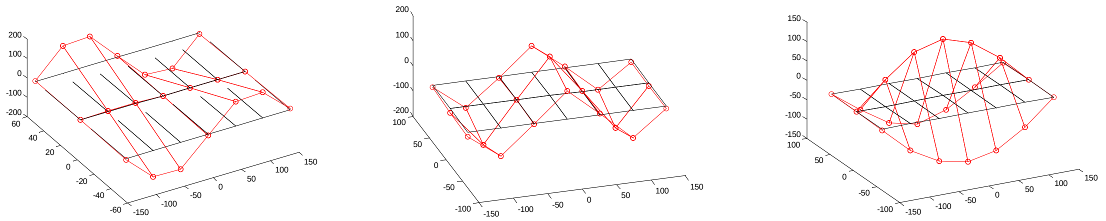

Torsion Mode 2
f_4 =38.996 Hz

Bending Mode 3
f_5 =72.831 Hz

Butterfly Mode 1
f_6 =80.058 Hz

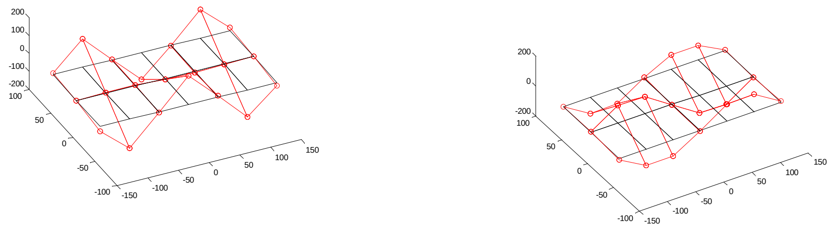

Torsion Mode 3
f_7 =82.695 Hz

Butterfly Mode 2
f_8 =88.324 Hz

Figure 5.16: Mode Shapes from Impact Test

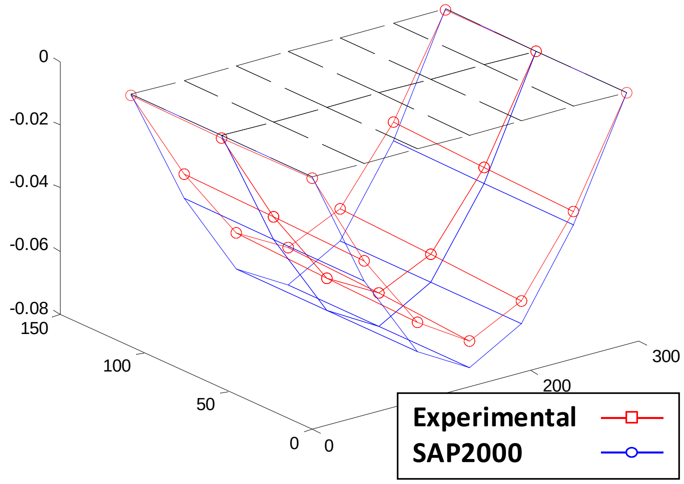

Figure 5.17: 3D Deflection Profile for Impact Test

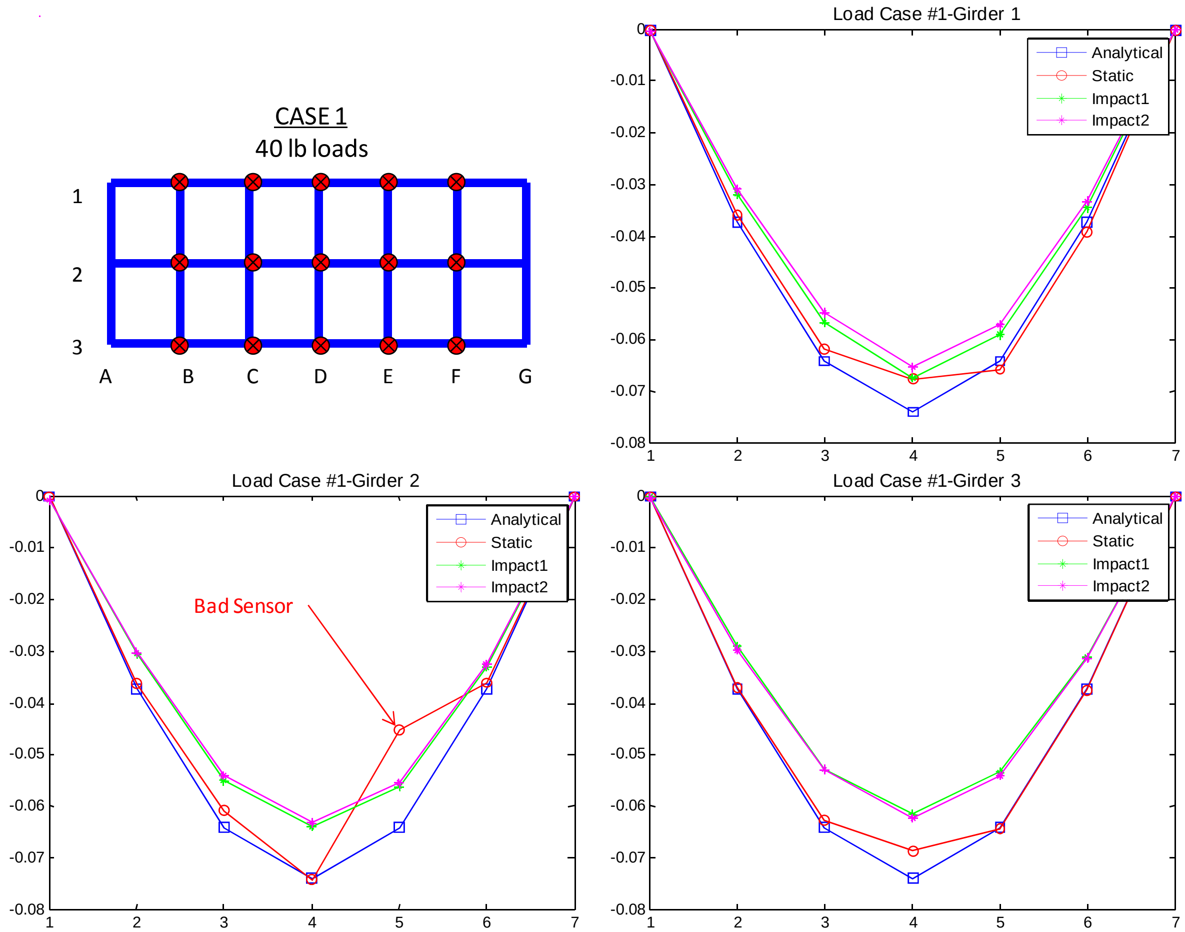

Figure 5.18: Elevation Deflection Profiles for Impact Tests

5.4.2 Dynamic Shaker Testing

Dynamic shaker testing was performed on the grid by attaching the armature of the shaker to the underside of the grid at the same nodal locations where accelerometers were present. The shaker was attached to the structure with a stinger coupled with a load cell and clamped to the structure, as can be seen in Figure 5.19. Attaching the load cell in line with the shaker force allowed for capturing the actual input force being supplied to the structure. A burst random signal with a frequency range of 100 Hz, input for 16 sec, was generated through a Data Physics Corp. hardware and software package. The system also captured all response channels, and performed a real time transfer function computing A/F (acceleration over force) and coherence. This allowed for rapid validation of testing techniques and signal capture, and therefore sped up the process of data collection. Ten averages with no windowing were performed for each input location. All 15 internal DOFs of the structure were used as input points along with all 21 accelerometer responses, thus creating a 21x15 FRF matrix. It was found that using a low amplitude input signal achieved the best results, and was verified by Mayes & Gomez (2006). Voltage control was used on the shaker amplifier, which produced a quieter signal from the shaker body. When using a voltage controlled amplification, the *displacement* of the armature of the shaker tries to match the input signal. When using a current controlled amplification, the *acceleration* of the armature of the shaker tries to match the input signal (Allemang, 1999). Since a burst random signal was used (see Figure 4.17), the signal jumped around very quickly, which produced a chattering noise from the shaker body when current controlled amplification was used. This chattering noise was also felt in the ground, and it is hypothesized that the floor vibrations from this chattering noise transferred to the supports of the structure and into the response measurements, thereby producing the erroneous results recorded. Voltage controlled amplification did not produce this chatter, and gave a much cleaner signal with very good coherence. As expected, the support locations still showed an undesirable coherence value since the signal to noise ratio at these locations was very high. This high signal to noise ratio was perceived to produce the bad coherence. Figure 5.20 shows the FRF with coherence at a support location, while Figure 5.21 shows the cleaner FRF with better coherence at the D2 location.

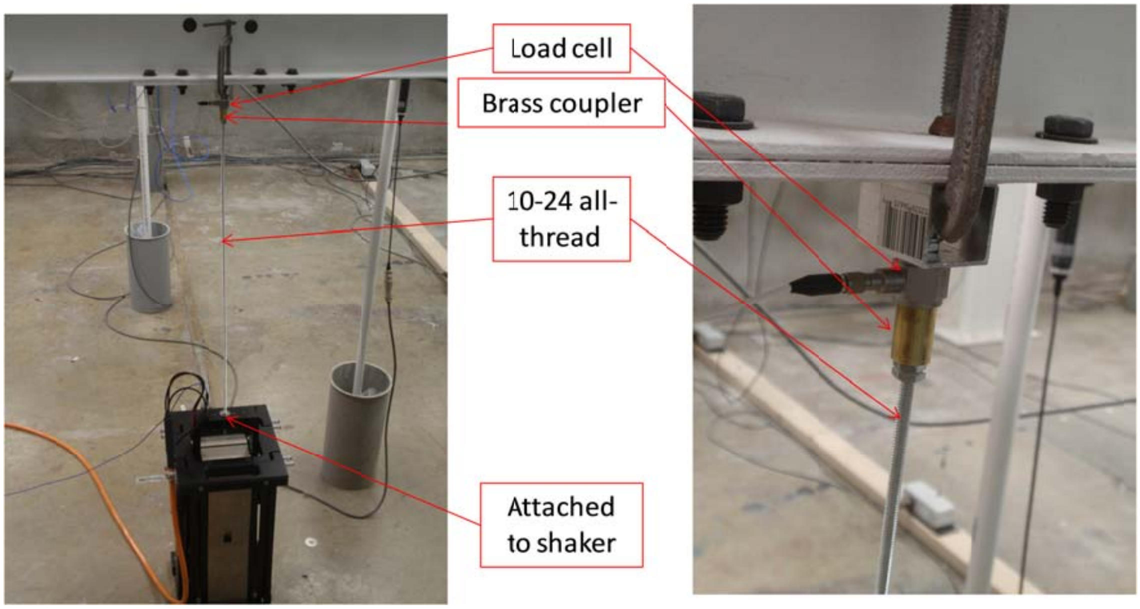

Figure 5.19: Shaker Setup Used on Grid Model

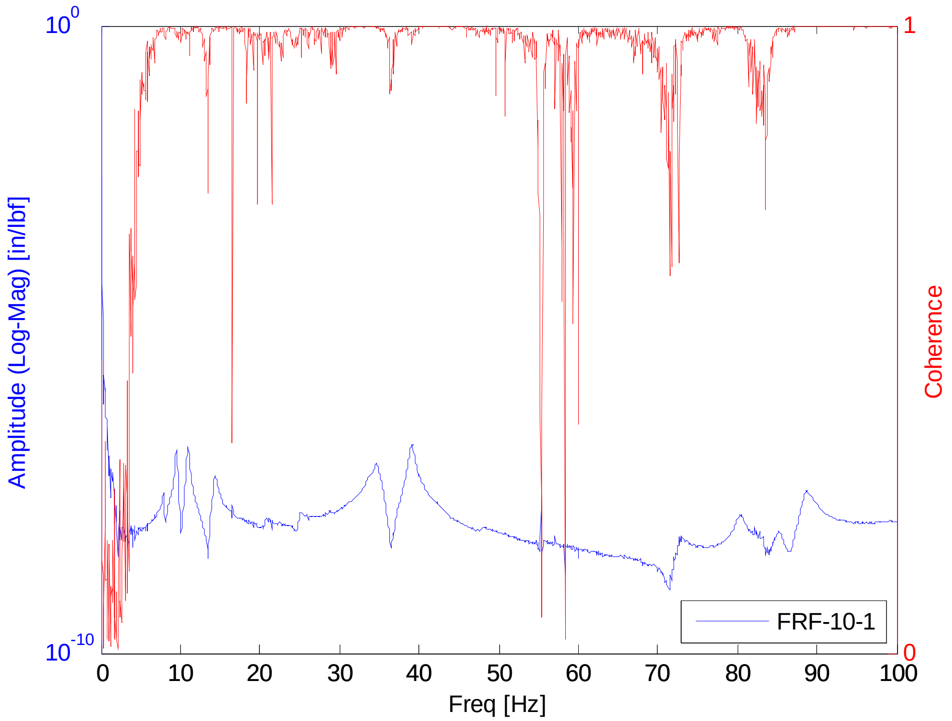

Figure 5.20: FRF at Support Location

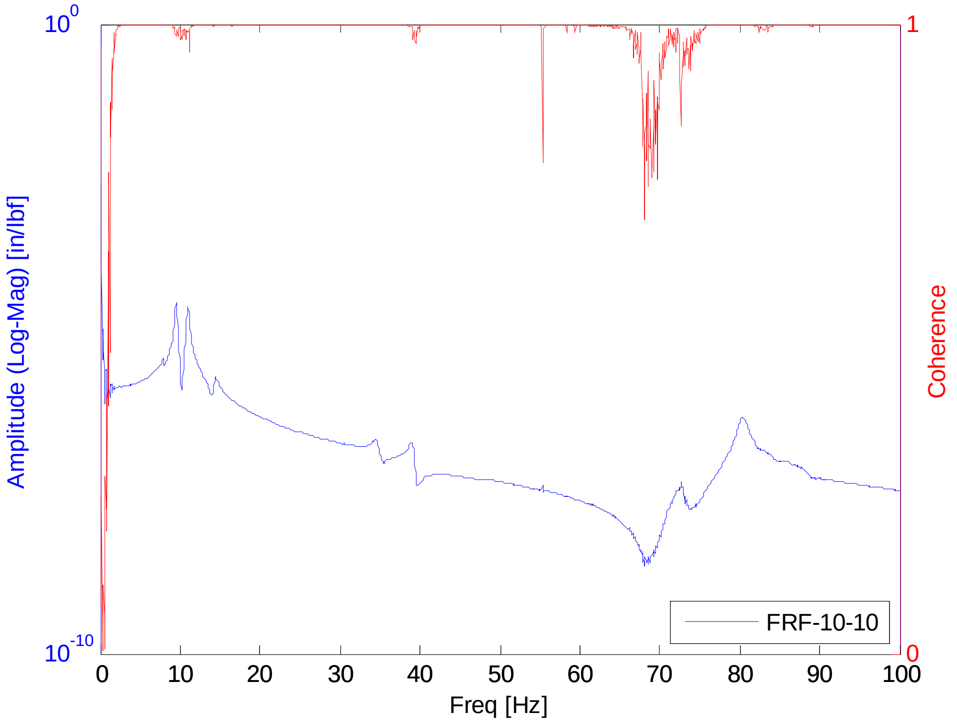

Figure 5.21: FRF at D2 Location

The shaker testing FRF measurements were easily exported to MATLAB, and were then used in the CMIF parameter estimation algorithm. After converting the A/F signals to X/F, singular value decomposition was performed and the CMIF plot (Figure 5.22) was produced. From this graph the peaks were then picked in order to locate the natural frequencies. When compared to the impact test CMIF (Figure 5.15) the shaker test did not provide as smooth of a spectrum but all of the same modes were present at nearly the same frequencies. From these peaks, the enhanced frequency response functions were created, and the modal parameters were found, including modal flexibility. Figure 5.23 shows the mode shapes found from the shaker test, which showed to be very similar to the hammer impact test. Figure 5.24 shows the deflection profile obtained from modal flexibility along with the previous deflection profile of the two impact tests, static test, and analytical model. The resulting modal flexibility obtained from shaker testing was around 5.5% from the flexibility obtained from impact testing.

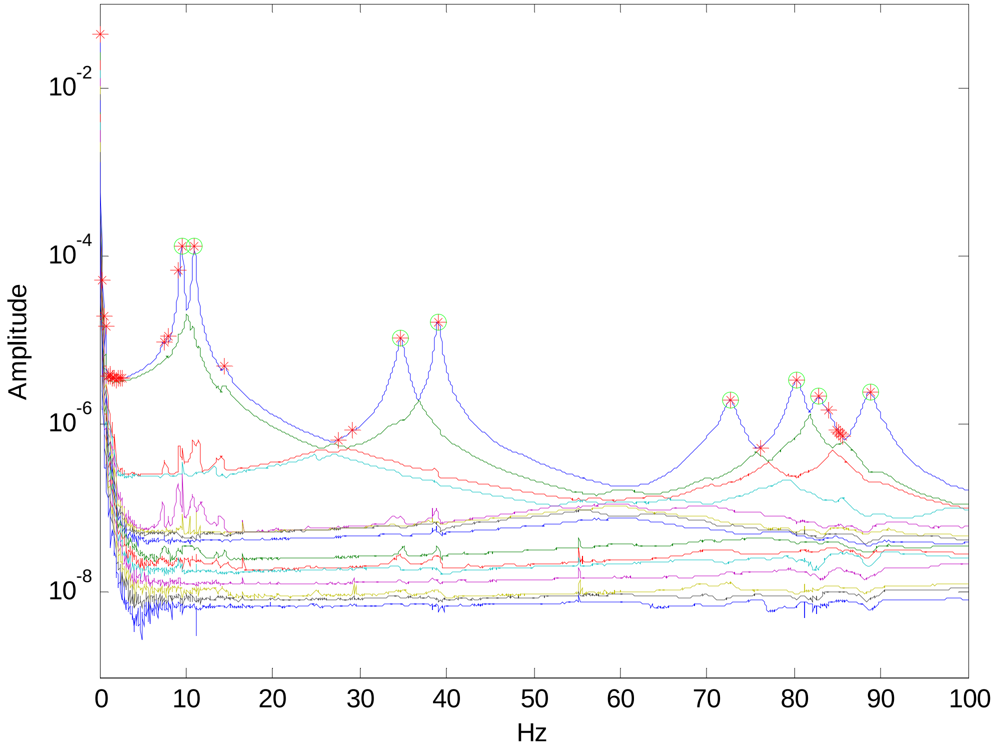

Figure 5.22: CMIF Plot of Undamaged Grid for Shaker Test

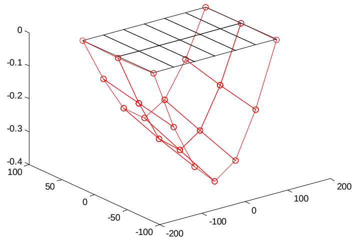

Bending Mode 1 Torsion Mode 1 Bending Mode 2

f_1=9. 521 Hz f_2=10.948 Hz f_3=34.699 Hz

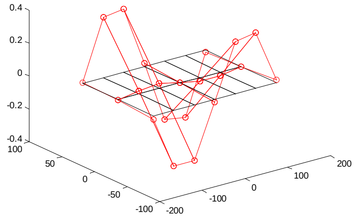

Torsion Mode 2 Bending Mode 3 Butterfly Mode 1

f_4=39.023 Hz f_5=72.645 Hz f_6=80.366 Hz

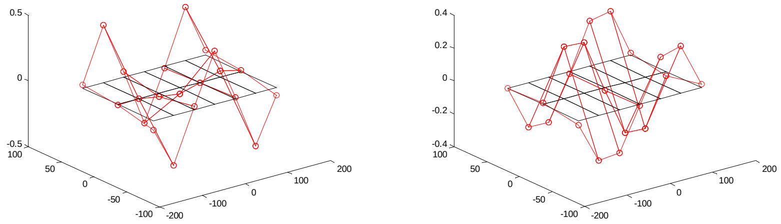

Torsion Mode 3 Butterfly Mode 2

f_7=82.787 Hz f_8=88.737 Hz

Figure 5.23: Mode Shapes from Shaker test

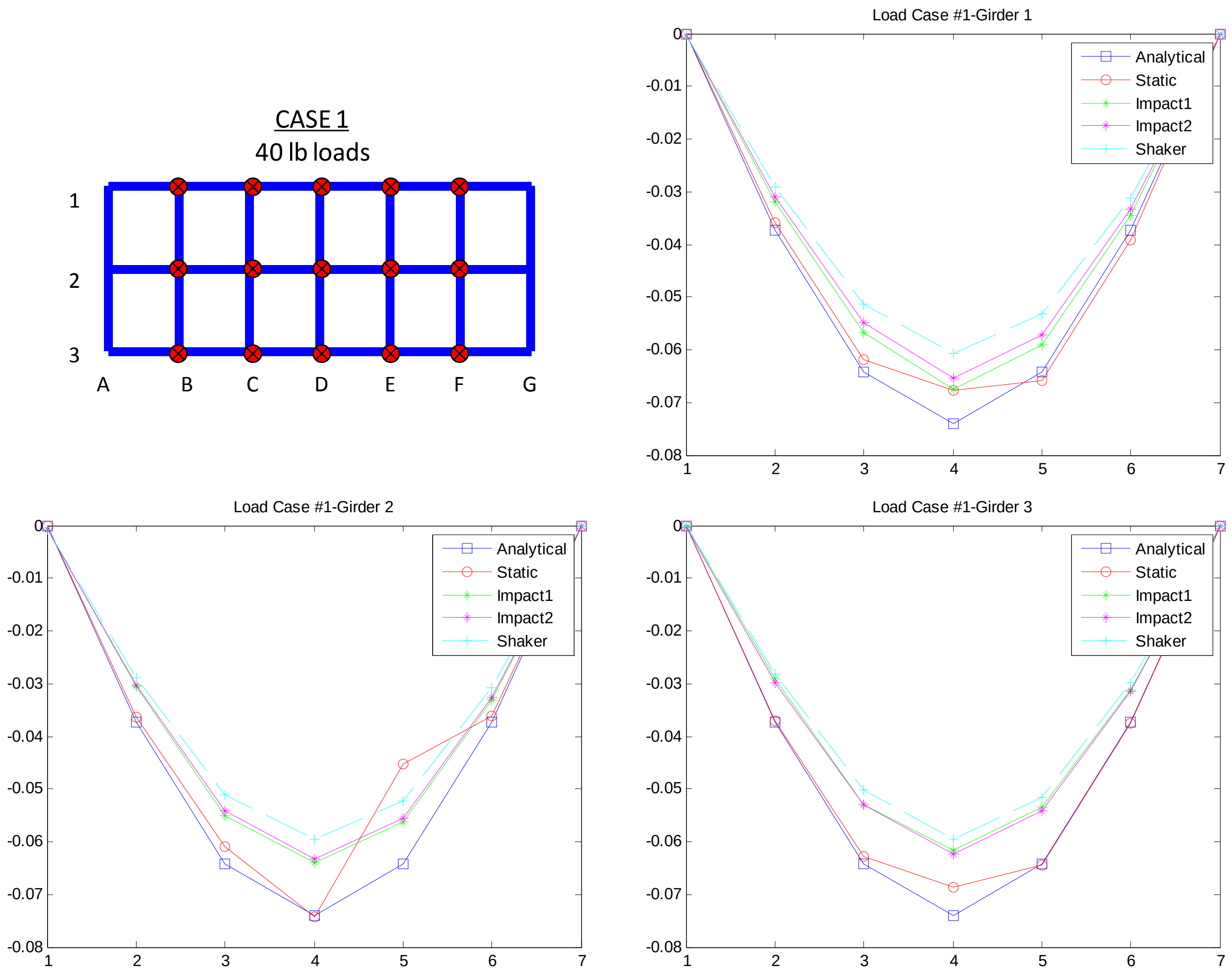

Figure 5.24: Deflection Profile of Undamaged Grid for Shaker Test

5.4.3 Ambient Vibration Testing

Ambient vibration testing was performed on the undamaged grid structure with several different types and sources of input, none of which were measured. When testing an in-service bridge, plenty of excitation exists from traffic, wind, waves, machinery, etc. In the laboratory setting, with the grid model fixed to a stiff concrete slab, the excitations were less apparent. Several different excitation sources were tested as inputs, including:

1. Quiet laboratory setting
2. ERSA machine running
3. Uncoupled dynamic shaker
4. Coupled dynamic shaker

The first type of test, performed in a quiet laboratory setting, consisted of collecting measurements from the accelerometers when the lab was relatively quiet. No attention was paid to talking, doors opening and closing, and so forth. This data was collected for around one hour. The second type of test was similar to the first, with the exception of a large piece of machinery running two rooms away. The ERSA (Evaluator for Rutting and Stripping of Asphalt) machine was running constantly during these tests, and produced a regular "thump-thump" vibration that was slightly able to be felt through the floor in the lab with the grid model. The third test was performed with the shaker on the floor underneath the grid model, but unattached to the grid. This shaker provided a random vibration that was translated through the floor into the supports, and therefore into the structure. The fourth test was performed by attaching the shaker to the grid, as with the shaker testing, and supplying a random signal. The difference with this fourth test and the dynamic shaker testing are: (1) very small input signal into the grid, (2) no input was measured, (3) pure random signal used as opposed to burst random, (4) input and response measured for 30 min. per input node. The benefit of this fourth type of test was that a broad range, Gaussian white noise signal was directly applied to the structure. An in-service bridge would also receive this type of direct input in the form of traffic driving across the top of the bridge.

Relying on a quiet laboratory setting did not provide ample excitation to the structure, and did not produce clear results. The power spectral density (PSD) of each channel was taken, and should have produced peaks at the natural frequencies of the structure. As seen in Figure 5.25, these peaks were present, but appeared very noisy and hard to distinguish without having prior knowledge of their locations (especially the lower modes). The normalized power spectral density (NPSD) was also taken, and should have produced a more magnified peak at each natural frequency, and can be seen in Figure 5.26. One can see that this method of ambient excitation was not an ideal method.

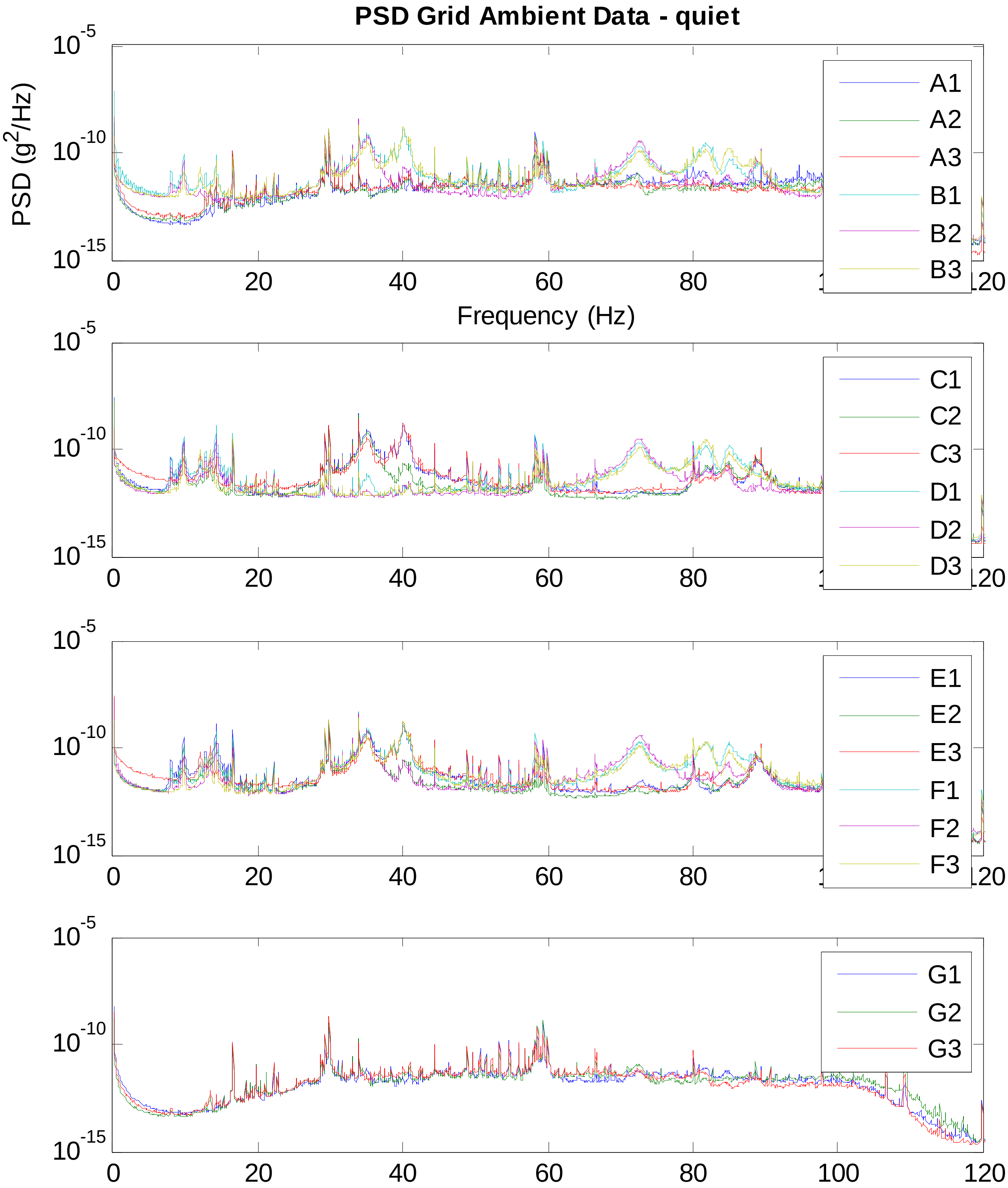

Figure 5.25: PSD of Undamaged Grid from "Quiet" Ambient

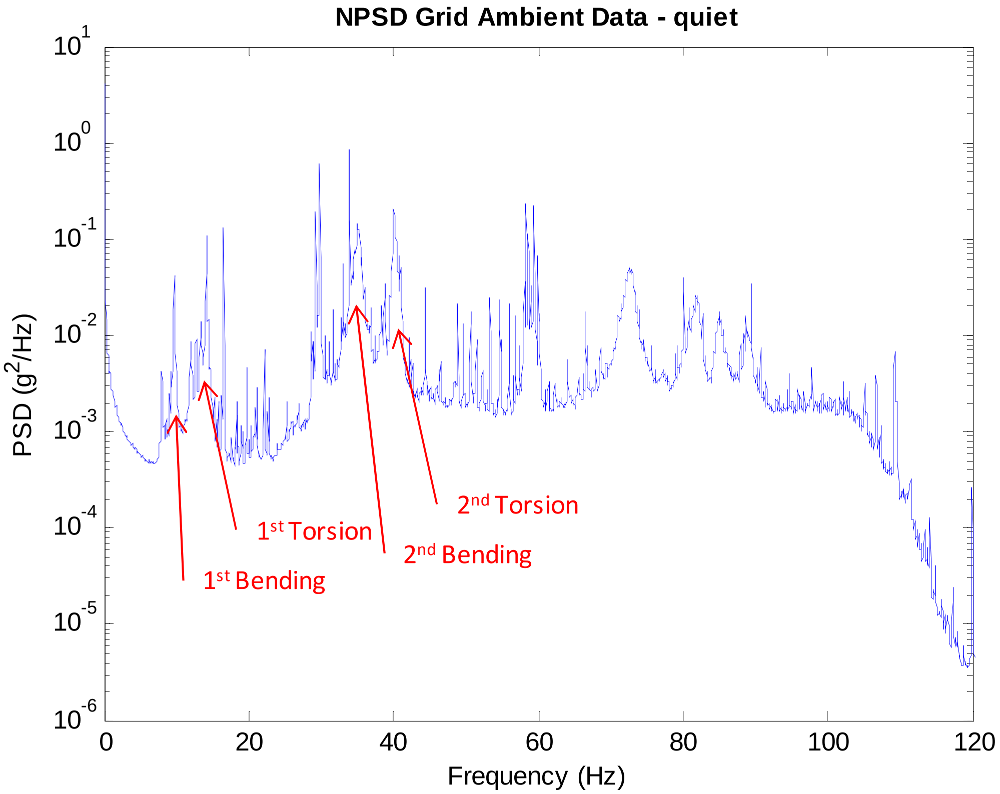

Figure 5.26: NPSD of Undamaged Grid from "Quiet" Ambient

The second input type, containing the ERSA machine, was found to produce extremely unclear results. The machine produced a thumping vibration through the floor. Initially this floor vibration was thought of as helpful for exciting the modes of the structure. A typical response channel reading (in the time domain), with ERSA running is shown in Figure 5.27. In reality though, the consistent set of thumps from ERSA produced very noisy and erroneous data, as can be noted from Figure 5.28 and Figure 5.29. All further testing therefore contained the additional parameter that the ERSA machine could not be running during the test.

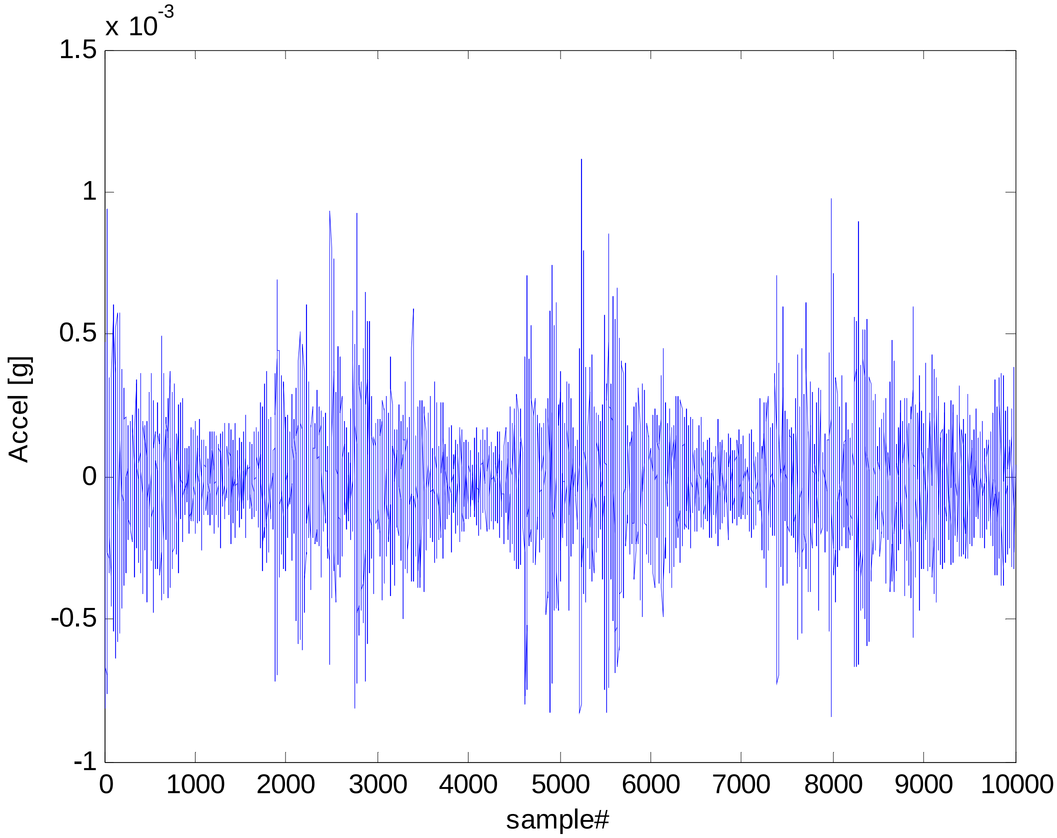

Figure 5.27: Time Response due to ERSA

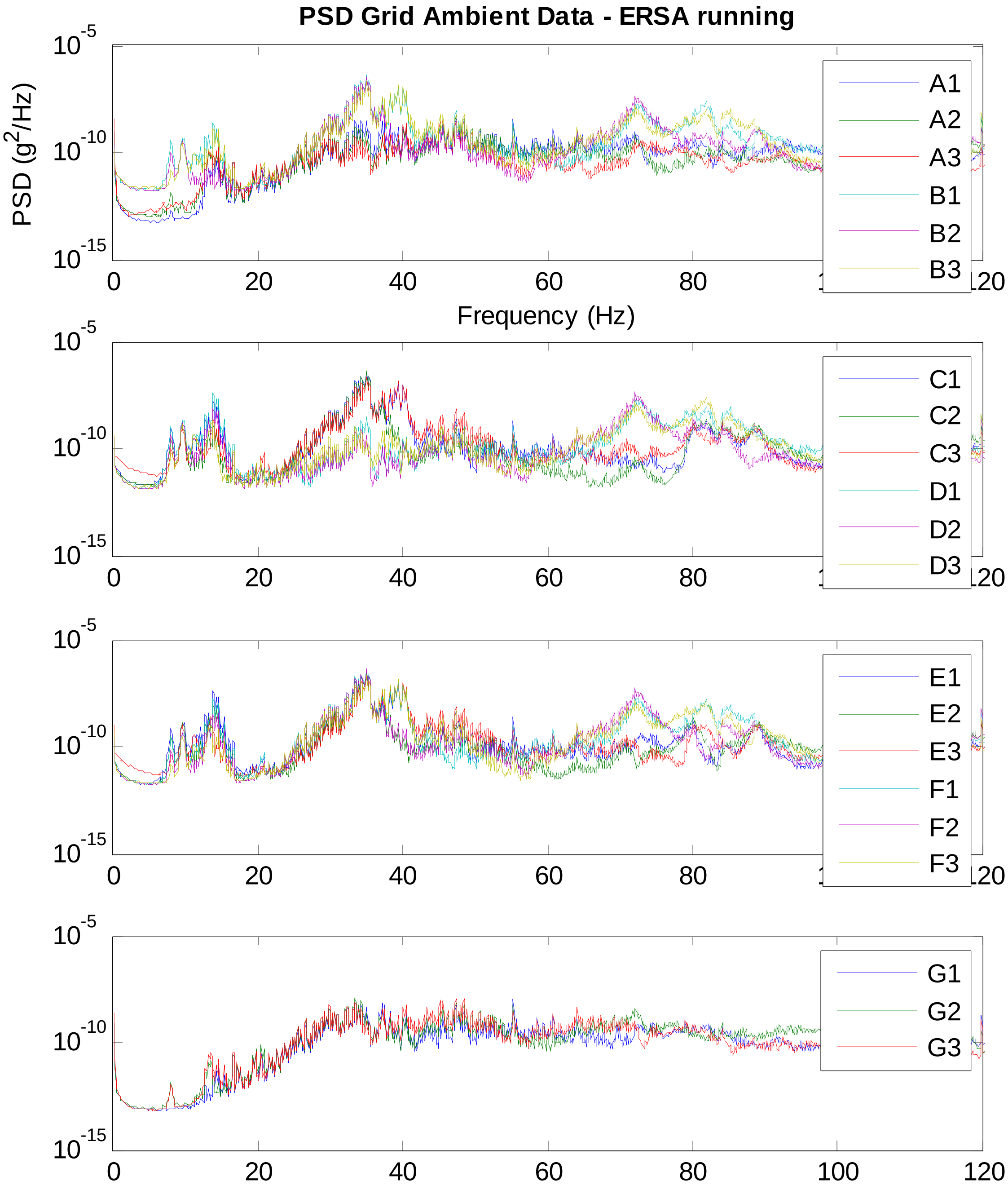

Figure 5.28: PSD of Undamaged Grid from "ERSA" Ambient

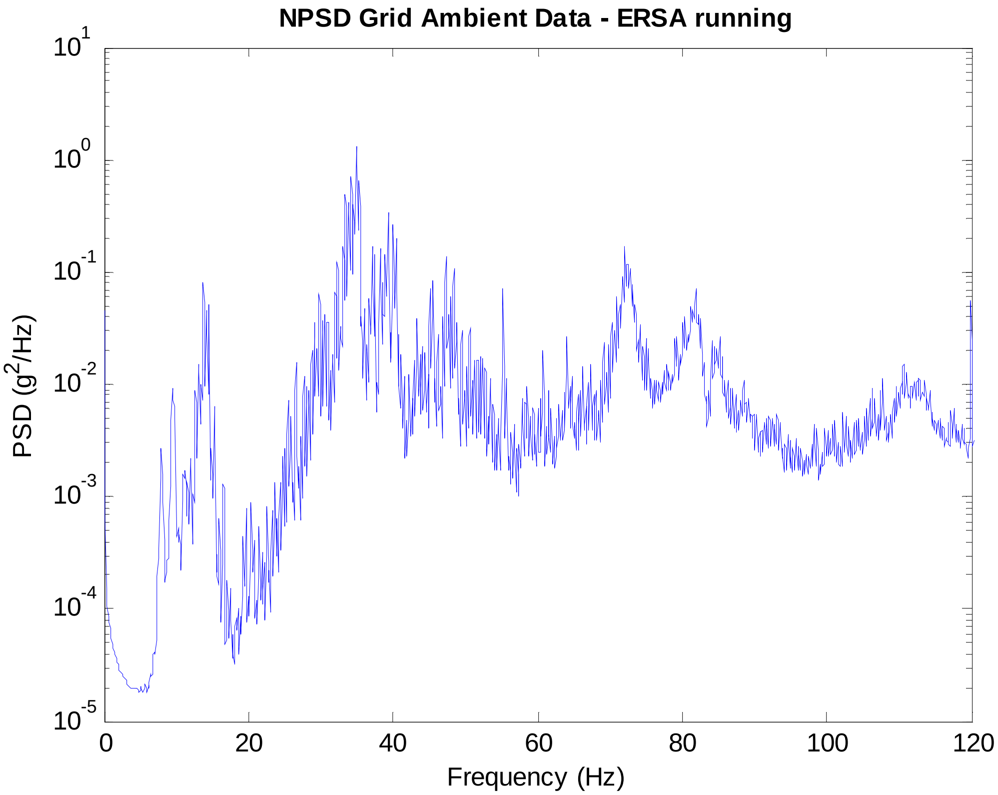

Figure 5.29: NPSD of Undamaged Grid from "ERSA" Ambient

Uncoupling the shaker from the grid and putting a steady white noise input into the floor produced decent results but still contained some noise. On the other hand, coupling the shaker to the grid and putting a very low amplitude white noise signal into the structure produced very clear results (Figure 5.30). It was found that the identifiable peaks were dependent on input location. For example, when the input was only applied to grid location D2, the peaks associated with Torsion Mode 1, Bending Mode 2, and Torsion Mode 2 (as well as others) did not appear even though a broadband input was used. This was due to location D2 being a nodal point (a point of zero movement) in these modes. By supplying input at several locations, all of the first nine modes were able to be excited. The difference found from one input versus several inputs is illustrated in the CMIF plots shown in Figure 5.31.

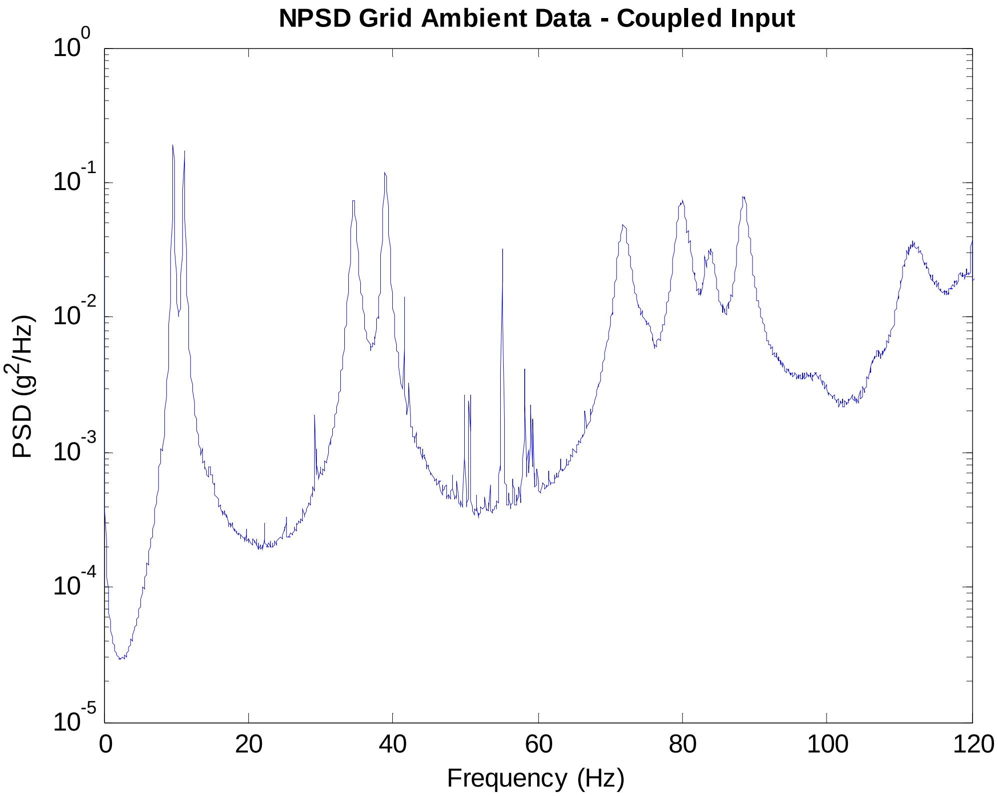

Figure 5.30: NPSD of Undamaged Grid from Coupled Ambient Input

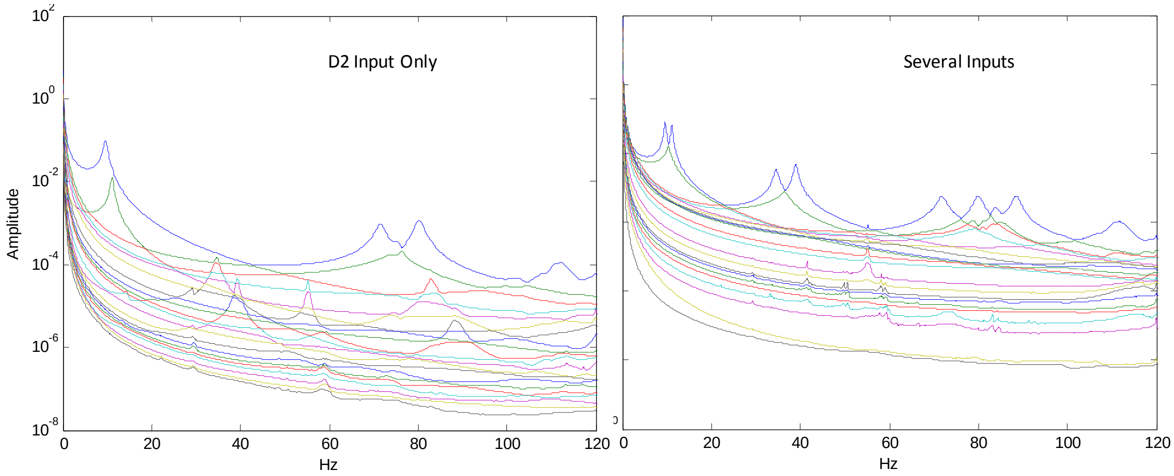

Figure 5.31: CMIF Plot with Different Input Locations

Besides producing a PSD and NPSD plot to locate natural frequencies, mode shapes were also able to be extracted from ambient vibration data. At any given frequency, the position of all sensors in relation to one sensor produces a mode shape. Therefore, at each frequency there exists several mode shapes, one for each channel of reference. By plotting all of these mode shapes on top of one another, it is easy to tell when a true mode shape has been found, because all of the plots snap together. By using this method, mode shapes at each peak of the NPSD was found. These mode shapes and frequencies coincided very well with the mode shapes and frequencies found from other dynamic testing methods, and a sampling of the first two mode shapes can be seen in Figure 5.32.

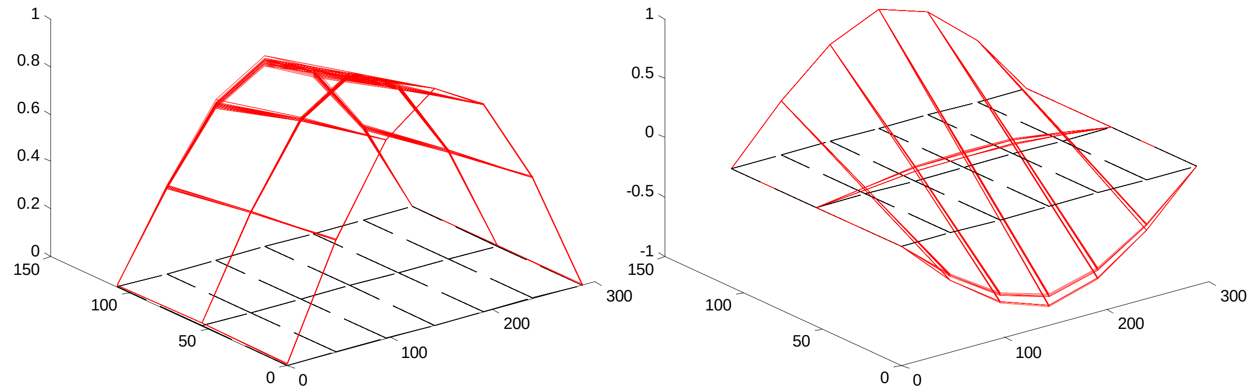

Bending Mode 1
9.603 Hz

Torsion Mode 1
11.149 Hz

Figure 5.32: Mode Shapes from Ambient Testing

A second post-processing method was employed with ambient vibration testing in order to use the CMIF algorithm developed. Since ambient vibration testing does not provide a measurement of the input, mass scaled mode shapes are not obtainable, and therefore a scaled flexibility is not obtainable. By using auto and cross correlation functions, a pseudo impulse response function (PIRF) from the ambient data was able to be found. This PIRF looked like an actual impact response, exponentially decaying to zero, but was found from raw ambient data. These PIRFs were compiled for each channel, and processed as if it were actual impact data. The benefit in this process was being able to use CMIF to obtain a pseudo modal flexibility, which was then compared to flexibility obtained through the other testing methods to note any similarities. The disadvantage to this method was that the data was "smeared" together in the sense that each channel did not produce a separate mode shape as with the previous method; only one mode shape was produced. Therefore, any sensor errors or localized problems encountered did not show up as pronounced in this method.

Using the data from the coupled shaker input, the results from this PIRF method was able to produce FRFs very comparable to FRFs from other dynamic tests, and is shown for the driving point at location E1 in Figure 5.33. The natural frequencies were analogous to other tests, and they also produced clear mode shapes. Overall, the PIRF method proved to be useful in identifying frequencies and mode shapes. Conversely, the pseudo modal flexibility obtained from this method was not very similar to the flexibility obtained from the other methods. While the deflection profiles displayed a similar shape, the magnitude of each girder deflection relative to the other girders was very different. In other words, girder #3 deflected far more than girder #1, in the order of three times the amplitude. The overall deflection profile vector was compared to both the impact and shaker deflections with the Modal Assurance Criteria (MAC), and values of 0.842 and 0.847 were found, respectively. The differences in girder deflections are reflected in these numbers. It was also found that obtaining pseudo modal flexibility from the other ambient input types proved to be of no use. Overall, while the PIRF method was useful for identifying mode shapes and natural frequencies, the pseudo modal flexibility obtained was dissimilar to the flexibilities obtained though the other testing methods.

After reviewing the results of the different ambient testing techniques, it was decided that two different input sources would be used for the damage scenarios implemented on the grid structure: quiet input and coupled shaker input. These two input types, utilizing both ambient post-processing techniques explained previously, were to be compared with the other testing methods (impact and shaker) to evaluate the best method of obtaining a post-damage characterization.

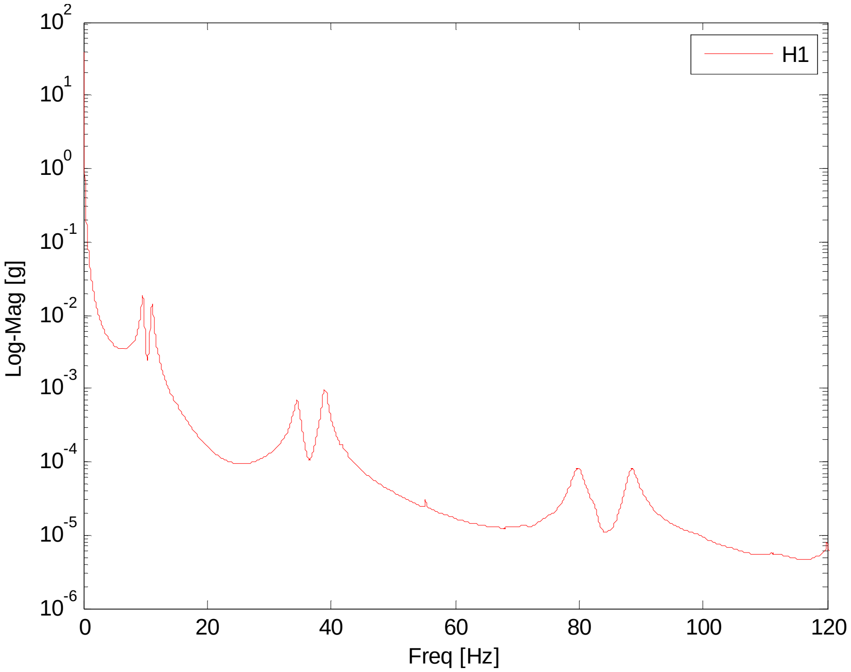

Figure 5.33: FRF at E1 from Ambient PIRF Data

5.5 EXPERIMENTAL OPTIMIZATION AND PARTICIPATION STUDIES

Of the different input sources used, shaker testing proved to be the most time consuming and most difficult to set up. The shaker had to be moved from node to node, each time uncoupling from one location and re-coupling to the next location. After running the given test at that location, the moving/setup process began again. Since the shaker weighs over 100 lbs, a subset of input locations that would closely excite the structure in the same manner as a full input location test was desired in order to limit the moving and setup associated with shaker input. This was also useful information for designing an optimal structural health monitoring strategy, since having fewer input locations was desirable. According to a preliminary study done in SAP2000 the highest contributing modes were thought to be 1st Bending Mode and 3rd Bending Mode, with the butterfly modes contributing slightly to the overall flexibility. It followed that applying input to the structure that excites these modes specifically would be of the most importance. Working with this assumption, applying an input at line 'B', line 'D', and line 'F' would excite 1st and 3rd bending modes, whereas applying input at lines 'C' and 'E' would not excite 3rd bending mode (see Figure 5.34). This was employed by taking the full shaker data set, and deleting columns from the FRF matrix in order to delete input locations, thus preserving the same errors or noise present from the full test. Seven different cases were employed to experimentally verify the analysis from SAP2000, and are shown in Figure 5.35.

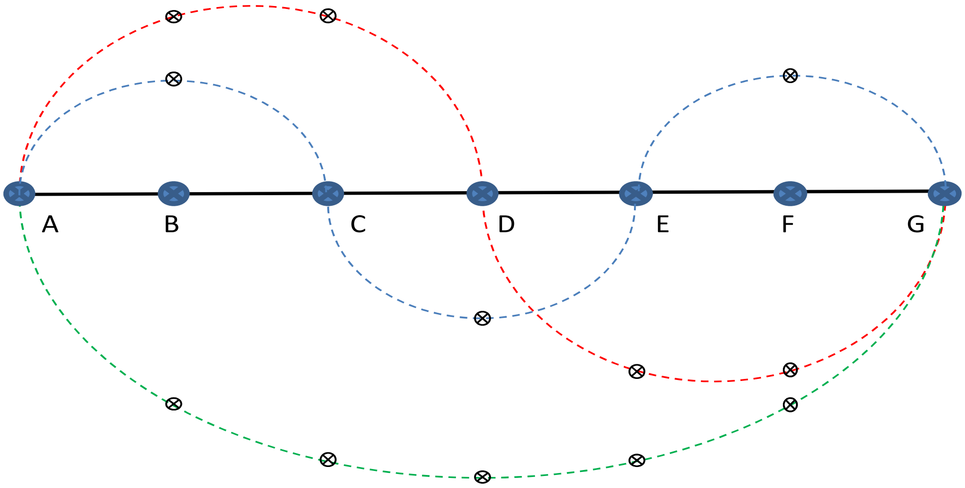

Figure 5.34: Nodal Movements due to Bending Modes

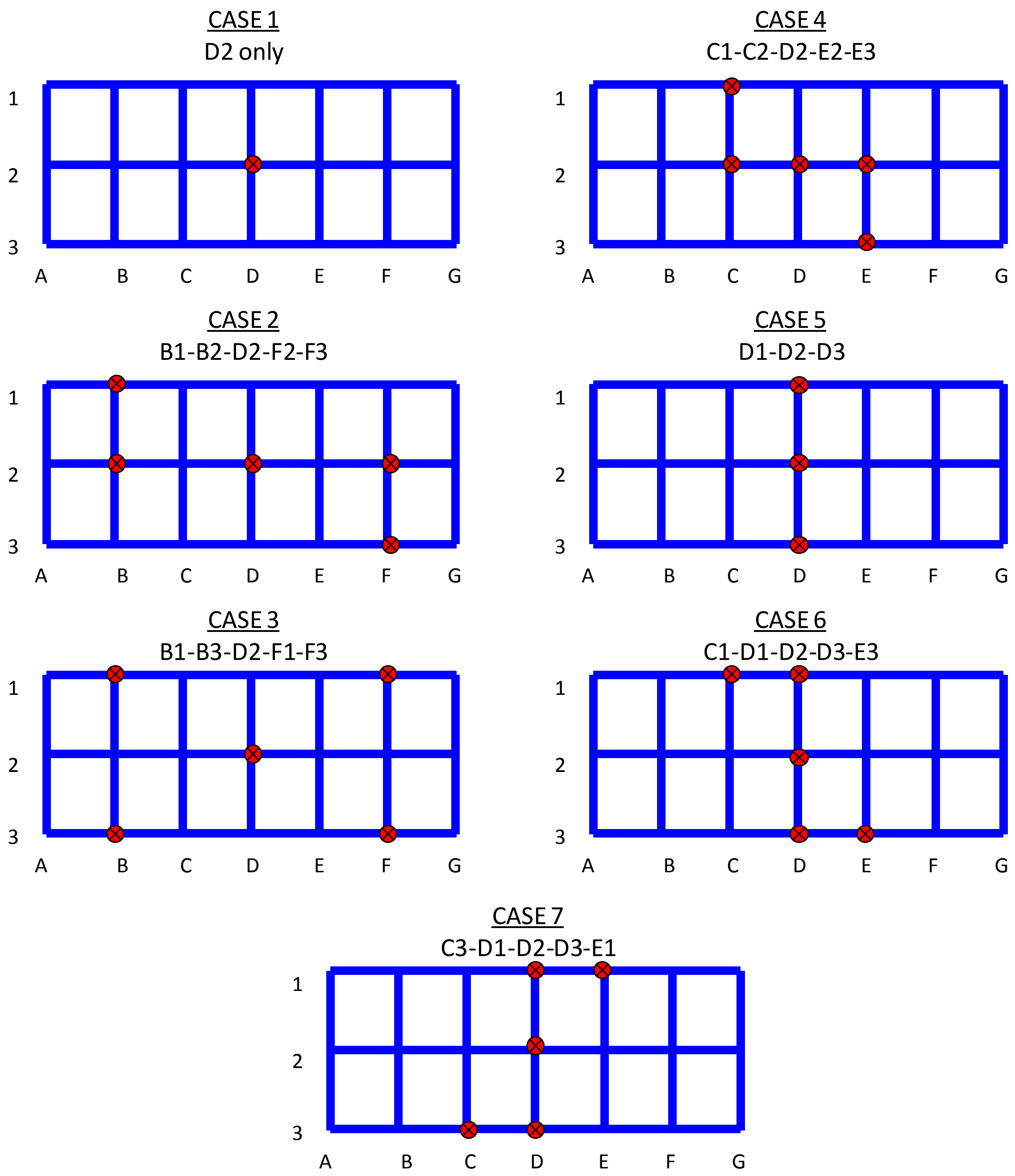

CASE 1
D2 only

CASE 4
C1-C2-D2-E2-E3

CASE 2
B1-B2-D2-F2-F3

CASE 5
D1-D2-D3

CASE 3
B1-B3-D2-F1-F3

CASE 6
C1-D1-D2-D3-E3

CASE 7
C3-D1-D2-D3-E1

Figure 5.35: Input Optimization Study Cases

By comparing the resulting deflection profiles produced from each of the load cases presented in Figure 5.35, it was found that Cases 1-3 produced plots that were very far off from the full input plots. This showed that the assumptions derived from the SAP2000 analysis proved to be wrong. Additional input scenarios were tested, and Cases 5-7 produced the closest representation, with cases six and seven each producing a nearly identical representation when compared to the full data set. This exercise proved that blindly following data produced from an analytical model must be done with great caution. The analytical model does not take into account imperfections in materials and support conditions, uneven bolt tightening, and other factors inherently present in constructed structures.

The results found from this study were further verified by looking at the modal contribution in the impact test data. An experimental modal truncation study was undertaken. Since modal flexibility is the summation of each contributing mode (Eq. (3.11)), this experimental study was performed calculating modal flexibility by including only mode 1, then modes 1 & 2, then modes 1, 2, & 3, etc. The deflection profiles from each of these cases were then plotted on top of one another and compared. It was found from this study that the greatest contributing modes were 1st Bending and 1st Torsion, with some contribution from 1st Butterfly.

By experimentally performing input optimization and modal contribution studies, it was found that the analytical model produced in SAP2000 did not accurately predict the experimental results. By comparison, it was found that 1st Bending, 1st Torsion, and 1st Butterfly modes contributed the most to modal flexibility, and were therefore key modes to capture during subsequent testing. It was also found that supplying input from the shaker into locations C3-D1-D2-D3-E1 produced nearly identical results as supplying input to all locations. Therefore, subsequent shaker tests only included inputs at these locations, whereas subsequent impact tests included inputs at all locations for comparison purposes.

5.6 SUMMARY

The undamaged grid model was extensively tested in order to obtain a baseline characterization to be used for future comparison of the damage scenarios. Static load testing was used to update the analytical model created in SAP2000, even though some of the static measurements contained experimental errors. The analytical model was then used as a starting tool for finding the possible locations of natural frequencies and for providing insight into modal contributions.

Dynamic testing was carried out utilizing three different input sources in order to compare the effectiveness of each type of input, and is summarized in Table 5.5. During impact and shaker testing the input force was measured, whereas during ambient testing the input force was not measured. Both impact and shaker testing provided very similar natural frequencies and mode shapes, and provided a modal flexibility matrix within 5.5% of each other. The modal flexibility from the impact test was around 14% from the analytical and static models due to modal truncation and was considered acceptable.

The ambient vibration testing provided similar natural frequencies and mode shapes, and produced an un-scaled pseudo modal flexibility. Using a MAC value comparison of the deflection profiles, this pseudo flexibility was found to be dissimilar to the flexibility derived from impact and shaker testing. The pseudo flexibility produced girder line deflections that contained the general shape of the deflection, but varied significantly in amplitude from girder to girder.

Input optimization and modal contribution studies were performed experimentally and it was found that the analytical model produced in SAP2000 did not accurately predict the experimental results. By comparison, it was found that 1st Bending, 1st Torsion, and 1st Butterfly modes contributed the most to modal flexibility, and were therefore key modes to capture during subsequent testing. It was also found that supplying input from the shaker into the right subset of the total locations produced nearly identical results as supplying input to all locations.

Table 5.5: Undamaged Grid Summary

		Natural Frequencies [Hz]			
Mode Number	*Mode Description*	***Analytical Model***	***Impact Test***	***Shaker Test***	***Ambient Test***
1	1st Bending	9.172	9.570	9.521	9.609
2	1st Torsion	10.015	10.958	10.948	10.853
3	2nd Bending	36.229	34.714	34.699	35.883
4	2nd Torsion	39.629	38.996	39.023	38.914
5	3rd Bending	78.791	72.831	72.645	69.295
6	1st Butterfly	83.583	80.058	80.366	80.032
7	3rd Torsion	87.394	82.695	82.787	85.354
8	2nd Butterfly	91.117	88.324	88.737	88.381

		Damping [%]			
Mode Number	*Mode Description*	***Analytical Model***	***Impact Test***	***Shaker Test***	***Ambient Test***
1	1st Bending	-	1.37	1.10	-
2	1st Torsion	-	1.32	1.14	-
3	2nd Bending	-	0.94	1.12	-
4	2nd Torsion	-	0.70	0.76	-
5	3rd Bending	-	1.03	1.18	-
6	1st Butterfly	-	0.85	0.78	-
7	3rd Torsion	-	1.15	1.05	-
8	2nd Butterfly	-	0.89	0.84	-

6. CHARACTERIZATION OF A DAMAGED GRID MODEL

In order to validate the testing and analysis methods described in the previous chapters, as well as the applicability of using modal flexibility to quantify damage, three different damage scenarios were implemented on the grid model. For each damage case all of the previously described dynamic testing methods (impact, shaker, and ambient vibration) were implemented in the same manner as on the undamaged grid model. This way, a direct comparison was able to be made between the damaged and undamaged grid models, and insight was found regarding the effectiveness of modal flexibility as a damage detection and quantification tool.

The three damage cases chosen represent possible failures that could occur due to some hazard event. Damage Case #1 was the removal of a bearing support. This damage represented not only a loss of bearing, but could be extended to represent support settlement, scour, or abutment movement due to a large lateral impact. Damage Case #2 was the removal of two transverse beams, which may represent some sort of change in the deck structure or other lateral stiffness member. Damage Case #3 was the removal of all gusset plates at six nodes. This would represent a loss of stiffness, possibly due to a blast type load. Each of these damage scenarios were fully tested and compared with the undamaged grid characterization and with each other.

The finite element model of the grid was also updated with each of the damage scenarios in order to validate the responses obtained through dynamic testing. In each case, the damage was able to be detected in the mode shapes and frequencies of both the FE model and the experimental model.

6.1 DAMAGE CASE #1

Damage Case #1 was the removal of a bearing support at location G3. Figure 6.1 shows both the location in plan view and the physical implementation. The support removed was a roller type support, thus freeing the vertical direction of movement of the third girder.

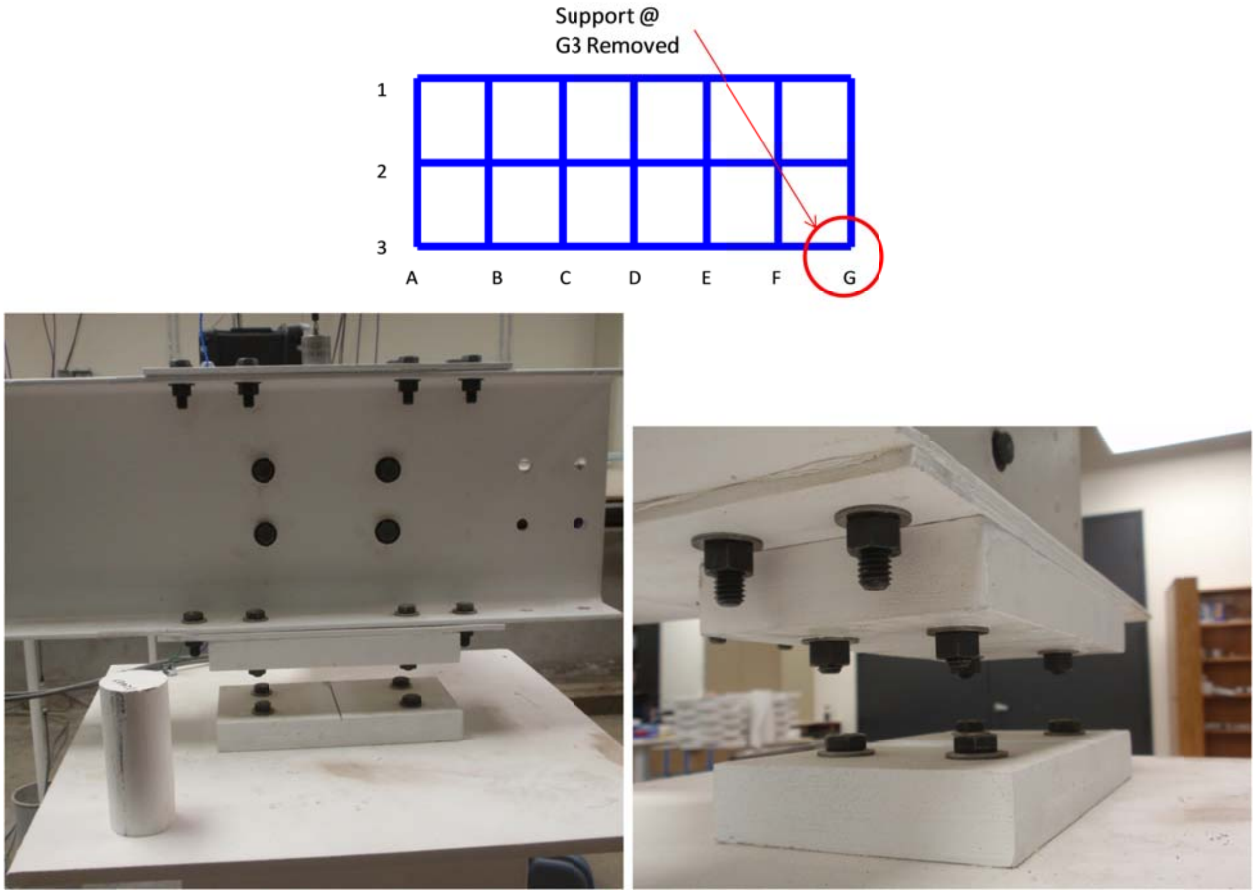

Figure 6.1: Damage Case #1 – Removal of Support Bearing

Impact testing was implemented in the exact same manner as with the undamaged grid model. The same number of hits, same averaging, same rubber impact tip, and the same sampling frequency were all used. When the FRFs were processed into a CMIF, the peaks were very clean and distinguishable, as seen in Figure 6.2. The most important thing to note about this CMIF plot is that when compared to the undamaged grid, some of the peaks changed locations, and two new peaks appeared. Each of these peaks produced the mode shapes seen in Figure 6.3, with the far back right corner representing location G3. Several of the mode shapes seem to be similar to the undamaged grid, but when one looks closely, the support can be seen moving in many of the modes. These mode shapes clearly showed the damage applied to the structure.

Evidence of a change in the structural characteristics of the grid was evident in that two new mode shapes appeared, one at approximately 29 Hz and one at approximately 48 Hz. As seen in Figure 6.3, the first new mode could be described as girder #1 remaining stationary while girder #3 bent in a 2nd bending type of shape. It can be seen that in this bending mode that the end of the beam was far away from the support at location G3, which was the removed support. The second new mode appeared to take on the characteristics of torsion, with the node at G3 moving with much greater amplitude than the rest of the structure.

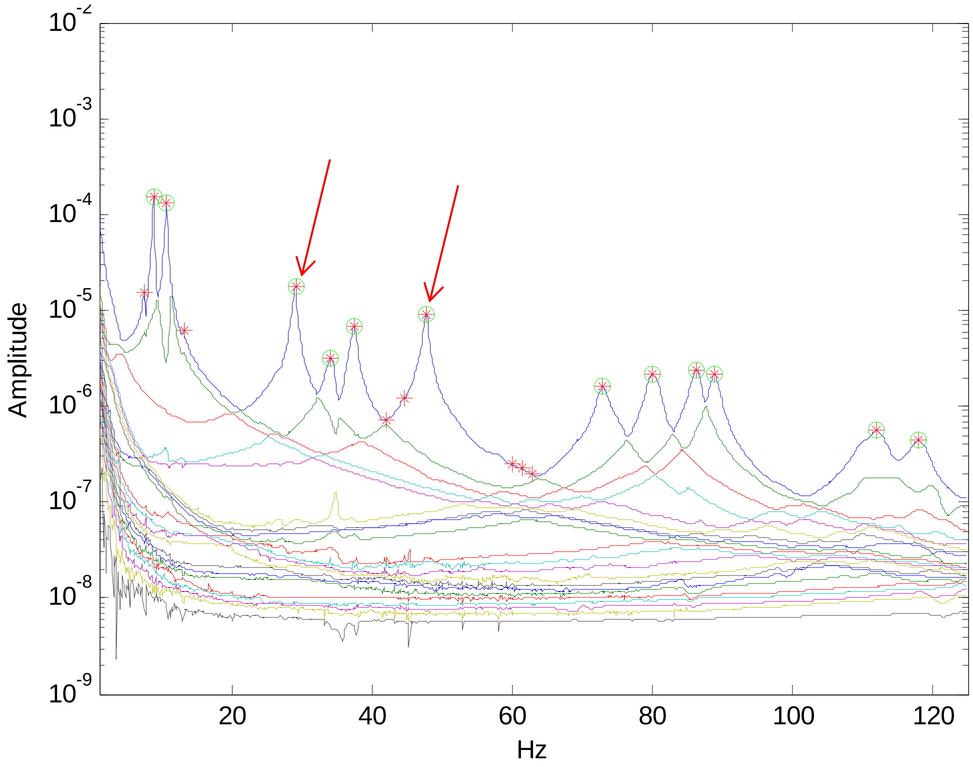

Figure 6.2: CMIF Plot – Impact Test for Damage Case #1

Another interesting difference to note when looking at the CMIF plot is that two distinct peaks occurred in the 30-40 Hz range. These two peaks were located at similar frequencies to 2nd Bending Mode and 2nd Torsion Mode from the undamaged grid scenario, but the two mode shapes appeared nearly identical to each other in the damaged state. These two mode shapes appeared to be the symmetric opposite of the new mode discovered at approximately 29 Hz.

It is important to note that by looking at the mode shapes and frequencies, the damage implemented at G3 was able to be detected. While many of the mode shapes looked similar to the undamaged case, the majority of them showed significant movement of the node at support G3, indicating damage. This, along with the new mode shapes and shifts in natural frequencies, pointed to the damage inflicted.

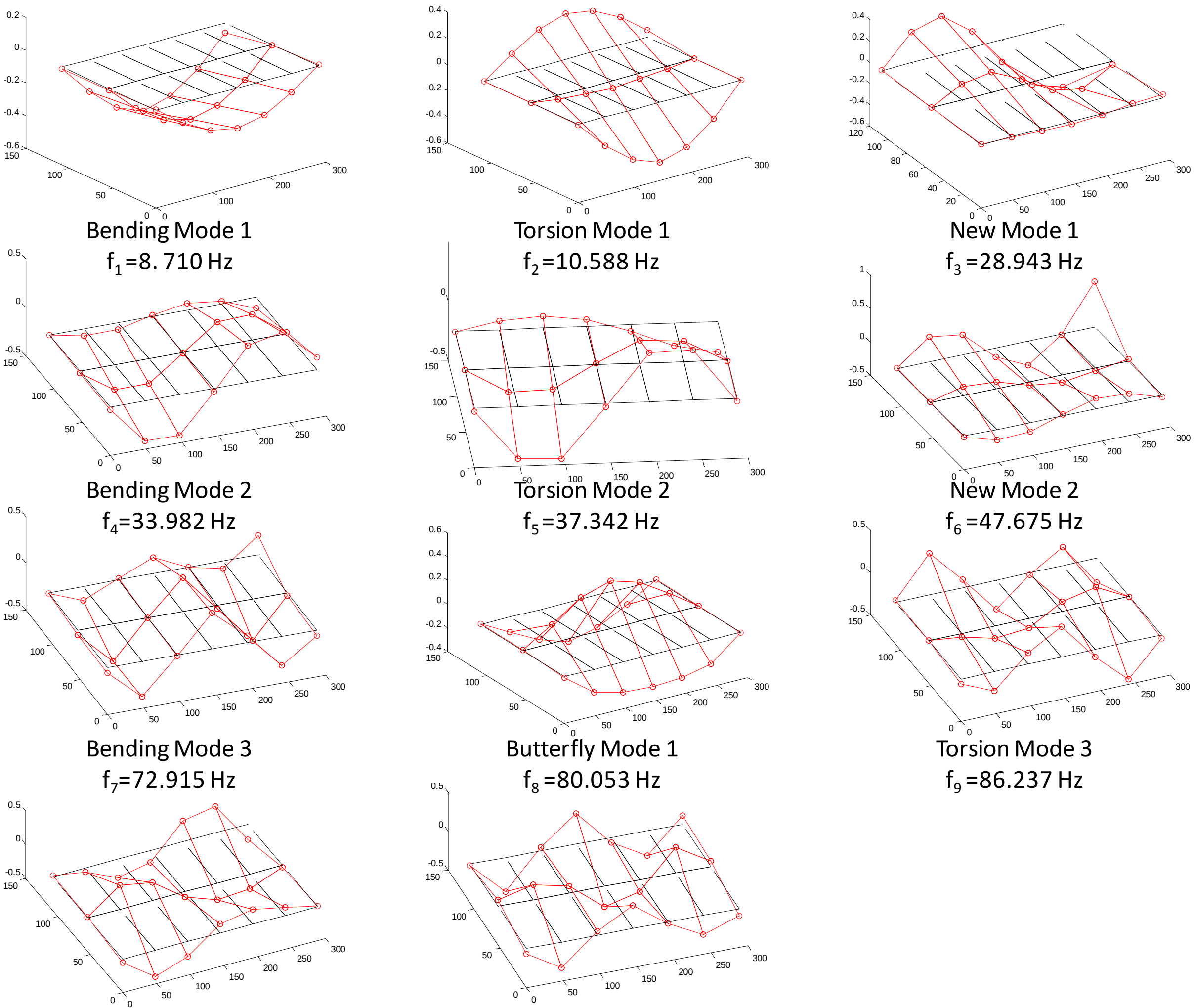

Bending Mode 1
f_{1}=8. 710 Hz

Torsion Mode 1
f_{2}=10.588 Hz

New Mode 1
f_{3}=28.943 Hz

Bending Mode 2
f_{4}=33.982 Hz

Torsion Mode 2
f_{5}=37.342 Hz

New Mode 2
f_{6}=47.675 Hz

Bending Mode 3
f_{7}=72.915 Hz

Butterfly Mode 1
f_{8}=80.053 Hz

Torsion Mode 3
f_{9}=86.237 Hz

Butterfly Mode 2
f_{10}=88.862 Hz

Butterfly Mode 3
f_{11}=112.024 Hz

Figure 6.3: Experimental Mode Shapes from Damage Case #1

This damage scenario was also modeled in SAP2000 by removing the support at node G3. A static analysis was performed to obtain a flexibility matrix. Dynamic modal analysis was also performed and mode shapes that were very similar to those found from experimental testing were found, including the two new modes (Figure 6.4). Two main differences were found between the analytical model and the experimental model. The first was that the frequencies were generally higher in the analytical model and shifted farther away in the higher modes. The second difference was with respect to the 2nd bending and 2nd torsion mode shapes found experimentally. In the analytical model only one mode was found at 37.8 Hz, whereas in the experimental model two were found (33.9 Hz and 37.3 Hz).

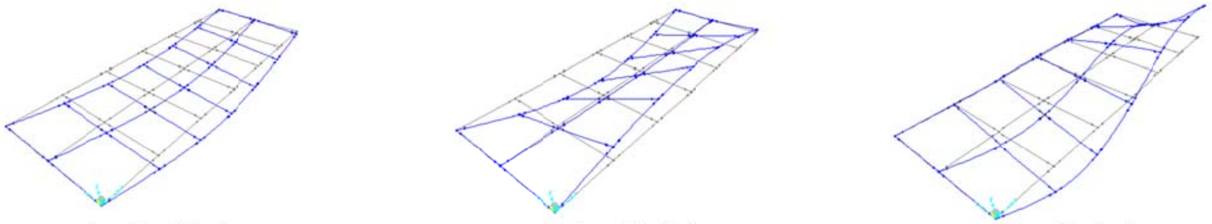

Bending Mode 1
f_1=9.024 Hz

Torsion Mode 1
f_2=9.847 Hz

New Mode 1
f_3=32.099 Hz

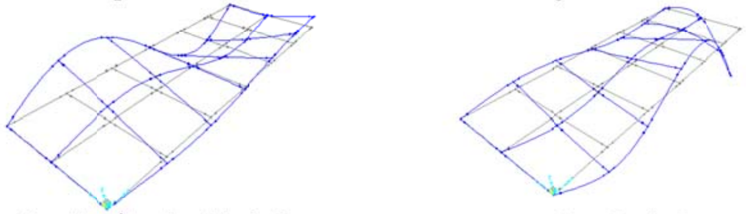

Bending/Torsion Mode 2
f_5=37.819 Hz

New Mode 2
f_6=54.454 Hz

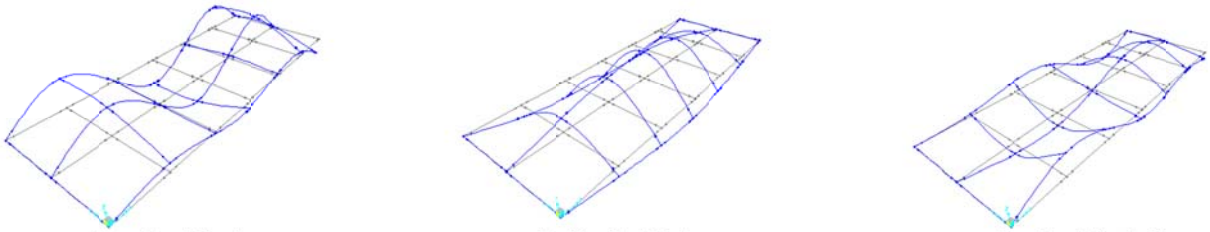

Bending Mode 3
f_7=80.401 Hz

Butterfly Mode 1
f_8=83.591 Hz

Torsion Mode 3
f_9=90.653 Hz

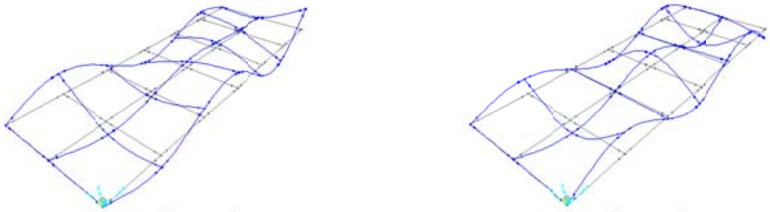

Butterfly Mode 2
f_{10}=93.851 Hz

Butterfly Mode 3
f_{11}=119.510 Hz

Figure 6.4: Analytical Mode Shapes from Damage Case #1

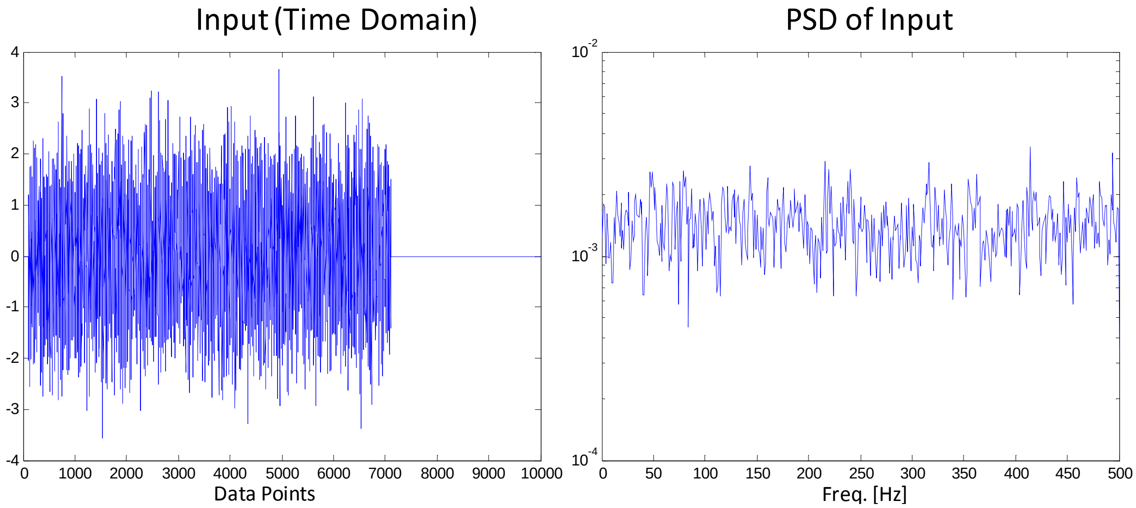

Figure 6.5: Input Signal for Shaker Testing

Shaker testing was also implemented on the damaged grid model. As noted earlier, the shaker input was applied to only five locations in order to fully excite the structure but also to limit the time involved in testing. Between the time of finishing the testing and processing of the undamaged grid model and implementing the first damage case, the original data acquisition equipment used for the shaker testing was damaged during a field test. In light of this, shaker testing was done with a National Instruments PXI data acquisition hardware unit, with the signal generated through an Agilent 3320A waveform generator. A burst random signal with Gaussian white noise distribution was created in MATLAB and saved into the waveform generator. This signal was very similar to the signal produced by the original data acquisition hardware from Data Physics Corp., with a 16s time frame and uniform power distribution, as can be seen in Figure 6.5.

The resulting CMIF from the shaker test (Figure 6.6) showed to be noisier than the impact test results, even with ten averages taken. Since it was not as evident in the previous shaker testing, the additional noise was attributed to the change in hardware used for data collection. From the shaker test, the same peaks were noted, including the new modes present at approximately 29 Hz and approximately 48 Hz. Similar mode shapes and frequencies were found from the post-processing of the data, and a modal flexibility was found. Since the modal flexibility from the shaker test was found from only five input locations, the impact data was also processed with the same five inputs in order to have an equal comparison between the different types of tests. Figure 6.7 shows the deflection profiles of the modal flexibility with the undamaged grid impact test as a reference, and three deflections from the first damage case: full impact test, five location impact test, and five location shaker test. As seen from the figure, the full impact plot is very comparable to the impact plot from using only five inputs. The shaker test showed to deflect slightly more than the impact tests, but was within reason. An important thing to note from the modal flexibility deflection profiles was the clear display of damage located on the third girder, at the end. The deflection plots all went to zero at the ends except for the end where the support was removed. Though this value may not be fully quantifiable, it clearly demonstrates the damage induced into the structure, and is of great value.

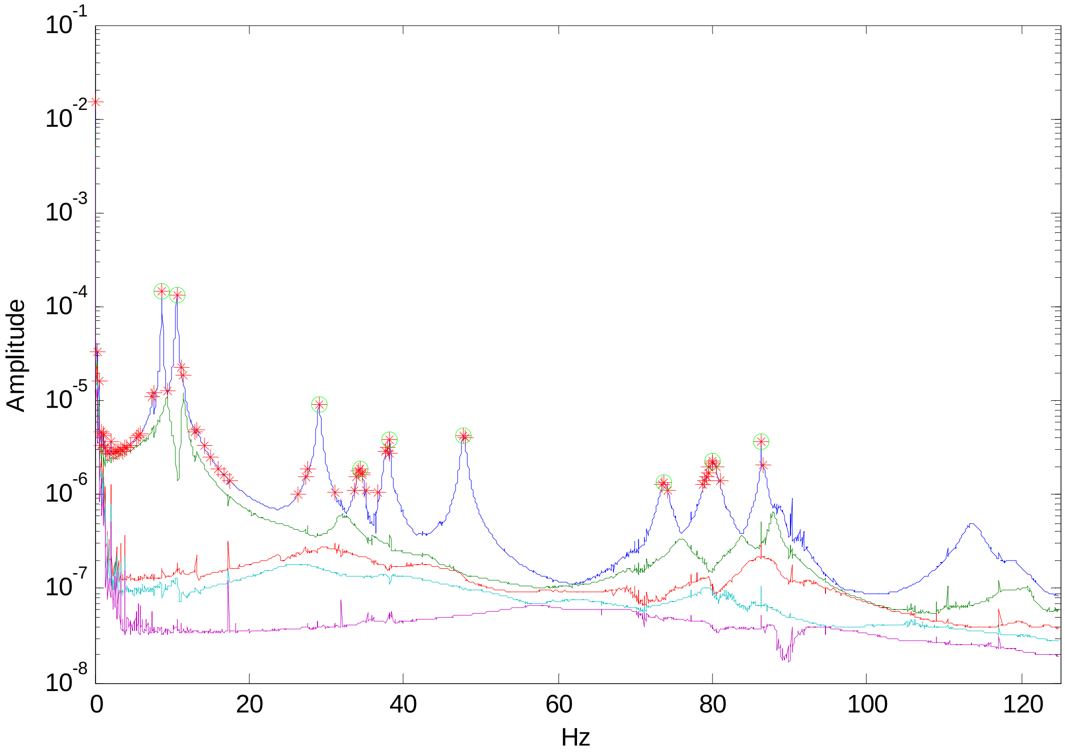

Figure 6.6: CMIF Plot – Shaker Test for Damage Case #1

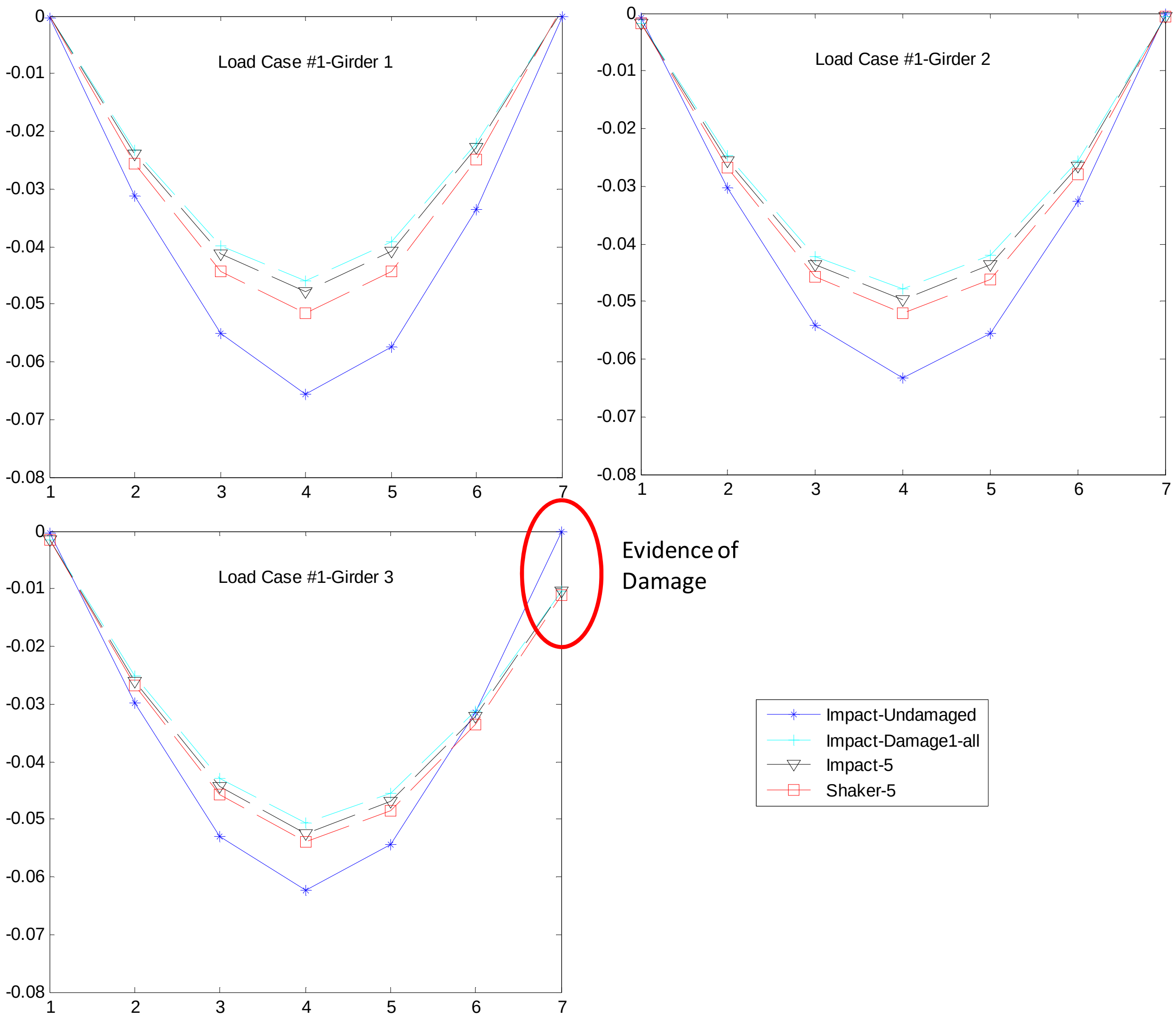

Figure 6.7: Deflection Profiles for Damage Case #1

The third set of tests executed on the damaged grid was a series of ambient tests. As noted earlier, only two types of inputs were used for the ambient tests: quiet input and coupled shaker input. Two different types of processing were also used for each input type. The first type of processing found mode shapes and frequencies from Power Spectral Densities (PSDs) and Cross-Power Spectral Densities (CPSDs). The second processing technique used correlation functions to create pseudo impact response functions (PIRF) in order to process the data with the CMIF algorithm developed. The goal was to compare the effectiveness of the different processing techniques, as well as to investigate whether or not a correlation could be made between the ambient test results and the impact and shaker test results.

The quiet input provided a noisy normalized PSD, as seen in Figure 6.8, which made peak picking especially difficult. Peak picking was the method used to obtain modal frequencies and modal vectors (mode shapes) for the given data set. Each peak may represent a natural frequency with a corresponding mode shape. By looking closely at the amplitude of the peak as well as the mode shapes plotted, one can determine if the chosen peak is indeed a natural frequency. Since so many peaks were present in the noisy data set, finding natural frequencies was difficult, but not impossible. When the PIRFs were created in order to use the CMIF processing techniques, the quiet input data produced a CMIF plot that did not clearly show each mode, as seen in Figure 6.9. In fact, when the data was processed further, seven of the ten mode shapes chosen ended up representing the new mode at 29 Hz, as shown earlier. This new mode dominated the response of the structure, thus indicating damage, but not in the way expected. With the impact and shaker tests, each mode was clearly evident and several of the modes showed the damage whereas with ambient processing, one mode dominated the spectrum.

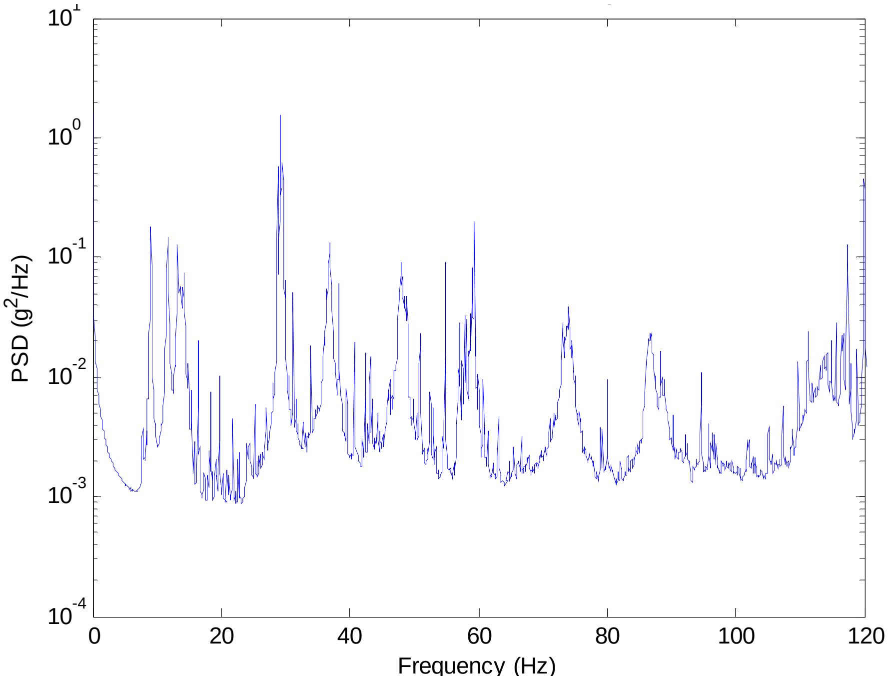

Figure 6.8: NPSD – Ambient Quiet Input for Damage Case #1

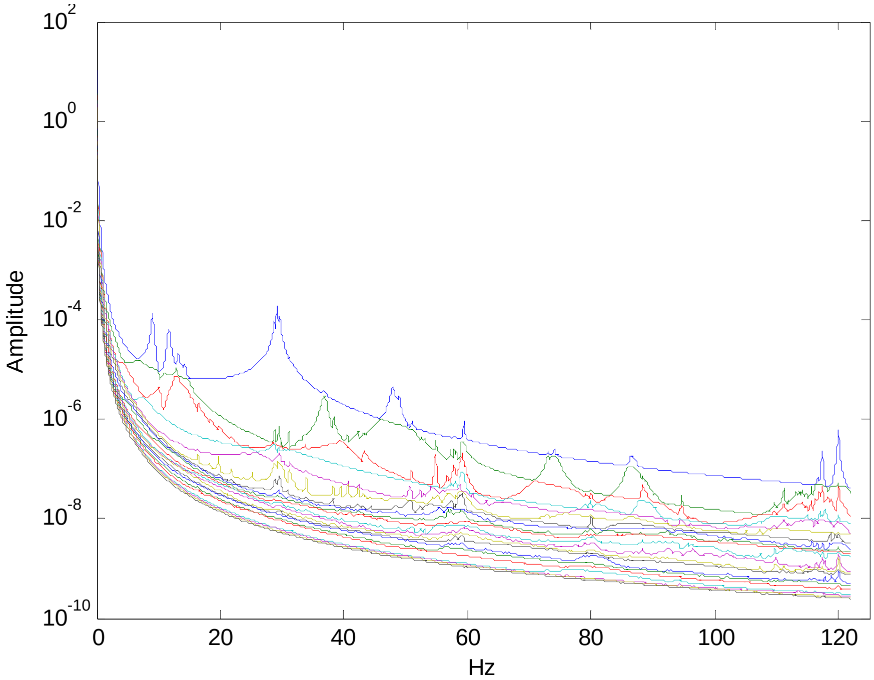

Figure 6.9: CMIF Plot – Ambient Quiet Input for Damage Case #1

The coupled ambient input, on the other hand, provided very good excitation and clear peaks in the normalized PSD seen in Figure 6.10. These sharp peaks produced clear natural frequencies and corresponding mode shapes. All of the modes found from the measured input tests, with the exception of 2nd Bending Mode, were present in the data. When processed using correlation functions into PIRFs, the CMIF plot showed very clear peaks at all of the modes of the structure and can be seen in Figure 6.11. These two plots showed a noticeable contrast when compared to the quiet input, and pointed to the better excitation of the modes of the structure from the coupled input. Using the CMIF algorithm to identify modal parameters proved to be ineffective. The 1st bending and 1st torsion modes switched locations, and several of the other modes were out of place or non-existent. These discrepancies were also noted in the enhanced frequency response functions (eFRFs), which were supposed to isolate each mode and decouple the system into a series of SDOF systems. The eFRFs did not properly decouple the system, and the peaks did not show up where expected.

Overall, the coupled shaker input provided a much better excitation of the modes of the structure when compared to quiet excitation. Clear mode shapes and natural frequencies were found from the PSD method which were very comparable to the impact and shaker tests performed. The CMIF method of processing proved to be ineffective in properly identifying mode shapes and natural frequencies, with either type of ambient input.

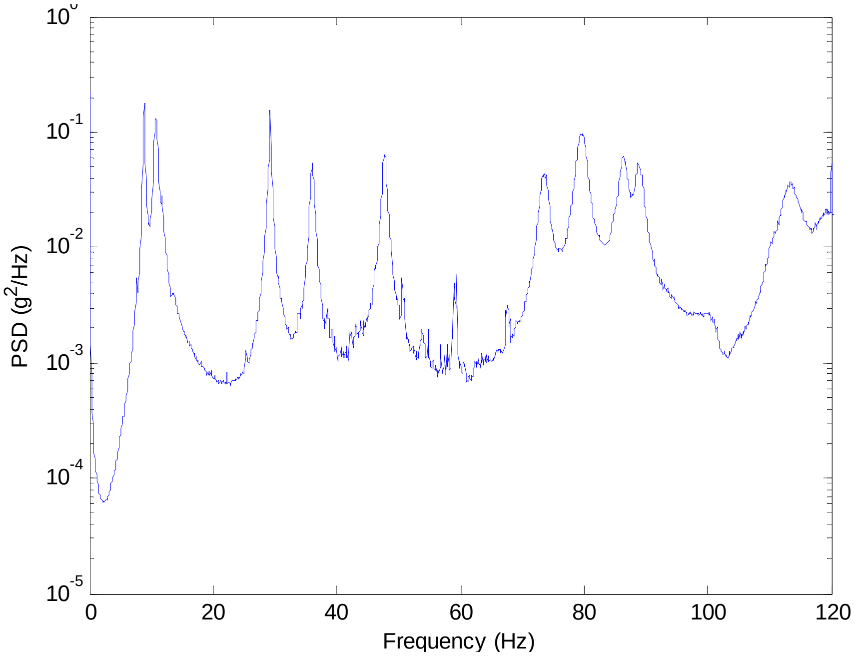

Figure 6.10: NPSD – Ambient Coupled Input for Damage Case #1

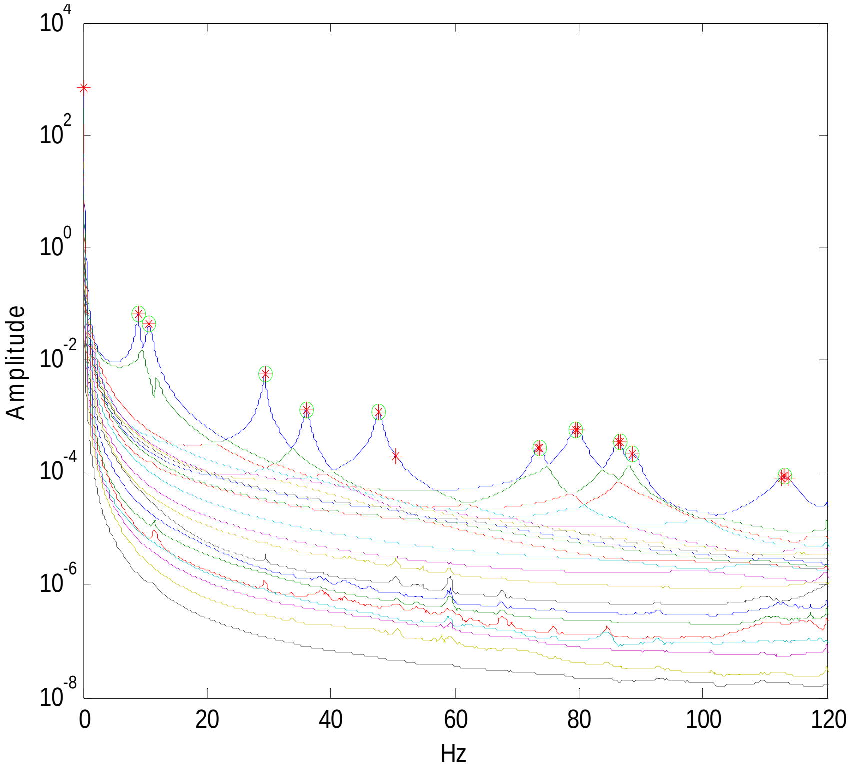

Figure 6.11: CMIF Plot – Ambient Coupled Input for Damage Case #1

6.2 DAMAGE CASE #2

Damage Case #2 was the removal of the transverse beams at location D. Figure 6.12 shows the location of the damage. It was expected that by removing these members, the structure would lose some of its stiffness. It was also expected that load distribution would be adversely affected.

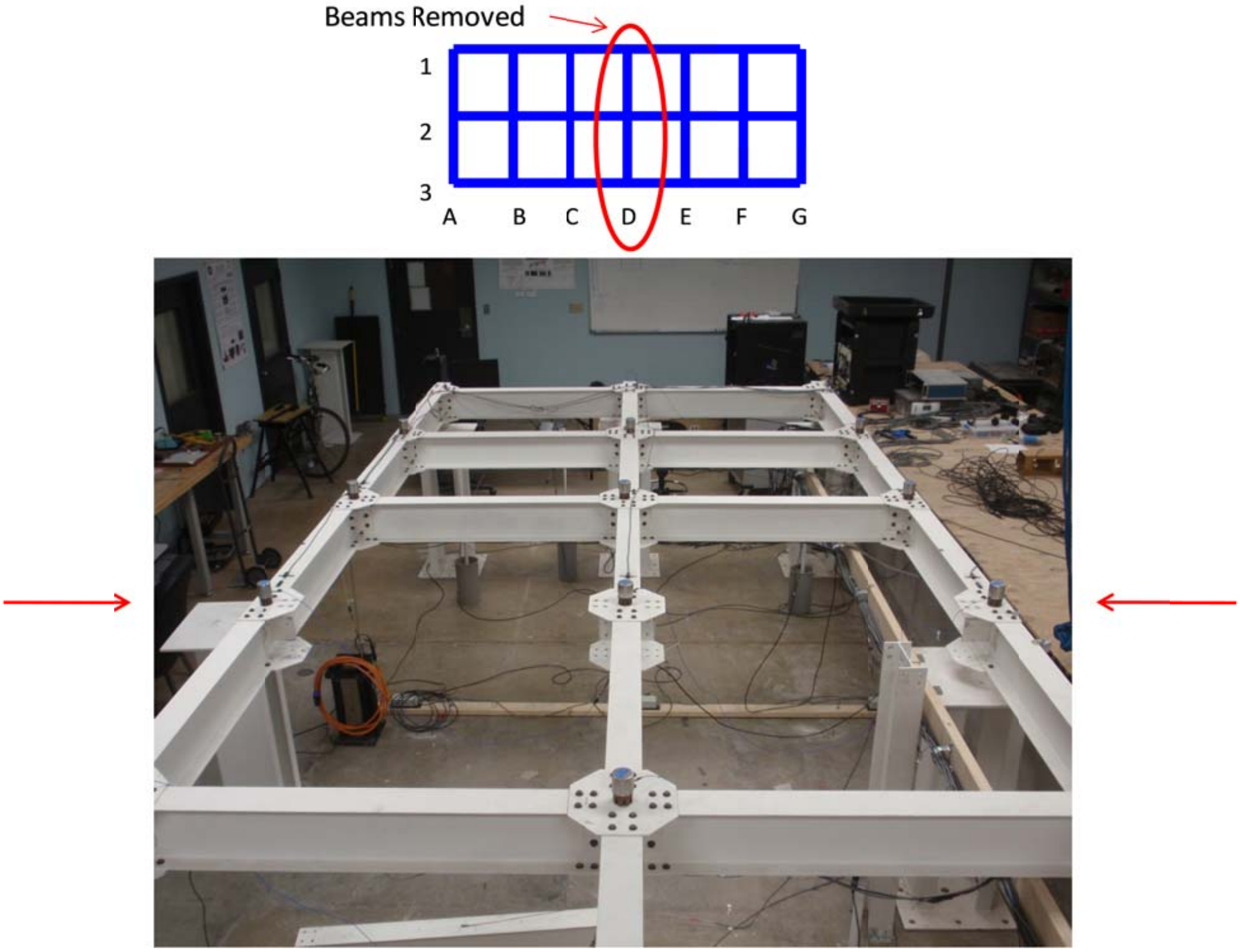

Figure 6.12: Damage Case #2 – Removal of Transverse Beam D

Impact testing was implemented in the exact same manner as with the undamaged grid model. When the FRFs were processed into the CMIF spectrum, the peaks were very clean and sharp, as seen in Figure 6.13. Overall, the mode shapes and frequencies were nearly unchanged from the undamaged grid model, with two key exceptions. The 1st butterfly mode shifted significantly, from 80 Hz to 64 Hz. Also, a new mode appeared in the experimental data at around 59 Hz that was similar to the butterfly mode, except with inverted bending near the transverse beam D. These mode shapes can be seen in Figure 6.14. Other than these two changes, the evidence of this damage case was unseen.

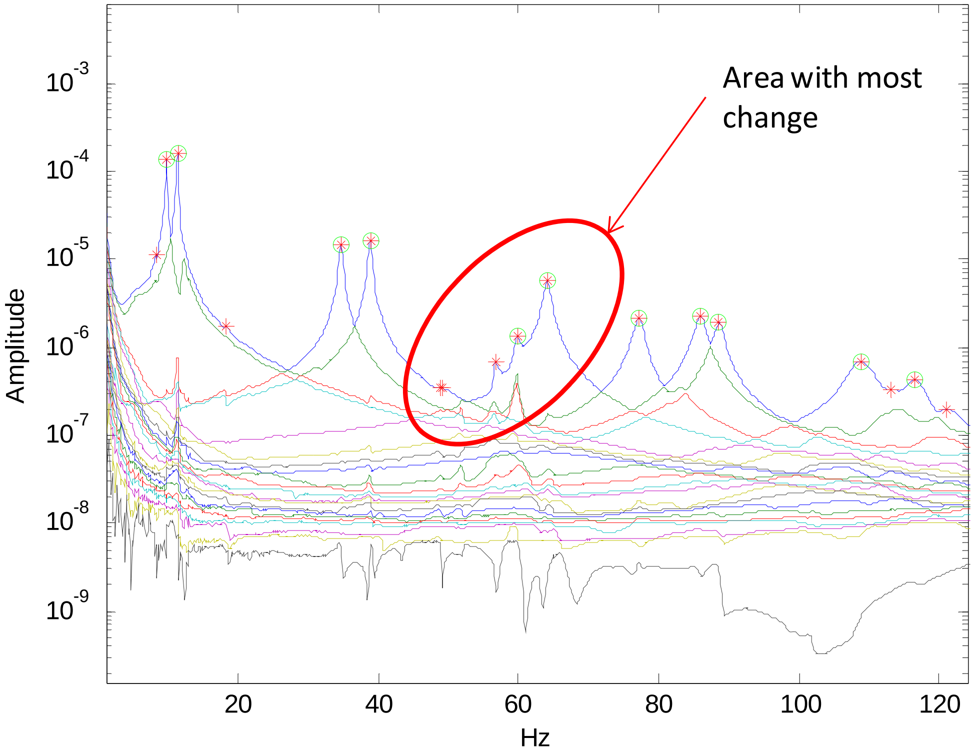

Figure 6.13: CMIF Plot – Impact Test for Damage Case #2

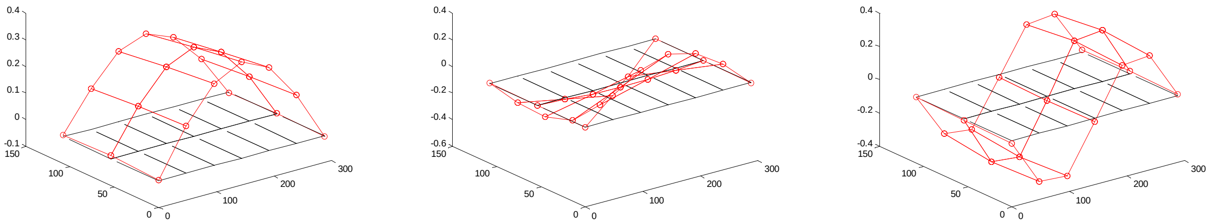

Bending Mode 1
f_1=9.750 Hz

Torsion Mode 1
f_2=11.314 Hz

Bending Mode 2
f_3=34.664 Hz

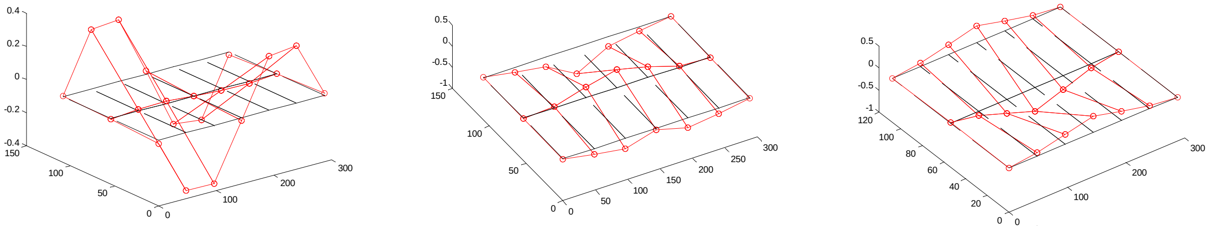

Torsion Mode 2
f_4=38.823 Hz

New Mode 1
f_5=59.793 Hz

Butterfly Mode 1
f_6=64.088 Hz

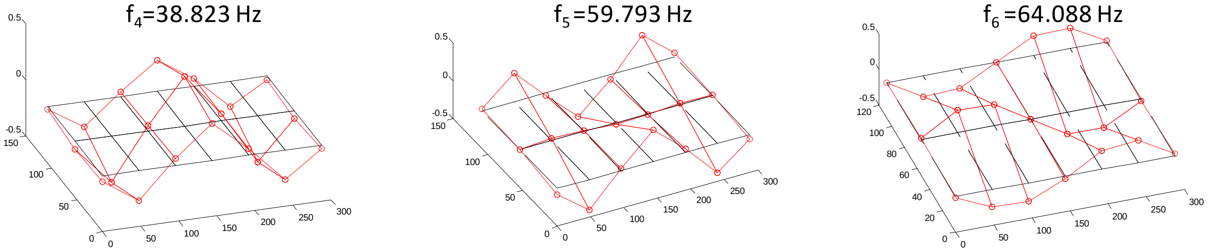

Bending Mode 3
f_7=77.141 Hz

Torsion Mode 3
f_8=85.964 Hz

Butterfly Mode 2
f_9=88.617 Hz

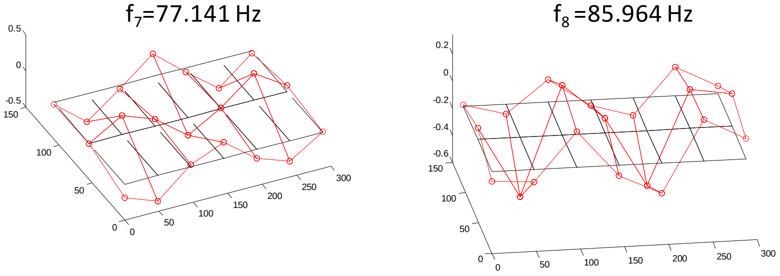

Butterfly Mode 3
f_{10}=108.844 Hz

Bending Mode 4
f_{11}=116.587 Hz

Figure 6.14: Experimental Mode Shapes from Damage Case #2

This damage scenario was also modeled in SAP2000 by removing the transverse beam elements at D and the corresponding stiffened members in line with D near the nodes. A static analysis was performed to obtain a flexibility matrix. Dynamic modal analysis was performed and produced mode shapes that were very similar to those found from experimental testing. These can be seen in Figure 6.15. Interestingly, the new mode at 59 Hz was not found from the SAP2000 model. The remaining mode shapes were very similar to the experimentally found mode shapes, with some variation in the natural frequencies found.

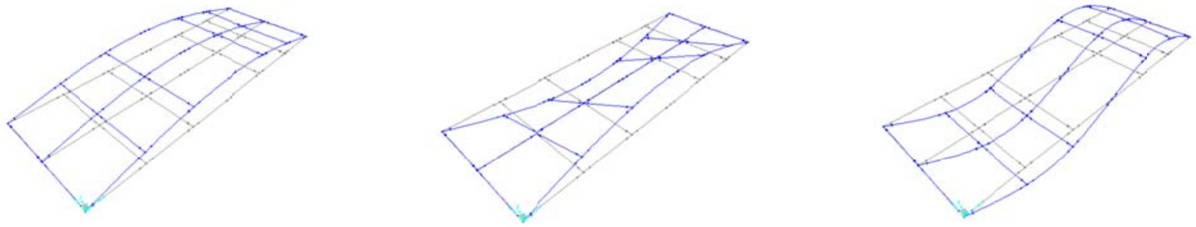

Bending Mode 1
f_1=9.000 Hz

Torsion Mode 1
f_2=10.593 Hz

Bending Mode 2
f_3=36.229 Hz

Torsion Mode 2
f_4=39.626 Hz

Butterfly Mode 1
f_6=69.572 Hz

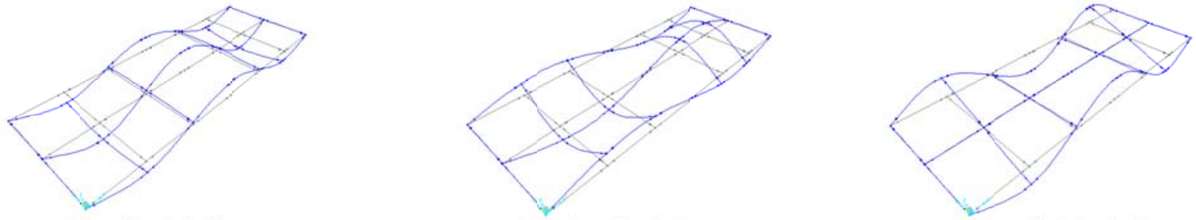

Bending Mode 3
f_7=86.150 Hz

Torsion Mode 3
f_8=91.113 Hz

Butterfly Mode 2
f_9=92.960 Hz

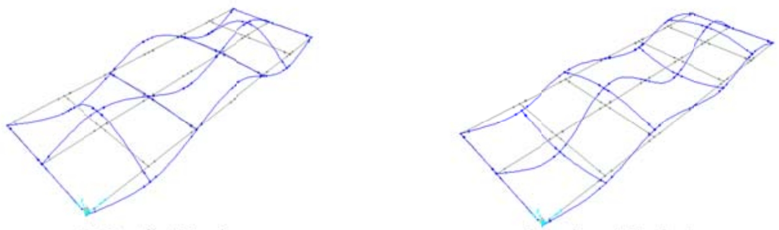

Butterfly Mode 3
f_{10}=115.560 Hz

Bending Mode 4
f_{11}=130.840 Hz

Figure 6.15: Analytical Mode Shapes from Damage Case #2

Shaker testing was implemented for the second damage case. The resulting CMIF from the shaker test again showed to be noisier than the impact test results, even with ten averages taken (Figure 6.16). This slight jump in noise was attributed to the change in hardware used for data collection. The same peaks were present, as well as the new mode at 59 Hz. Similar mode shapes and frequencies were found from the remaining processing, and modal flexibility was found. The deflection profiles of the modal flexibility are plotted in Figure 6.17 with the undamaged grid impact test as a reference, and three deflections from the second damage case: full impact test, five location impact test, and five location shaker test. As seen from the figure, the full impact plot is very comparable to the impact plot from using only five inputs. The shaker test however, showed to deflect considerably more than the impact tests, and was not as close to the five input impact test as was expected. When compared with all the different shaker tests performed for all damage cases, this deflection was in-line with expectation, and is further discussed in Section 6.4.

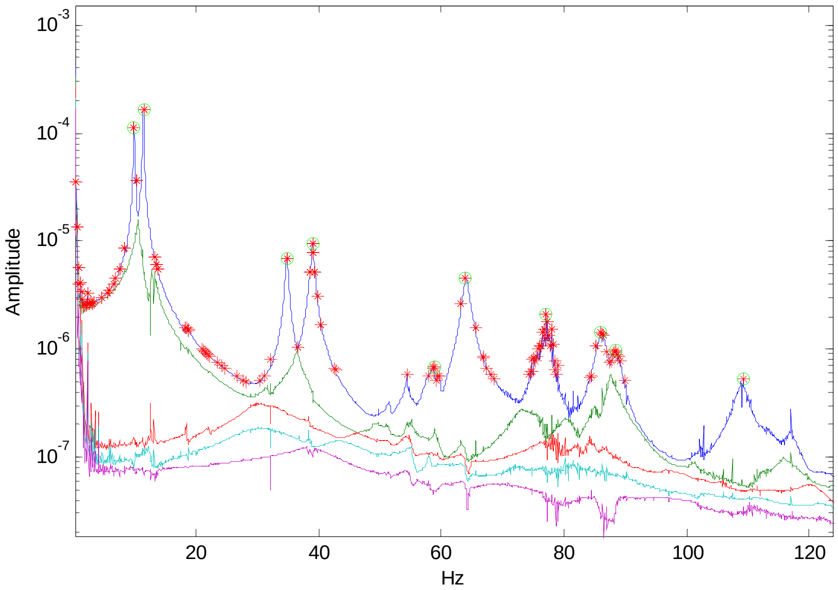

Figure 6.16: CMIF Plot – Shaker Test for Damage Case #2

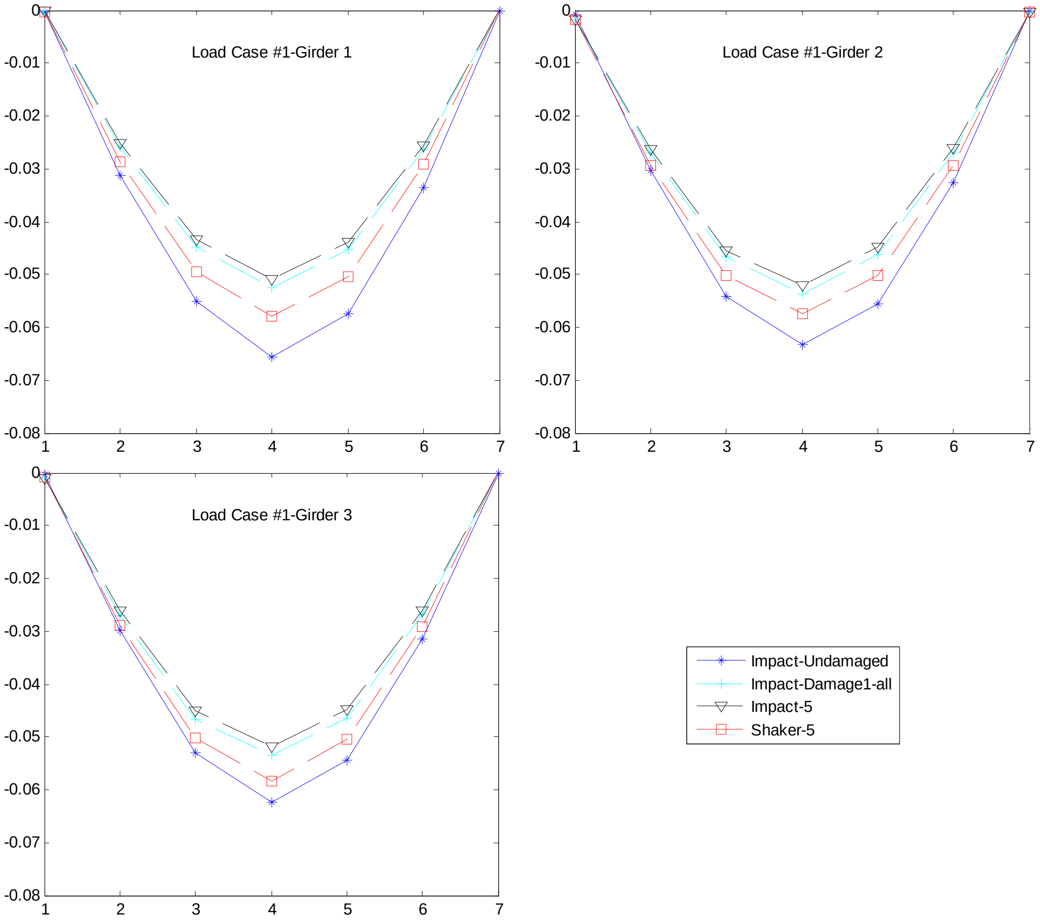

Figure 6.17: Deflection Profiles for Damage Case #2

As with the first damage case, a series of ambient tests were also performed on the grid while in the second damage case configuration. The quiet input provided a noisy normalized PSD, as seen in Figure 6.18, but was less noisy than the previous damage case with the natural peaks more evident. Peak picking was somewhat difficult, but manageable, and produced decent mode shapes and natural frequencies. When the PIRFs were created in order to use the CMIF processing techniques, the quiet input data produced a CMIF plot that did not show the first two modes as clearly as the others (Figure 6.19). When the data was processed further, several of the modes did not appear, and several modes showed the structure leaving the supports.

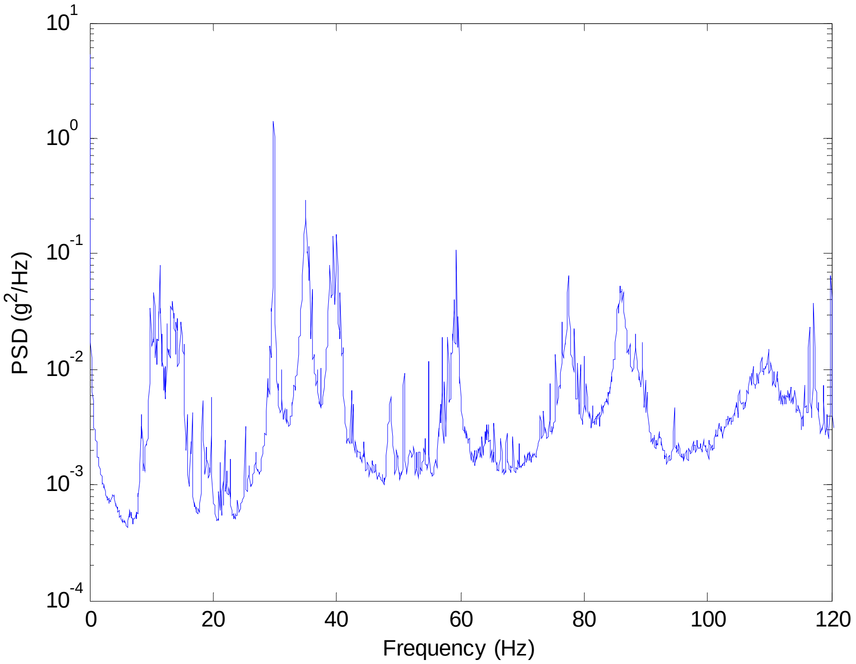

Figure 6.18: NPSD – Ambient Quiet Input for Damage Case #2

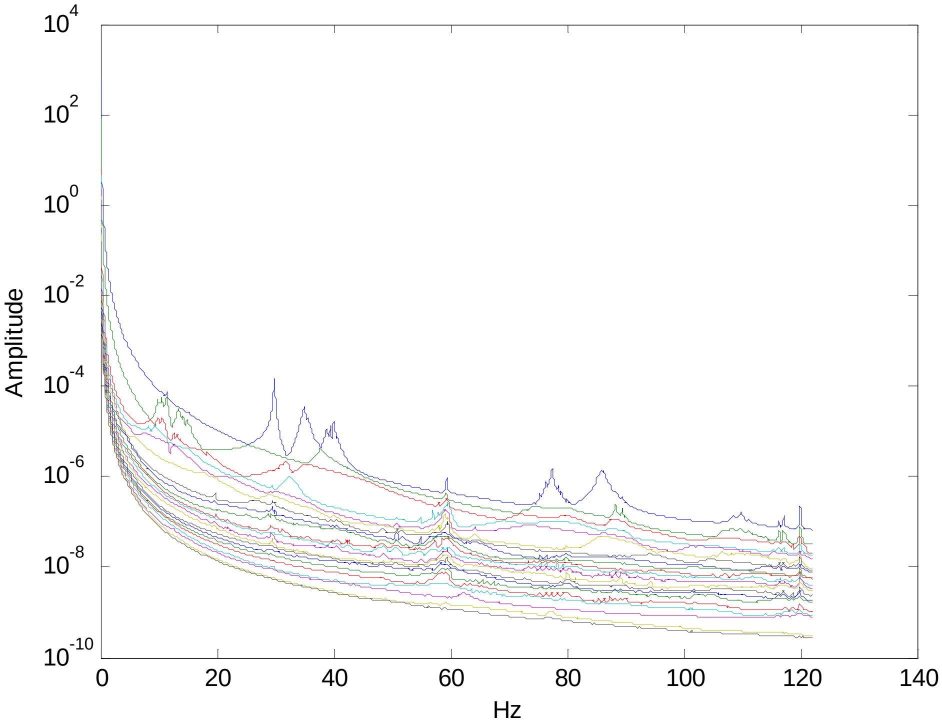

Figure 6.19: CMIF Plot – Ambient Quiet Input for Damage Case #2

The coupled ambient input, however, provided very good excitation and relatively clear peaks in the normalized PSD seen in Figure 6.20. These peaks produced clear natural frequencies and corresponding mode shapes. All of the modes found from the measured input tests were present in the data. When processed using correlation functions to create PIRFs, the resulting CMIF plot showed relatively clear peaks at all of the natural frequencies of the structure and can be seen in Figure 6.21. These two plots show a noticeable contrast when compared to the quiet input, and point to the better excitation of the modes of the structure from the coupled input. Using the CMIF algorithm to identify modal parameters proved to be ineffective. The 1st bending and 1st torsion modes switched locations. Several of the other modes were not clear or were non-existent. Also, the 1st butterfly mode showed up at four distinct locations, and dominated the output of the structure. While the regular FRFs were clear, these discrepancies did show up in the eFRFs. The eFRFs did not decouple the system and the peaks did not show up where expected.

Overall, the coupled shaker input provided much clearer excitation of the modes of the structure when compared to quiet excitation. Clear mode shapes and natural frequencies were found from the PSD method which were very comparable to the impact and shaker tests performed. The CMIF method of processing proved to be ineffective in properly identifying mode shapes and natural frequencies with either type of ambient input.

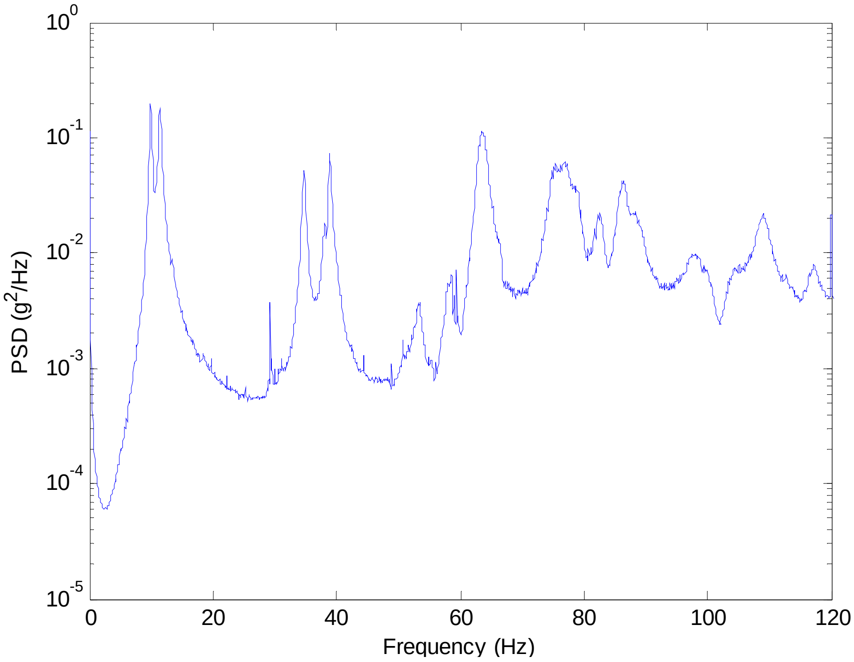

Figure 6.20: NPSD – Ambient Coupled Input for Damage Case #2

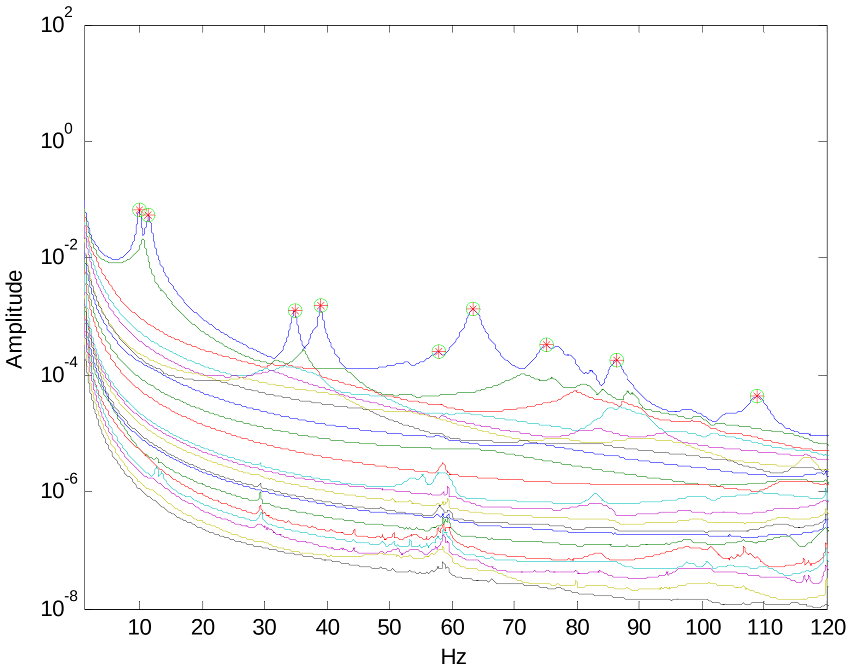

Figure 6.21: CMIF Plot – Ambient Coupled Input for Damage Case #2

6.3 DAMAGE CASE #3

Damage Case #3 consisted of the removal of the top and bottom gusset plates at six nodes. Removal of the gusset plates was done in an asymmetric manner about the mid-span so as to more easily identify the damage inflicted after processing the experimental data. Figure 6.22 shows the damage and its location. It was expected that by removing the gusset plates, an obvious change in the structure's stiffness would be realized. The vertical clip angles were left intact, thus connecting the transverse beams to the longitudinal beams. In steel connection design, the clip angles are taken to be shear connections only, where the gusset plates on top and bottom are taken to be moment resisting. It was found that the clip angles still transferred a significant amount of moment. This was attributed to physical characteristics of the system such as member depth, distance between nodes, and stiffness of the members.

Impact testing was implemented in the exact same manner as with the undamaged grid model. When the FRFs were processed into the CMIF spectrum, the peaks were very clean and sharp, as seen in Figure 6.23. All of the mode shapes from the CMIF plot can be seen in Figure 6.24. Several items of importance should be noted here. First, several peaks changed locations from the undamaged grid model, most notably the first butterfly moved from 80 Hz to 44 Hz. It can also be seen that the shape of the butterfly mode changed to become centered around transverse lines 'D' and 'E,' giving evidence of the damage inflicted. Also, at between 82 Hz and 83 Hz two peaks can be seen in the CMIF plot, though not on the same line. One of the benefits of using the CMIF algorithm is the ability to distinguish closely spaced modes by using modal filter vectors to isolate each individual mode. From further processing, the two mode shapes were determined to be 2nd Butterfly Mode and 3rd Torsion Mode. Other methods were not able to distinguish these two closely spaced modes.

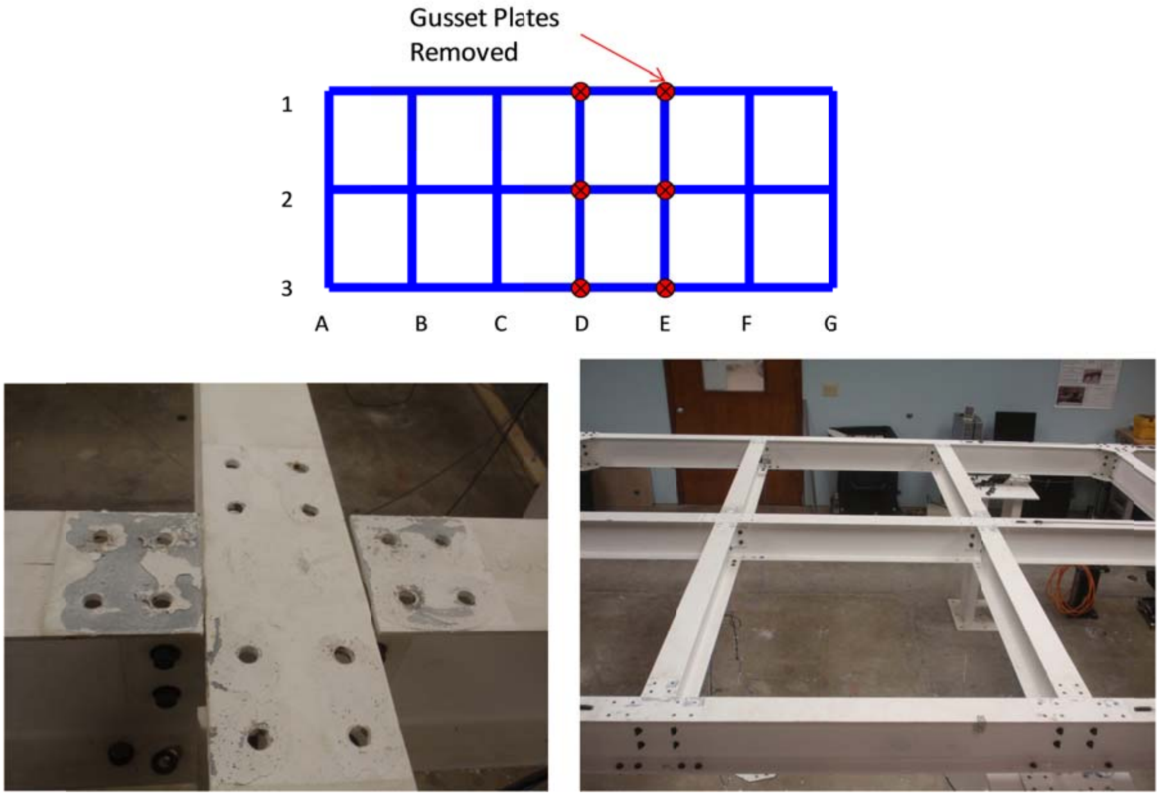

Figure 6.22: Damage Case #3 – Removal of Gusset Plates

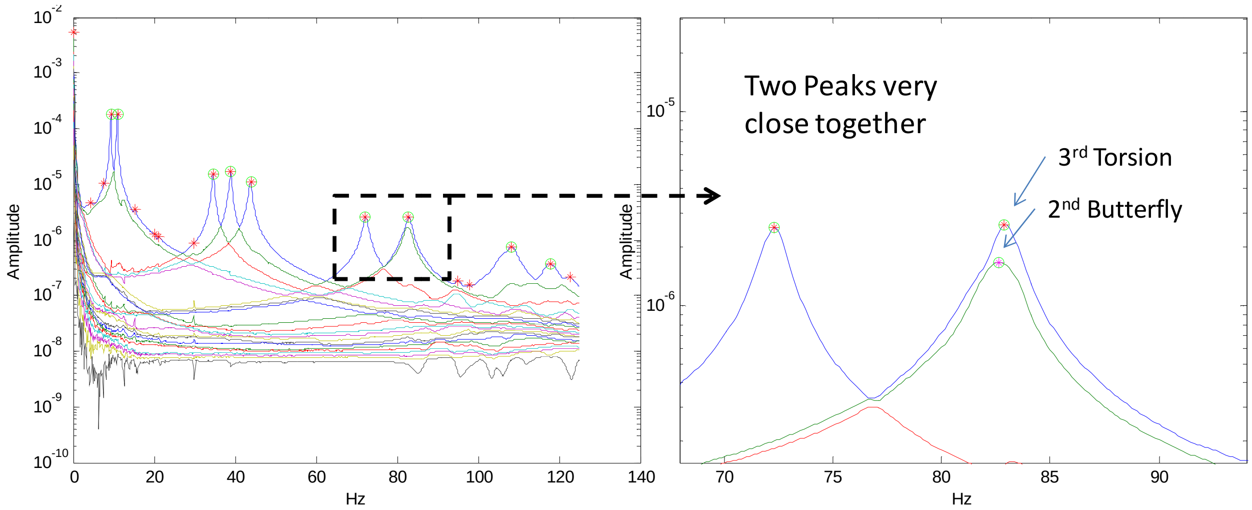

Figure 6.23: CMIF Plot – Impact Test for Damage Case #3

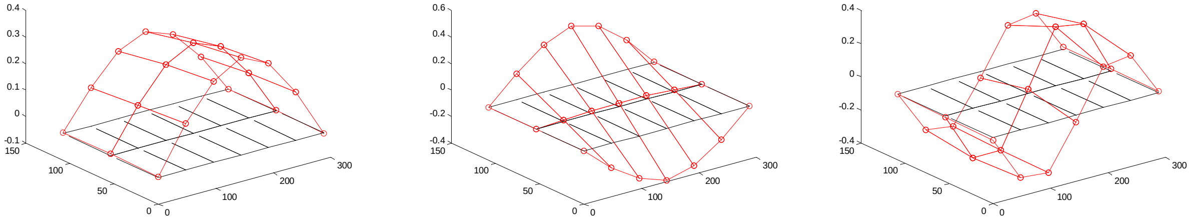

Bending Mode 1
f_1=9.336 Hz

Torsion Mode 1
f_2=10.945 Hz

Bending Mode 2
f_3=34.585 Hz

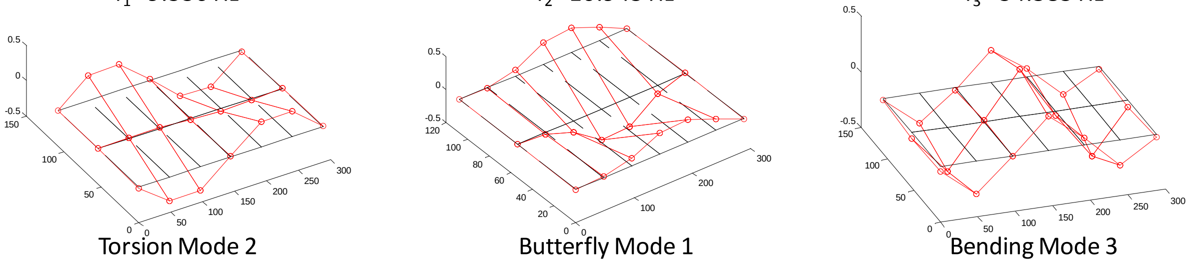

Torsion Mode 2
f_4=38.920 Hz

Butterfly Mode 1
f_5=43.797 Hz

Bending Mode 3
f_6=72.258 Hz

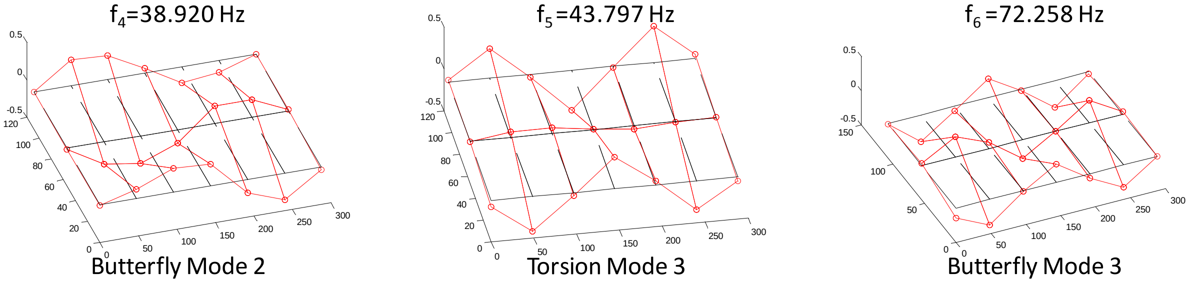

Butterfly Mode 2
f_7=82.609 Hz

Torsion Mode 3
f_8=82.923 Hz

Butterfly Mode 3
f_9=108.252 Hz

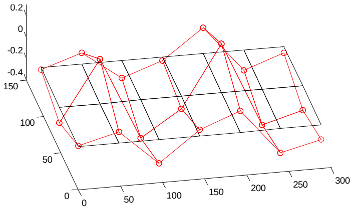

Bending Mode 4
f_{10}=117.792 Hz

Figure 6.24: Experimental Mode Shapes from Damage Case #3

The third damage scenario was modeled in SAP2000 by removing the stiffened sections at each of the nodes and replacing them with standard W8x10 sections, and also by removing the rotational fixity at the end of the transverse beam elements. Dynamic modal analysis was performed and mode shapes were found that were very similar to those found from experimental testing, yet with higher frequencies. Also, the shape of the first butterfly mode shifted towards the damage, as was seen in the experimental testing. These shapes and their corresponding frequencies can be seen in Figure 6.25.

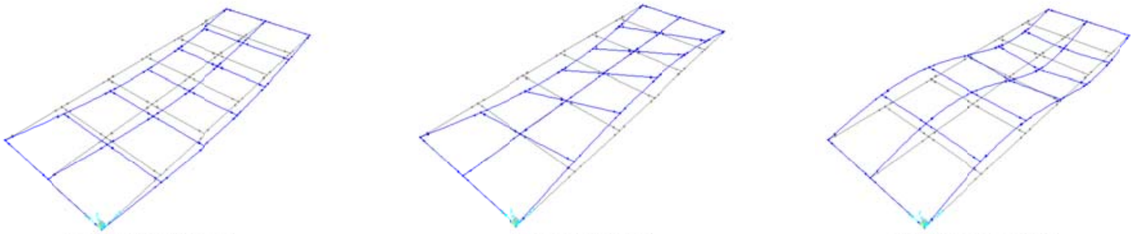

Bending Mode 1 f_1=9.024 Hz

Torsion Mode 1 f_2=9.847 Hz

Bending Mode 2 f_3=32.099 Hz

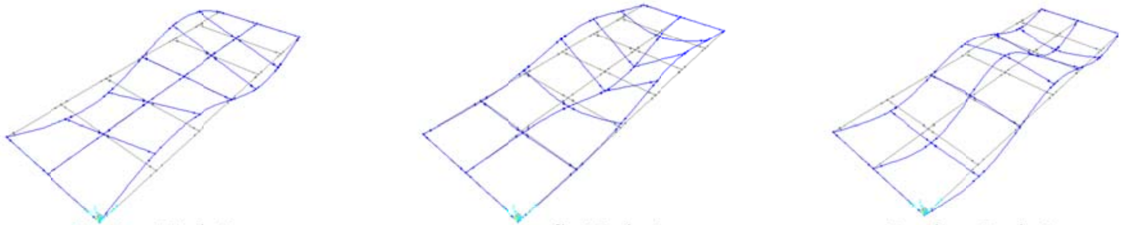

Torsion Mode 2 f_4=37.819 Hz

Butterfly Mode 1 f_5=54.454 Hz

Bending Mode 3 f_6=80.401 Hz

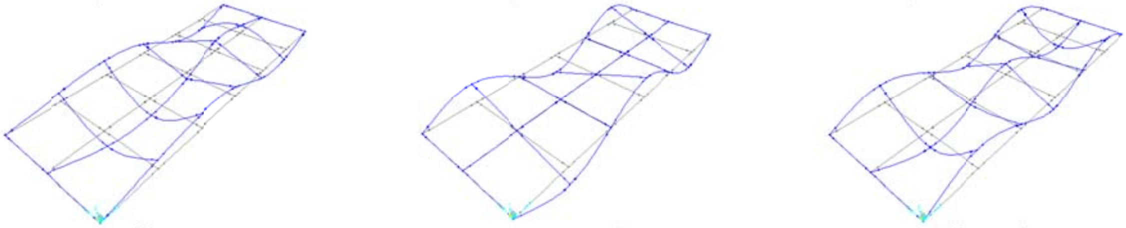

Butterfly Mode 2 f_7=83.591 Hz

Torsion Mode 3 f_8=90.653 Hz

Butterfly Mode 3 f_9=93.851 Hz

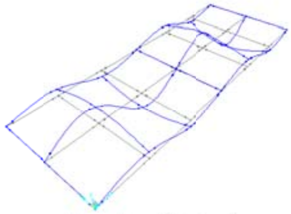

Bending Mode 4 f_{10}=119.510 Hz

Figure 6.25: Analytical Mode Shapes from Damage Case #3

The resulting CMIF from the shaker test again showed to be noisier than the impact test results, even with ten averages taken. The shaker CMIF also showed the two closely spaced modes, just as the impact CMIF did. All of the same peaks were present, including the shift in the butterfly mode. Similar mode shapes and frequencies were found from the remaining processing, and modal flexibility was found. Deflection profiles similar to ones previously presented did not easily show the change from the damage case. Therefore a different type of deflection profile was implemented, and can be seen in Figure 6.26. Instead of showing deflection by girder line, this deflection profile shows all nodes together. Node one represents location A1, node two location A2, and so on. One can notice that the deflection from one end of the girder to the other end was asymmetric, indicating the damage inflicted by the removal of the gusset plates. This resulted in a local loss of stiffness, which caused the girders to deflect farther near the 'E' and 'F' beams. This same shift was noticed in 1st Butterfly Mode, as noted earlier.

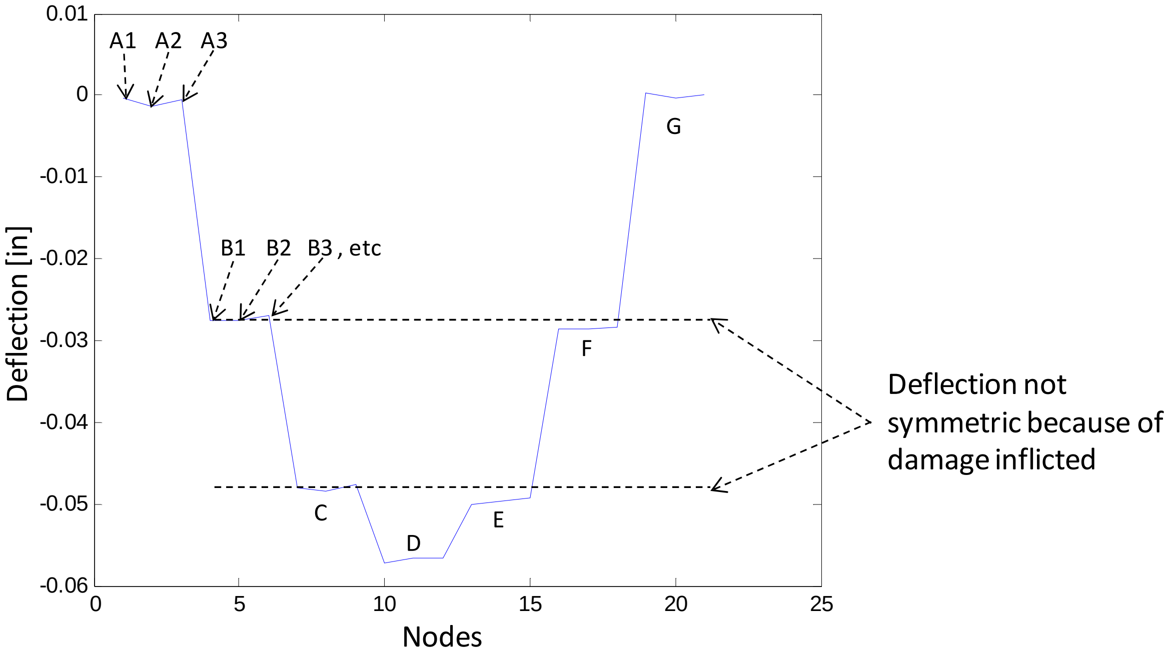

Figure 6.26: Deflection Profiles for Damage Case #3

Similar to the previous damage scenarios, a series of ambient tests were also performed on the grid while in the third damage case configuration. The quiet input provided a noisy normalized PSD, as seen in Figure 6.27. Peak picking produced comparable mode shapes and natural frequencies. When the PIRFs were created in order to use the CMIF processing techniques, the quiet input data produced a CMIF plot that did not contain 1st or 2nd butterfly modes, and both the 1st and 2nd torsion modes were replaced by 2nd bending. The CMIF plot can be seen in Figure 6.28. A sharp peak also appeared at 29 Hz which did not represent a clear mode shape.

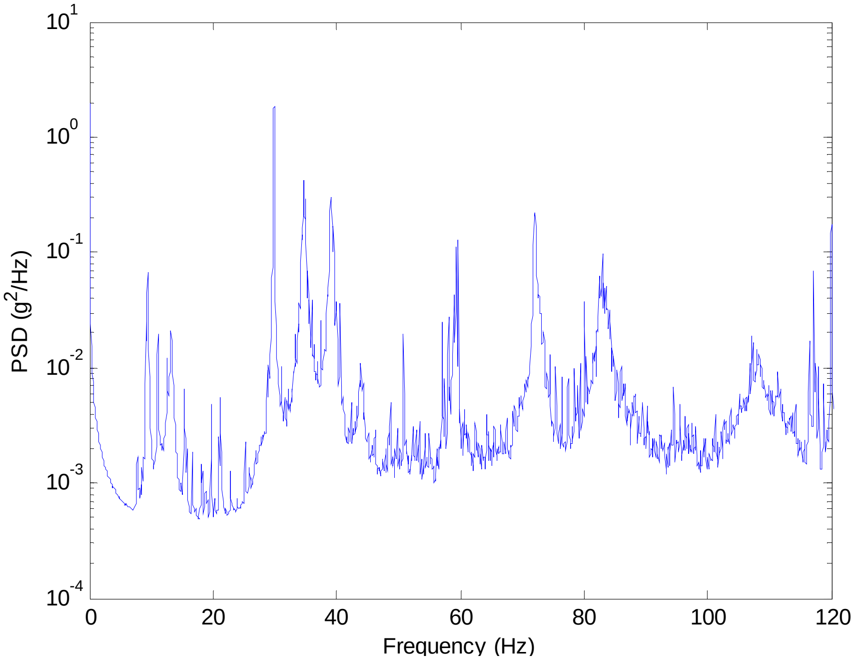

Figure 6.27: NPSD – Ambient Quiet Input for Damage Case 3

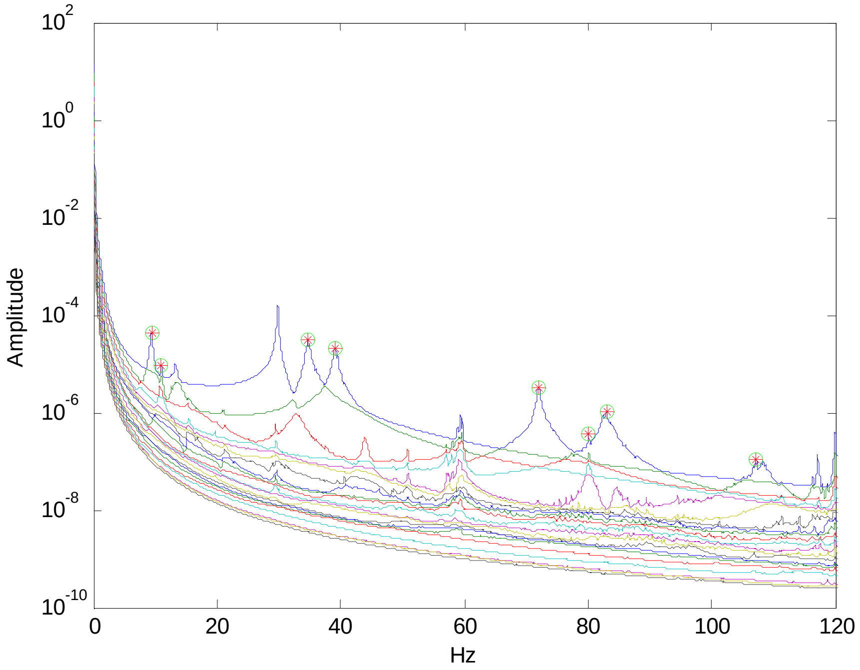

Figure 6.28: CMIF Plot – Ambient Quiet Input for Damage Case #3

The coupled ambient input provided very good excitation and clear peaks in the normalized PSD seen in Figure 6.29. These peaks produced clear natural frequencies and corresponding mode shapes. All of the modes found from the measured input tests were present in the data, with one exception. In the proximity of 82 Hz, both 2nd Butterfly Mode and 3rd Torsion Mode were found from the impact and shaker tests. As noted earlier, one benefit of the CMIF algorithm is the ability to distinguish closely spaced modes such as these. When using the PSD method, these two modes became meshed together to make a hybrid mode which contained elements of both mode shapes, and was therefore difficult to distinguish. The CMIF plot showed relatively clear peaks at all of the modes of the structure, including the two peaks near 82 Hz. The CMIF plot can be seen in Figure 6.30. In this instance, the CMIF algorithm was able to distinguish the two closely spaced modes at 82 Hz, but had trouble identifying modes at other frequencies. 1st Bending Mode was replaced by 1st Torsion Mode, 1st Butterfly Mode showed up at two locations, and several other modes were not clearly identifiable. Due to these discrepancies the CMIF algorithm was not able to identify modal parameters effectively.

Overall, the coupled shaker input provided much clearer excitation of the modes of the structure when compared to quiet excitation. Clear mode shapes and natural frequencies were found which were very comparable to the impact and shaker tests performed from the PSD method, with the exception of the two closely spaced modes near 82 Hz. The CMIF method of processing proved to be less effective in properly identifying all of the mode shapes and natural frequencies with either type of ambient input.

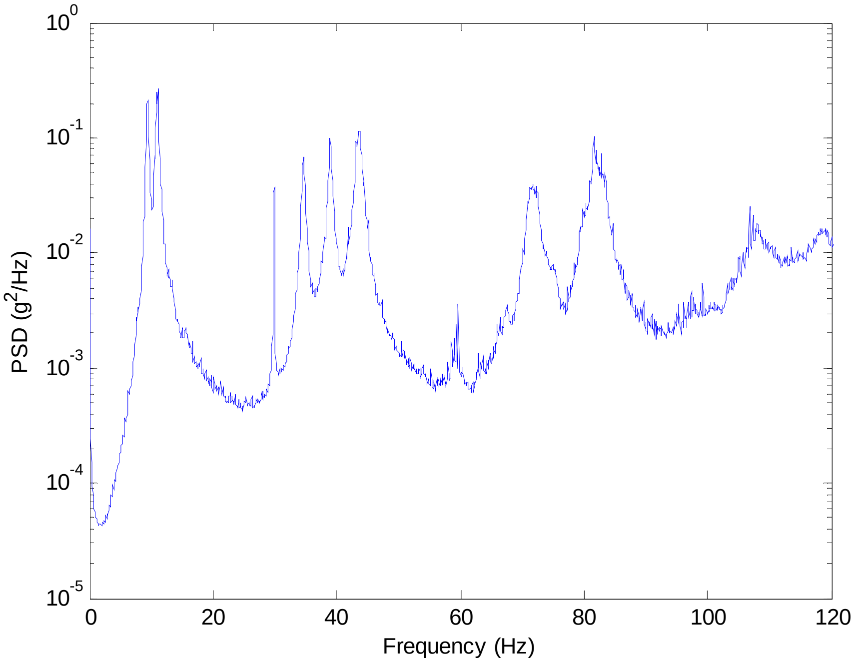

Figure 6.29: NPSD – Ambient Coupled Input for Damage Case #3

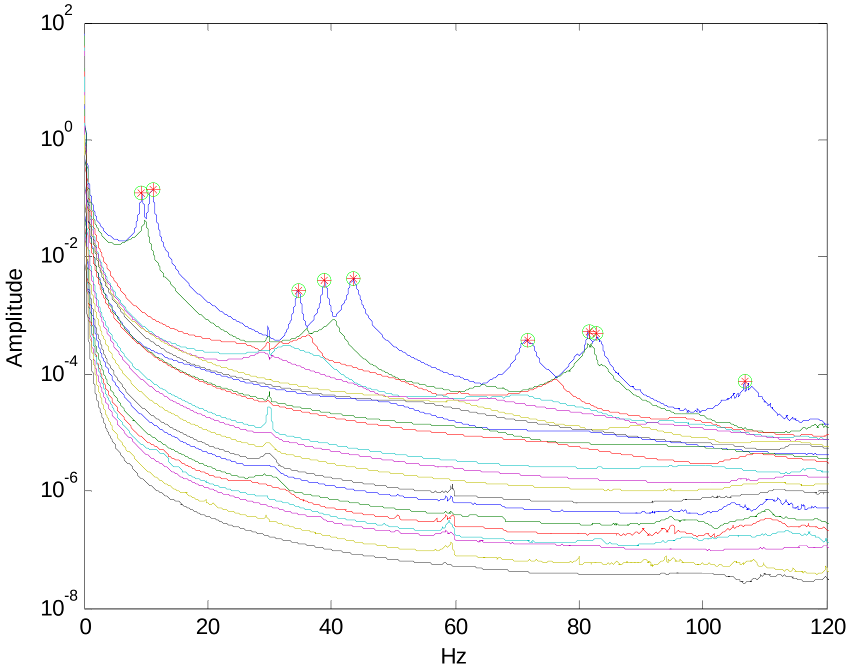

Figure 6.30: CMIF Plot – Ambient Coupled Input for Damage Case #3

6.4 SUMMARY

In order to validate the testing and analysis methods described in the previous chapters, as well as the applicability of using modal flexibility to quantify damage, three different damage scenarios were implemented on the grid model. For each damage case, several dynamic testing methods were implemented including impact testing, shaker testing, and ambient vibration testing.

The three damage cases were chosen to represent a few possible failures that could occur due to some hazard event. Damage Case #1 was the removal of a bearing support. Damage Case #2 was the removal of two transverse beams. Damage Case #3 was the removal of the gusset plates at six nodes. Each of these damage scenarios were fully tested and compared with the undamaged grid characterization and with each other.

The finite element model of the grid was also updated with each of the damage scenarios in order to validate the responses obtained through dynamic testing. In each case, the damage was able to be detected in the mode shapes and frequencies of both the FE model and the experimental model. In general, the natural frequencies found from the FE model were slightly higher than the frequencies found experimentally, with the margin of difference increasing with higher modes. Table 6.1, Table 6.2, and Table 6.3 summarize the natural frequencies found from each damage scenario. From these tables, one can clearly see that all three experimental methods resulted in nearly identical natural frequencies, showing agreement and confidence in the testing methods. The resulting mode shapes obtained at each of the natural frequencies (shown previously) displayed much similarity between testing methods. Natural frequencies and mode shapes were able to be qualitatively identified and located from the damage in the structure.

Table 6.1: Natural Frequencies from Damage Case #1

		Natural Frequencies [Hz]				
Mode	*Mode Description*	*Undamaged Grid*	*Impact Test*	*Shaker Test**	*Ambient Test*	*Analytical Model*
1	1st Bending	9.570	8.710	8.741	8.870	9.0238
2	1st Torsion	10.958	10.588	10.633	10.742	9.8467
3	New Mode 1	-	28.943	29.038	29.297	32.099
4	2nd Bending	34.714	33.982	34.331	-	-
5	2nd Torsion	38.996	37.342	38.223	36.051	37.819
6	New Mode 2	-	47.675	47.799	47.689	54.454
7	3rd Bending	72.831	72.915	73.759	73.731	80.401
8	1st Butterfly	80.058	80.053	80.091	79.590	83.591
9	3rd Torsion	82.695	86.237	86.259	86.507	90.653
10	2nd Butterfly	88.324	88.862	-	88.704	93.851
11	3rd Butterfly	-	112.02	113.60	113.36	119.51

* From PSDs with Coupled Input

Table 6.2: Natural Frequencies from Damage Case #2

		Natural Frequencies [Hz]				
Mode	*Mode Description*	*Undamaged Grid*	*Impact Test*	*Shaker Test**	*Ambient Test*	*Analytical Model*
1	1st Bending	9.570	9.750	9.819	9.928	9.900
2	1st Torsion	10.958	11.314	11.325	11.393	10.593
3	2nd Bending	34.714	34.664	34.721	34.831	36.229
4	2nd Torsion	38.996	38.823	38.969	38.900	39.626
5	New Mode 1	-	59.793	58.601	58.594	-
6	1st Butterfly	80.058	64.088	63.995	63.477	69.572
7	3rd Bending	72.831	77.141	77.231	76.904	86.150
8	3rd Torsion	82.695	85.964	86.103	86.426	91.113
9	2nd Butterfly	88.324	88.617	88.383	88.379	92.960
10	3rd Butterfly	-	108.84	109.22	109.05	115.56
11	4th Bending	-	116.58	-	117.18	130.84

* From PSDs with Coupled Input

Table 6.3: Natural Frequencies from Damage Case #3

		Natural Frequencies [Hz]				
Mode	*Mode Description*	*Undamaged Grid*	*Impact Test*	*Shaker Test**	*Ambient Test*	*Analytical Model*
1	1st Bending	9.570	9.336	9.372	9.440	9.024
2	1st Torsion	10.958	10.945	10.944	11.068	9.847
3	2nd Bending	34.714	34.585	34.648	34.668	32.099
4	2nd Torsion	38.996	38.92	39.010	38.981	37.819
5	1st Butterfly	80.058	43.797	43.759	43.701	54.454
6	3rd Bending	72.831	72.258	71.750	72.266	80.401
7	2nd Butterfly	88.324	82.609	82.31	82.845	83.591
8	3rd Torsion	82.695	82.923	83.076	82.845	90.653
9	3rd Butterfly	-	108.25	107.85	106.77	93.851
10	4th Bending	-	117.79	-	118.49	119.51

* From PSDs with Coupled Input

The modal flexibility matrix was represented by deflection profiles, and these deflections were plotted for each type of input in order to compare pre- and post- damage. Figure 6.31 shows the compiled deflection profiles for all 21 nodes for the finite element model. It can be seen that the second damage case did not change the flexibility in any noticeable fashion. It can also be seen that the bearing removal from the first damage case was noticeable different from the undamaged deflection profile, specifically that the third girder line deflected much more than the other two girder lines. The resulting loss from Damage Case #3 was also evident since the entire profile deflected more than the undamaged profile.

Figure 6.32 shows the compiled deflection profiles for all 21 nodes for the impact tests performed. It is clear that all profiles were different, pointing to the different damages imposed on the model. Between the three different damage cases, the flexibility increased from Damage Case #1 to Damage Case #3, as would be expected. The loss of bearing support at location G3 was very evident since girder #3 near the support deflected much more than all other cases. Interestingly, all three damage profiles showed to be less flexible (more stiff) than the undamaged model. This goes against the notion that the damage inflicted would reduce stiffness, and may show that the impact testing method is less accurate than the shaker input.

Figure 6.33 shows the compiled deflection profiles the shaker tests performed. As with the impact data, the three different damage cases were very evident, yet began as slightly more stiff than the undamaged model. When compared to the SAP2000 model, the deflection profiles from the shaker tests showed to be generally more representative than the impact tests. Damage Case #2 was very close to the undamaged case, as with the analytical model. Damage Case #1 showed to be less flexible at girders #1 and #2, and more flexible at girder #3. The analytical model showed girder #1 to be less flexible, and both girders #2 and #3 to be more flexible than the undamaged case. Damage Case #3 showed the entire structure to be more flexible, which seems reasonable given that the gusset plates were removed, thus reducing the global stiffness.

Overall, it is difficult to draw a concrete conclusion about the different tests. The impact test showed Damage Case #1 very well, but was stiffer in all cases than the undamaged test. The shaker tests showed similar results to the analytical model, with the exception of Damage Case #1, which was slightly less representative in its shape than the impact test. Fortunately, both types of inputs were accurately able to identify the damage in a qualitative manner, by comparing the mode shapes and frequencies between the damaged case to the undamaged case. Between these two inputs, the shaker test proved to be the best overall.

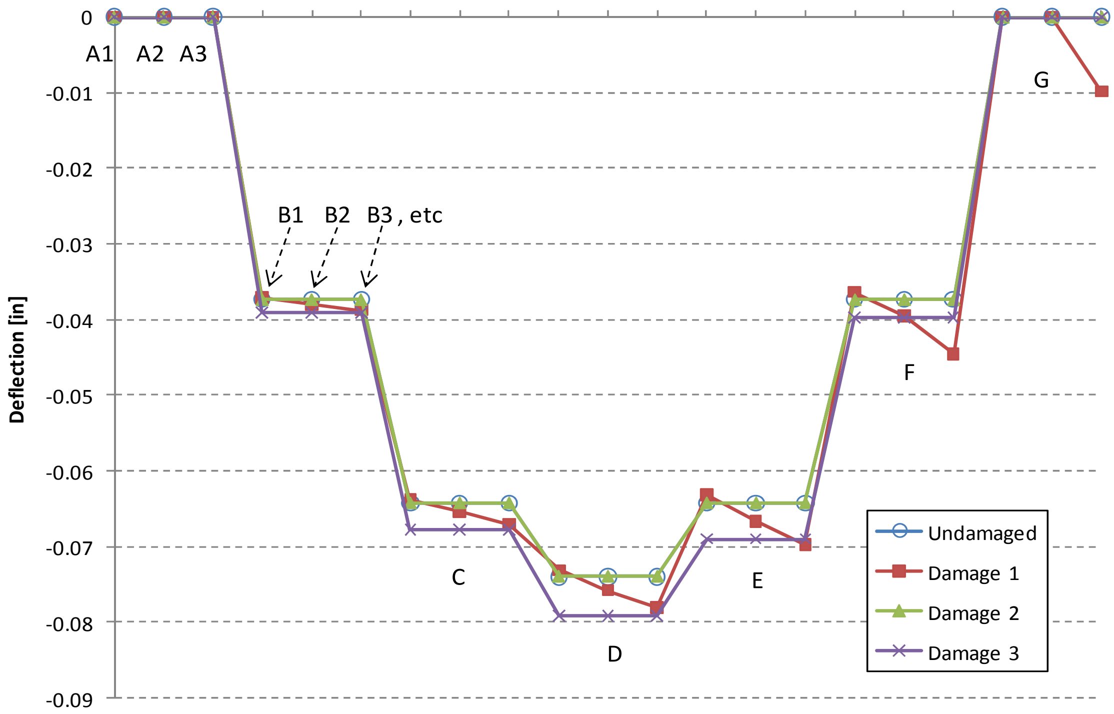

Figure 6.31: Deflection Profiles from SAP2000 Model

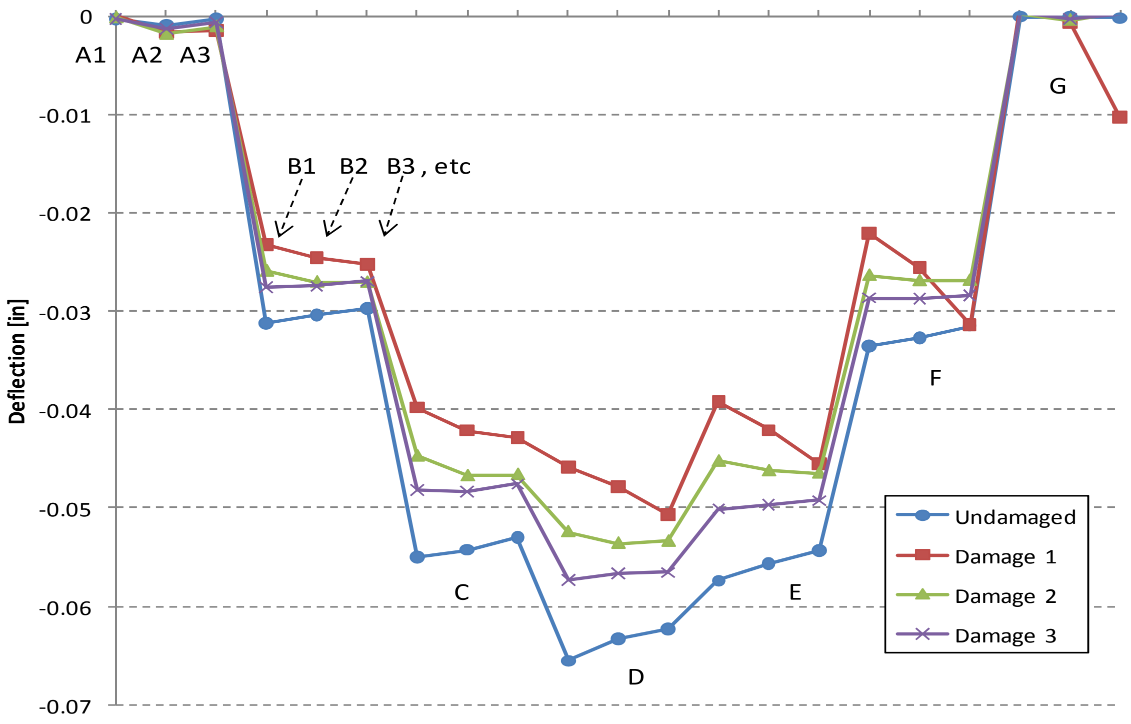

Figure 6.32: Deflection Profiles from Experimental Impact Tests

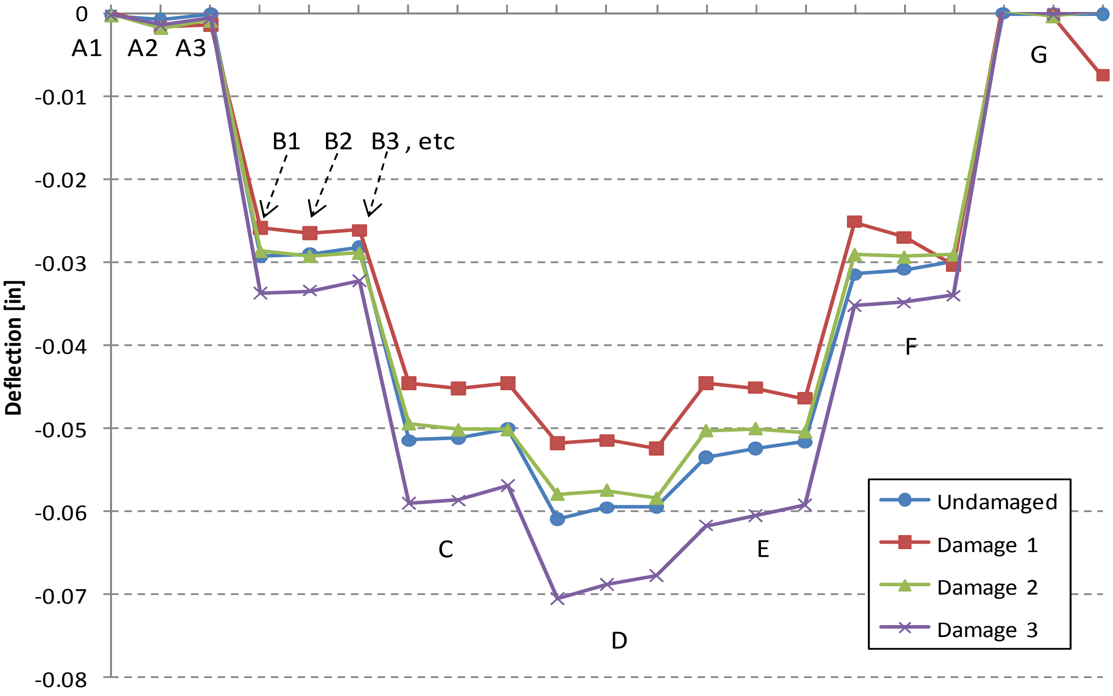

Figure 6.33: Deflection Profiles from Experimental Shaker Tests

Ambient testing using PSDs to find mode shapes and frequencies provided an accurate characterization of the structure with all damage scenarios. The problem with only using PSDs and ambient data was that no scaling could be found in order to find a scaled modal flexibility. By using correlation functions, one was able to produce a pseudo impulse response function, and was then able to use the CMIF algorithm to find a pseudo modal flexibility. When implemented on the grid model with the damage cases, a representative modal flexibility could not be found. The CMIF algorithm tended to "smear" the data, and provided only one mode shape per frequency line. This smearing effect resulted in several of the mode shapes not appearing. In fact, in each damage case, one mode shape would show up at several locations, thus dominating the response found. This dominant mode shape pointed to the damage inflicted on the grid, but using this mode shape only to identify and quantify damage was not the most robust method. Overall, with ambient data the CMIF algorithm was ineffective at picking mode shapes and providing flexibility, but all mode shapes and natural frequencies were able to be found using the PSD peak picking method.

When comparing the input types used in ambient testing, the coupled shaker input provided a much clearer excitation of the modes of the structure than quiet excitation. Clear mode shapes and natural frequencies were found and were very comparable to the impact and shaker tests performed. Since the testing was done in a quiet laboratory setting, it is expected that adequate excitation of an in-service bridge would be possible with using only ambient noise from wind, traffic, noise, etc. This excitation could be used with the PSD peak picking method to adequately identify damage from some hazard event.

7. LOAD RATING

Thus far, all of the comparisons between modal flexibility cases have been qualitative comparisons. Several of the figures were represented as deflection profiles in order to facilitate easy comprehension of the complicated matrix type results. In order to better serve engineers, bridge owners, transportation officials, and emergency management personnel, a more quantitative assessment of the state of a bridge subject to a hazard event was needed. In order to achieve this, a modification to the bridge rating was pursued.

Load rating of bridges is performed according to "The Manual for Bridge Evaluation," published by AASHTO (2008). Section 8.8 of the manual presents methods to evaluate a modified load rating through static load testing, and encompasses two cases: diagnostic load tests and proof load tests. In a proof load test the structure is tested with a given loading truck, and if no undesired effects are noted, that load becomes the new proven load rating. The proof loads provide a lower bound on the load rating capacity of the structure (AASHTO, 2008). AASHTO recommends that the loads be increased incrementally in order to verify linear-elastic behavior. In a diagnostic test, the full capacity of the bridge is not tested by a corresponding load. Instead, a load is applied to the bridge, and the actual measured strains are recorded corresponding to the location of the load. This method requires both strain measuring devices and a loading truck. The measured strains are then compared to the theoretical strains due to the same loading at the same location, and an adjustment factor, K, is found. This adjustment factor is then multiplied by the analytical load rating to provide a new adjusted load rating that can be greater than, equal to, or less than the analytical load rating.

It should be noted that either of the static load rating procedures prescribed by AASHTO would take a great deal of time to implement. Time is a critical concern for emergency response and recovery operations following hazard events. Developing load capacity ratings by static load testing of a bridge or numbers of bridges affected by a hazard event requires both expertise in bridge evaluation and testing, and heavy trucks must be brought to each test bridge. Given these logistical constraints, establishing the load capacity ratings for bridges through static load testing would not be the optimal approach for supporting time-sensitive emergency response and recovery operations.

Given that static load testing was not ideal for rapid evaluation, dynamic characterization was proposed. Section 8.4 (AASHTO, 2008) provides allowance for dynamic testing methods for bridge testing, but gives no clear guidance as to how to acquire or interpret the results. It has been shown previously that the dynamic characterization of a structure is directly related to its stiffness and mass properties, and thus provides insight into any damage induced to the structure. In this research project, a method was proposed to utilize the properties identified from dynamic testing to develop a load rating modification factor. This proposed method is analogous to the static diagnostic load testing method outlined by AASHTO.

7.1 OVERVIEW OF LOAD RATING

An adjusted load rating is achievable through the steps outlined in AASHTO's "The Manual for Bridge Evaluation," (2008) and is further explained in a report from the National Cooperative Highway Research Program (NCHRP & Lichtenstein, 1998). The flowchart shown in Figure 7.1 provides an overview of the steps required to obtain the modified load rating, and is derived from the NCHRP report. In a static diagnostic load test, the measured strains are compared to the theoretical strains. Therefore, in order to obtain the modification factor, the strains were needed from the dynamic tests performed. This was achieved through the creation and manipulation of the modal flexibility matrix. The details of each step are further described in the following sections.

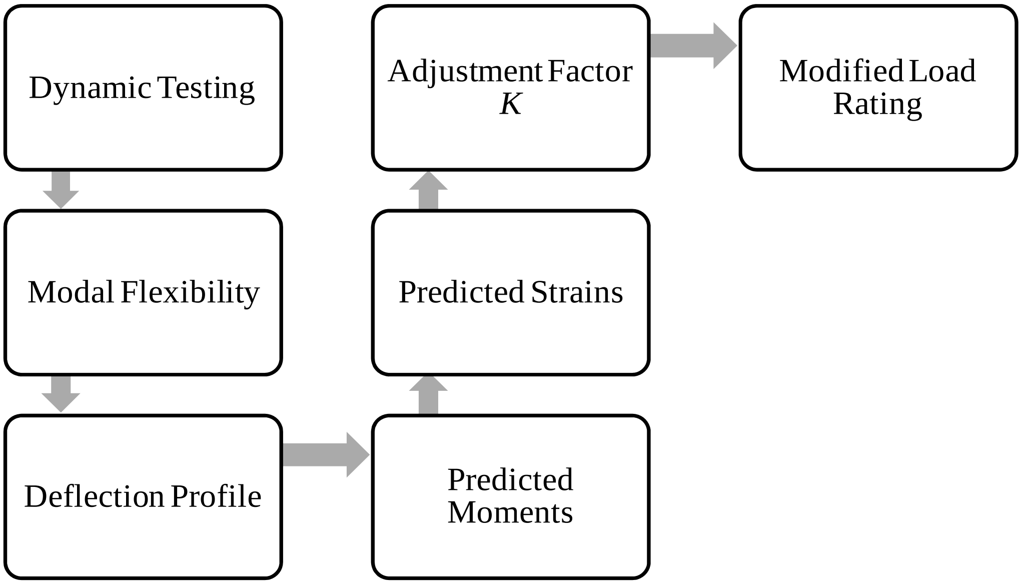

Figure 7.1: Modified Load Rating by Dynamic Testing

7.1.1 Dynamic Testing

Dynamic testing was performed using a variety of methods which included both measured and unmeasured inputs. The implementation and results of these different dynamic tests were presented and explained in previous chapters.

7.1.2 Modal Flexibility

As explained in Chapter 3, modal flexibility can be found from dynamic testing. Each of the dynamic tests performed for the undamaged and damaged cases of the grid model resulted in a modal flexibility matrix which represented the flexibility of the structure. In order to attain a modified load rating, the strain in the member due to a load was needed. Therefore a correlation between modal flexibility and strain was required, and this was found through Euler-Bernoulli beam theory. This is discussed further in the following sections.

7.1.3 Deflection Profiles

The Euler-Bernoulli beam equation is shown as follows:

$$\frac{\partial^2}{\partial x^2}\left(EI \frac{\partial^2 y(x)}{\partial x^2} \right) = q(x) \tag{7.1}$$

where

y(x) = deflection of element with respect to x.

x = distance from support.

q(x) = applied distributed load with respect to x.

EI = flexural rigidity properties of element.

This equation can then be reduced and rearranged to the following:

$$\frac{\partial^2 y(x)}{\partial x^2} = \frac{M(x)}{EI} \tag{7.2}$$

where

M(x) = the moment in the beam at location x.

In order to find moment, from which one can find strain, deflection profiles were found from the modal flexibility matrix. These deflection profiles were obtained by multiplying the flexibility matrix by a virtual load vector, resulting in the displacement of each node due to the virtually applied load.

$$\begin{bmatrix} f_{1,1} & f_{1,2} & \cdots & f_{1,j} \\ f_{2,1} & f_{2,2} & & \vdots \\ & & \ddots & \vdots \\ f_{i,1} & \cdots & \cdots & f_{i,j} \end{bmatrix} * \begin{bmatrix} p_1 \\ p_2 \\ \vdots \\ p_j \end{bmatrix} = \begin{bmatrix} u_1 \\ u_2 \\ \vdots \\ u_i \end{bmatrix} \tag{7.3}$$

where

flexibility coefficient $f_{i,j}$ is the displacement at *i* due to a unit load at *j.*

Deflections u_1 through u_i, represent the displacements of DOF1 through DOF*i*, respectively, due to the applied load vector [*p*]. Several of these deflection profiles have been shown in the previous chapters, and it was shown that the deflections produced from the flexibility matrix closely approximated the actual deflections, with the differences associated with modal truncation.

In order for Eq. (7.2) to be valid, a distributed load must be applied to the beam as denoted by *q(x)* in Eq. (7.1). Since the representation of each girder is discretized as several nodes, applying a true distributed load is not possible. With several closely spaced nodes, a close approximation of a distributed load is possible. As the number of nodes decrease, the approximation becomes less accurate. Consequently, the load vector applied to the grid model was a uniform load at every node in the girder, to as closely as possible represent a distributed load.

7.1.4 Predicted Moments

A 4th degree polynomial trend line was fit to the displacement profile of the beam with the largest deflection due to a given load case. The beam with the largest deflection was selected because the largest deflection would indicate the largest internal moment. The trend line, *y(x)*, provided a very close representation of the deflection of the beam. By taking the 2nd derivative of this function with respect to x, the quantity *M(x)/EI* was found as per Eq. (7.2). The right hand side of this equation contains terms for both bending moment and flexural rigidity, which is a product of the section and material properties of the beam. If damage were to occur to a bridge due to some hazard event, the change in stiffness would not be known. Being able to find the moment with the flexural rigidity allowed the uncertainty related to the change in stiffness to be bypassed since this is already incorporated in the modal flexibility matrix. The bending moment and flexural rigidity terms could be translated into bending strain at the critical section, a key component of the modification factor.

7.1.5 Predicted Strains

Bending strain at any point on the cross section can be readily obtained from the bending moment at a particular section from basic mechanics of materials principles. Bending stress, σ, is related to moment, M through the following expression:

$$\sigma = \frac{M * c}{I} \tag{7.4}$$

where

c = perpendicular distance to point of interest from neutral axis of the cross section.

I = second moment of area of cross section.

Using Hooke's Law, the relationship between bending stress and strain, ε, is:

$$\sigma = \varepsilon * E \tag{7.5}$$

Combining Eq. (7.4) and Eq. (7.5), the bending strain then becomes:

$$\varepsilon = \frac{\sigma}{E} = \frac{M * c}{E * I} \tag{7.6}$$

Since the *M/EI* term was found earlier from the deflection profiles, that value could simply be multiplied by the distance to edge of girder, *c*, and the maximum strain found. This strain was then used to find the adjustment factor, *K*.

7.1.6 Adjustment Factor K

The previous steps discussed were important because they linked the deflection found from modal flexibility to the strain present in the girder member. According to the NCHRP report (NCHRP & Lichtenstein, 1998), the adjustment factor *K* is given by:

$$K = 1 + K_a K_b \tag{7.7}$$

where

K_a accounts for the benefit or detriment derived from the load test.

K_b accounts for the understanding of the load test results when compared with those predicted by theory, the type and frequency of follow-up inspections, and failure mode consideration.

It should be noted that there is risk associated with extrapolating diagnostic test results to levels higher than actually applied to the structure. Validation of these methods must be undertaken in order to prove the effectiveness of generating the adjustment factor *K* from dynamic test data.

K_a was the component of Eq. (7.7) that was generated from the dynamic test results, with K_a defined as follows:

$$K_a = \frac{\varepsilon_c}{\varepsilon_T} - 1 \tag{7.8}$$

where

ε_T = maximum strain during load test.

ε_c = corresponding theoretical strain due to the loading applied and its position, in order to obtain ε_T.

In the laboratory setup the strain, ε_T, due to an implemented damage scenario was found from Eq. (7.6), while the strain, ε_c, was found from the undamaged case with the same loading scenario. In a real world application to a bridge, the strain, ε_T, would be found from testing after a hazard has occurred, and the strain, ε_c, would be found from the analytical model on file with the same loading scenario.

The K_b factor is a multiplicative combination of three factors tabulated in the NCHRP report, but not reproduced here. Assuming that the deflections would increase in the linear elastic range and that the load applied could be extrapolated to a larger value, it was chosen that $K_{b1} = 0.8$. Assuming that a follow-up, in depth inspection would occur within one year, $K_{b2} = 1.0$. Finally, assuming fatigue would not control, and that redundancy may have been lost due to the hazard, $K_{b3} = 0.9$. These values would need to be chosen for each structure and each type of hazard event individually, but were chosen as noted here for illustrative purposes only. Multiplying the various values together gives $K_b = 0.72$.

7.1.7 Modified Load Rating

If no test were performed, $K = 1$, but generally after a load test $K \neq 1$. If $K > 1$, then some benefit would be realized from the load test, proving that the structure could hold more than originally rated for as is often the case for diagnostic static load tests. If $K < 1$, then actual response of the bridge would be worse than originally rated for, and may be the case for an unknown damage event.

The modified load rating is therefore:

$$RF_T = RF_c * K \tag{7.9}$$

where

RF_T = the modified load rating based on the diagnostic test.

RF_c = the analytical load rating based on prior calculations.

The analytical load rating is assumed to be on record for the bridge of concern. This load rating, multiplied by the modification factor *K*, would produce a new modified load rating that emergency response and recovery personnel could use to determine whether a bridge was safe to use or not.

7.2 ADJUSTMENT FACTOR FOR ANALYTICAL DAMAGE CASES

In order to validate the previously described processes, a numerical example was explored. A uniformly distributed load of 0.1 k/ft was applied to a W8x10 beam that was 25 ft long. The deflections and moments at seven locations due to the applied load were found from the closed form deflection equations available in the AISC Manual of Steel Construction (AISC, 2005). A 4th degree polynomial trend line was fit to the deflection data, and the second derivative of the polynomial was taken in order to represent the moments. These were compared to the closed form solution for the moments, and were found to match them exactly. The same analysis was performed a second time, with the load being changed to a 1 kip point load in the center of the beam. The actual moment variation due to this type of loading linearly increases to the maximum, at the midpoint, then linearly decreases to zero at the support. It was found that the moment found from the displacement curve contained negative moment at the supports, while the moment at mid-span was around 15% off. This can be seen in Figure 7.2. It was shown that as the number of nodes in the beam decreased, the load applied became less like an actual distributed load, and therefore the moment calculated from the deflection curve decreased in accuracy.

The process was further validated by evaluating the SAP2000 model of the grid. A uniformly distributed load was placed on the structure in the form of equal loads at each node, and static analysis was performed. Both displacements and moments were found from the static analysis. The displacements were plotted for only the nodes where the longitudinal beams intersected the transverse beams, since these were the nodes where accelerometers were placed on the experimental model. A trend line was fit to the displacements, and the moments were found as described earlier. These displacements were then compared with the moments found from the static analysis in SAP2000, as can be seen in Figure 7.3. The differences in moments were found to be around 11%, with the error associated with the fact that the distributed load was idealized as a series of point loads.

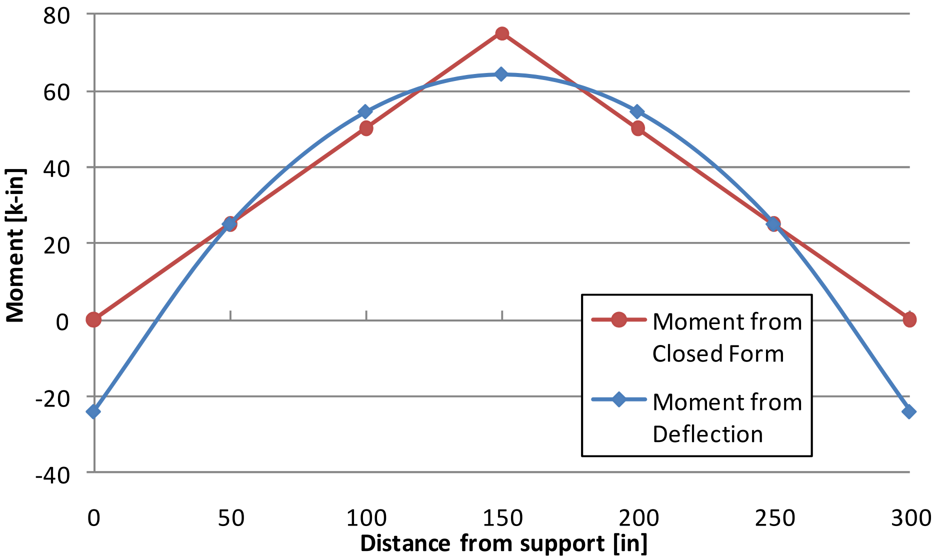

Figure 7.2: Moment Comparison for Simple Beam with Point Load

The same procedure was implemented for the three damage scenarios, and the moments computed from the displacement curve compared to the moments produced in SAP2000. It was found that the difference in moments varied from 4% to 11%. This difference in moments arose from discretizing the distributed load at the nodes. Therefore, it was proposed that a confidence factor, ϕ, be set to 1.15 and multiplied by the maximum moment found from the displacement in order to amplify the computed response. By amplifying the response, one can be more certain that the moment used to find the modification factor is within reason. This amplified moment would further reduce the modification factor K, thereby adding a level of safety to the analysis. With further study, this confidence factor may be updated and changed.

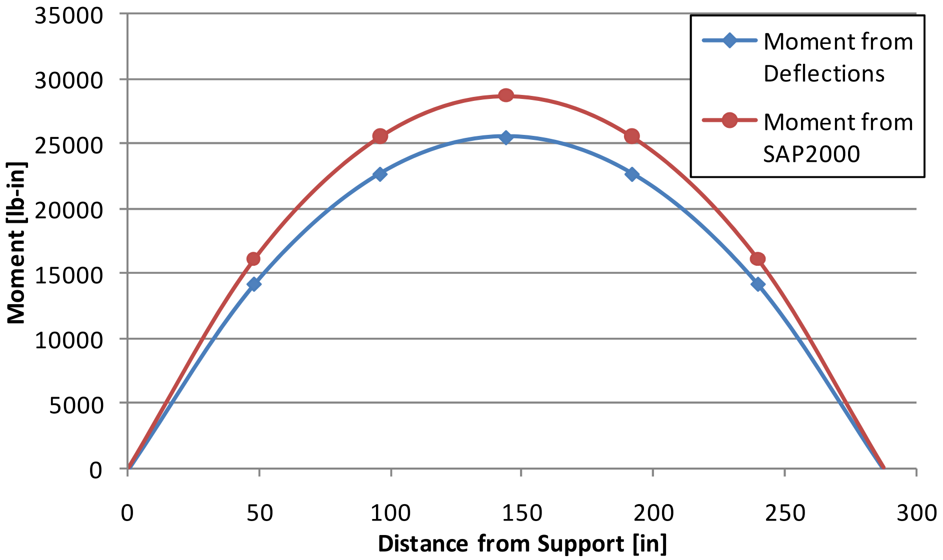

Figure 7.3: Moment Comparisons of Undamaged Analytical Model

7.2.1 Damage Case #1

Damage Case #1 did not greatly affect the deflection profile of girder #1, but did greatly affect girder #3 (see Figure 6.31). This is understandable since the support was removed at location G3, thus allowing the beam to sag some at the end with it being held up by the contribution of the surrounding members. The deflection of each node due to a uniform load placed on girder #3 was found to cause the most deflection. The deflection points on the girder were taken and a 4th degree polynomial trend line was fitted to the data. From this data, the M/EI term was found as a function of x, and is shown in Figure 7.6. The maximum value from this figure was found to be 2.8503E-5 in^{-1}. When multiplied by ϕ=1.15, this value became 3.2778E-5 in^{-1}. Since the W8x10 section has a c value of 3.945 in., the strain ε_T was found to be 129.31 microstrain. The strain calculated from the undamaged analytical model, ε_c, was found to be 126.81 microstrain from the same applied load at the same location. These values are summarized for this case and the other cases in Table 7.1. From these values, the modification factor K was found to be 0.986. This value would indicate a 1.4% loss of stiffness to be applied to the posted/recorded load rating, showing a very insignificant change. The contributing stiffness of the nearby members was able to adequately support the unsupported corner of the structure. Since the structure was made of relatively stiff members with short distances between nodes, this seems reasonable.

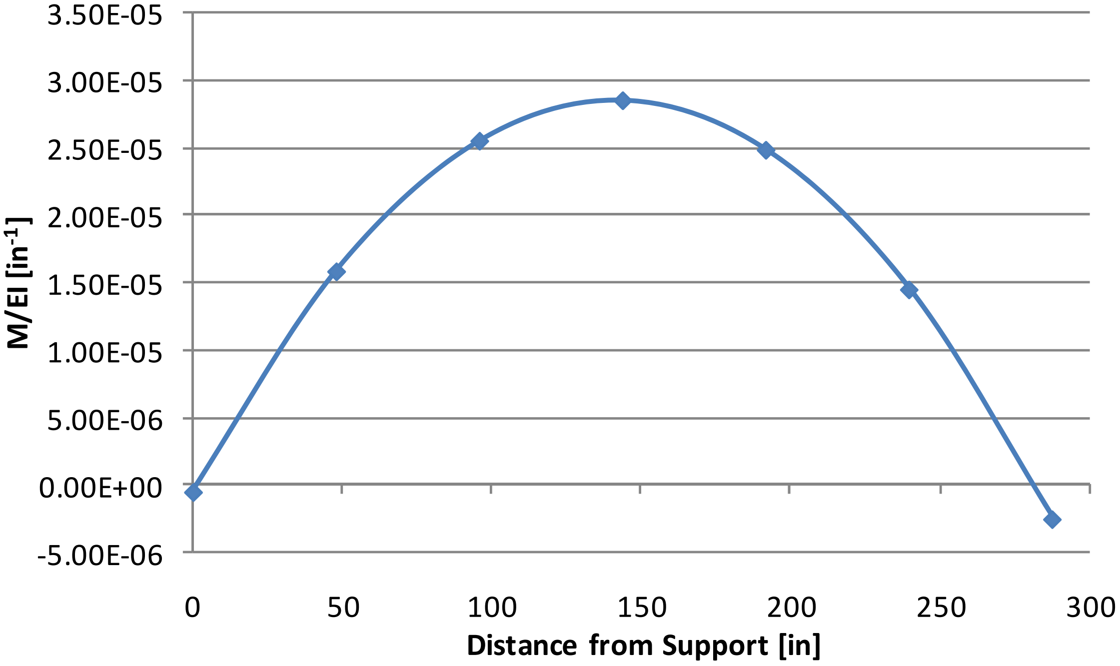

Figure 7.4: M/EI for Analytical Damage Case #1

7.2.2 Damage Case #2

Damage Case #2 (the removal of transverse beam D) did not noticeably change the deflection profile of the grid model, as shown by Figure 6.31. The deflection of each node due to a uniform load placed on an edge girder was found. The girder with the load deflected the most, with the middle girder deflecting much less, and the far girder arching upwards from the load. From the trend line of the deflection, the M/EI term was found as a function of x, and is shown in Figure 7.6. Following the previously described procedures, the modification factor K was found to be 0.980 (Table 7.1). This value would indicate a 2% loss of stiffness to be applied to the posted/recorded load rating, and is not a very significant change which is understandable given the small damage that was implemented.

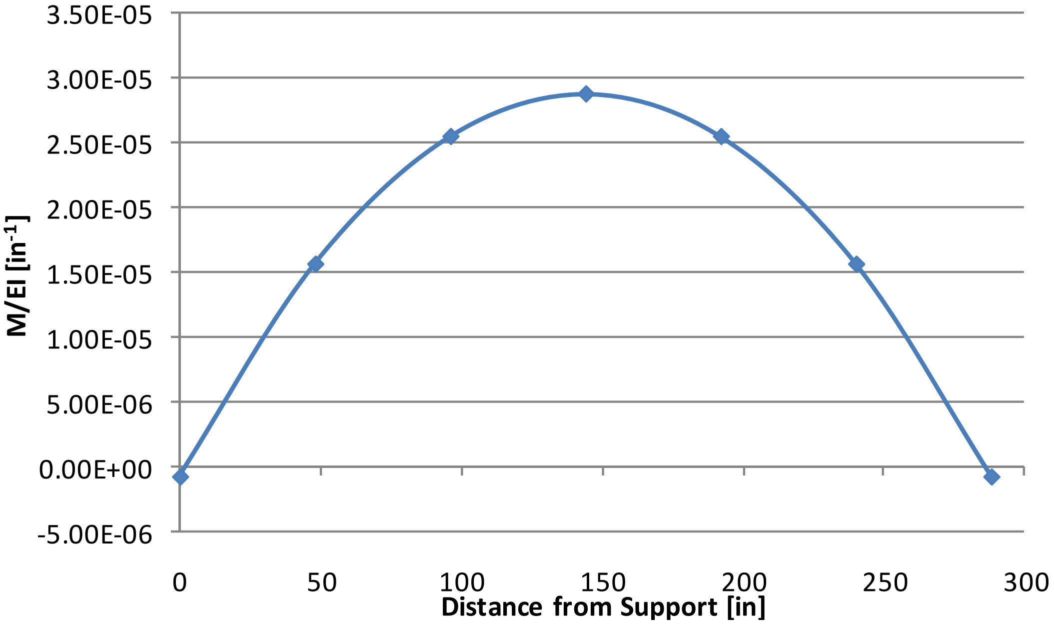

Figure 7.5: M/EI for Analytical Damage Case #2

7.2.3 Damage Case #3

Unlike the two previously described damage scenarios, Damage Case #3 (the removal of several gusset plates) affected the flexibility very noticeably. As seen in Figure 6.31, the damaged deflection profile deflects much more than the undamaged case, as would be expected with such a loss of stiffness. The modification factor *K* was found to be 0.915 (Table 7.1). This value would indicate a 9.5 % loss of stiffness to be applied to the posted/recorded load rating. This is a much larger loss of stiffness than the other two damage scenarios. This reduction in stiffness is acceptable given the reduction in stiffness from the damage inflicted and the resulting larger deflections seen in the girders.

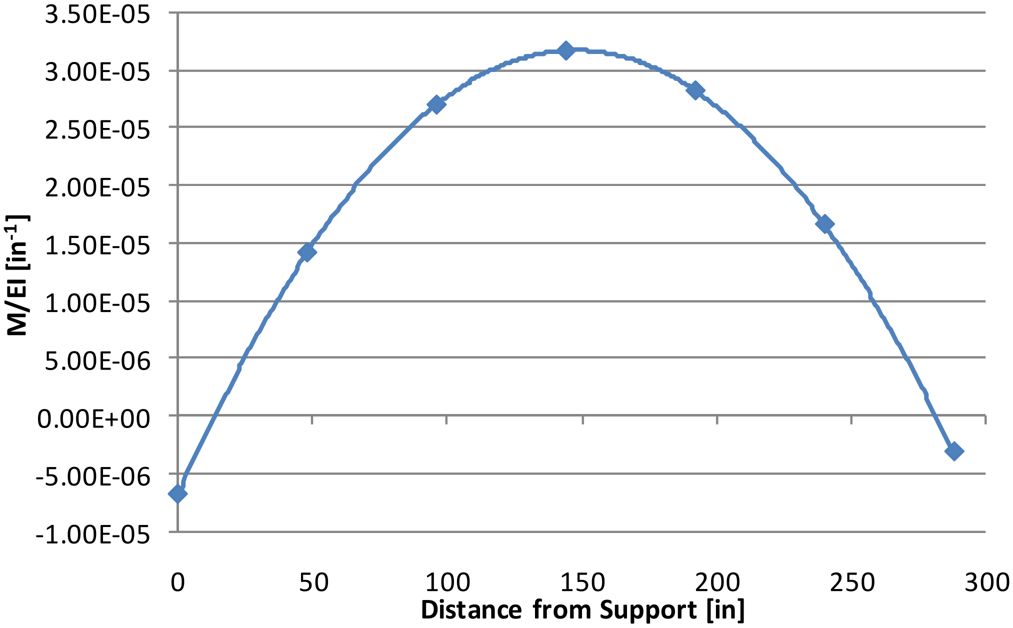

Figure 7.6: M/EI for Analytical Damage Case #3

7.3 ADJUSTMENT FACTOR FOR EXPERIMENTAL DAMAGE CASES

The process described in the previous sections for obtaining a load rating adjustment factor, *K*, was also applied to the experimentally obtained data. Given that impact testing proved overall to be less reliable than shaker testing, only the shaker testing results were used to find the load rating adjustment factor.

7.3.1 Damage Case #1

Referring back to Figure 6.33, it can be seen that the damage induced by Damage Case #1 did not closely reflect the damage simulated by the analytical model shown in Figure 6.31. That being the case, the analysis still was performed on the shaker test data since the impact test data was not representative of the damage either.

Three different loading scenarios were virtually applied to the modal flexibility matrix, with each scenario consisting of a distributed load applied to one girder only. The loads applied to the edge girders caused significantly more deflection than the load applied to the center girder. This is understandable since the load applied to the center girder is also distributed to the two edge girders through the stiff transverse beams. The controlling case was found to be a distributed load applied to girder #3, which is also understandable given that the support was removed from that girder. *M/EI* was found as a function of x, and is shown in Figure 7.7.

The maximum value (2.0818E-5 in^{-1}) was found to occur at a distance of 147.99 in. from the support location as shown in Figure 7.7. Using the *c* value of 3.945 in., the strain ε_T was found to be 94.444 microstrain. The strain calculated from the undamaged model,

ε_c, was found to be 93.668 microstrain from the same applied load at the same location. These values are tabulated in Table 7.2. From these values, the modification factor K was found to be 0.994. This value would indicate a very small loss of stiffness due to the loss of support. This modification factor was very similar to the factor found from the analytical model.

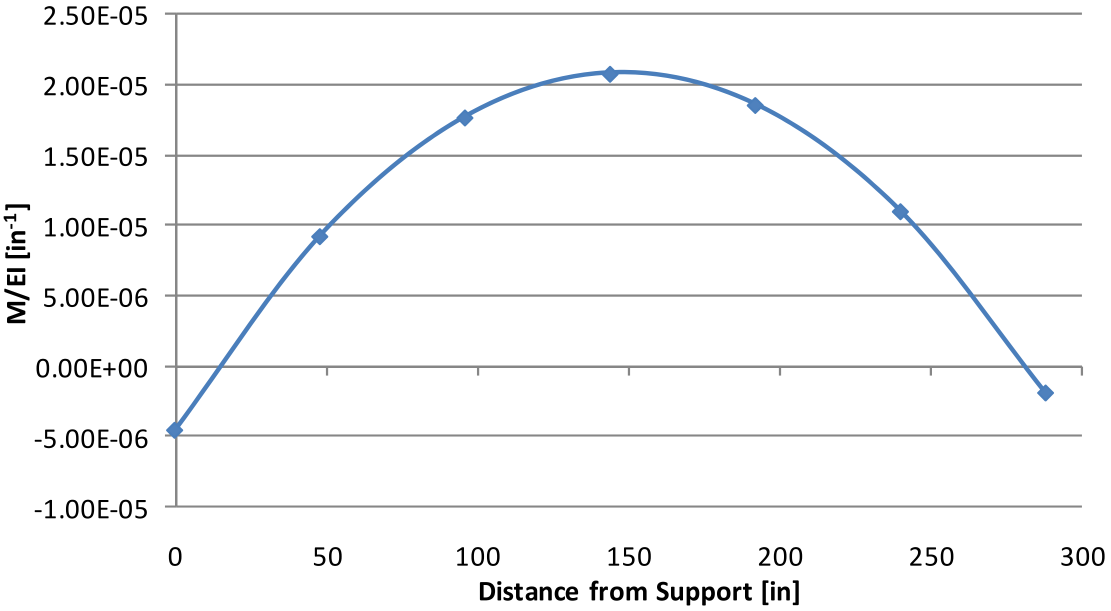

Figure 7.7: M/EI for Experimental Damage Case #1

7.3.2 Damage Case #2

Referring back to Figure 6.33, it can be seen that the damage induced by Damage Case #2 did not significantly affect the deflection profile. These results were similar to the results represented by the analytical model.

From the three different loading scenarios applied, the controlling case was again found to be a distributed load applied to girder #3. The *M/EI* term was found as a function of x, and is shown in Figure 7.8. The maximum value was located at a distance of 153.5 in. from the support, which was different from the previous case and shifted right of center. The exact mid-span of the girder was located at 144 in., and the difference was associated with unique characteristics of the constructed system. When the damage scenarios were implemented on the SAP2000 model (section 7.2), the point of maximum moment was found to exactly at 144 in. The SAP2000 model assumes that the system as perfectly symmetric and that all of the connections have the same properties. In the actual model, the connections may have differences in bolt tightening patterns, differences in support height, and slight differences in material properties. All of these unique factors played a role, and the non-symmetric nature of the structure became evident through the dynamic testing.

Using the maximum value found from Figure 7.8, the modification factor K was found to be 0.917. This value indicated an 8.3% loss of stiffness to be applied to the posted/recorded load rating, showing that the actual model was affected more by the damage than the analytical model. As a comparison, when the confidence factor, ϕ, was changed to be 1.0, the overall modification factor K was found to be 1.012. This shows that the structure would be relatively unchanged due to the damage. Given the errors found from idealizing the distributed load as a series of point loads, it is recommended that the confidence factor remain ϕ = 1.15.

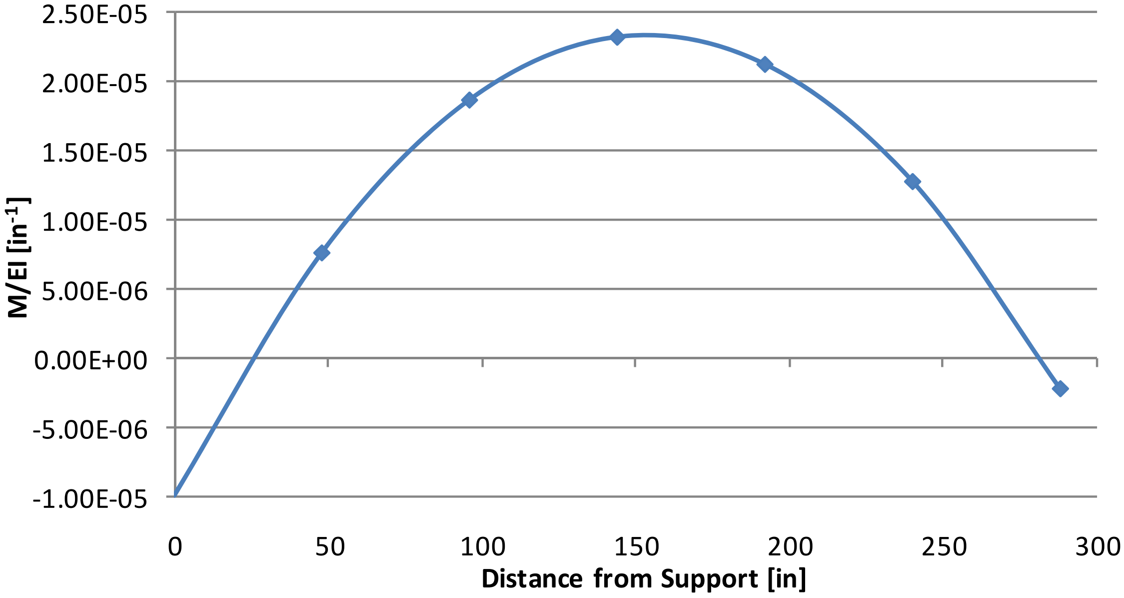

Figure 7.8: M/EI for Experimental Damage Case #2

7.3.3 Damage Case #3

The damage induced by Damage Case #3 significantly affected the deflection profile by making the structure more flexible (Figure 6.33). These results were similar to the results represented by the analytical model. When the three different loading scenarios were virtually applied to the modal flexibility matrix the controlling case was found to be a distributed load applied to girder #1, with M/EI shown in Figure 7.9.

The maximum value was located at a distance of 153.89 in., which was similar in location to Damage Case #2. From the values summarized in Table 7.2, the modification factor K was found to be 0.820. This value would indicate an 18% loss of stiffness to be applied to the posted/recorded load rating, reflecting the substantial loss due to the gusset plate removal.

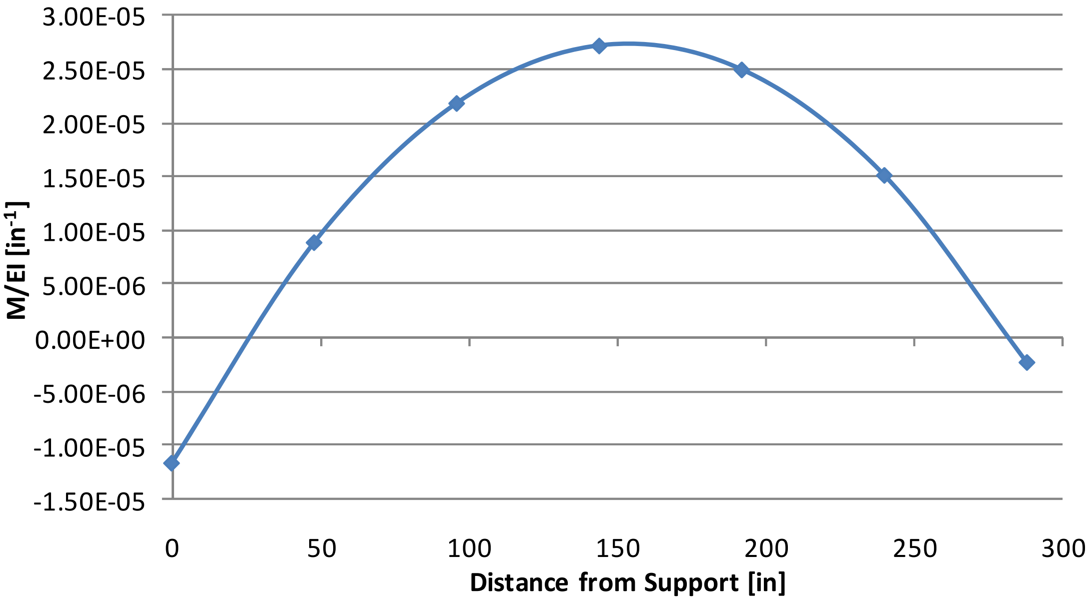

Figure 7.9: M/EI for Experimental Damage Case #3

7.4 SUMMARY

The modification factor, *K*, was developed for use from dynamic testing data, namely the modal flexibility matrix. This modification factor was a factor to be applied to an existing load rating to reduce the posted capacity of a bridge following a hazard event.

In both the analytical and experimental models, the method for acquiring K was shown. In order to obtain the strains needed for obtaining the modification factor, the moment was found from the deflection profiles. A uniform distributed load was used in each case, and was applied to each girder independently. The controlling case was always an edge girder, but changed between the two edge girders depending on the case. The center girder dispersed more of its load to the edge girders, causing significantly less deflection. When the moment was predicted, some error was found especially near the boundaries. At the supports, where the moment should be zero, the moment turned out to be a negative value. This was due to trend line fitting, as well as idealizing the uniformly distributed load assumed by the differential equation relating deflection to bending moment as a series of point loads at the nodes of the structure. A summary of the results from the analytical study is shown in Table 7.1. A summary of the results from the experimental data obtained from shaker tests on the grid model is shown in Table 7.2.

Table 7.1: Summary of Analytical Load Rating Modification Factor Values

	Description	*Damage Case 1*	*Damage Case 2*	*Damage Case 3*
M/EI	Moment / Flexural Rigidity	2.8503E-05	2.8751E-05	3.1703E-05
x_{max}	Max Moment Location	141.59	144.00	144.00
ϕ	Confidence Factor	1.15	1.15	1.15
c	Dist. to extreme fiber	3.945	3.945	3.945
ε_T	Measured Strain	1.2931E-04	1.3044E-04	1.4383E-04
ε_c	Analytical Strain	1.2681E-04	1.2681E-04	1.2681E-04
K_a	$\varepsilon_c/\varepsilon_T - 1$	-0.019	-0.028	-0.118
K_b	System Specific	0.72	0.72	0.72
K	Modification Factor	**0.986**	**0.980**	**0.915**

Table 7.2: Summary of Experimental Load Rating Modification Factor Values

	Description	*Damage Case 1*	*Damage Case 2*	*Damage Case 3*
M/EI	Moment / Flexural Rigidity	2.0818E-05	2.3375E-05	2.7351E-05
x_{max}	Max Moment Location	147.99	153.50	153.89
ϕ	Confidence Factor	1.15	1.15	1.15
c	Dist. to extreme fiber	3.945	3.945	3.945
ε_T	Measured Strain	9.4444E-05	1.0605E-04	1.2408E-04
ε_c	Analytical Strain	9.3668E-05	9.3757E-05	9.3078E-05
K_a	$\varepsilon_c/\varepsilon_T - 1$	-0.008	-0.116	-0.250
K_b	System Specific	0.72	0.72	0.72
K	Modification Factor	**0.994**	**0.917**	**0.820**

The trend between the three damage cases is clear in both of the tables. Damage Case #1 had the least change, while Damage Case #3 had the greatest change. In the experimental case, the change between the first two damage cases was very small, while in the experimental case it was much larger. The same was true when looking at Damage Case #3. Overall, the experimental cases showed more change than the analytical cases, and is attributed to the as-constructed attributes of the grid model.

The exact mid-span of the girder was located at 144 in. from the supports. When damage scenarios two and three were implemented with the SAP2000 model, the point of maximum moment was found to be exactly at 144 in., which is the location for the undamaged scenario. On the other hand, Damage Case #1, produced a maximum moment slightly to the left of center (141.59 in). The experimental model showed a similar trend, with the point of maximum moment shifting left for damage scenario one compared to the other cases. Interestingly, the point of maximum moment for the second, third, and undamaged cases was found to be around 153 in. The differences were attributed to the unique characteristics of the constructed system. The analytical model was constructed in SAP2000 assuming that the system was perfectly symmetric and that all connections and supports were exactly the same, thereby producing a midpoint of 144 in. In the actual model, the connections have differences in bolt tightening patterns, differences in support height, and slight differences in material properties. All of these unique factors play a role and shifted the point of maximum moment slightly off center.

8. EXPERIMENTAL SENSOR OPTIMIZATION STUDY

The final area of research was on the topic of optimization. Ideally, a large number of sensors would be used on a given structure to most closely identify all of the contributing modes and accurately depict the associated mode shapes. Using more sensors increases the spatial resolution of any identified modes, and also provides redundancy to the instrumentation setup. If a sensor is later found to have malfunctioned, it could be disregarded and one could rely on the remaining sensors. In reality though, sensors cost money, and each additional channel in a given Data Acquisition Unit will add cost to the system. This research compared the effects of different sensor setups on the identification results in an attempt to find the most critical sensors for each setup.

Initially, the analytical model of the grid was used as a tool for optimizing the input locations for testing of the grid (see Section 5.5). Results based on pure analytical guidance proved to not be the most accurate, and a more accurate relationship was found through experimental methods. From these tests, the number of inputs was reduced from every location to just five locations, with very little loss of accuracy in modal flexibility.

In the same manner, a systematic removal of response sensors from the testing setup was performed. The actual sensors were not removed from the structure. Instead, the response readings were removed from the full test data sets in the form of removing an entire column from the FRF matrix. This way, the exact same test data was used and the uncertainty associated with taking new data was eliminated. The modal flexibility was re-calculated and compared with the results containing the full set of sensors. The results from these tests help to show where sensors are of the most use in a testing setup used to characterize a bridge. Since more sensors translate to higher costs in hardware, software, and setup time, these results will be extremely useful for bridge testers.

The response measurements were recorded for all 21 nodes of the grid during shaker testing. The only input locations used were a reduced set of five locations as explained in Section 5.5. Each removal scheme was implemented for all three of the damage scenarios. A summary of the different removal schemes is shown in Figure 8.1, and the results are further described in the following sections.

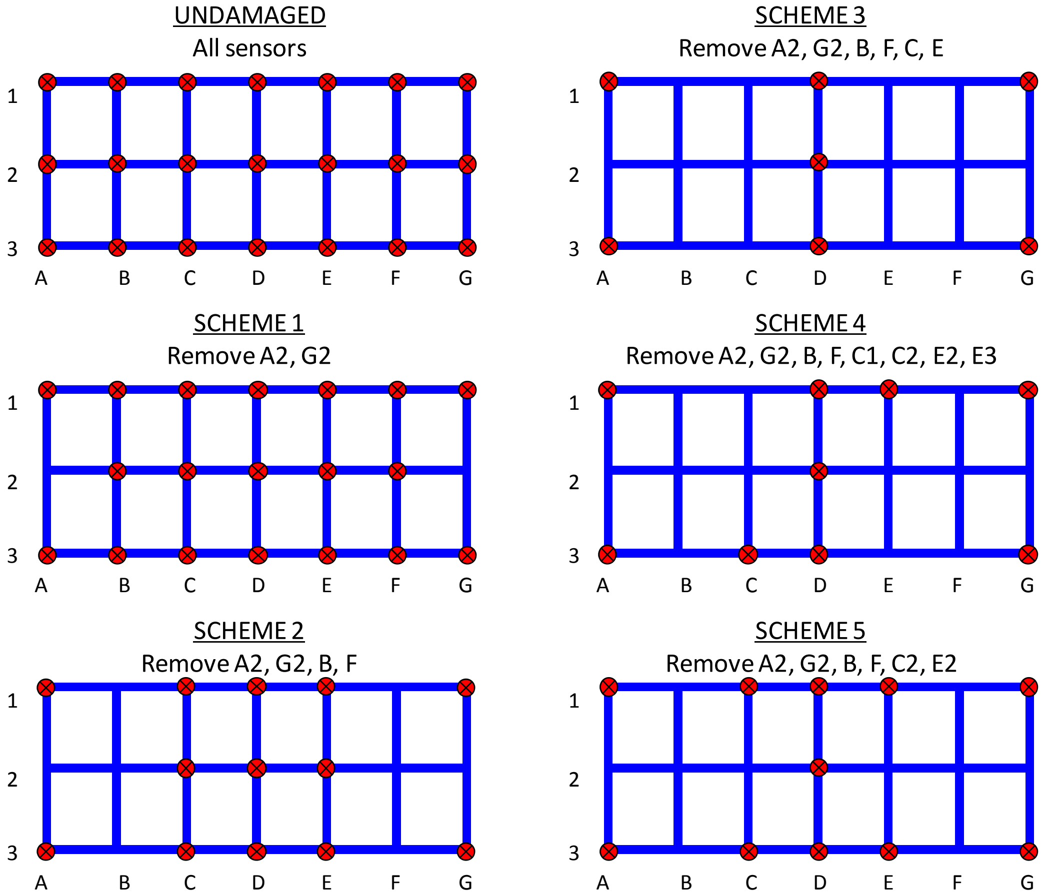

Figure 8.1: Sensor Removal Schemes

8.1 DAMAGE CASE #1

The first removal of sensor columns in the FRF matrix was implemented by removing the sensors at locations A2 and G2. As seen previously, the support sensors were important for capturing a loss of bearing type damage. It follows that having only the outside corners would be enough to capture a loss of support if the abutment were to experience scour or differential settlement. It was observed that no significant change occurred with the removal of these two sensors.

The sensors on transverse girders B and F were then removed in addition to the sensors at A2 and G2. This resulted in a slight loss of accuracy compared with the previous schemes.

Scheme #3 removed the sensors located on transverse girders C and E in addition to the previous removals, leaving only the sensors in the very middle of the grid in place. The CMIF plot from the full array of sensors is reproduced as Figure 8.2 for convenience. When compared to Figure 8.3, which is the CMIF plot for the removal of sensors for Scheme #3, it can be seen that some of the modes/peaks were affected by the reduced sensor layout. The overall amplitudes of the peaks were also reduced. This resulted in the modal flexibility being significantly changed, as noted by the deflection profiles in Figure 8.4.

The reduction of sensors in Scheme #4 matched the reduced input location setup used for the shaker testing. The problem resulting from this setup was a skewing of the results in the flexibility matrix towards one side.

Scheme #5 produced nearly the same results as Scheme #2, but did so with two additional sensors removed from the setup. This would translate to additional monetary savings while still achieving the same results.

A summary of the deflection profiles from each of the sensor removal schemes is shown in Figure 8.4. It can be seen that Scheme #3 produced very poor results. It can also be seen that Scheme #4 skewed the data to the right, while the other schemes retained high levels of accuracy.

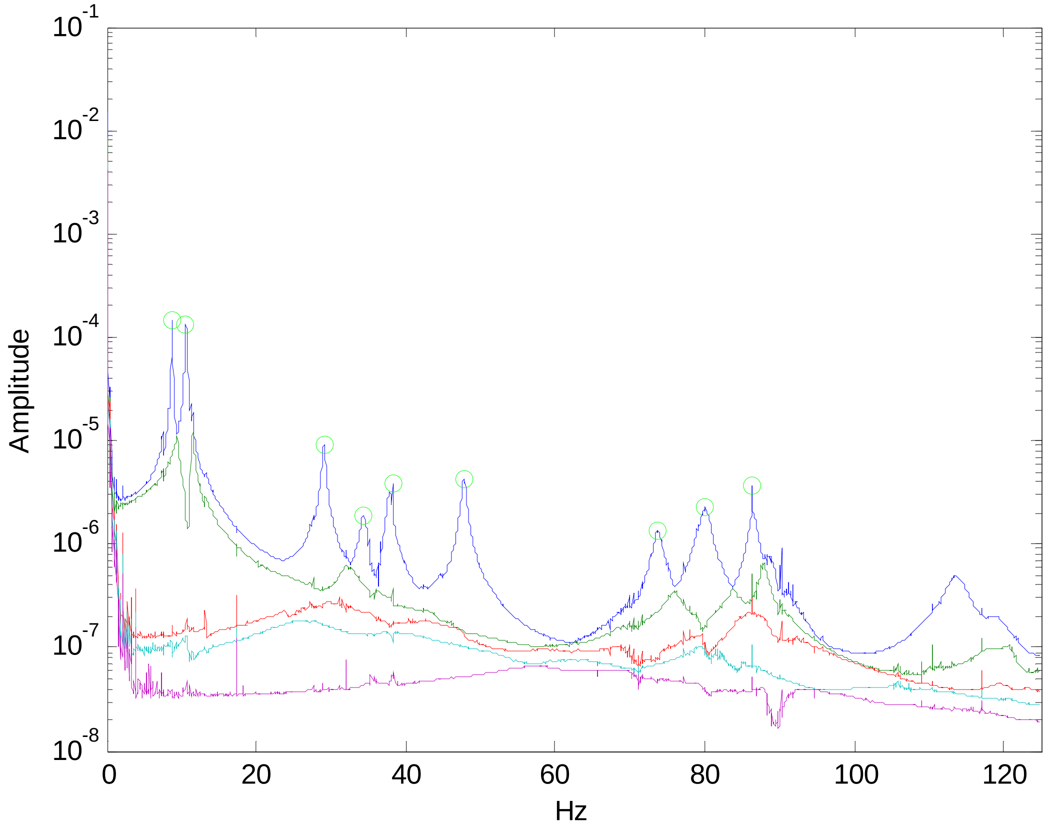

Figure 8.2: CMIF Plot - All sensors for Damage Case #1

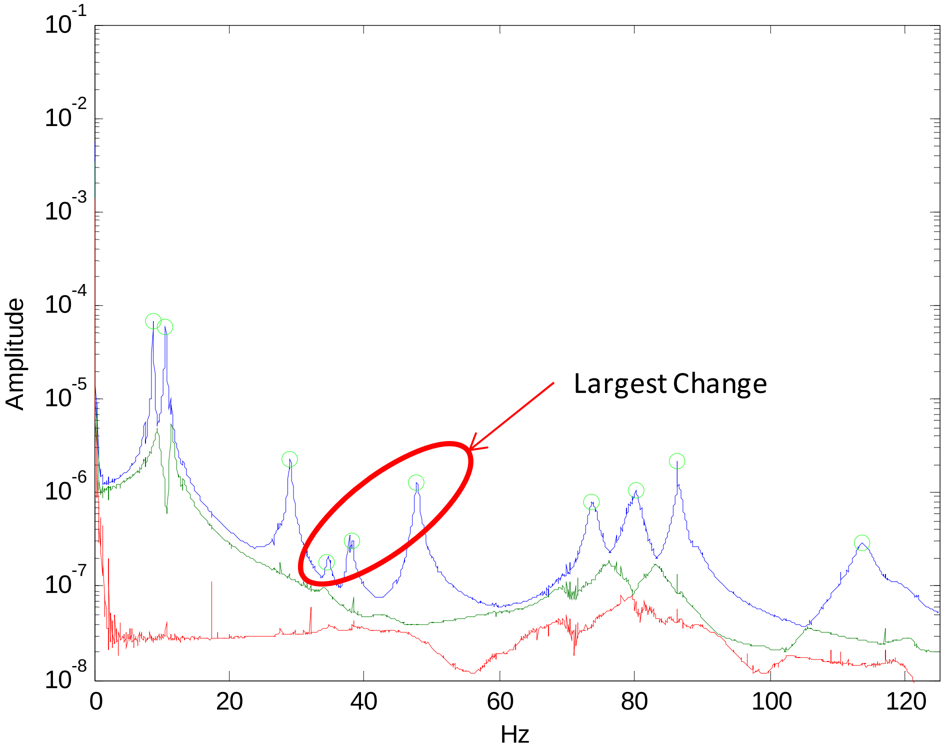

Figure 8.3: CMIF Plot – Scheme #3 for Damage Case #1

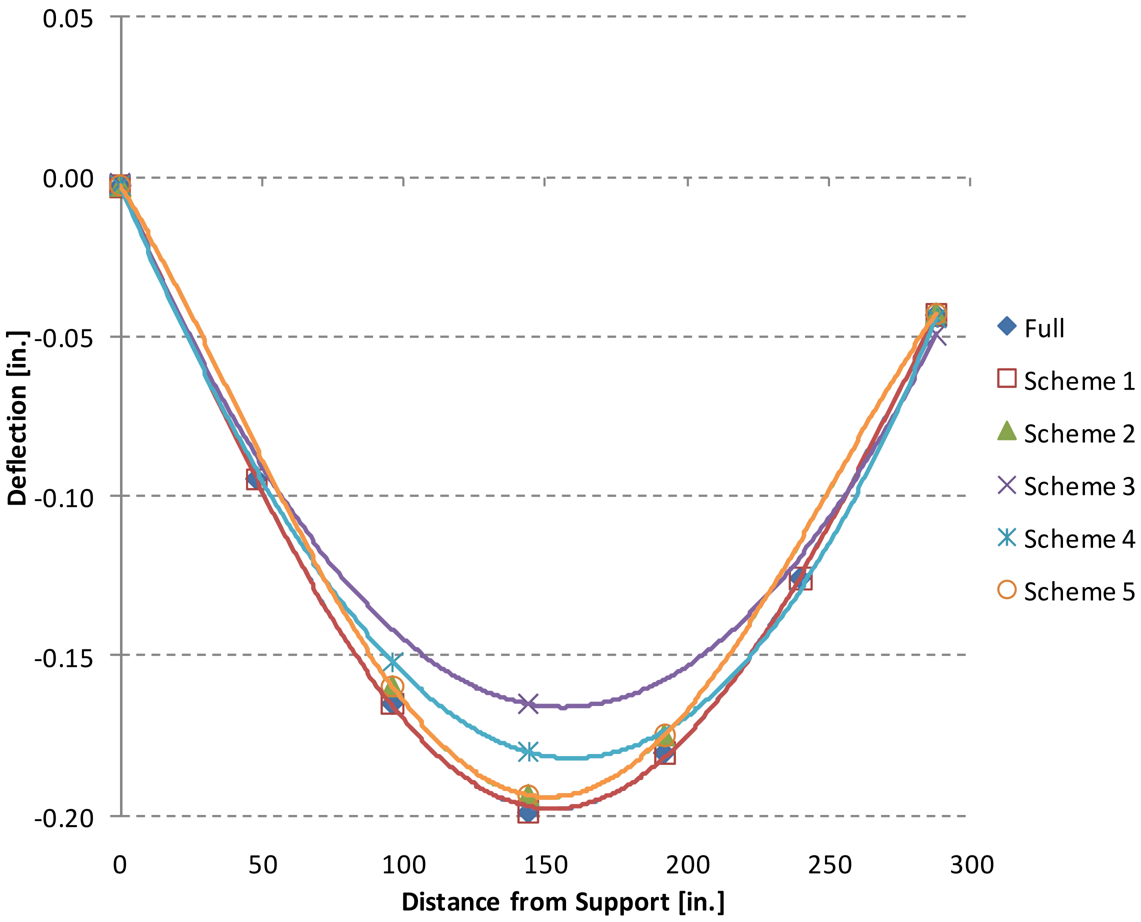

Figure 8.4: Deflection Profile for Damage Case #1

8.2 DAMAGE CASE #2

For Damage Case #2, the same systematic removal of sensors was followed, with similar results. Schemes #1 and #2 produced good results, while Scheme #3 produced very erroneous results. The CMIF plot from Scheme #3, shown in Figure 8.6, reveals that several modes were not present due to the lack of spatial resolution. Scheme #4, which matched the input locations, saw a shift in deflection profile to one side, as with Damage Case #1. Further discrepancies are also evident from the CMIF plot in Figure 8.7 which, when compared with the all sensor plot, show a reduction of the mode at around 88 Hz. This mode would likely not have been found without prior knowledge of the location. Scheme #5 showed to be identical to Scheme #2 both producing reliable results. A summary of the deflection profiles is shown in Figure 8.8.

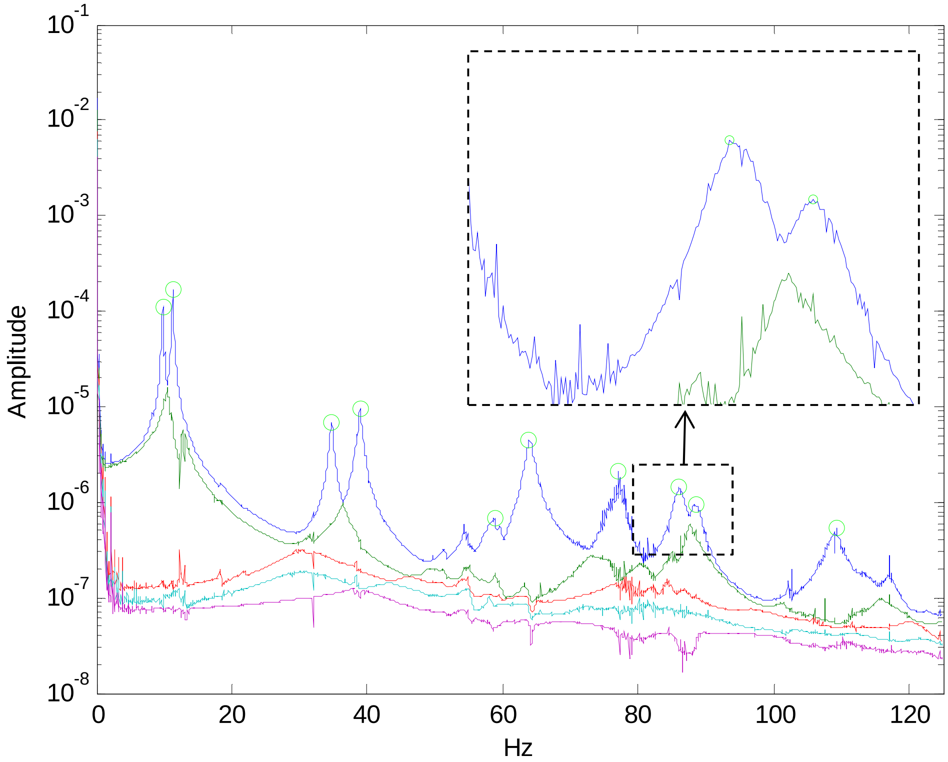

Figure 8.5: CMIF Plot - All sensors for Damage Case #2

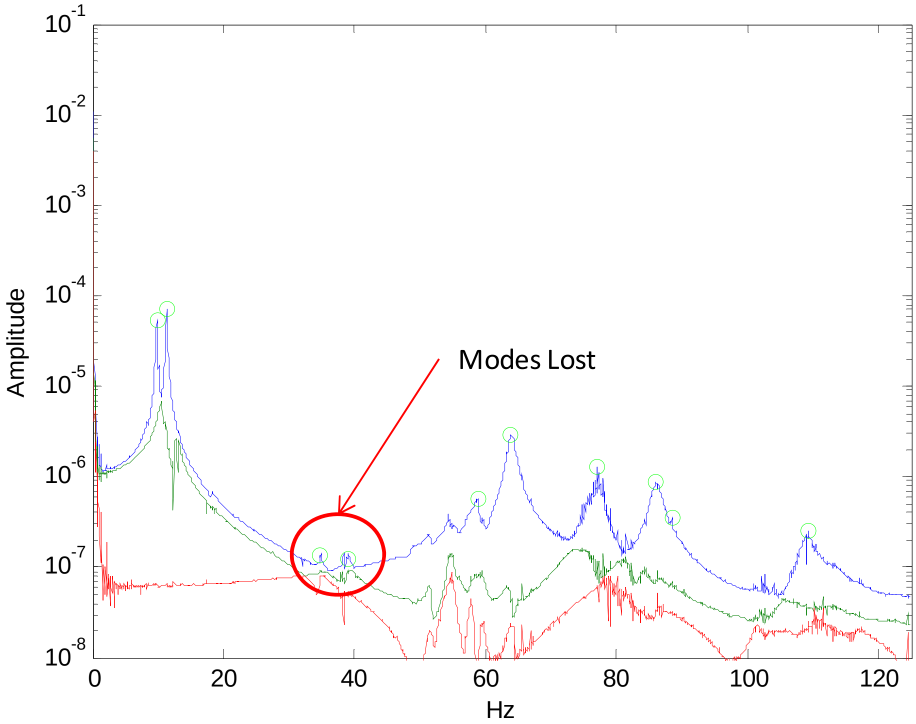

Figure 8.6: CMIF Plot – Scheme #3 for Damage Case #2

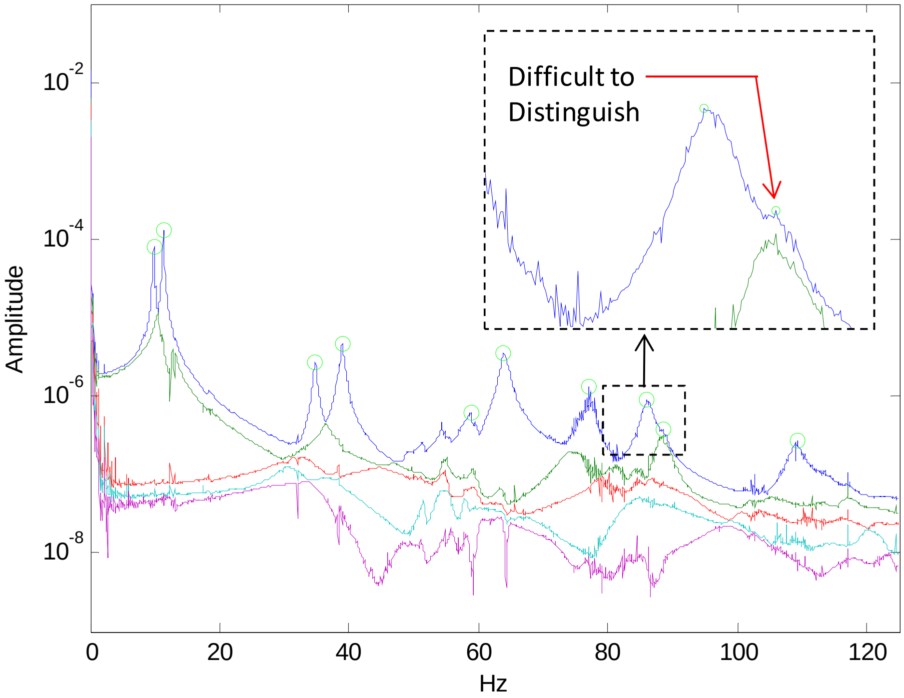

Figure 8.7: CMIF Plot – Scheme #4 for Damage Case #2

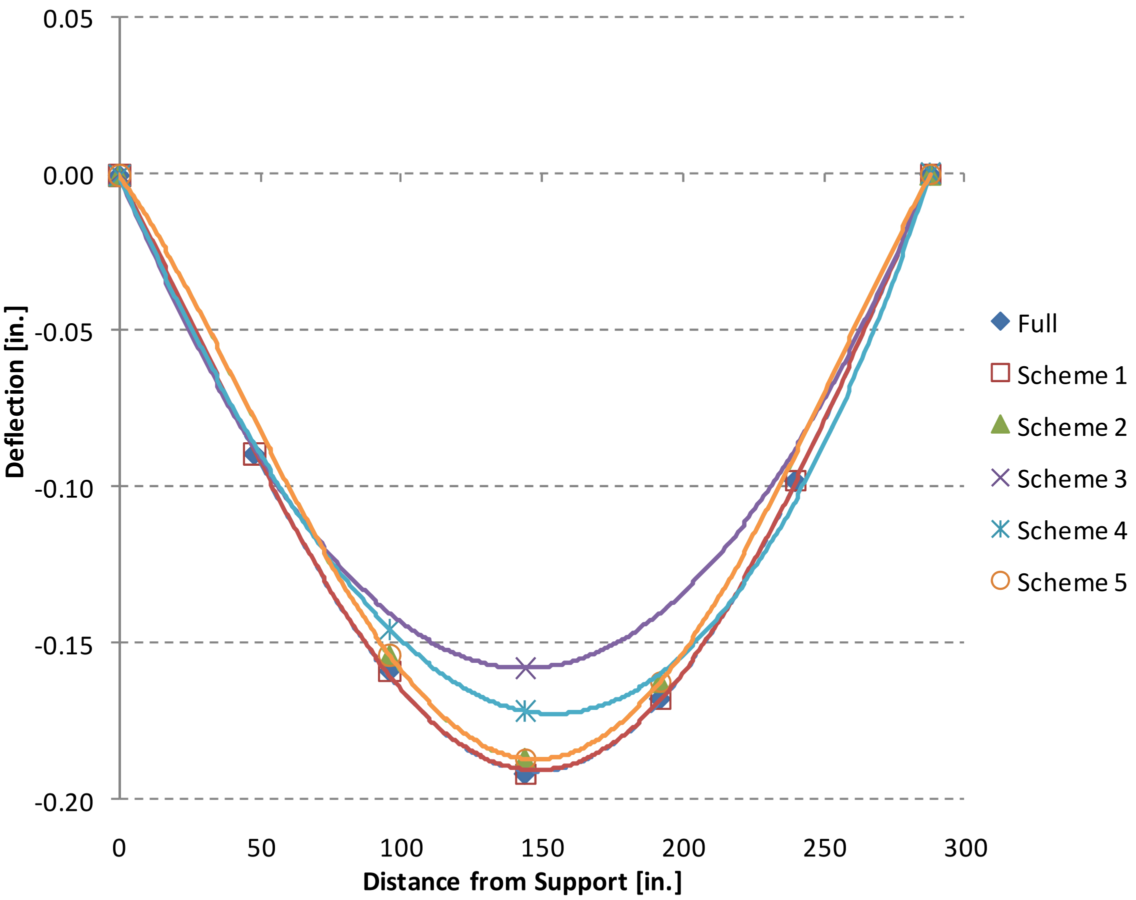

Figure 8.8: Deflection Profiles for Damage Case #2

8.3 DAMAGE CASE #3

Applying the reduction of response sensors to Damage Case #3 showed the same trends noted in the previous damage cases. The deflection profiles are summarized in Figure 8.9. Again, Scheme #3 and Scheme #4 proved to be unreliable, while the others retained a high level of accuracy. Schemes #2 and #5 saw only a slight change from the full sensor setup, and were therefore recommended as the most economical setups.

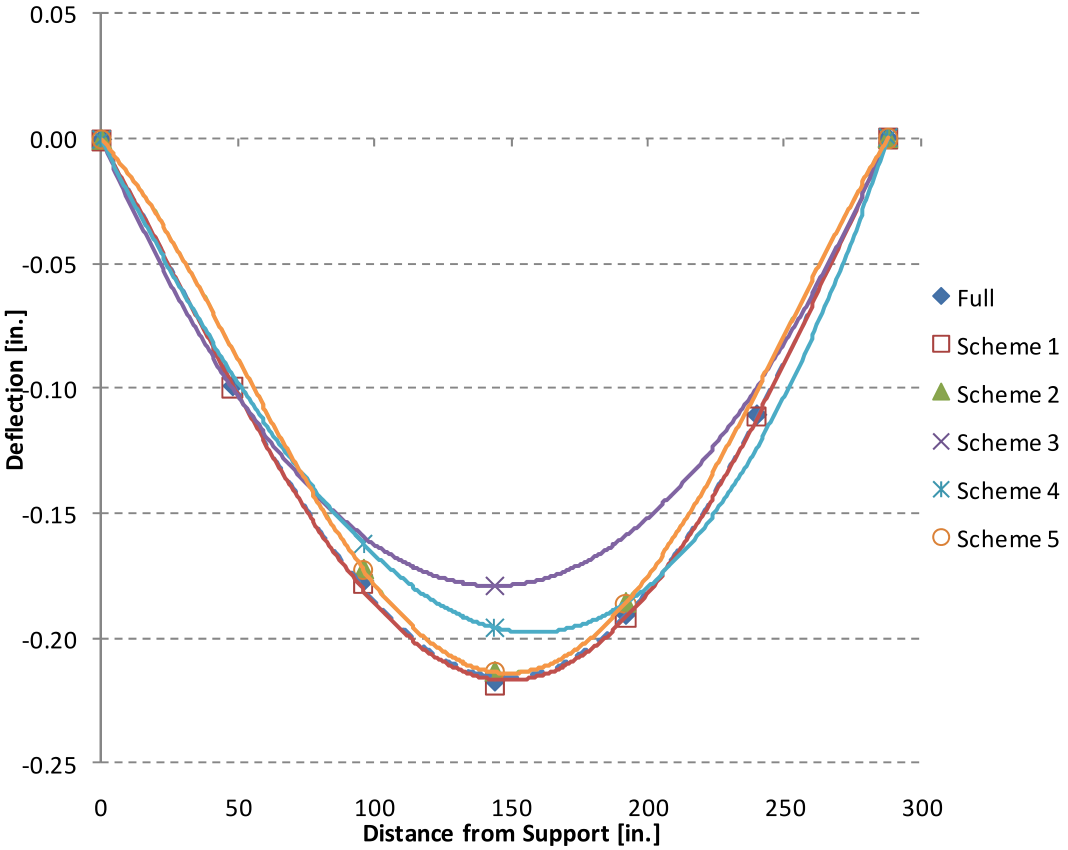

Figure 8.9: Deflection Profiles for Damage Case #3

8.4 SUMMARY

For each of the three damage scenarios, five different sensor removal schemes were implemented on the experimental data sets in the form of removing columns from the FRF matrices. The resulting data sets were processed into modal flexibility matrices, and the deflection profiles were created. It was found that Scheme #5 provided the optimal balance between the number of sensors and the accuracy of output.

When implementing high reduction of response sensors, some of the contributing modes of the response were lost. This loss resulted in a modal flexibility that was less accurate than one produced from a setup containing a high spatial resolution of sensors. It was also observed that when a high number of sensors were removed, some of the mode shapes became more difficult to distinguish. A large number of sensors on the structure led to a high spatial resolution, which facilitated easy verification of contributing modes. Also, with some of the removal schemes (#4 and #5), interpolation began to be necessary in order to connect the nodes to one another. This further reduced the clarity of the higher modes of the structure. These concepts are illustrated in Figure 8.10. When looking at the figure, the top two illustrations represent two mode shapes with all 21 response sensors. When Scheme #2 was implemented, the sensors closest to the supports were removed. As seen in the figure, the motion of the removed nodes must be assumed. When further reduced (#4 and #5), more interpolation became necessary and the shapes began to resemble other shapes. This is further amplified in the bottom of the figure, where the two shapes look nearly identical to 1st Bending Mode and 1st Torsion Mode. As can be seen, great care must be taken when interpolating results from a reduced sensor scheme.

It was also found that to obtain a reduced setup, reducing the input force locations to the central region of the structure produced the best results (Chapter 5). When the shaker device was placed near the supports, it is hypothesized that a portion of the applied force transferred to the supports from the supporting slab, producing erroneous results. In a similar manner, reducing the response sensors to the central region of the structure led the best results in a reduced sensor layout. This was attributed to the high signal to noise ratio found near the supports. Due to these factors and the results previously presented, Scheme #5 was found to be the most economical placement of response sensors. Very similar results were obtained from this sensor setup compared to the full setup, with very little loss in accuracy when comparing the deflection profiles.

Some general guidelines can be extracted from the above results for applying this approach to actual in-service bridge structures. These guidelines would be applicable to the general class of simply supported bridge structures whose dynamic behaviors are dominated by vertical bending responses. The general instrumentation scheme shown in Figure 8.11 is recommended for dynamic testing of such bridges. The instrumentation scheme for such bridges should include at least three accelerometers at the midspan location. The accelerometers should be spatially located at the outermost edges of the cross section cut through midspan, and at the centerline of the transverse cross section. The midspan location is critical for capturing the modes that contribute the most to the structure's dynamic response. The spatial distribution at the midspan section is necessary to distinguish between vertical, torsional, and butterfly modes. Accelerometers should also be located at 1/3 span length points on the extreme edges of the transverse cross section to provide additional spatial resolution to the critical modal vectors. Accelerometers should also be placed at the support locations if the goal is to monitor changes in the support conditions. Excitation locations should include each of the midspan accelerometer locations described above and at the diagonally opposed edge accelerometers in order to adequately excite the bending, torsion and butterfly modes that contribute to the modal flexibility.

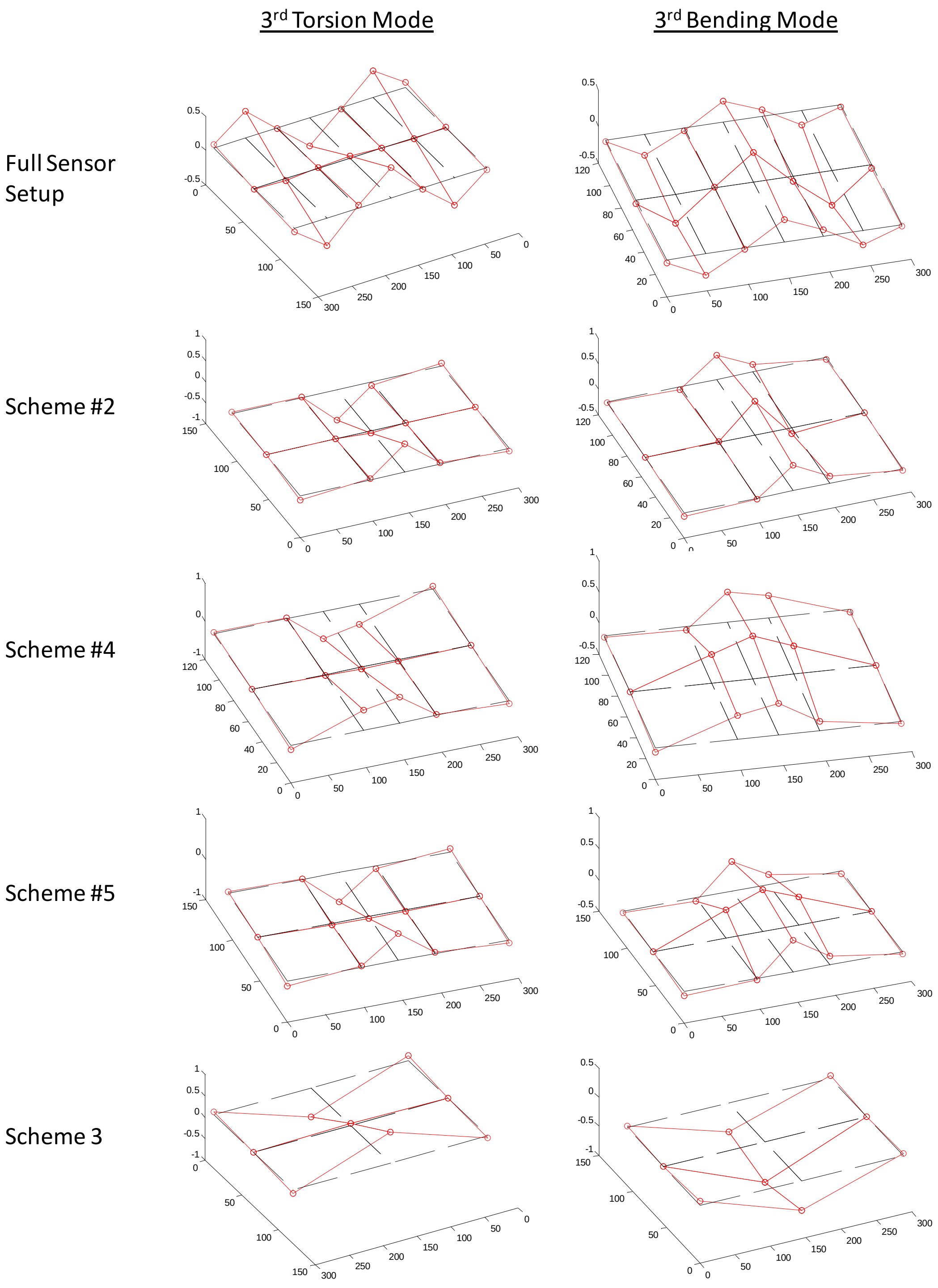

Figure 8.10: Spatial Resolution Example

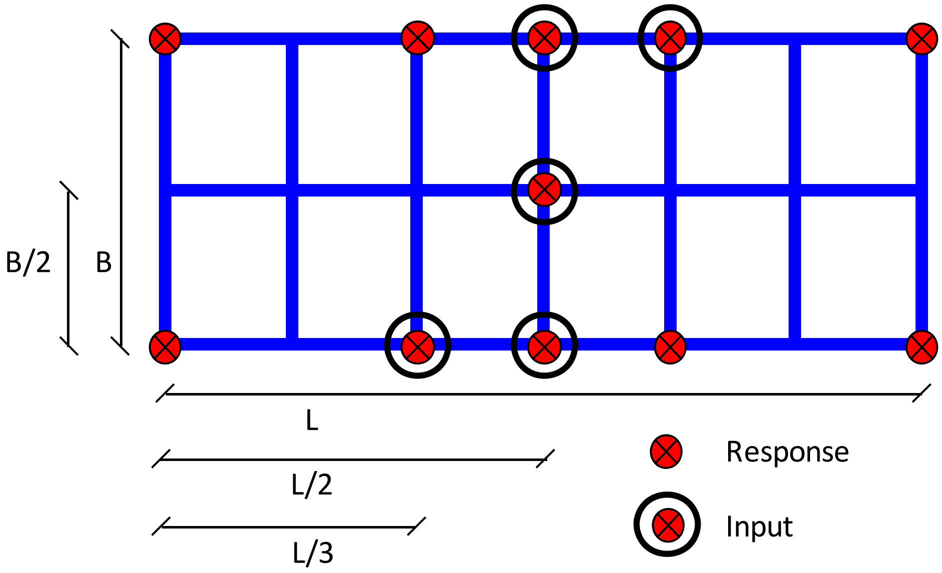

Figure 8.11: Normalized Sensor Layout

9. CONCLUSIONS

This research thesis had four primary objectives:

1. To develop an optimum bridge health monitoring strategy.
2. To explore the pros and cons of different dynamic testing strategies.
3. To experimentally optimize a sensor setup.
4. To develop a modified load rating from dynamic characterization.

The research was completed exclusively in the laboratory; however, this was considered a necessary starting point for the research to be subsequently applied to in-service bridge structures. A cantilever beam model was used as a simple model in the laboratory in order to verify the dynamic testing strategies and characterization procedures. After testing on the cantilever beam was completed, a larger steel grid structure was fully tested and characterized in its undamaged state as well as in three different induced damaged states.

In order to fulfill the first objective of research, the other three objectives had to be met. The results and conclusions from those three objectives are presented first, followed by conclusions from the first objective.

9.1 DYNAMIC TESTING STRATEGIES

The grid model was tested using a variety of dynamic and static testing strategies. The static load testing proved to be reliable, but static testing of an in-service structure can be difficult to accomplish. Obtaining measurements from strain devices on the structure proved to be inaccurate, but since several other researchers have obtained good results from strain measurements, the errors were attributed to either improper installation of the strain gages or inconsistencies arising from the cabling and data acquisition setup and the small level of loading used relative to the structure's stiffness.

All three of the dynamic testing strategies (impact, shaker, and ambient testing) provided very similar natural frequencies and mode shapes. Mode shapes from ambient testing were harder to locate than mode shapes from the forced input methods due to the amount of extraneous noise present. In all three cases, when damage was induced to the structure, the damage could be detected by a change in natural frequencies and mode shapes. In some scenarios the shifts in natural frequencies were not very large, whereas the changes in mode shapes were very noticeable in each damage scenario. In some damage cases, new mode shapes were detected from the damage induced.

One key characteristic that was extracted from the dynamic testing was the modal flexibility matrix. A properly scaled modal flexibility matrix can only be found directly from the dynamic testing results in which input force was measured, namely the impact and shaker testing. The modal flexibilities from these two testing strategies for the undamaged model were found to be very close to one another, and were between 14 - 19% from the analytical model. This difference was attributed to modal truncation. An un-scaled, pseudo modal flexibility was extracted from the ambient testing, but proved to be very unreliable. Correlation functions that transformed the random ambient vibration data into pseudo impulse response functions were used in conjunction with the CMIF algorithm to obtain the pseudo modal flexibility matrix.

In order to evaluate the effectiveness of the different testing methods when it came to pre- and post- damage, all three dynamic tests were also performed after each damage scenario. While impact testing was easier to implement in the laboratory setting, the shaker testing provided better results when the damage scenarios were considered. Impact testing proved to be rapid to implement and setup with a lower cost, but would require on-site personnel in a bridge testing situation. Shaker testing was more difficult to set up due to the weight and cumbersome size/shape of the shaker device, but would be able to be setup for remote controlling on a bridge. The downside to this approach would be the high cost of the shaker device. When the modal flexibilities from the impact testing for the three damage cases were compared with the undamaged case, the results were somewhat confusing. All three of the damage cases appeared to result in a structure that was stiffer than the undamaged case, but each of the induced damage scenarios should have led to a reduction in stiffness. On the other hand, the shaker test results showed a similar trend to the analytical model, where each damage case showed a greater reduction of stiffness. By performing both types of tests before and after the damage, a direct comparison between the tests could be performed. Overall, the shaker testing provided better results.

It was hoped that ambient testing would provide a means of long term monitoring and bridge evaluation, given that it is a proven, low-cost structural health monitoring method. Several researchers have shown the effectiveness of using ambient monitoring to detect changes in a structure thereby pointing to needed maintenance. This has helped bridge owners to maintain their bridges more efficiently. Applying this same concept to rapid response and recovery operations by providing a quantifiable bridge safety would have been ideal. Therefore, being able to correlate ambient results to impact or shaker results is desirable. Through this study, it was found that a reliable correlation between these different testing types was not possible. Disregarding amplitude differences, the pseudo modal flexibility found from ambient testing did not resemble the modal flexibility found from either impact or shaker testing. While mode shapes and frequencies were similar to the other methods, these indicators alone only pointed to the fact that damage occurred, and could not quantify the damage.

Three different data acquisition architectures were used for the testing performed. The National Instruments SCXI device with capacitive accelerometers did not contain the resolution necessary, and provided inferior results. The National Instruments PXI device with piezoelectric accelerometers provided very good results. The Data Physics Corp. DAQ device also provided very good results. The down side to the Data Physics device was the cost. A similar setup with a NI PXI device was around half the cost yet still provided good results. When shaker testing was performed with the Data Physics device, the results were cleaner due to internal filtering and anti-aliasing hardware which was not present in the NI

PXI. Overall, the National Instruments PXI device provided the best economy for being able to set up a remote monitoring system and obtain usable results.

Some off-the-shelf software was also used and evaluated for comparison purposes. M+P International's software, "Smart Office," was used as a testing setup and post-processing program. Several problems were encountered with this software. The software was very prone to crashing, and proved to be an unstable platform for post-processing of data. It also did not allow the direct computation of modal flexibility, the end goal of the dynamic characterization. The modal properties were not easily exportable to other programs such as MATLAB, and the overall usability was poor. The benefit of the software was its ability to provide the framework for impact testing. This testing platform was easy to use and follow.

The Data Physics device came with proprietary software and was able to facilitate impact testing. It was also able to facilitate shaker testing and ambient testing, and proved to be a very easy to use program. Being able to facilitate all three different dynamic tests was an advantage. This program also did not contain the capability for finding modal flexibility or other dynamic characterization properties. As noted earlier, the limiting factor was cost.

The post processing was therefore performed in MATLAB with code written by the author. This proved to be the best method for post-processing the data into the desired results. Thinking forward, the downside to this approach would be the need for training individuals to use the code written in an efficient and effective manner.

Overall, the NI PXI data acquisition architecture coupled with shaker testing and post processing in MATLAB proved to be the best choice for a pre- and post- hazard condition evaluation of bridges.

9.2 EXPERIMENTAL SENSOR OPTIMIZATION

Both input and output optimization studies were performed experimentally on the grid model. From these studies, it was found that the analytical model produced in SAP2000 did not accurately predict the experimental results. By comparison, it was found that 1st Bending, 1st Torsion, and 1st Butterfly modes contributed the most to modal flexibility, and were therefore key modes to capture during subsequent testing. It was found that supplying input from the shaker into five central locations produced nearly identical results as supplying input to all locations on the structure. Input Cases #6 and #7, as discussed in Section 5.5, proved to provide the best combination of accuracy coupled with a low number of needed input locations.

Five different sensor removal schemes were implemented on the experimental data in the form of removing columns from the FRF matrix. The resulting data was processed into modal flexibility, and the deflection profiles were created and compared to the full array of sensors. It was found that Scheme #5 (see Section 5.5) was the optimum balance between number of sensors and accuracy of output.

It was also found that when implementing a high reduction of response sensors, some of the contributing modes of the response were lost. This loss resulted in a modal flexibility that was less accurate. It was observed that when a high number of sensors were removed, some of the mode shapes became more difficult to recognize because of low spatial resolution, also leading to a less accurate modal flexibility.

Overall, it was found that keeping both the input and response locations in the central region of the structure produced very accurate results, while keeping input and response locations only near the supports produced marked changes in the modal flexibility of the structure. However, having response sensors on the supports allowed for locating damage caused from a change is support condition. For application on a simply supported in-service bridge structure, a normalized sensor setup was created (Section 8.4). It was found that the first bending and torsion modes, as well as the first butterfly mode were important contributors to accurate modal flexibility, and were able to be accurately represented with sensors in the central region of the structure. An important discovery was that the analytical modeling did not accurately represent the modes with the highest contributions. Therefore, using computer algorithms based upon these analytical models, as many researchers have done, may not be the most accurate approach. An analytical model is simply one of many possible idealizations of an actual structure that may or may not accurately reflect the actual behavior of the structure, especially more complex structures.

9.3 MODIFIED LOAD RATING

The dynamic characterization of a grid model structure was presented in the form of natural frequencies, mode shapes, and modal flexibility. These values represent a quantitative way of presenting the status of a bridge following a hazard event. Many engineers would not know how to interpret the data, let alone the bridge owners, transportation officials, etc. Therefore, in order to present results that would be more conceptual and useful to bridge owners and others, a modified load rating procedure was developed that utilizes these dynamic characterization results. The modified load rating represents a simple number that officials could use to assess the safety and serviceability of a bridge following a hazard event. The modification factor, K, was developed for use from dynamic testing data, namely the modal flexibility matrix. This modification factor is a factor to be applied to an existing load rating to reduce the posted capacity of a bridge following a hazard event. The benefit with this approach was twofold: one, eliminating the need for bridge inspectors to immediately assess the safety of a bridge subjected to a hazard event, and two, eliminating the need for a finite element model that must be updated in order to obtain a new load rating following the hazard.

The modification factor was developed from the AASHTO specifications applicable to static load testing of in service bridges. It was shown that the modal flexibility derived from the dynamic testing of the structure could be used to create a modified load rating for a bridge.

Many assumptions were used in the development of the modification factor. The bridge must be a simply supported, single span structure. Multiple spans would work as long as they are simply supported, and are not continuous over supports. Also, the assumption of a uniformly distributed load was used. To mitigate the error found from discretizing the uniformly distributed load into a series of point loads, a confidence factor, ϕ = 1.15, was created. Using this factor reduced the modification factor, K, thereby producing a lower modified bridge rating which would therefore be conservative. It was also assumed that the deflections predicted by modal flexibility could be interpolated to higher values, i.e. rating truck values. Assuming that the structure will behave in the linear elastic range up to the loads produced by a rating truck is unproven, and needs further study. It is recommended that a series of static diagnostic and proof load tests be performed alongside dynamic characterization on an in-service bridge to validate the effectiveness of this approach.

The internal strains used in the calculation of the modification factor were found from the deflections produced from multiplying the modal flexibility matrix by a load vector. Some error was found near the supports and at mid-span from this method, and was due to the uniformly distributed load being represented as point loads at discrete points. It is therefore recommended that further study be done with the flexibility matrix to find the internal strains from matrix structural analysis using element stiffness coefficients. This could then be compared to the aforementioned procedure to validate and compare its effectiveness. It is believed that the use of deflection profiles to find strains, as outlined in this thesis, would be easier for engineers and bridge owners to use, and may be more applicable for personnel training purposes.

9.4 OPTIMUM BRIDGE HEALTH MONITORING STRATEGY

The overarching objective of the research was to recommend an optimum bridge health monitoring strategy. While this was the primary objective, the previously mentioned three objectives were important contributors to this goal.

It is important to note that the laboratory study presented had a limited scope. The grid model that was tested was a simply supported, girder-type structure. Therefore, the applications presented are limited to simply supported girder bridge structures. The results of this study would not be applicable to other types of bridge structures (trusses, arches, long-span structures, etc.) without further investigation since the behaviors of these structures are fundamentally different than a simply supported girder bridge. The grid model also did not contain a concrete deck. A concrete deck would substantially change the response of the structure because of the added stiffness as well as the composite action that could be provided by the slab. While the lab model did not include a slab, it is hypothesized that the approaches presented here would still be applicable to actual bridges, whether or not their concrete decks are composite, because the dynamic behavior of these structures will still be governed by bending responses.

In order to rapidly and remotely assess the damage to a bridge following a hazard event, a dynamic testing approach was needed. It was found that dynamic testing by shaker testing provided the best results, and is recommended as the best test strategy for quantifying damage. It should be noted that any dynamic method utilized in structural characterization will contain some error. Even when testing a very simply cantilever beam, errors of around 7% were found. This was further amplified when the grid model was tested, and is expected to increase further when an in-service structure is tested.

While shaker testing was found to be the best method, it still has some inherent difficulties associated with it. One problem encountered with shaker testing was the cost and size of the shaker. A long stroke dynamic linear mass shaker was used for the laboratory testing, but very little amplitude was needed to excite the structure. This shaker was coupled to the structure and placed on the supporting slab underneath the structure.

For an in-service bridge situation, this would be difficult and expensive to accomplish, especially given that using several excitation locations provides the best results. It is therefore recommended that the use of multiple, small-scale mass shakers be studied. Several manufacturers produce low cost mass shakers, primarily for the audio industry, to enhance the felt bass effect of sound. Given that only a small force amplitude is needed in order to accurately characterize a structure, these shakers may prove to be an ideal solution for remotely characterizing bridges by dynamic testing. An array of these shakers could be set up on a monitored bridge and remote control of the input would be possible, eliminating the need for on-site personnel.

It was also found that only a small number of sensors (as little as seven) were needed to accurately characterize the structure, and these were located in the central region of the span. While a full array of sensors would provide the best results and resulting characterization, using a smaller number still provides very usable results. The recommended optimum sensor scheme was presented in Chapter 8.

Because of the variability of constructed systems, along with the observation that finite element modeling alone cannot predict the uniqueness of a constructed system, it is recommended that a pre-incident test be completed on any monitored bridge. This pre-incident, or "baseline," test would need to be done with the same excitation device used for the post-incident evaluation. It would be ideal for this pre-incident test to be completed with a full array of sensors in order to gain a more complete and reliable dynamic characterization. The sensor setup could then be reduced to the scheme presented here for long term monitoring and post-incident measurements. While ambient testing does provide some insight, it is not recommended for specific hazard assessment analysis. A measured input is needed in order to achieve a modified load rating, and this may be more feasible using small-scale shakers.

Finally, it was found that a load rating modification factor can be obtained using the dynamic test results. This was accomplished in a laboratory setting alone and therefore needs more research and verification on in-service bridges in order to evaluate its full effectiveness. It is recommended that the modification factor, *K*, found from dynamic testing be compared to the modification factor found from a static diagnostic load test on a girder bridge to validate its effectiveness. The method employed in this research was based off of a simple approach derived from the AASHTO bridge evaluation specifications and utilized deflection profiles obtained using the modal flexibility matrix. While this was a simple approach, it was found to be effective. Further investigation using matrix transformations to find the internal strains directly from the flexibility matrix is recommended as a possible alternative means of obtaining the data necessary for a modified load rating.

Implementing the guidelines presented here would enable bridge owners, DOT personnel, and emergency response personnel to have confidence when evaluating the condition of a bridge subjected to a hazard event. The approach presented here could be implemented both rapidly and remotely with minor amount of additional effort and cost, thereby decreasing the time necessary to evaluate the serviceability and safety of bridges affected by hazard events. This would in turn create a faster emergency response and restore critical supply chains to an affected area.

10. BIBLIOGRAPHY

AASHTO, American Association of State Highway and Transportation Officials. (2008). *The manual for bridge evaluation* (First Edition ed.). Washington, DC: AASHTO.

AASHTO, American Association of State Highway and Transportation Officials. (2010). *Bridging the gap.* Retrieved 11/3, 2010, from www.transportation1.org/bridgereport/problems.html

AISC, American Institute of Steel Construction. (2005). *Steel construction manual* (Thirteenth Edition ed.). The United States of America: American Institute of Steel Construction.

Aktan, A. E., Catbas, F. N., Grimmelsman, K. A., Pervizpour, M., Curtis, J. M., Shen, K., & Qin, X. (2002). Health monitoring for effective management of infrastructure. *Proceedings of SPIE, 4696* 17.

Aktan, A. E., Lee, K. L., Chuntavan, C., & Aksel, T. (1994). Modal testing for structural identification and condition assessment of constructed facilities. *Society of Photo-Optical Instrumentation Engineers (SPIE) Conference Series, 2251* 462.

Allemang, R. J., & Brown, D. L. (2006). A complete review of the complex mode indicator function (CMIF) with applications. *Proceedings of ISMA International Conference on Noise and Vibration Engineering, Katholieke Universiteit Leuven, Belgium.*

Allemang, R. J. (1999). *Vibrations: Experimental modal analysis. UC-SDRL-CN-20-263-663/664 course notes*. Cincinnati, Ohio: UC-Structural Dynamics Research Laboritory. Retrieved from http://www.sdrl.uc.edu/academic-course-info/vibrations-iii-20-263-663

ASCE, American Society of Civil Engineers. (2009). *Infrastructure fact sheet.* Retrieved 11/01, 2010, from http://www.infrastructurereportcard.org/sites/default/files/RC2009_bridges.pdf

Brownjohn, J. M. W., Xia, P. Q., Hao, H., & Xia, Y. (2001). Civil structure condition assessment by FE model updating: Methodology and case studies. *Finite Elements in Analysis and Design, 37*(10), 761-775.

Bureau of Transportation Statistics. (2010). *National transportation statistics.* Washington, DC: Bureau of Transportation Statistics. Retrieved from http://www.bts.gov/publications/national_transportation_statistics/

Catbas, F. N. (1997). *Investigation of global condition assessment and structural damage identification of bridges with dynamic testing and modal analysis.* University of Cincinnati).

Catbas, F. N., & Aktan, A. E. (2002). Condition and damage assessment: Issues and some promising indices. *Journal of Structural Engineering, 128*, 1026.

Catbas, F. N., Brown, D. L., & Aktan, A. E. (2004). Parameter estimation for multiple-input multiple-output modal analysis of large structures. *Journal of Engineering Mechanics, 130*, 921.

Catbas, F. N., Brown, D. L., & Aktan, A. E. (2006). Use of modal flexibility for damage detection and condition assessment: Case studies and demonstrations on large structures. *Journal of Structural Engineering, 132*, 1699.

Catbas, F. N., Ciloglu, S. K., & Aktan, A. E. (2005). Strategies for load rating of infrastructure populations: A case study on T-beam bridges. *Structure and Infrastructure Engineering, 1*(3), 221-238.

Catbas, F. N., Gul, M., & Burkett, J. L. (2008). Damage assessment using flexibility and flexibility-based curvature for structural health monitoring. *Smart Materials and Structures, 17*, 015024.

Chopra, A. K. (2007). *Dynamics of structures: Theory and applications to earthquake engineering* (Third Edition ed.). Upper Saddle River, New Jersey: Pearson-Prentice Hall.

Ciloglu, S. K. (2006). *The impact of uncertainty in operational modal analysis for structural identification of constructed systems.* Drexel University).

Cloutier, D., & Avitabile, P. (2009). Shaker/Stinger effects on measured frequency response functions. *IMAC 27,* Orlando, Florida.

Craig Jr., R. R., & Kurdila, A. J. (2006). *Fundamentals of structural dynamics* (Second Edition ed.). Hoboken, New Jersey: John Wiley & Sons, Inc.

Doebling, S. W., & Farrar, C. R. (1996). Computation of structural flexibility for bridge health monitoring using ambient modal data. *Proceedings of the 11th ASCE Engineering Mechanics Conference,* 1114–1117.

Farrar, C. R., Doebling, S. W., Cornwell, P. J., & Straser, E. G. (1997). Variability of modal parameters measured on the alamosa canyon bridge. *Proceedings-SPIE The International Society for Optical Engineering,* 257-263.

Friedland, I. M., Ghasemi, H., & Chase, S. B. (2006). The FHWA Long-Term Bridge Performance Program. *Technical Memorandum of Public Works Research Institute, 4009*, 175-181.

Kangas, S., Wang, X., Padur, D., Li, Z., Lui, L., Helmicki, A., Hunt, V. (2004). Field test-based calibration of bridge finite element models for condition assessment. *Proceedings of ASNT Structural Materials Technology VI: An NDT Conference,*

Mayes, R. L., & Gomez, A. J. (2006). Part 4: What's Shakin', Dude? Effective Use of Modal Shakers. *Experimental Techniques, 30*(4), 51-61.

Michael Baker Jr., I., & United States. (1995). *Bridge inspectors training Manual/90*. Washington, D.C.: U.S. Department of Transportation, Federal Highway Administration.

Moore, M., Phares, B., Graybeal, B., Rolander, D., & Washer, G. (2001). *Reliability of Visual Inspection for Highway Bridges, Volume I: Final Report*

National Bridge Inspection Standards; Final Rule, 69 Federal Register 239 (14 December 2004), pp. 74419-74439.

NCHRP, National Cooperative Highway Research Program, & Lichtenstein, A. G. (1998). *Manual for bridge rating through load testing* Transportation Research Board, National Research Council.

Phillips, A. W., & Allemang, R. J. (1998). The enhanced frequency response function (eFRF): Scaling and other issues. *Proceedings of the International Seminar on Modal Analysis, 1* 385-392.

Raghavendrachar, M., & Aktan, A. E. (1992). Flexibility by multireference impact testing for bridge diagnostics. *Journal of Structural Engineering, 118*, 2186.

Ren, W. X., Harik, I. E., Blandford, G. E., Lenett, M., & Baseheart, T. M. (2004). Roebling suspension bridge. II: Ambient testing and live-load response. *Journal of Bridge Engineering, 9*, 119.

Schwarz, B. J., & Richardson, M. H. (1999). Experimental modal analysis. *CSI Reliability Week, Orlando, FL*

Toksoy, T., & Aktan, A. E. (1994). Bridge-condition assessment by modal flexibility. *Experimental Mechanics, 34*(3), 271-278.

Turner, L. L., Wald, D. J., & Lin, K. W. (2009). ShakeCast: Caltrans deploys a tool for rapid postearthquake response. *TR News,* (261) U.S. Department of Transportation. (2010). *National transportation statistics 2010.* Washington, DC: Bureau of Transportation Statistics.

Weingroff, R. F. (1996, Federal-aid highway act of 1956: Creating the interstate system. Public Roads, 60(1)

Zhang, Z., & Aktan, A. E. (1998). Application of modal flexibility and its derivatives in structural identification. *Research in Nondestructive Evaluation, 10*(1), 43-61